

Università degli Studi di Napoli *Federico II*

DOTTORATO DI RICERCA IN
FISICA

Ciclo XXXIII

Coordinatore: prof. Salvatore Capozziello

Exploring the transient Universe in the multi-messenger Astronomy era

Settore Scientifico Disciplinare FIS/05

Dottorando
Fabio Ragosta

Tutor
Dott.ssa Maria Teresa Botticella
Prof. Giovanni Covone

Anni 2018/2021

Contents

Introduction	5
1 Supernova types	10
1.1 SN empirical classification	10
1.2 SN progenitors and explosion mechanisms	16
1.2.1 Thermonuclear SNe	16
1.2.2 Core Collapse SNe	20
1.2.3 Different explosion mechanisms	22
1.3 The SN remnants	23
2 SN progenitors	27
2.1 Direct detection of SN progenitors	30
2.2 Hydrodynamic modelling of the spectro-photometric evolution	33
2.3 SN rate and progenitors	35
2.3.1 Core Collapse SN rate	36
2.3.2 Thermonuclear SN rate	38
3 SN rates	44
3.1 The first SN survey and rate measurement	44
3.2 Control Time and detection efficiency	47
3.3 SN rate in a cosmic volume and in a galaxy sample	50
3.4 SN surveys and rate measurements	52
4 SUpernova Diversity And Rate Evolution	57
4.1 SUDARE	57

4.2	Image reduction and difference image analysis	62
4.3	Transient detection	63
4.4	Detection efficiency	74
4.5	Transient classification	76
4.6	SN sample	79
4.7	Galaxy sample	80
4.8	SN rate measurements	91
4.8.1	SN rate per unit volume	93
4.8.2	SN rate as function of galaxy colour	100
4.8.3	SN rate as function of sSFR	102
4.9	Conclusion	103
5	Transient searches with large synoptic surveys	105
5.1	The Vera C. Rubin Observatory	106
5.1.1	The Simonyi Survey Telescope	107
5.1.2	Legacy Survey of Space and Time	109
5.2	Transient searches	111
5.3	Operation simulator, <code>OpSim</code>	115
5.4	SN rates with LSST	117
5.5	True novelties	120
5.5.1	True anomalies proper motion	126
5.5.2	Color and time evolution	136
5.5.3	Footprint and Minisurveys	146
5.6	Conclusion	152
6	Transient studies in the multimessenger Astronomy era	154
6.1	Gamma Ray Bursts	155
6.2	MAGIC	156
6.3	GRB190114C	160
6.4	Gravitational Waves	161
6.5	LIGO/VIRGO interferometers	167
6.6	GW170817	172
6.7	GW190814	177
6.8	Conclusion	188

Introduction

Supernovae (SNe) are transient events and consist in very energetic explosions associated with the death of a star, with a typical total energy of $E_{tot} \sim 10^{53}$ ergs. Two different mechanisms occur for massive and low mass stars: Core collapse SNe occur when a massive star ($M \gtrsim 8M_{\odot}$) form a degenerate iron core, and the mantle collapse onto it reaching the Chandrasekhar limit¹. For low mass stars in a binary system, SNe can also occur for a carbon oxygen white dwarf that accretes material from a companion, if this process allows the mass of the stellar core to reach the limit mass for the explosion (Thermonuclear SNe). The corresponding remnant also takes different forms: a compact neutron star or a black hole as the result of a Core Collapse SN, or no compact remnant, when the star is disrupted by a thermonuclear explosion. Even though the understanding of the SN phenomena has improved in the last decade, we are really far to fill all the gaps of the theory. The theoretical models, which became more detailed and elaborate thanks to the development from different fields of astrophysics, are still not able to link each type of SN event to a specific progenitor star with a proper explosion mechanism. SNe allow us to study the final phases of the stellar evolution through the analysis of the material expelled due to the explosion, the ejecta, and their spectro-photometric evolution. When the ejecta become optically thin, the star shows its internal structure and provides constraints on the effects of the rotation and mass loss on the stellar evolution. Because

¹The Chandrasekhar limit is the maximum mass of a stable white dwarf star. The currently accepted value of the Chandrasekhar limit is about, $1.39 M_{\odot}$ ($2.765 \times 10^{30} kg$, *Chandrasekhar*, 1957). White dwarfs gravitational collapse primarily through electron degeneracy pressure, compared to main sequence stars, which resist collapse through thermal pressure. The Chandrasekhar limit is the mass above which electron degeneracy pressure in the star's core is insufficient to balance the star's own gravitational self-attraction. Stars with masses up to the limit remain stable as white dwarf.(Carroll, 2007)

the ejecta expand until they are mixed with the interstellar material, SN explosions provide either a chemical enrichment of the environment (polluting the interstellar material with the elements synthesized in the inner parts of the star during its evolution and the ones produced the explosion) either dynamical feedback igniting the density fluctuation of the medium that fire the star formation, due to the interaction between the ejecta and the environment. SN ejecta are also an important site for the dust formation in galaxies.

The high luminosity and relatively uniform light curves and intrinsic properties of Thermonuclear SNe have made them primary distance indicators and placed them in a leading role in cosmology. SNe Ia have been used for the measurements of the Hubble constant, i.e. the current expansion rate of the universe, and the accelerated cosmic expansion directly inferred from the apparent faintness of distant SNe (Perlmutter et al., 1998; Riess et al., 1998; Schmidt et al., 1996). Together with other probes of the cosmic history SNe Ia can help us to characterise dark energy and possibly discover its nature.

Even though the SNe show a typical luminosity that can be much greater, in some cases, of its parent galaxy, just about 1% of SN total energy is detectable through the electromagnetic (EM) radiation. The energy (10^{49} ergs) is emitted over a wide range of the EM spectrum from the X-ray to radio, and the analysis of the SN light curve at all wavelengths gives us information to constrain the progenitor star and explosion mechanism. The observation of the SN spectro-photometric evolution in a larger wavelength range will be possible thanks to the next generation facilities such as the Square Kilometre Array (SKA), the Vera Rubin Observatory, Euclid and the James Webb Telescope (JWST). SKA telescope will allow to observe the deep sky in radio bands by using thousands of low frequency antennas. Moreover the space telescope Euclid and the JWST will observe SNe in near-infrared (NIR) bands. A huge push for the increase SN statistics in the optical bands (ugrizy) is expected to be given by the Legacy Survey of Space and Time (LSST Science Collaboration, 2009). The goal of this project is to conduct a deep survey over an enormous area of sky with a frequency that enables images of every part of the visible sky to be obtained every few nights for ten years to achieve astronomical catalogs thousands of times larger than previously compiled.

Where the rest of 99% of the SN energy goes? It is used to sustain the dynamics

of the phenomenon in producing other detectable signals.

Due to the energy of the SN explosion a number of nuclear reactions can take place in the ejecta that lead to their cooling during the expansion, those reactions are the main channel for the galactic γ -ray at very high energies (van Putten et al., 2019). Besides, SN explosions are source of Gravitational Waves (GW). For CC SNe the GWs are assumed due to the protoneutron star rotation, in addition other phenomena can contribute to the GW signal, such as: anisotropic neutrino emission, global pre-collapse asymmetries in the iron core and surrounding burning shells, aspherical mass ejection, magnetic stresses and late time formation of a black hole (see Ott, 2009, and references therein). Also SNe Ia can produce GW signals from the inspiralling and merging binary white dwarf, but also due to the asymmetry of the explosion, which is reflected theoretically in the production of GWs signal both if the white dwarf companion is a degenerate star or not (Falta et al., 2011; W. and L., 2019; Zou et al., 2020).

Thus SNe can be studied also through the analysis of the different messengers they produce (GWs, neutrinos, high energy particles). In the last decade new instruments were developed to detect neutrinos, GWs and high energy cosmic rays: IceCube (Michaely and Perets, 2018); CTA telescope (Acero et al., 2017); LIGO and VIRGO (Abbott et al., 2018). Thus, the analysis of the signal from neutrinos, relativistic cosmic particles and GW can be an important piece of the puzzle in our understanding the SN physics.

Within the presented scientific framework I analysed the SUDARE survey data, this is to acquire a consolidated and well defined method for the SN search and to study the detected SN sample using a statistical approach (I measured the SN rate as a function of cosmic time and parent galaxy parameters: mass, color and sSFR) in order to constrain SN progenitor models. The results of SUDARE survey data analysis open a discussion on how to improve the SN search with next generation of synoptic surveys; thus, I simulate a SN search as it would happen within LSST to analyse how the SN statistics and classification will be improved. Moreover, I exploit the method for SN search to study the impact of the new synoptic surveys in the detection of unknown transients, and eventually to study transients discovered using different messengers, to detect their optical counterpart.

In summary this thesis presents a detailed analysis on the transient search in multi-

messenger era from the unbiased search of SNe to the search of unknown classes of transients in particular the optical counterpart of the GW sources called kilonovae. In the first three chapters, I introduce the scientific framework of this thesis presenting a review of the state of the art on the knowledge and the methods to search and to study SN events.

In chapter 4, I present an analysis of the SUPernova Diversity And Rate Evolution (SUDARE) survey data. The SUDARE survey is a four years observing campaign which aims to obtain accurate measurements of the SN rate for both Core Collapse and Thermonuclear SNe to constrain their progenitors. In particular, I analyse the data following all the steps required to measure the SN rates: the difference image process, the detection of the transient sources on the difference images, the light curve analysis and transient classification, the estimate of the detection efficiency with artificial experiments, the detection of the galaxies on multi-band deep stacks, the estimate of their photometric redshift, mass and star formation rate. The results will be also published in Ragosta et al. (in preparation, a).

In chapter 5, the critical issues of the method presented in chapter 4 are discussed considering the future synoptic surveys with LSST and how these can be designed to improve the SN detection and SN rate measurements. Hence, I present a set of simulations on the detection and classification of SNe in the future synoptic survey with LSST, and inspect the possibility to explore regions of transient parameter space that are still not covered. Specifically, I perform several simulations of the transient search adopting different observational cadences. I exploit the Operations Simulator (OpSim), an application that simulates the field selection and image acquisition process of the LSST over the 10-year life of the planned survey. On these simulated data I analysed the figures of merit for different science cases aimed at detecting and classifying the different SN types at discovering unprecedentedly observed. The results will be also published in Ragosta et al. (in preparation, b) and Xialong et al. (in preparation).

In chapter 6, I present examples on how the method used in the SN search can be extended in the search for electromagnetic counterpart of a GW source GW190814, the first observation of a compact binary coalescence involving a black hole and a compact object and the optical follow up of GRB190114C which has been observed for the first time also in tera-electronvolt regime. In particular, I exploit the methods

and techniques adopted for the supernova survey to search the optical counterpart of a gravitational wave source in collaboration with the members of ENGRAVE, an international collaboration bringing together astronomers who use the ESO facilities to study gravitational wave events. I also analysed the optical emission of GRB190114C. The results are published in Abbott et al. (2020) and MAGIC Collaboration et al. (2019). The last chapter is then dedicated to the conclusions.

Chapter 1

Supernova types

SNe events differs from each other morphologically (the shape of the light curve), and spectroscopically, the difference is due to the different evolutionary path of the parent star. To recognise if the SN progenitors have common evolution, historically, it has been analysed if the events show common features, grouping in specific classes. A first attempt to outline a classification scheme has been made by Minkowski (1941) after the systematic SN search conducted by Zwicky and Baade in the 1941, using the Palomar 18-inch Schmidt telescope. Their survey discovered 19 SNe in the first year. Minkowski proposed a classification based on the presence (type II) or absence (type I) of H lines, such as $H\alpha$ 6563Å and $H\beta$ 4861Å in the early spectra. In this chapter I present the general scheme of the SN taxonomy, considering both the point of views of the observed features and their physical origin.

1.1 SN empirical classification

Generally the SN classification is performed on optical spectra and to some extent also on their light curves. Early spectra consist of thermal continuum and P-Cygni profile due to resonant scattering. This means that the classification is led by the chemical and physical properties of the outermost layer of the exploded star (Turatto, 2003).

The first classification of SN explosions was introduced by Minkowski (1941) based on spectroscopic observations of 14 events. Minkowski designated the larger subgroup of 9 nearly homogeneous events as type I, while the other 5 events were designated

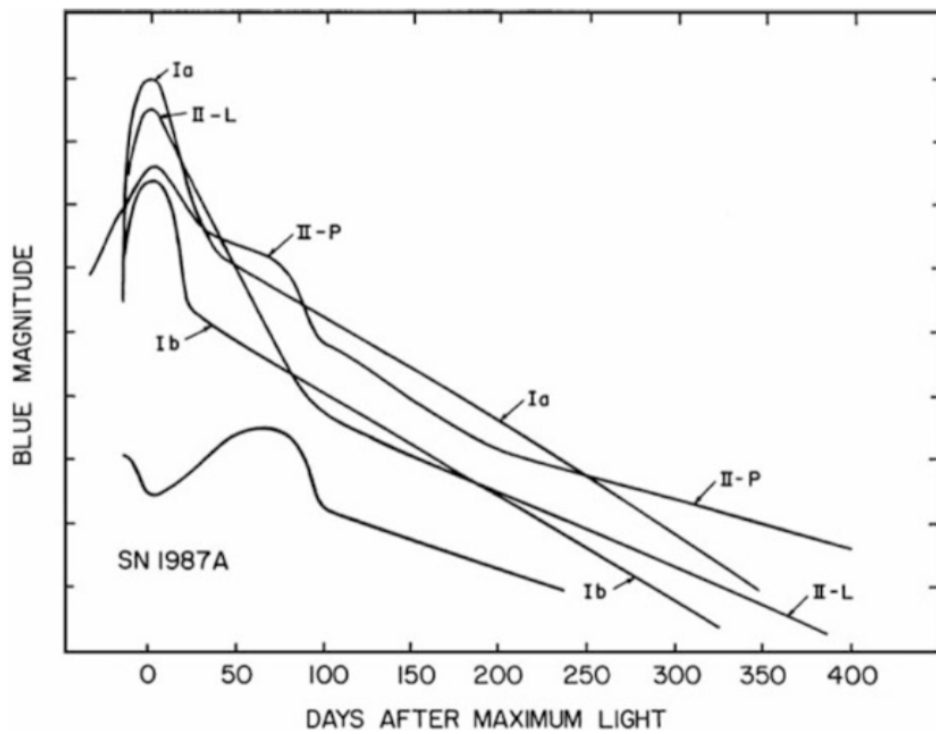


Figure 1.1: A comparison of characteristic light curves. From "Introduction to Supernovae" (Wheeler, 1990)

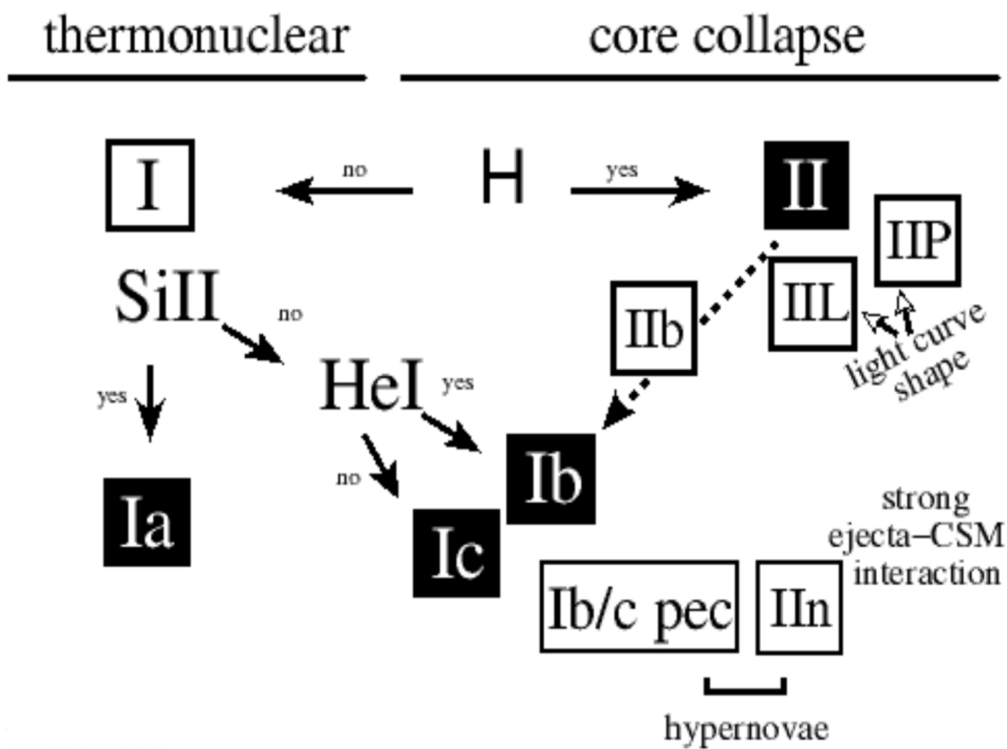


Figure 1.2: The figure, from (Turatto, 2003), shows the standard scheme for SN classification.

as type II. The spectra of type II SNe were quite diverse but all showed signatures of hydrogen, while type I SNe did not. Wheeler and Levreault (1985) identified a subclass of SNe I which differs spectroscopically from the dominant population, Elias et al. (1985) coined the terms SN Ia for the dominant group and SN Ib for this new subclass. Later, Harkness et al. (1987) identified signatures of He I peak in spectra of SNe Ib and Wheeler and Harkness (1990) introduced the term SN Ic for a subclass of SNe Ib that did not show strong helium but were otherwise similar to SNe Ib (and different than SNe Ia). Among type II SNe, Barbon et al. (1979) divided two photometric subclasses characterised by light curves showing prominent plateau (II-P) or declining in a linear fashion (II-L), see figure 1.1. The plateau is due to the recombination of the H in the ejecta due to the cooling phase in its expansion. Two additional spectroscopic subclasses of SNe II were introduced later: SNe IIb that transition from having hydrogen-rich early spectra to He-dominated SN Ib-like events near peak (Filippenko, 1988) and SNe IIn that show strong and relatively narrow emission lines of hydrogen (Schlegel, 1990). Filippenko (1997) reviewed SN classification in detail. Since 1997, numerous additional SN groups have been identified and new sub-classes proposed, most notably the class of broad-line SNe Ic (SN Ic-BL) that are associated with high energy Gamma-Ray Bursts (GRBs) and X-Ray Flashes (XRFs; Woosley and Bloom, 2006) and the newly-defined class of superluminous supernovae (SLSN; Gal-Yam, 2012);

Besides the difference in the spectra, Type I SNe have similar evolution of the light curve showing an initial increase in luminosity until a maximum peak, than a fast decrease which evolves in a steeper drop of luminosity. The tail of the light curve of the type I SN is related to the ^{56}Co decay.

If circumstellar material (CSM) is present around the progenitor, the ejecta can interact with it when spread in the environment. The SN blast wave shocks this material, and the kinetic energy is converted to radiative energy by the emission lines in the spectra of the type IIn SNe as indirect byproduct of the shock collisions, as they are produced in the photoionised unshocked CSM. Early phase spectra contains narrow Balmer emission features placed over a blue continuum. The most prominent features (e.g. H_α) typically exhibit multiple components, which consist of narrow cores (full width at half maximum FWHM_n of tenths to hundreds of kms^1) that are often situated on top of intermediate-velocity components ($\text{FWHM}_i \sim 1000\text{kms}^1$)

and broad bases (FWHM_i of a few thousand kms^1) (Taddia et al., 2013, and reference in therein). This kind of SN event is referred as type IIn SN ("n" stands for the narrow shape of the spectral lines). If the CSM is H-poor it can happen that the spectra will show high He component, this will arise as a He peak in the spectral feature of the source, and the phenomenon will be referred as a type Ibn event. Any type of core collapse or thermonuclear SN can appear as a SN IIn or SN Ibn. All that is required is a fast ejecta with sufficient energy crashing into slower CSM with sufficient density. The nature of different interactive SNe remains an open issue the is a cause of uncertainty in the SN classification (Smith, 2017).

To summarize the complex scheme presented, the current classification is shown in Figure 1.2. This empirical classification is based on the early spectra. It happens that the spectral feature change with time, due to the characteristics of the progenitor or of the CSM. Transitional types have been added to the classification scheme such as type Ibn and type Iib SN (Pastorello et al., 2015). Type Iib SNe shows weak H lines in the early phase spectra, later on the H emission becomes undetectable, and spectrum closely resembles that of a type Ib SN.

With the observation of a higher number of SN light curves and spectra it appears that there is a complex taxonomy related to SN diversity, the discriminant from the main classes and other subclass can be peculiar luminosity to the maximum peak, or peculiar diffusion velocity of the ejecta or peculiar evolution of the spectra. It is the case of Super Luminous SNe (SLSNe) that are SNe much more luminous than the mean maximum luminosity of the known SNe (Gal-Yam, 2017). These SNe show absolute peak magnitude in the range $M \leq -21$ mag, so they are intrinsically brighter than normal type I and type II SNe by at least 2 magnitudes. SLSNe are characterized by an energy associated to the luminosity flux equal to the total energy realized by a normal SN and can show a persistent P-Cygni absorption (see figure 1.3). Observationally, SLSNe can be classified as H rich (SLSN-II), and H poor (SLSN-I, the most luminous class). When H is present in the spectrum, it usually appears in the form of strong, multi-component emission lines, almost certainly indicating interaction with the CSM. Such objects are classified as "SLSNe-IIn", by analogy with the fainter SNe-IIn. In the family of high energetic SN event it needs to be mentioned the hypernova. A hypernovae is a very energetic supernova thought to result from an extreme core-collapse scenario.

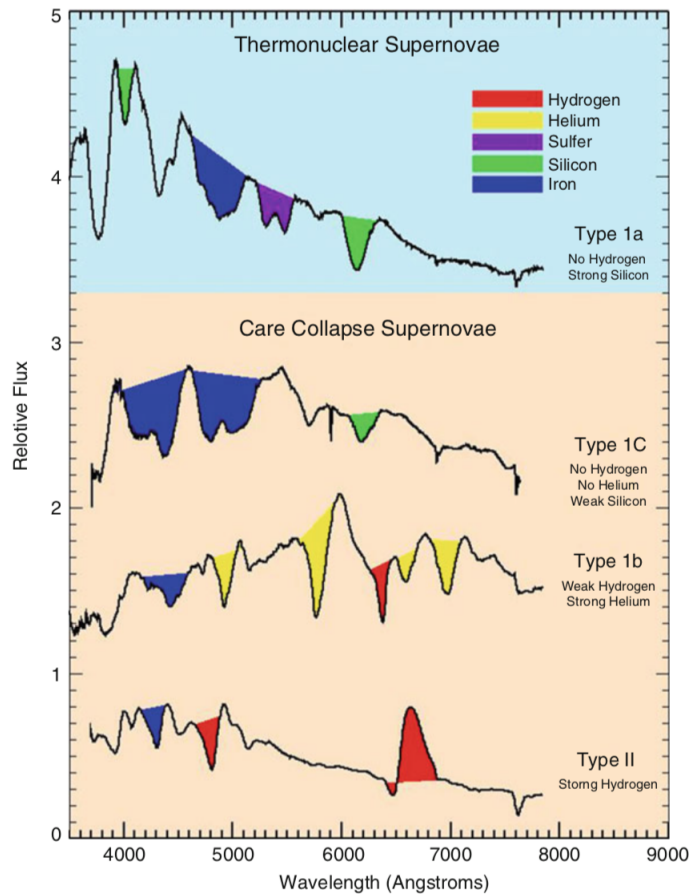


Figure 1.3: Spectral features P-Cygni profiles characterized by an emission around the rest wavelengths of the line and a blueshifted absorption that reflects formation of the lines in an expanding medium. Type I SNe don't show any H lines in the spectra, while type II SNe do. Moreover, type I SNe show a further spectroscopic classification based on the presence (type Ia) or absence (type b/c) of strong Si I, Si II lines; SNe Ib show He lines, while SNe Ic show weak Si and no He lines (credits: David Kasen).

In the wide and complex frame of SN taxonomy SN impostors are also possible. Mass loss episodes can happen in a star during its evolution. These outbursts have been associated to massive stars close to their Eddington luminosity¹, L_{Edd} . The light curves of SN impostors present a variety in peak magnitudes and evolution. They can be distinguish by real SNe because they are fainter than SNe and the decline from the luminosity peak of the SN impostors is typically faster and more sporadic than in the case of real SN events (Pastorello and Fraser, 2019; Pastorello et al., 2019a). Possible examples of SN impostors include the 1843 eruption of Eta Carinae, P Cygni, SN 1961V, (Kochanek et al., 2011) and SN 2009ip (Pastorello et al., 2013).

1.2 SN progenitors and explosion mechanisms

Each SN class shows spectral features that are related to the stellar composition and thus the evolution of the progenitor star or system of stars. Theoretical models help us to understand the processes leading to the explosion. The possibility to link these models to a certain progenitor system allows to develop a classification scheme based on the relation of the explosion mechanisms and the progenitor stars.

1.2.1 Thermonuclear SNe

Thermonuclear explosion of a Carbon Oxygen white dwarf (C-O WD) accreting mass in a binary system is the most accredited scenario in the description of SN type Ia event. The model assumes that the WD reaches the mass limit of Chandrasekar and starts to collapse producing a shock wave that ignite the explosion.

There are two possible channels that leads to the above configuration:

- A single Degenerate system (SD), formed by a main sequence star (or super giant) and a WD;

¹The Eddington luminosity, also referred to as the Eddington limit, is the maximum luminosity a body (such as a star) can achieve when there is balance between the force of radiation acting outward and the gravitational force acting inward. The state of balance is called hydrostatic equilibrium. When a star exceeds the Eddington luminosity, it will initiate a very intense radiation-driven stellar wind from its outer layers. Since most massive stars have luminosities far below the Eddington luminosity, their winds are mostly driven by the less intense line absorption. (Van Marle et al., 2008)

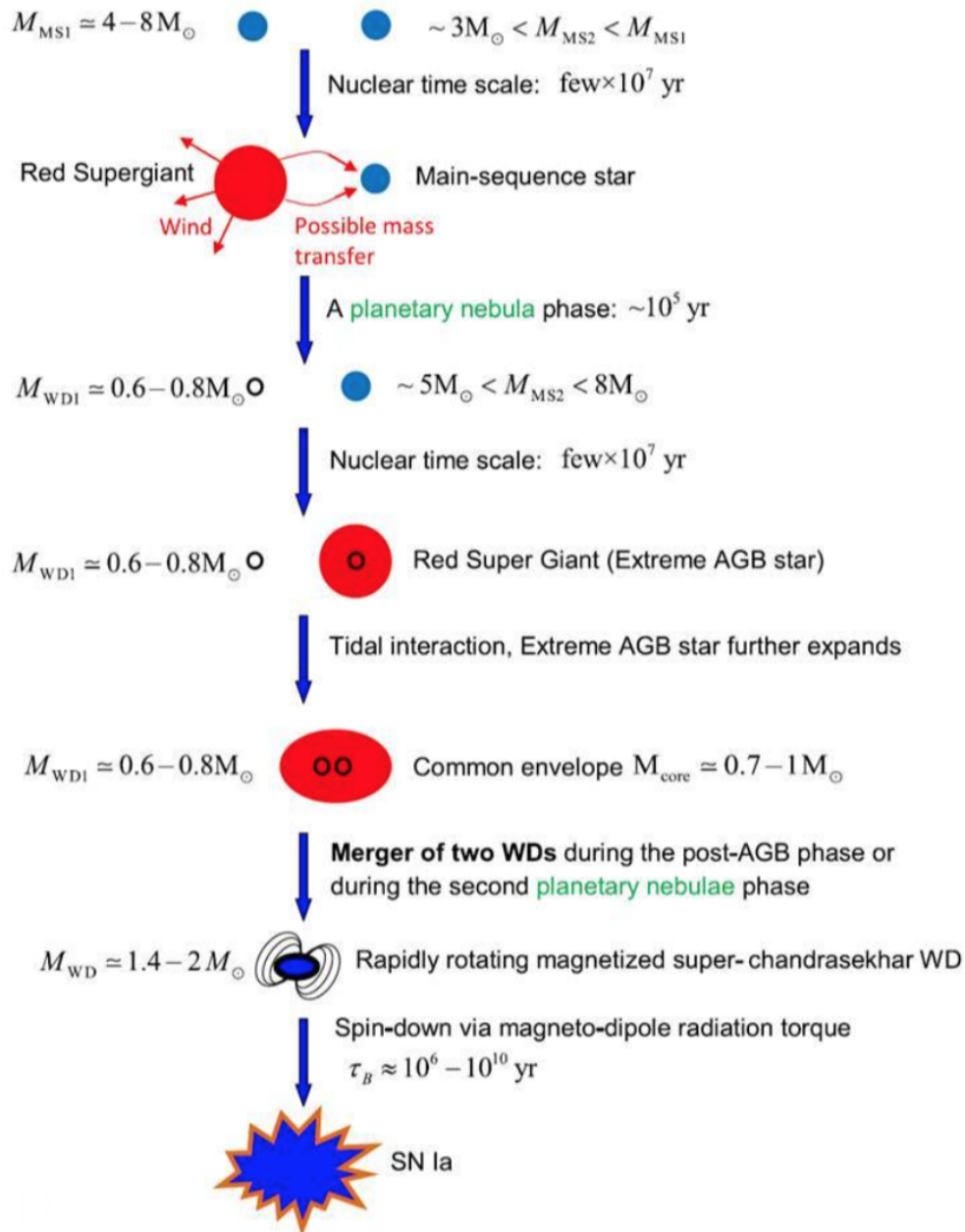


Figure 1.4: The DD model starts from two main sequence stars in the binary system aging with mass transfer episodes. The two stars first share a common envelope and then merge the degenerate cores (with the emission of GWs) producing a rotating magnetized super-Chandrasekhar WD, which ends its life in a SN explosion. Figure from Ilkov and Soker (2012).

- A double Degenerate system (DD), formed by two WDs.

In the SD scenario the WD accretes mass overcoming the Roche Lobe transferring material, so that its mass can easily approach to the Chandrasekar limit. In the second case the process driving the explosion is the merging of the two degenerate components of the system with the production of GWs (general scheme in Figure 1.4). Typically a type Ia SN is characterized by an explosion energy of $\sim 10^{51}$ erg and a production of roughly $0.6M_{\odot}$ of radioactive ^{56}Ni .

A number of aspects during the explosion are related to the progenitor properties:

- Early light curve and spectral evolution;
- Radio, X-ray, CSM emission;
- narrow time-variable absorption lines;
- CS dust and light echoes.

The properties of the explosion strongly depend on how the shock wave propagates inside the WD, bearing in mind that these characteristics are different for the case of a Chandrasekhar progenitor or a sub-Chandrasekhar progenitor. Indeed models describe SN Ia explosion produced by progenitor that either reach the Chandrasekhar limit either form progenitor with mass below the limit. Due to the difficulties in treating several physical processes involved in the explosion as well as to the numerical issues in performing a detailed modelling of the explosion, we are still facing with non-negligible uncertainties on what really occurs in an exploding WD. In the case of the C-O WD, the models describe two different outcomes: a central ignition of the shock wave, or the case in which the gravitational attraction of the two WDs in a binary system creates a common envelope in which the two cores merge creating a new core with enhanced mass. If the mass of the merged core reach the Chandrasekhar limit it will produce GWs, which could be optically detected as a SN Ia (Branch and Wheeler, 2017). In the case of a Chandrasekhar WD progenitor, the high electron degeneracy in the core leads to an explosive burning of carbon. The reactions induced by the burning of the carbon produce the incineration of the material into Fe-peak elements. This leads to an explosive burning flame which starts to propagate outwards; this phenomena act as a deflagration if the velocity of the propagation is subsonic.

How the deflagration propagates into the stellar structure can be predicted by the Rayleigh Taylor instability (Branch and Wheeler, 2017). The properties of the flame propagation are strongly influenced by the effect of the instability, and the description of how its presence affects the evolution of the phenomenon is related on how it is managed in the numerical simulations (which are quite complicated and not yet completely reliable). Behind the flame front, the stellar material undergoes explosive nuclear burning of Si, O, Ne and C. The exact composition of the nuclear processed material strongly depends on the maximum temperature achieved inside the burning front, which is related to the density of the layers crossed by the explosive wave. For density values in the range $\sim 10^{10} - 10^6 \text{ gcm}^{-3}$, the chemical composition of the burnt material ranges from elements of the Fe-peak (mainly ^{56}Ni) to intermediate-mass elements such as S and Si, and to C and O in the external layers.

Other models can describe a thermonuclear explosion: in the *delayed detonation scenario*, the initial speed of the flame is so low that only a very little amount of ^{56}Ni ($\sim 0.1M_{\odot}$) is produced. In this model the transition from deflagration to detonation occurs at densities of the order of $\sim 10^7 \text{ gcm}^{-3}$, when the star has already significantly expanded. This scenario allows a better reproduction of the typical velocities of intermediate-mass elements observed in the spectra of typical type Ia SNe. Another model that it is worth to mention is the *pulsating delayed-detonation* scenario (Bravo and García-Senz, 2009, and references therein), which assumes that the evolution from the deflagration to the detonation step does not occur during the propagation of the deflagration wave. If the initial flame speed is low enough, the burning is quenched by the expansion of the outer layers, before the binding energy of the structure becomes positive. As a consequence, the WD remains bound and experiences a strong pulsation. At maximum compression, the burning can be reignited, and the speed of the new-born burning flame is now supersonic, so it becomes a detonation. As in the delayed-detonation, this configuration predicts that the detonation flame starts at low density ($\sim 10^7 \text{ gcm}^{-3}$ or lower) with a consequently better reproduction of the velocities of intermediate-mass elements in the spectra. In the case of a sub-Chandrasekhar progenitor for type Ia SN, it is commonly assumed that the central explosive C-burning, which should have the characteristics of a detonation, is induced by the shock wave generated by the He-detonation on top of the degenerate CO core (Branch and Wheeler, 2017).

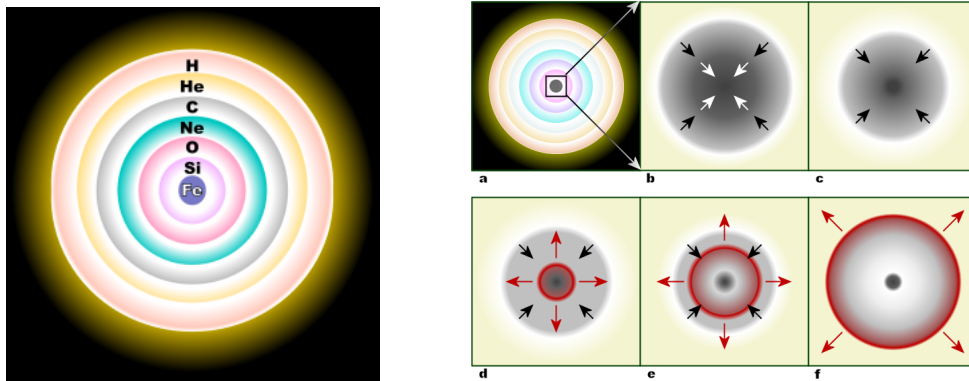


Figure 1.5: In the figure (credits: Moriya et al., 2015) Within a massive, evolved star (a) the onion-layered shells of elements undergo fusion, forming a Ni-Fe core (represented in detail in the right panel) (b) that reaches Chandrasekhar-mass and starts to collapse. The inner part of the core is compressed into neutrons (c), causing infalling material to bounce (d) and form an outward-propagating shock front (red). The shock starts to stall (e), but it is re-invigorated by neutrino interaction. The surrounding material is blasted away (f), leaving only a degenerate remnant.

1.2.2 Core Collapse SNe

Stars more massive than $\sim 8M_{\odot}$ arrive in their last evolutionary phases with an "onion"-like configuration (see Figure 1.5) and an Fe core experiencing a different explosion mechanism compared to the thermonuclear runaway. Fe has the highest binding energy per proton so it can only undergo endo-energetic reactions that remove energy and pressure support for the star leading to its collapse. The collapse stops as the core reaches the neutron star density, thus other material that falls on the core bounces, producing an outward shock wave that ignites a breakout which leads to the SN event.

The energy associated to the shock wave is $\sim 10^{51}$ erg, enough to drive the explosion itself compared to the binding energy of the star in the degenerate configuration, but the interaction with the in-falling material stops the shock wave, and energy is absorbed by the bouncing envelope. This flux has a mean free path comparable with the dimension of the star, because its extreme degenerate configuration. Thus, the neutrinos are forced to interact with the material, giving rise to the shock wave that leads to the explosion.

In this description, the rates of r- and s- processes involving the production of heavier elements in the core during the most advanced evolutionary phases are very important. The production of these elements through r- and s- processes leads to a nuclear reaction chain that can explain the amount of neutrinos that help the shock wave to propagate into the stellar structure.

H rich SNe

Type II SNe are recognized by the presence of H in their spectra. Massive stars with all the H envelope, or most of it, show the presence of a plateau phase due to a change in the opacity of the exterior layers. The shock wave ionizes the H in the outer envelope resulting in a significant increase in the opacity. This prevents photons from the inner parts of the explosion from escaping. During the subsequent months a SN IIP continues to radiate some of the energy deposited by the shock, at a nearly constant temperature, that of the H recombination, which is about 5500 K. This is the diffusive plateau phase of approximately constant luminosity.

The difference between SNe II-P and the II-L is believed to be related to the loss of H from the progenitor's outer layers configuration (Doggett and Branch, 1985). In the case of stars that lose the outer H envelope because of mass loss during their evolution, during the latest stages of the evolution and a very short time before the SN explosion, the SN spectra show characteristic narrow emission lines. This is due to the interaction between the ejecta and the CSM, as in the case of SNe IIn (Taddia et al., 2013).

Stripped envelope SNe

Intermediate and massive stars can experience in the RGB phase strong mass loss, due to outbursts related to the ignition of nuclear reactions to sustain the star's evolution, or because of the presence of a companion star in a binary system. Thus, the outer envelope is partially or totally removed, due to the intensity of the mass loss mechanism. The progenitors lose their outer H and possibly also He shells (e.g. Podsiadlowski et al., 1992a), ending their evolution as type Ib/c SNe. Based on the relative CCSN rates from the LOSS sample, Smith et al. (2011) concluded that the majority of type Ib/c SNe would originate from progenitors in such a Roche-lobe over-

flow binary system (see, also, Claeys et al., 2011). SNe I Ib show H in their spectra similar to normal type II SNe, but later the spectra will evolve Ib-like (Filippenko, 1988; Woosley et al., 1987). The general hypothesis that SNe Ib/c have stripped progenitors is greatly supported by the discovery of links between SNe II and SNe Ib/c. As discussed by Filippenko (1988), near the maximum brightness SN 1987K was undoubtedly a SN II, but months later the spectrum was changed into a SN Ib. The simple interpretation is that SN 1987K had a H atmosphere at the time it exploded, and as the ejecta thinned out the spectrum would become dominated by emission from the deeper and denser layer. The progenitor was probably a star that lost almost all its H envelope through mass transfer onto a companion or via stellar winds. Another example comes from SN 1993J (Filippenko et al., 1993), showing several early time spectra of SN 1993J showing the evolution of the typical He I features of SNe Ib. Later analysis on the pre-explosion images conducted by Dyk et al. (2002) showed the spectral energy distribution of the SN 1993J progenitor is consistent with a K-type supergiant star with a mass of $13 - 22M_{\odot}$. A star of such low mass cannot lose its entire H envelope without considering mass transfer from a companion. Thus, the progenitor of SN 1993J probably lost most of its hydrogen through mass transfer to a bound companion 3-20 AU away. Maund et al. (2004b) showed a detection of Balmer lines from a probable companion of SN 1993J, providing a proof that sustains the binary star.

1.2.3 Different explosion mechanisms

Aside the presented explosion mechanisms, models predict different scenarios that can lead to a SN explosion.

Electron capture SNe

Massive stars that evolve to the evolutionary stage when C is ignited in the core, will end their evolution in a SN explosion driven by different mechanisms respect those previously described, these depend on the mass of the progenitor.

For stars with mass in the range between $8M_{\odot}$ and $12M_{\odot}$, the star is able to ignite C, but the nuclear reactions chain stops at the Ne. The core is composed of O/Ne/Mg, at this stage, and it experiences a strong degeneration with the production of a neutrino

flux because of electron capture $e^- + p \leftrightarrow \nu + n$ or $\bar{\nu} + p \leftrightarrow e^+ + n$.

The production of neutrino can drive the shock wave produced by the collapse igniting the explosion (Colgate and White, 1966).

Pair instability SNe

Very massive stars, stars from $65M_{\odot}$ to $130M_{\odot}$ (for a configuration with rotation) and from $140M_{\odot}$ to $260M_{\odot}$ (for a configuration without rotation), the core does not experience a degenerate configuration, but reaches extremely dense condition ($T \geq 10^9\text{K}$; $\rho \leq 10^5\text{gcm}^{-3}$) where electron - positron pairs are copiously produced. This softens the equation of state and making the star dynamically unstable. The resulting explosions are called *pair-instability SN* (PISN). This kind of explosion does not leave any remnants.

1.3 The SN remnants

A SN remnant (SNR) is the structure resulting from the explosion of a star. SNR consists of ejected material expanding from the explosion, and interstellar material swept up and shocked along the path (Branch and Wheeler, 2017).

The resulting strong shock wave from the SN explosion heats the upstream plasma up to temperatures above millions of K. The shock continuously slows down over time, as it sweeps up the ambient medium, but it can expand over hundreds or thousands of years and over tens of parsecs before its speed falls below the local sound speed.

In our Galaxy are known about 300 SNR, mostly detected as extended sources of synchrotron radio emission. They appear mainly in the Galactic plane region where the optical bands are highly extinguished. Although SNRs are detected mainly in the radio, where the extinction by dust is not an issue, the radio sample of Galactic SNRs is incomplete. Indeed, surveys generally are restricted to within a few degrees of the Galactic plane and it is difficult to recognize SNRs of low radio surface brightness in directions where the diffuse Galactic radio emission is strong (Xiao et al., 2009). Nevertheless, the limited angular resolution of radio surveys constrain the possibility to distinguish SNRs of small angular size (≤ 10 arcminutes) from background radio sources. SNRs in more distant galaxies are difficult to identify in radio and X-rays

because of their lower fluxes and smaller angular sizes. To overcome the problem, SNRs can be identified as extended sources of optical emission lines characterized by a relatively high ratio (≥ 0.4) of [S II] $\lambda \sim 6717, 6731\text{\AA}$ to H_α flux, caused by shock-heating of the ISM (Mathewson and Clarke, 1973), where generally the extinction is moderate. In photoionized nebulae, sulfur is more highly ionized hence this flux ratio is lower. The strength of the [Fe II] $\lambda \sim 1.644 \mu\text{m}$ line also is useful (Blair et al., 2014).

Theoretical models assume that a SNR passes through the following stages as it expands (Reynolds, 2008; Spitzer Jr, 2008; Woltjer, 1972):

1. Free expansion of the ejecta, until they sweep up their own weight in circumstellar or interstellar medium. This can last tens to a few hundred years depending on the density of the surrounding gas.
2. Sweeping up of a shell of shocked circumstellar and interstellar gas. This triggers the Sedov-Taylor phase, which can be well modeled by a self-similar analytic solution. Strong X-ray emission traces the strong shock waves and hot shocked gas.
3. Cooling of the shell, to form a thin ($\leq 1 pc$), dense (1-100 million atoms per cubic metre) shell surrounding the hot (few million K) interior. This is the pressure-driven snowplow phase. The shell can be clearly seen in optical emission from recombining ionized hydrogen and ionized oxygen atoms.
4. Cooling of the interior. The dense shell continues to expand from its own momentum. This stage is best seen in the radio emission from neutral hydrogen atoms.
5. Merging with the surrounding interstellar medium. When the supernova remnant slows to the speed of the random velocities in the surrounding medium, after roughly 30,000 years, it will merge into the general turbulent flow, contributing with its energy to the turbulence.

Depending on the SN progenitor, the explosion condition, density variations in the interstellar medium and Rayleigh-Taylor instabilities three main types of SNR can be distinguished:

Shell-type remnants, as the name suggests, emit most of their radiation from a shell of shocked material. They appear to be a bright ring, since the edges of the three-dimensional shell has more shocked material along the line of sight than elsewhere in the shell. This is known as limb brightening. Shell-type remnants are typically SNe Ia remnants. Cassiopea A (Cas A) is a representative shell-type remnant, with an angular diameter of 4 arcminutes (for a linear diameter of ≥ 4 pc) and an age of only about 330 years, Cas A provides the best example of a young, oxygen-rich remnant of a core-collapse supernova. In X-rays, radio, and IR, the most conspicuous feature of Cas A is a bright and approximately circular ring. Low-density ejecta that have crossed the reverse shock provide most of the X-ray luminosity, while ejecta regions of higher density provide most of the optical and IR emission (Patnaude and Fesen, 2014). Slower, cooler, low-luminosity matter inside the reverse shock is less conspicuous, but can be detected by means of IR emission lines (Karl et al., 2012; Milisavljevic and Fesen, 2017), IR and submillimeter continuum radiation from $\sim 1M_{\odot}$ of dust that has formed in the ejecta, and free-free absorption of radio synchrotron emission (DeLaney et al., 2014).

Crab-type remnants, alternatively named plerions, are typically remnants of CC SNe, the prototype: the famous Crab Nebula. They are powered by a pulsar located at their centre and, in contrast to shell-type remnants, they emit most of their radiation from within the expanding shell. This means that they appear as a filled region of emission or filaments rather than a ring of emission. The Crab Nebula is the remnant of a CC SN of 1054 AD that was observed and recorded in China, Japan, and Korea. The supernova was visible in daytime for 3 weeks and at night for 21 months. The Crab is a filled-center remnant powered from within by a pulsar. With an angular diameter of 6 arcminutes at a distance of 2 kpc (Virginia, 1973), the linear diameter is ~ 4 pc and the mean expansion velocity is about 1000 km s^{-1} . At the heart of the nebula is the pulsar, detectable across the electromagnetic spectrum from radio to γ -rays. The pulsar is a rotating neutron star with $\geq 10^{49}$ ergs remaining in rotational kinetic energy and a $\sim 10^{12}$ G magnetic field, with the dipole axis tilted with respect to the rotation axis. The pulsed emission from X-rays to radio is synchrotron radiation.

Finally a third class of SNRs are the composite remnants. These remnants are a cross between the other two remnant types, and appear either shell-like or Crab-like,

depending on the wavelength of the observations. Generally plerionic composites appear Crab-like at both radio and X-ray wavelengths, but also show shell structures. An example is the Tycho SNR (G120+1.4;3C10), the remnant of SN 1572, is unique among Galactic SNRs in that both its age and its supernova type are firmly known. A light-echo spectrum established that SN 1572 was a spectroscopically normal SN Ia (Krause et al., 2008). Even before the light-echo spectrum was obtained, the light curve and colors already had been inferred to be those of a normal SN Ia (Ruiz-Lapuente, 2004). No evidence of a neutron star in the SNR was found, as expected for the remnant of an SN Ia. In Warren and Blondin (2013) is shown through a 3D hydrodynamical modeling that Rayleigh–Taylor instabilities at the interface between the ejecta and a uniform ambient medium are capable of generating such a structure without invoking initial clumping of the ejecta or the ambient medium. The only optical emission is from faint filaments, the spectra of which show Balmer lines that have both narrow and much broader (1800 km s^{-1}) components. Analysis on the chemical composition of the SNR showed that Fe must be generally inside the silicon, as it is in the explosion model. Observations of thermal X-rays indicate that Ti and Cr are spatially co-located with Fe, as expected (Miceli et al., 2015), and observations of hard X-rays from the ^{44}Ti decay chain imply, for a distance of 3.6 kpc, that $\geq 10^{-5} M_{\odot}$ of ^{44}Ti was synthesized in the explosion (Troja et al., 2014). Herschel observations indicate the presence of $\sim 10^{-2} M_{\odot}$ of cool (90 K) dust in swept-up ISM, but provided no evidence that dust formed in the ejecta (Gomez et al., 2012). This is consistent with other evidence that SN Ia are not important dust producers. A G-type subdwarf was suggested to be a former donor star in a SD system, but the identification is not conclusive (Bedin et al., 2014).

Chapter 2

SN progenitors

The correlation between the SN classes and the SN spectro-photometric evolution is not strictly determined. There are uncertainties on mass loss, rotation convection, metallicity and binary system parameters (Dominguez et al., 1998; Limongi and Chieffi, 2003). Moreover different progenitors can lead to the same SN Type, or particular environment conditions can drive the evolution of a SN Type.

There are different approaches to establish the link between SN progenitors and SN types:

- direct detection of SN progenitors on the pre-explosion images;
- hydrodynamic modelling of the SN spectrophotometric evolution;
- analysis of SN remnant;
- SN rate measurements as a function of the age of the parent stellar population.

In this chapter these methods for the analysis of SN progenitors will be presented, focusing on SN rate measurements.

SN	type	source	SN	type	source
<i>1961V</i>	IIn?	Bertola (1964); Zwicky (1964)	2009hd	II-L?	Elias-Rosa et al. (2011)
1978K	IIn	Ryder et al. (1993)	2009ib	II-P	Takáts et al. (2015)
<i>1987A</i>	II-P(pec)	Gilmozzi et al. (1987b); White and Malin (1987)	<i>2009ip</i>	IIn?	Foley et al. (2011); Smith et al. (2010)
<i>1993J</i>	I Ib	Aldering et al. (1994); Cohen et al. (1995)	2009kr	II-L?	Elias-Rosa et al. (2010); Fraser et al. (2010); Maund (2015)
1996al	III-L?	Benetti et al. (2016)	2009md	II-P	Benetti et al. (2016); Fraser (2011); Maund (2015)
<i>1997bs</i>	IIn?	Van Dyk et al. (2000)	<i>2011dh</i>	I Ib	Maund et al. (2011); Van Dyk et al. (2011a)
1999ev	II-P?	Maund et al. (2014); Van Dyk et al. (2002)	2012A	II-P	Tomasella et al. (2013)
<i>2003gd</i>	II-P	Smartt et al. (2004a); Van Dyk et al. (2003b)	<i>2012aw</i>	II-P	Fraser et al. (2012); Van Dyk et al. (2012)
<i>2004A</i>	II-P	Hendry et al. (2006)	2012ec	II-P	Maund et al. (2013)
<i>2004et</i>	II-P	Crockett et al. (2011); Li et al. (2005)	2013df	I Ib	Van Dyk et al. (2014)
<i>2005cs</i>	II-P	Li et al. (2006b); Maund et al. (2005)	<i>2013ej</i>	II-L?	Fraser et al. (2014)
<i>2005gl</i>	IIn	Gal-Yam and DC (2009); Gal-Yam et al. (2007)	<i>iPTF13bvn</i>	Ib	Cao et al. (2013)
<i>2006my</i>	II-P	Leonard et al. (2008); Li (2007); Maund et al. (2014)	2014C	Ib/IIn	Milisavljevic et al. (2015)
2006ov	II-P	Crockett et al. (2011); Li (2007)	ASASSN-14ha	II-P	—
<i>2008ax</i>	I Ib	Crockett et al. (2008)	2015bh	IIn	Elias-Rosa et al. (2016); Thöne et al. (2017)
<i>2008bk</i>	II-P	Mattila et al. (2008); Van Dyk et al. (2011b)	2016bkv	IIn?	—
<i>2008cn†</i>	II-P	Elias-Rosa et al. (2009); Maund et al. (2005)	2016gkg	I Ib	Kilpatrick et al. (2017); Tartaglia et al. (2017)

Table 2.1: Direct SN progenitor detections to date (Van Dyk, 2017)

SN	type	source	SN	type	source
1994I	Ic	Barth et al. (1996)	2004gt	Ic	Gal-Yam et al. (2005); Maund and Smartt (2005)
1999an	II-P	Maund et al. (2005); Van Dyk et al. (2002)	2005V	Ib/c	Eldridge et al. (2013)
1999br	II-P	Maund and Smartt (2005); Van Dyk et al. (2003b)	2005at	Ic	Eldridge et al. (2013)
1999em	II-P	Smartt et al. (2002a)	2006bc	II-P	Smartt et al. (2009)
1999ga	II-L	Pastorello et al. (2009b)	2007aa	II-P	Smartt et al. (2009)
1999gi	II-P	Smartt et al. (2001)	2007gr	Ic	Crockett et al. (2007a)
2000ds	Ib	Maund and Smartt (2005); Van Dyk et al. (2002)	2009H	II-P	—
2000ew	Ic	Maund and Smartt (2005); Van Dyk et al. (2002)	2009N	II-P	—
2001B	Ib	Maund and Smartt (2005); Van Dyk et al. (2002)	2009jf	Ib	—
2001du	II-P	Smartt et al. (2003); Van Dyk et al. (2003a)	2010O	Ib	Kankare et al. (2014)
2002ap	Ic-bl	Crockett et al. (2007b); Smartt et al. (2002b)	2010P	Ib	Kankare et al. (2014)
2002hh	II-P	Smartt et al. (2009)	2010br	Ib/c	[67]
2003ie	II-P(pec?)	Smartt et al. (2009)	2010jl	IIin	[75]
2003jg	Ic	Eldridge et al. (2013)	2011am	Ib	Eldridge et al. (2013)
2004am	II-P	Mattila et al. (2013)	2011hp	Ic	Eldridge et al. (2013)
2004cc	Ic	Eldridge et al. (2013)	2012P	IIb	Fremling et al. (2016)
2004dg	II-P	Smartt et al. (2009)	2013dk	Ic	Elias-Rosa et al. (2013)
2004dj	II-P	Maíz-Apellániz et al. (2004); Wang et al. (2005)	2016adj	??	—
2004gn	Ic	Eldridge et al. (2013)	2016cok	II-P	Kochanek et al. (2017)

Table 2.2: Upper limits to SN progenitor detections to date (Van Dyk, 2017)

2.1 Direct detection of SN progenitors

Since the end of the 1990's the SN community has been extensively searching publicly available archives for high resolution and deep images of nearby galaxies which host SNe.

The main limitation of this method is, first of all, the high resolution limit of the instrumentation used to take the images. In the case of Hubble Space Telescope (HST) it was imposed from the difficulty in retrieving photometry of resolved individual massive stars beyond distance $d \sim 28$ Mpc. Additionally, the galaxy number count increases as the distance cubed, consequently the relative number of galaxies with high quality archival imaging rapidly decreases. Hence the probability of finding coincidences of SN discoveries combined with existing pre-explosion images of the galaxies.

The existence of pre-explosion images has allowed direct identification of the progenitor stars of the nearest CC SNe (e.g Li et al., 2006a; Maund, 2011; Schuyler et al., 2003; Smartt, 2015; Smartt et al., 2004b). The fact that numerous RGSs are observed producing the most common class of SNe IIP is a validation of modern stellar evolution theory. Indeed, pre-explosion images show that the progenitor candidates of Type II SN are RSG stars of initial masses between $\sim 8M_{\odot}$ and $\sim 17M_{\odot}$.

The progenitor of SN 1987A was identified in archival images as a star known as Sk-69°202 (Gilmozzi et al., 1987a; Kirshner, 1987). The star showed no sign that it was about to explode, a fact that has been little remarked and virtually unstudied. The progenitor was identified as a blue supergiant, of spectral type B3I. Given the distance to the LMC of 50 kpc (170000 light years), the bolometric luminosity of the progenitor was $\sim 1.3 \times 10^5 L_{\odot}$. According to standard single-star evolutionary models, this luminosity implies a helium-core mass of about $5 - 6M_{\odot}$ and a ZAMS mass of about $18M_{\odot}$ (Podsiadlowski et al., 1992b). Barring an exotic binary evolution, the mass of the immediate presupernova would have been lower than the ZAMS mass, owing to mass loss by winds during the progenitor's evolution. Analysis of the light curve and spectra suggest a hydrogen envelope of about $8M_{\odot}$, for a total mass of about $13M_{\odot}$ at the time of explosion. There is evidence that the envelope was enriched in helium, with mass fraction $Y \sim 0.4$. The expectation was that such a moderately massive star should explode as an RSG. The blue supergiant nature of the progenitor

of SN 1987A accounted for the unorthodox light curve, but the physical reasons for its explosion in this state remain uncertain.

Inspection of pre-explosion images showed UV flash from a young IIP SNe interpreted as the shock breakout signature in a RSG progenitor (Gezari et al., 2008a), which was more probable to be observed due to the larger radius of the progenitor.

The search for progenitor for Ibc didn't help in build a empirical basis for the understanding of the origin of these events; pre-explosion images did not give any result, but allowed to set an upper limit to the progenitor's parameters. As detailed in Smartt (2009), there are 10 SNe classified as Ibc that have deep pre-explosion images available and none of them have a progenitor detected. Progenitors of SNe type Ic remained elusive. In (Van Dyk, 2017), the environments of SNe Ic is pointed out as one of the main issue for the detection of their progenitors. Indeed, SNe Ic are generally found in crowded environments (e.g. very near luminous stellar clusters, or dusty environments) from their light curves can be outlined that SNe Ic experience reddening of $E(B - V) \geq 0.4$ mag (Drout et al., 2011). One example is SN Ic 2003jg, for which the lack of progenitor detection is consistent with $E(B - V) \approx 1.32$ mag for the SN (Eldridge et al., 2013). Another example is the SN Ic 2013dk, which occurred at the edge of a cluster in the Antennae and also was reddened by $E(B - V) \approx 0.49$ mag (Elias-Rosa et al., 2013).

In Maund et al. (2004a), the spectral features of a Type Ib SN time and the photometry showed an excess in ultraviolet and B-band colours. A binary system model for the progenitor would have explained the observed feature. The analysis of the remnant in the post SN explosion, showed a signature related to a companion for the SN 1993J, which allows to identify a $13 - 20 M_{\odot}$ supergiant that had lost almost its hydrogen envelope.

Cao et al. (2013) identified an object in multi-band HST images from 2005 at the position of the SN Ib iPTF13bvn. The brightness and colour of the detected object were initially interpreted as being a single Wolf-Rayet (WR) star (Cao et al., 2013; Groh et al., 2013). In Eldridge et al. (2014) the progenitor candidate's actual brightness was too high for a WR, but more in line with a mass-transfer binary system. The progenitor vanished (Eldridge and Maund, 2016). Van Dyk (2017) pointed out that the SN light was probably still contributing to the flux seen at the SN position in follow-up HST 2015 imaging.

For type Ia progenitors the pre-explosion images of the binary system can show only the companion star (in the case it is a RSG or a main sequence star). This is because the usual luminosity of a WD is lower than the HST limiting magnitude. However, detection of the companion in the pre-explosion images (Li et al., 2011b), ruled out luminous red giants and helium stars as a companion for the WD in the case of Type Ia SN 2011fe in M 101. Another similar example can be found in Pérez-Torres et al. (2014) for the type Ia SN 2004J; the analysis of pre-explosion images allow to constrain progenitor parameters setting an upper limit on the mass and delay time population (see Kelly et al., 2014; Lundqvist et al., 2015; Nielsen et al., 2014, for more details). SN 2014J was discovered by Fossey et al. (2014) in the nearby (3.5 Mpc) irregular starburst galaxy M82, 7 days after the explosion, which was well determined from archival pre- and post-explosion observations (Goobar et al., 2015; Zheng et al., 2014). The extinction was high, $A_V \sim 2.0$, nearly due to interstellar dust with a steep extinction curve, $R_V \sim 1.4$ (Amanullah et al., 2014; Brown et al., 2015; Kawabata et al., 2014; Patat et al., 2015). Archival pre-explosion observations constrained the nature of the progenitor system, with the non-detection of X-rays excluding a single-degenerate binary system containing a white dwarf of radius comparable to that of a near-Chandrasekhar-mass white dwarf, and a mass accretion rate in the range in which stable nuclear burning can occur (Nielsen et al., 2014). The SD scenario was also ruled out by the non-detection of near-UV to near-IR emission excluded the presence of a bright red giant (Kelly et al., 2014). Aside to the pre-explosion images, direct detections of a remnant in the post-explosion images help to characterize the phenomenon. The absence of a source in the location of a SN event helps to discriminate a proper observation of a SN event from a SN impostor.

A list of direct detections, is presented in table 2.1. In the table can be distinguish entries in *italic*, that are referred to those SNe for which the progenitors have been shown to vanish, and entries that are struck out in the table, for those SNe that have progenitors which identification changed respect the one originally made. The SN 2008cn progenitor was originally identified as a yellow supergiant (Elias-Rosa et al., 2009), but was later shown to be a red supergiant star (Maund, 2015). In the cases of SN 1961V, SN 2009ip and SN 2015bh, it is still under debate whether the events were actual terminal explosions, although, in all three cases, a precursor object has been identified. Moreover, SN 1997bs was originally classified as an "SN impostor"

(Pastorello et al., 2019b; Van Dyk et al., 2000), but now appears probably to have been an unusual core-collapse SN (Adam and Kochanek, 2015). Table 2.2 shows SNe for which upper limits to progenitor detection.

2.2 Hydrodynamic modelling of the spectro-photometric evolution

Some properties of the progenitors can be retrieved through the analysis of spectro-photometric evolution of the SN. In the case of CC SNe, modelling the optical light curve, making assumption on the pre-SN star, can provide information on various explosion parameters: the observed ^{56}Ni mass produced in the explosion and the progenitor mass, the velocity of the ejecta, the explosion energy and the presence of CSM around the SN (see Ricks and Dwarkadas, 2019).

The ^{56}Ni mass can be determined comparing the estimated bolometric luminosity in the early tail phase with the theoretical value of fully trapped ^{56}Co deposition, which is given by (Jerkstrand et al., 2012):

$$L_{^{56}\text{Co}}(t) = 9.92 \times 10^{41} \frac{M_{^{56}\text{Ni}}}{0.07M_{\odot}} (e^{-t/111.4d} - e^{-t/8.8d}) \text{ erg s}^{-1}. \quad (2.1)$$

The fundamental assumptions of this equation are that the deposited energy is instantaneous re-emitted and that no other energy flux has any influence on the bolometric luminosity. The progenitor's mass is linked to the optical light curve through the relation between the last-stage evolution of the progenitor and the light curve's features (Morozova et al., 2020). For type I SNe, indeed, the stretch factor (which is parameterization of the light-curve width/shape, as described in Perlmutter et al., 1997) is used to estimate the ejecta's mass (Valenti et al., 2007), which is used to constraint the mass of the progenitor star through evolutionary models of pre-explosion scenarios. The photometric modeling is not the only way to constrain the progenitor mass. During the nebular phase ($t \geq 150$ days), the inner ejecta become visible, and various nuclear burning zones can be analyzed. Stellar evolution models predict the metal core mass to strongly increase with progenitor ZAMS mass (Woosley and Weaver, 1995), making possible to distinguish different progenitors by determining the nucleosynthesis yields. Emission lines of carbon, oxygen, silicon, sulphur, sodium, neon,

magnesium are the main signatures that constrain the progenitor mass. Spectral analysis needs complex tools to model transformation of energy from radioactive decay to emergent UVOIR radiation. Temperature and Non Local Thermal Equilibrium (NLTE) solutions for a large number of zones and elements, including non-thermal heating/ionization/excitation rates (Jerkstrand et al., 2012) and multi-line radiative transfer, are fundamental ingredients that must be calculated, together making up constraints whose self-consistent solution must be iteratively sought.

An example of the application of the method can be seen in Mazzali et al. (2002), where there is a detailed study on the type Ic SN 2002ap. The SN is spectroscopically similar to the hypernova SN 1997ef. The candidate progenitor is inferred to be a main-sequence star with $M \sim 20 - 25M_{\odot}$, which is also lower than that of hypernovae SN1997ef and SN1998bw. The features of Type Ia SN progenitor though spectrophotometric simulation are influenced by the interaction between the ejecta and a companion in the proximity of the explosion. During the phases following the thermonuclear process, the explosion is expected to produce some effects on the companion structure. The study of overall the asymmetries of the ejecta has also been used to set constraints on the progenitor system. Type II SNe present a wide range of variety in their parameters space, thus it is hard to constrain the values of the progenitors stellar parameters themselves. Zampieri (2007) shows a model to understand the progenitor of the Type II SN 1997D, they used a simulation to reproduce the bolometric light curve of the event. The model uses a semi-analytic approach to solve the system of relativistic radiation hydrodynamic equations. It couples the solution of the system with an accurate treatment of the radiative transfert as a self consistent treatment of the evolution of the ejecta, considering both the heating effect of the radioactive isotopes produced in the explosion and the gravitational effect of the compact remnant. These can affect the bolometric luminosity as the decreasing rate of the lightcurve, giving rise to the wide taxonomy observed for those type of SNe.

SN 1999em was discovered (Li, 1999) only a few days after its explosion in the nearby (12 Mpc) galaxy NGC 1637. The lack of detection of a progenitor in archival images indicated that the ZAMS mass of the star that exploded was $\leq 15M_{\odot}$ (Smartt et al., 2009). A nonrotating, massive, single star of solar metallicity with ZAMS mass about 8–30 M_{\odot} is expected to be a RSG when it core collapses. In addi-

tion to SN 1999em, well-observed, typical SN IIP include SN 1999gi (Douglas et al., 2002)(Leonard et al. 2002c), SN 2004et (Maguire et al., 2010), SN 2012A (Tomasella et al., 2013), SN 2012aw (Bose et al., 2013), SN 2012ec (Barbarino et al., 2015), and SN 2013ab (Bose et al., 2015). Hydrodynamic modeling of SN 1999em was carried out by three groups, each seeking a model that accounted for the light curves as well as the photospheric velocity at some chosen epoch on the plateau, as inferred from blueshifts of absorption components of lines of moderate strength (e.g., H_β , Fe II $\lambda \sim 5169$, Sc II $\lambda \sim 6246$). Baklanov et al. (2005) used the multigroup STELLA code to calculate light curves for comparison with multiband photometry and derived $R \approx 1000R_\odot$, $E \approx 1B$, $M_{ej} \approx 18M_\odot$, and $M_{Ni} \approx 0.06M_\odot$. Utrobin (2007) carried out single-group calculations for comparison with the bolometric light curve and derived $500 R_\odot$, $1.3 B$, $20.6 M_\odot$, and $0.036 M_\odot$. From single-group calculations and the bolometric light curve, Bersten et al. (2011) derived $800 R_\odot$, $1.25 B$, $19 M_\odot$, and $0.056 M_\odot$. Hydrodynamical modeling of a somewhat stronger SN IIP, SN 2004et (Maguire et al., 2010; Sahu et al., 2006), yielded $R \approx 1500R_\odot$, $E \approx 2.3B$, $M_{ej} \approx 24.5$, and $M_{Ni} \approx 0.068M_\odot$ (Utrobin and Chugai, 2009). Values estimated for SN 2012A, SN 2012aw, and SN 2012ec using the radiation-hydrodynamics code of Pumo and Zampieri (2012) were $260R_\odot$, $0.5 B$, $12.5 M_\odot$, and $0.01 M_\odot$ (Tomasella et al., 2013), $430 R_\odot$, $1.5 B$, $20 M_\odot$, and $0.06 M_\odot$ (Dall’Ora et al. 2014), and $230 R_\odot$, $1.2 B$, $12.6 M_\odot$, and $0.04 M_\odot$ (Barbarino et al., 2015), respectively. A larger value of $R \approx 700 R_\odot$ was estimated for SN 2012A by Utrobin and Chugai (2015). Considering that the hydrodynamical modeling was based on somewhat different techniques and assumptions, and that the reasons for some of the discrepancies are apparent (e.g., the lower value of M_{Ni} inferred by Utrobin is due to the use of a smaller bolometric correction during the tail phase), the agreement of these parameters is good, although the inferred values of R spanned a factor of two.

2.3 SN rate and progenitors

The absolute number of SNe in a stellar system is related to two main parameters: the delay times distribution, which describes the distribution of the ages of the progenitor stars at the explosion and the number of SNe per unit of mass in a single stellar population.

On the evolutionary timescale of a simple stellar population, the timing for massive star to explode as a CC is very small, thus the distribution of CC SNe traces the star formation rate for the parent population. The trend of the frequency of Type Ia can provide deep insights on the nature of binary companion in Type Ia events. The time gap between the CC SN rate and the SN Ia rate is a constraint on SN Ia progenitor models and the parent stellar population (e.g. the initial mass fraction, chemical evolution, and star formation rate and history of galaxies). The rate of occurrence of a SN is therefore estimated by:

$$\dot{n}_{SN}(t) = \int_0^t \psi(t - t_D) k_{SN} f_{SN}(t_D) dt_D, \quad (2.2)$$

where t_D is the time for the star on the ZAMS to leave the main sequence (MS), because the time to the death of the stars is very short respect the time spent to the main sequence the death time is approximated with t_D , thus it depends on the mass of the star; $\psi(t - t_D)$ is the star formation rate (SFR) of the stellar population, while k_{SN} and $f_{SN}(t_D)$ are respectively the number of stars per unit of mass that end up like SN, and the time delay distribution (DTD) which gives the distribution of the time for the SN to explode. Because the SN rate is a tracer of the star formation history of the specific stellar population, and because different progenitors are related to different DTD profiles, the SN rate can give a constrain on the progenitor system.

2.3.1 Core Collapse SN rate

For a CC SN the number of events with delay time between t_D and $t_D + dt_D$ can be assumed to be equal to the number of stars with mass between M_D and $M_D + dM_D$, such that the evolutionary lifetime of M_D is equals t_D :

$$\dot{n}_{CC}(t_D) |dt_D| = \phi(M_D) |dM_D|, \quad (2.3)$$

where $\phi(M_D)$ is the initial mass function (IMF) of the stellar population, it gives the distribution of the masses for stars of a given age with respect to their initial mass. Indicating with $M_{CC,n}$ and $M_{CC,x}$ respectively the minimum and the maximum stellar mass that give rise to a CC SN event (see Figure 2.1):

$$f_{CC}(t_D) = \frac{\phi(M_D) |dM_D|}{\int_{M_{CC,n}}^{M_{CC,x}} \phi(M) dM}. \quad (2.4)$$

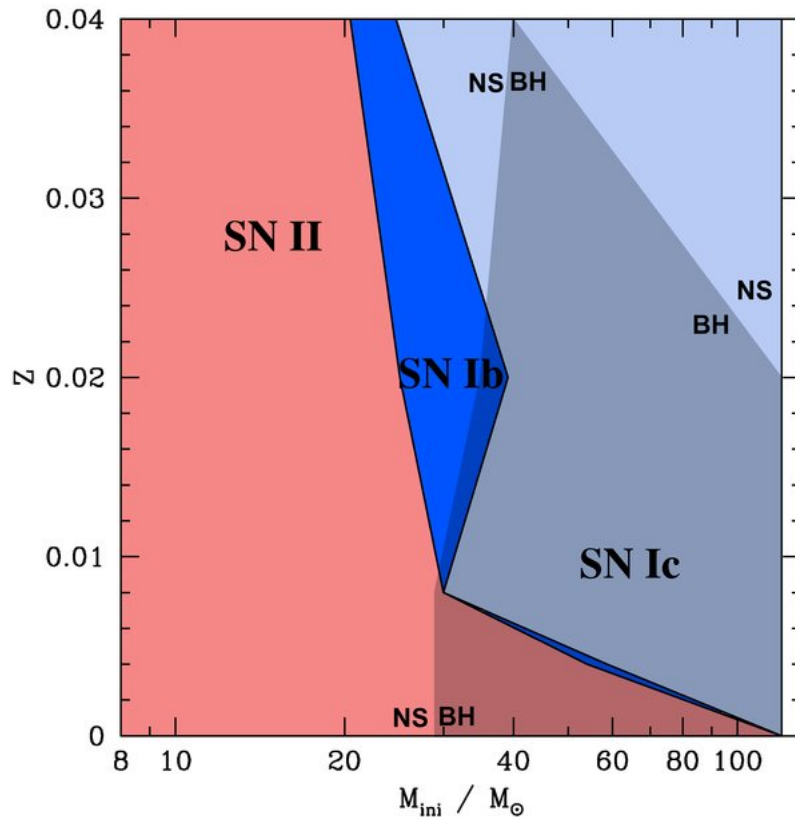


Figure 2.1: Progenitors masses and metallicities with respect to the CC SNe expected by the stellar evolution theories. The gray shaded areas on the right indicates the area where formation of a black hole (BH) is expected; elsewhere, the remnant is a neutron star (NS). Figure taken from Georgy et al. (2009).

Since

$$k_{CC} = \frac{\int_{M_{CC,n}}^{M_{CC,x}} \phi(M) dM}{\int_{M_i}^{M_s} \phi(M) dM}. \quad (2.5)$$

where $\int_{M_i}^{M_s} \phi(M) dM$ is the total mass of the stellar population and M_i and M_s are the lower and the upper limit for the stars to be formed. Thus, with the above assumptions the equation 2.2 can be written as:

$$\dot{n}_{CC}(t) = \int_0^t \psi(t - t_D) \tilde{\phi}(M_D) |\dot{M}_D| dt_D, \quad (2.6)$$

where $\tilde{\phi}(M_D) = \frac{\phi(M_D)}{\int_{M_i}^{M_s} \phi(M) dM}$ is normalized to the total mass of the stellar population. Since the lifetime of a star that end its life as a CC SN is short, one can approximate the SFR with the current rate $\psi(t) = \psi_0$, applying the approximation to the equation 2.6 and changing the integration variable:

$$\dot{n}_{CC}(t) = \psi_0 \int_0^t \phi(M_D) dM_D. \quad (2.7)$$

The last equation highlights that the CC SN rate is proportional to the death rate of a simple stellar population through the present star formation rate. The rate is determined by the interplay between the derivative of the mass of the dying star, which decreases with time, and the IMF term, which provides stars as the stellar population grows older. The result is an early peak in the death rate, which occurs a little later for steeper IMFs. At a delay time equal to the lifetime of the least massive progenitor the rate goes to zero. For a Salpeter slope, a burst forming $10^7 M_\odot$ of stars produces between 0.5 and 0.17 events/century, depending on its age (Greggio and Renzini, 2011).

2.3.2 Thermonuclear SN rate

The mathematical formalism that model the rate of occurrence of Type Ia events depends strictly to the time delay of the companion.

The typical formulation of the model to describe the occurrence rate of SN Ia considers a star with initial mass M_1 and a companion with initial mass M_2 (e.g. Fig. 2.2). The evolution of the model rests upon the definition of the distribution function

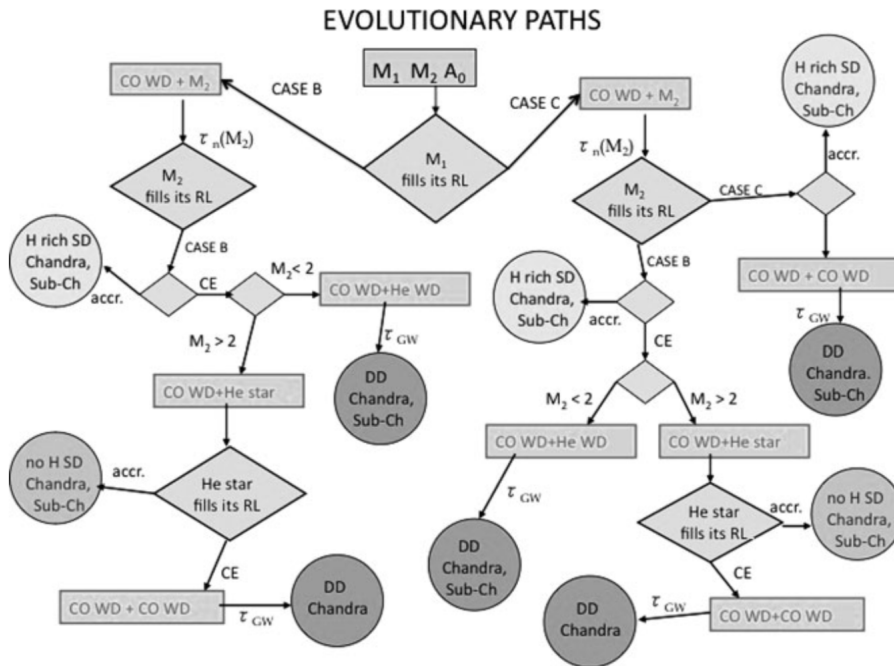


Figure 2.2: Evolutionary paths for close binaries with intermediate mass components, leading to SN Ia explosions (Greggio and Renzini, 2011).

of the delay times, $f_{Ia}(\tau)$, defined in the range (τ_i, τ_x) ; τ_i stands for the minimum evolutionary lifetime of the SN Type Ia precursors.

The formalism is model-dependent, in the sense that the SD model has a different delay time distribution with respect to DD model. For SD model τ_i is the nuclear lifetime of the most massive stars which produces a WD, that is an $\sim 8M_{\odot}$ star, which evolves off the MS in ~ 0.04 Gyr; for the DD model, τ_i could be larger than ~ 0.04 Gyr because of the additional gravitational delay.

τ_x , conversely, is the maximum delay time, and is sensitive to the progenitor model for the SN Type Ia. The main parameters that influence the delay time distribution can be summarized as follow:

- The maximum M_2 , determining the shortest delay time for both SD and DD channels.
- The minimum M_2 , determining the longest delay time for SD models, or the position of the cusp on the DTD of DD models.
- The accretion efficiency (the fraction of the envelope of the secondary, which is effectively accreted and burned on top of the CO WD) for the SD model.
- The shape of separations' distribution (A) of the DD systems at birth, and whether the common envelope induces a correlation between M_{DD} and A (CLOSE DD) or not (WIDE DD).

For the different features the DTD the formulation of the Type Ia rate has to be splitted in SN Ia rate of SD progenitors or a DD ones.

SD rate:

For this model, what drives the timing for the explosion is the companion star in the binary system. The primary star is typically an intermediate mass star with a CO WD companion (this is normal for low mass stars in a binary system with a companion that experienced the Helium flash). For a CO WD after filling its Roche Lobe (RL), the secondary star fills its RL; if the time to reach the RL and the accretion time scale to trigger the the explosion are smaller than the time to evolve outside the MS ($\tau_n(M_2)$), the explosion will produce a H-rich SD explosion. For the helium star channel (see Fig.

2.2), some corrections (of about 10%) should be applied to account for the He-burning lifetime of the secondary. $\tau_n(M_2)$ represents fairly well the total delay time also in this case. It should be noticed that if the first RL overflow is conservative, the secondary star may grow in mass, speeding up its evolution. Neglecting this complication, the number of events with delay time between t_D and $t_D + dt_D$ is proportional to the number of system with the secondary with mass between M_2 and $M_2 + dM_2$, such that $\tau_n(M_2) = t_D$:

$$n_{Ia}(t_D)dt_D \approx n(M_2)|dM_2| \quad (2.8)$$

where $n(M_2)$ is the distribution of the secondary masses in systems, which provide a successful explosion through the SD channel. From 2.4:

$$f_{Ia}(t_D) \approx n(M_2)|\dot{M}_2|. \quad (2.9)$$

The last factor, $|\dot{M}_2|$, is the changing rate of the stellar mass for stars that evolve off the main sequence. The factor $n(M_2)$ can be derived convolving the distribution of primary masses with the distribution of the mass ratio $f(q)$, where $q = \frac{M_2}{M_1}$, in binary systems is:

$$n(M_2) \approx \int_{M_{1,i}}^{8M_\odot} \frac{f(q)}{M_1} dM_1 \quad (2.10)$$

The integral extends over the range of mass for the primary in systems which provide explosions with a delay time $t_D = \tau_n(M_2)$.

The lower limit of this mass range $M_{1,i}$ results from three constraints:

- the primary must be more massive than the secondary;
- it must also be more massive than $2M_\odot$, to provide a CO, rather than a helium WD;
- its WD remnant must be massive enough to secure that the Chandrasekhar limit is reached after the mass accretion from the secondary.

DD rate:

In the DD model, the first part of the evolution is the same as in the SD model, but, no accretion on the WD takes place. Conversely, a common envelope (CE) phase sets in. This configuration leads to the complete ejection of the envelope of the secondary; as

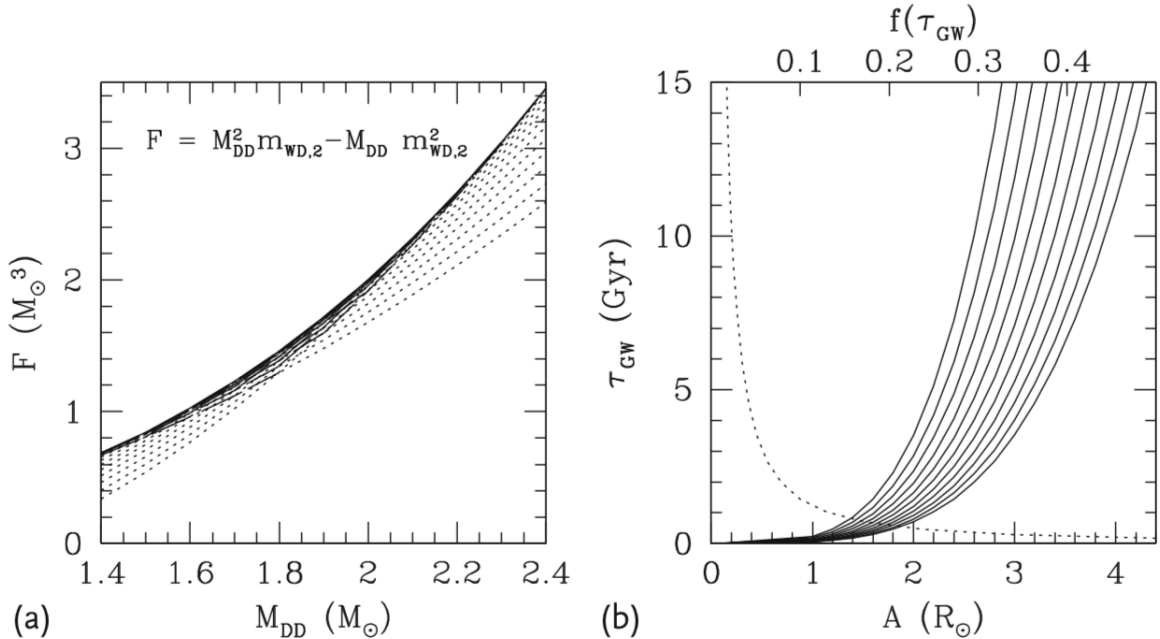


Figure 2.3: Dependence of the GW component of the delay time on the DD parameters. $F = M_{DD}^2 M_{WD2} - M_{DD} M_{WD2}^2$, where $M_{DD} = M_{WD1} + M_{WD2}$, represents the denominator of the equation for τ_{GW} . The dashed lines correspond to F in range $0.6 \leq M_{WD2} \leq 1.2 M_{\odot}$. The panel b) shows the GW delay, the solid lines show τ_{GW} for $1.4 \leq M_{DD} \leq 2.4 M_{\odot}$ (from the lower curve to the uppermost one). The dotted line shows the distribution of τ_{GW} (labelled on the upper axis) function of τ_{GW} (labelled on the left axis), assuming that the distribution of the separations A is flat.

a consequence the system evolve as a close binary of two WDs. The two components are bound and eventually merge due to the emission of GW, and in this case the delay time is:

$$t_D = t_{M_2} + \tau_{GW}, \quad (2.11)$$

where $\tau_{GW} = \frac{0.15A^4}{(M_{WD1} + M_{WD2})M_{WD1}M_{WD2}}$.

The GW component for the delay time depends on the distance separation of the two stars (A), and their masses. In the DD model, the derivation of the DTD is more complicated than in the SD model, because there is no one to one correspondence between the initial binary parameters and the delay time. The progenitor systems

should be born with a much wider separation (from several tens to several hundreds R_{\odot}), otherwise the model predicts the merging phase with a smaller delay time. It is also worth pointing out that most combinations of the parameters A and M_{DD} provide short τ_{GW} , as shown in Fig 2.3. This implies that, unless most DD SN Ia progenitors are born with low masses and with large separations, the distribution of the gravitational wave radiation delays will be skewed with short delays. Thus, the DTD that we use to estimate the rate from eq. 2.2 strictly depends on the type of progenitor, so from different progenitor we can predict different SN Ia rates related to SD or DD models. The predicted SN rate as function of progenitor system can be compared to the observed SN rate to discriminate between the two channels.

Chapter 3

SN rates

The previews two chapters highlight the power of a conceptually simple approach to constrain SN progenitors: the analysis of the dependence of the SN rate on the properties of the parent stellar population averaging over a population of galaxies with different ages in a cosmic volume and in a galaxy sample. Thus, the accurate measurements of the SN rate are fundamental to compare the observations with theoretical predictions based on different SN progenitor models. In this chapter I present the progress in SN search and rate measurements of the last century.

3.1 The first SN survey and rate measurement

The first attempt for a systematic search of SNe has been made by Baade and Zwicky (1934), who discovered the presence of two different groups of novae in the extensive study of the phenomenon in IC 4182 and NGC 1003. One of the two groups of extragalactic novae were characterized by a very bright absolute magnitude, which they called super-novae. They first proposed that the high energy released by these events is produced by the catastrophic explosion of a star. In the period from 1936 to 1940, Zwicky started a search for these events in the Virgo Cluster and in Ursa Major Cloud of galaxies with a 3-inch f/4.5 photographic camera mounted on the rooftop of the Astrophysics building of the California Insititute of Technology of Pasadena (Zwicky, 1942). Due to the condition of observations, the search did not give satisfactory results. In 1962 it was possible to start another SN survey at Palomar Observatory

with a 18-inch Schmidt Telescope. In the later 16 months the survey at Palomar observatory let Zwicky discover 7 SNe in the 175 fields in 65 deg^2 observed. The survey was conducted in two main steps: Zwicky and Josef Johnson from Caltech observed and identified the SNe; while at Mount Wilson Observatory, Baade studied the light curves and Rudolph Minkowski obtained the spectra with the 60- or 100-inch telescopes. The SN search was focused on galaxy clusters (initially the Virgo cluster) with the idea that greater the number of galaxies in the field, greater the chance of observing a supernova. By analyzing the SNe discovered during the search and the ancillary data relative to the serendipitous discovery of SNe in the years before this survey, Zwicky was able to draw some important conclusions and a first measurement of the frequency of appearance (Baade and Zwicky, 1934; Zwicky, 1970), called SN rate:

- a) SNe appear in all type of galaxies: spirals, ellipticals, or irregular stellar systems.
- b) The SN brightness is comparable with that of the galaxies.
- c) The frequency of appearance is of the order of one SN per century per bright galaxy. This conclusion is the most important, because it gave the confidence to start a systematic search with positive hope of success .
- d) SNe represent a different class of events, and have appeared in all galaxies at all times.
- e) SNe have quite ordinary progenitors whose masses are not greater than 10^{33} gr to 10^{81} gr.
- g) A common nova reaches maximum brightness in about two to three days. A SN reaches maximum brightness during about the same interval.

In Zwicky (1942), a new measurement of the SN rate was obtained with a new survey at the Palomar Observatory, for the general collection of three thousand galaxies. From Zwicky's first systematic search, members of an international search team first organized by him made many of the discoveries during the following four decades. Amateur astronomers also made, and continue to make, valuable discoveries: Reverend Robert Evans relied on his near-photographic memory of the appearance of

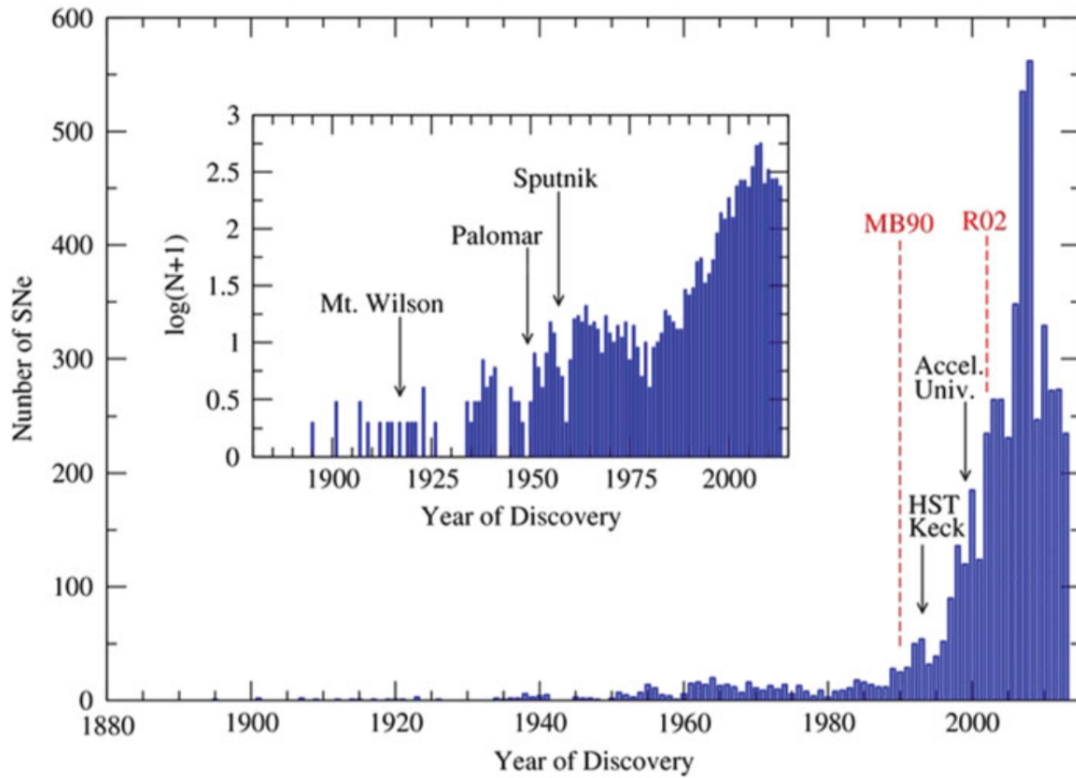


Figure 3.1: Number of supernovae discovered versus time. The inset shows the same data on a log scale. From "Absolute-magnitude Distributions of Supernovae" (Richardson et al., 2014).

thousands of bright galaxies to visually spot new supernovae, often before the time of maximum light (figure 3.1).

3.2 Control Time and detection efficiency

The “control time” (CT) is defined as the total interval of time during which a SN, of a given type and photometric evolution, is bright enough to be discovered during all observations of a given galaxy. The use of the control time to calculate the SN rate was first introduced by Zwicky (1942) and refined by van den Bergh (1991) and Cappellaro et al. (1993a, 1997b). The idea of being able to “control” a galaxy stems from the fact that SNe are transient phenomena, and stay visible for a certain length of time.

The CT depends mainly on the SN detection efficiency, the SN light curve and the amount of dust extinction. The detection efficiency (DE) of an image in a survey is the probability of detecting a SN-like point source in a image as a function of the difference between the SN brightness and the limiting magnitude of the image. The SN DE depends mainly on the survey strategy, instrumental set up and observing conditions. One of the approaches to estimate the DE curve of a SN candidate apparent magnitude for a given instrumental set up and exposure time, is via Monte Carlo simulations. In each simulation artificial point-like sources of different magnitudes are added to an image, which is then analysed using the same software as in the actual search for variable sources. The detection efficiency at a given magnitude is computed as the ratio between the number of recovered and injected artificial sources. SNe display a large diversity in their peak absolute luminosity and their photometric behaviour (see figure 3.2). Consequently, treating a given SN type with a single light curve shape and a single peak absolute magnitude is an oversimplification.

Nevertheless, the possibility to characterize a SN lightcurve is related not only to the cadence of the observations, but also to the observation condition (e.g. seeing, limit magnitude in a given night).

The CT of a survey can be estimated as:

$$\bar{CT}_i^{SN} = \int \tau_i^{SN}(m)\epsilon(m)dm, \quad (3.1)$$

where $\tau(m)$ is the time when a SN in the i -galaxy stay at a magnitude between m

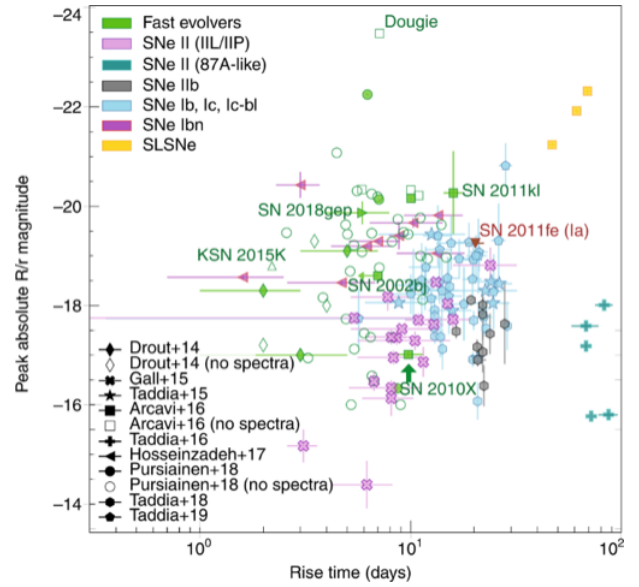
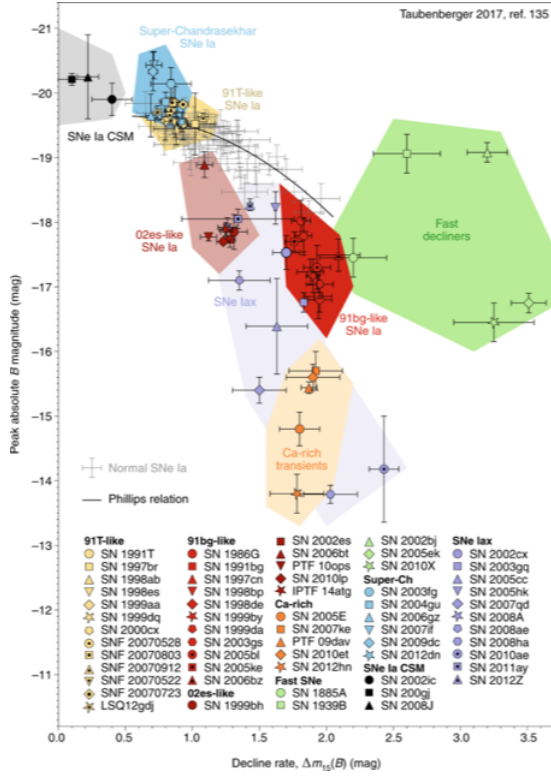


Figure 3.2: The top panel shows the distribution in the peak magnitude vs decline rate diagram of thermonuclear SNe from Taubenberger (2017); the bottom panel shows the peak magnitude vs rise time diagram for the CC SNe from Modjaz et al. (2019).

and $m + dm$ and $\epsilon(m)$ is the detection efficiency at the given magnitude. Then, the total control time CT can be computed by summing the contribution of individual observations. If the temporal interval elapsed since the previous observation is longer than the control time, the contribution is equal to the control time of the observation, otherwise it is equal to the interval of time between the two observations (Cappellaro et al., 1999).

As described in appendix A of Li et al. (2011b) we can estimate the CT of a survey in the following steps: $t_1, t_2, \dots, t_i, \dots$ are the epochs of observations, hence $t_i - t_{i+1}$ is the time interval between $i + 1$ and i observations. For a possible SN in the j -th galaxy, the control time, $CT_{i,j}^{SN}$ for a single image at the epoch t_i , can be evaluated as:

$$\bar{CT}_j^{SN} = \sum_{i=1}^n \delta t_i c_i^{SN} \quad (3.2)$$

where

$$\Delta t_i = \begin{cases} CT_{i,j}^{SN}, & \text{if } t_i - t_{i+1} > CT_{i,j}^{SN} \text{ or } i = 1 \\ t_i - t_{i+1}, & \text{otherwise} \end{cases} \quad (3.3)$$

and c_i is a factor that corrects for the SN discovery in the nuclear regions of galaxies in historical rate calculations. Eq. 3.3 does not consider the diversity of SN lightcurves, but is a good starting point to implement a comprehensive estimation of the CT. Not surprisingly, the final control time is the sum of the control time for each component weighted by its relative fraction in the luminosity function (LF). Let us consider a SN LF with n components and relative fractions of f_1, f_2, \dots, f_n . In Li et al. (2011b) two possible scenarios are presented. In the first scenario, a survey has complete control of every component of the SN LF during a total normalised control time of t , and a yield N discoveries. If we use CT_i as the total normalised control time and N_i as the number of SNe for the i -th component of the LF, we have the following equations:

$$\begin{cases} \sum_{i=1}^n f_i = 1 \\ CT_i = t & i = 1, 2, \dots, n \\ N_i = f_i \times N & i = 1, 2, \dots, n \\ r = \sum_{i=1}^n \frac{N_i}{t_i} = \frac{N}{t} \end{cases} \quad (3.4)$$

In the second scenario, a survey that has partial control of the individual components is considered. For the i -th component, N'_i SNe are discovered with a total normalised

control time of CT'_i . Under this assumption, $CT'_i \leq t$. Comparing the second scenario to the first, one has the following equations according to the concept of control times:

$$\frac{N'_i}{t'_i} = \frac{N_i}{CT_i} = \frac{N}{CT}, \quad (3.5)$$

this led to equation:

$$N'_i = \frac{N}{CT} \times CT'_i. \quad (3.6)$$

In this second scenario, the rate from the equations 3.4 is then rewritten:

$$r = \frac{N'}{\sum_{i=1}^n f_i CT'_i} = \frac{N'}{CT'} \quad (3.7)$$

where CT' is the total CT of the survey, thus:

$$CT' = \sum_{i=1}^n f_i CT'_i, \quad (3.8)$$

which means that the total control time is the sum of the control time of each component weighted by its fraction in the luminosity function.

3.3 SN rate in a cosmic volume and in a galaxy sample

The SN rate in a cosmic volume is defined as the ratio of the number of SNe exploded in the cosmic volume between the redshifts z_1 and z_2 , and the cosmic volume between the same redshifts, expressed as:

$$r_{SN}(z) = \frac{(1+z)}{V(z)} \frac{N_{SN}(z)}{CT_{SN}(z)}, \quad (3.9)$$

where $V(z)$ is the comoving volume for the given redshift and z is the mid-point of the redshift bin with extremes z_1 , z_2 :

$$V(z) = \frac{4\pi}{3} \frac{\Theta}{41253} \left[\frac{c}{H_0} \int_{z_1}^{z_2} \frac{dz'}{\sqrt{\Omega_M(1+z')^3 + \Omega_\Lambda}} \right]^3 Mpc^3 \quad (3.10)$$

which depends on the cosmological parameters H_0 , Ω_M , Ω_Λ and Θ , that is the search area in deg^2 . The normalization with respect to the survey volume does not consider

the intrinsic differences that could be in the environments. Thus, the assumption made above is that all the SNe exploded in the same environment.

To consider the intrinsic features of the host in the estimation the SN rate at a given redshift z , it can be evaluated as the ratio between the number of observed SNe and the control time of the monitored galaxies at that redshift:

$$r_{SN}(z) = (1 + z) \frac{N_{SN}(z)}{\overline{CT}_{SNi}(z)}, \quad (3.11)$$

where the factor $1 + z$ corrects the rate to the rest frame and \overline{CT}_{SNi} is the control time.

Since SNe are rare events the monitoring of large sample of galaxies allows us to collect a statistically significant number of events. To measure the SN rate we should take into account

1. the time the SN light curve is above the detection threshold limit of the survey, also referred as surveillance time (or control time, CT);
2. the SN absolute magnitude and luminosity evolution;
3. the host galaxy distance, mass or luminosity;

Pskovskii (1961, 1967) show how the SN rate is proportional to the host-galaxy luminosity. Thus, galaxies with an higher number of stars have higher probability to host a SNe. To compare the number of stars that will explode as SNe we need to normalize the rate measured in a galaxy sample per unit of mass or per unit of luminosity. The B band luminosity has been for a long time the only available parameter to normalise the SN rates in nearby galaxies (SNu unit). Since the B band luminosity is the result of the combined effects of the emission by both old and young stellar populations and their relative contributions change along the Hubble sequence, it is expected that CC SN rate normalised per unit B band luminosity shows a strong dependence on the galaxy morphological type (Cappellaro et al., 1999; Tammann, 1974). A different tracer of the population of massive stars is the total infrared luminosity (LTIR) since there is a good correlation between SN rate and LTIR (Cappellaro et al., 1999; Mannucci et al., 2003). Whereas the B band luminosity is unspecific to the stellar age, the luminosity in a reddish band, such as K band, is a good tracer of the old population

in a galaxy; therefore of the mean age of the stellar population. The combination of the K band luminosity and the B-K colour can be used as an indicator of the galaxy mass (Bell and de Jong, 2001). The data collected from 2MASS allowed Mannucci et al. (2005) to normalise the SN rates in a sub-sample of Cappellaro et al. (1999) per unit K band luminosity and per unit galaxy mass by using the relation of Bell and de Jong (2001) and adopting a diet Salpeter. Eventually the SN rate normalized by the galaxy luminosity is measured as:

$$r_{SN}(z) = (1 + z) \frac{N_{SN}(z)}{\sum_{i=1}^n L_i CT_{SNi}(z)}, \quad (3.12)$$

where, generally, L_i is the B band luminosity of the i -th galaxy in unit of $10^{10}L_{\odot}$.

3.4 SN surveys and rate measurements

Rate measurements, until the 1990, were based mostly on the Palomar SN search (Zwicky, 1942), the Asiago SN search (Cappellaro and Turatto, 1988), and Robert Evans' visual search (van den Bergh and McClure, 1990; Van den Bergh et al., 1987). The SN rates, normalised to the B-band luminosity of the host galaxies, were measured for galaxies of different Hubble types, and were compared to different tracers of star formation (e.g., broad-band colours, far-infrared luminosities, Cappellaro et al., 1993b; Cappellaro et al., 1999; Cappellaro et al., 1993a, 1997a). Mannucci et al. (2005) normalised the rates with the infrared K-band luminosity, as well as with the mass derived from the K-band luminosity and B-K colours of the galaxies. A study on radio galaxies, conducted by Della Valle et al. (2005), found that radio-loud early-type galaxies have a SN Ia rate that is a factor of 4 higher than that of the radio-quiet early-type galaxies. The discrepancy was suggested due to repeated episodes of interaction and/or merger events. Mannucci et al. (2008) found that SNe Ia are more common in cluster early-type galaxy with a factor of three, rather than in field early-type galaxies, perhaps due to galaxy interactions in the clusters.

Li2011 estimated the rate for SN Ia, Ib/c, and II to be 2.7×10^{-5} , 2.3×10^{-5} , 3.9×10^{-5} in $yr^{-1} Mpc^{-3} (\frac{h}{0.7})^3$ unit, with h ranging from 0.73 to 0.7. Due to the short lifetime of CC SN progenitors, the SN rate of such events is expected to track the cosmic SFR (Hopkins and Beacom, 2006; Maoz and Graur, 2017; Takeshi et al.,

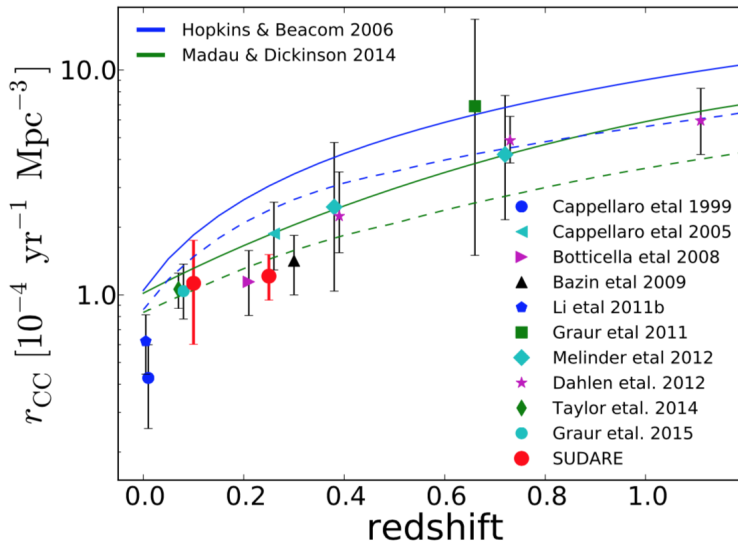


Figure 3.3: The figure from Cappellaro et al. (2015) shows the CC SN rate as function of redshift. All measurements do not account for the correction for hidden SNe. The predicted SN rate from the measured SFR adopt 8, 40 M_{\odot} as the lower and upper mass limits for SN CC progenitor and the proper IMF, Salpeter for Madau and Dickinson (2014) and SalA for Hopkins and Beacom (2006). The dashed lines show the predicted SN rate, assuming the fraction of hidden SNe given in Mattila et al. (2012).

2008; Wilkins et al., 2019). Because the cosmological implication of type Ia SNe, the searches for non local SNe, $z \geq 0.1$ are focused on the characterization of type Ia population. This introduces a severe bias for the detection and the classification of CC SNe and their rate measurement. Anyhow, observations highlighted that CC rate within the 11 Mpc is somehow greater than the expected value based on the local rate of star formation (Botticella et al., 2012; Horiuchi et al., 2011; Xiao and Eldridge, 2015).

In the redshift range $0.1 \leq z \leq 0.4$, as shown in Fig. 3.3, the CC rate is lower than a factor of two with respect to the expected value (Botticella et al.; Horiuchi et al., 2014), this may be because of observational biases (such as SNe intrinsically dim or heavily obscured by dust).

The LOSS SN search presented one of a major study on the SN rates in a volume

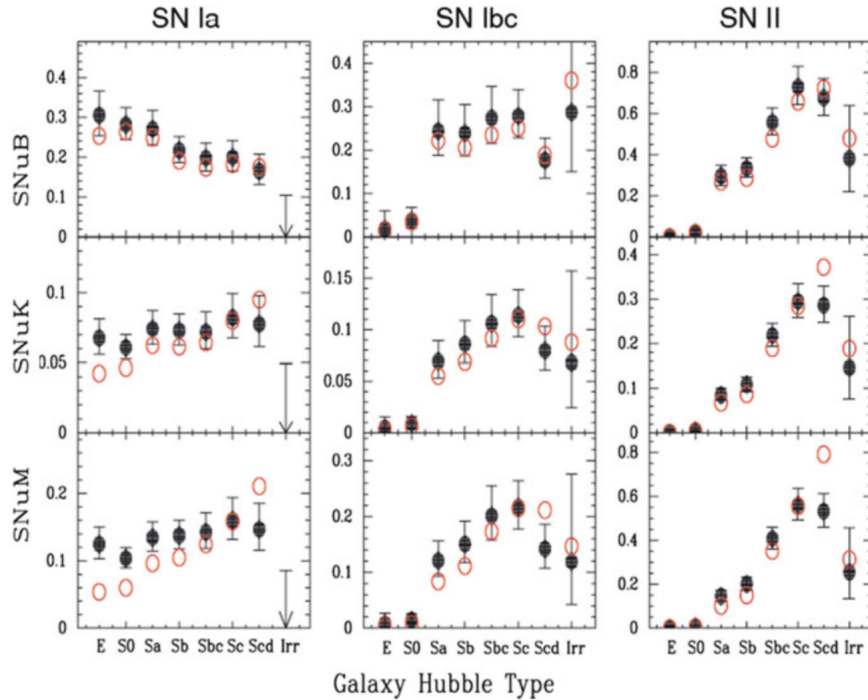
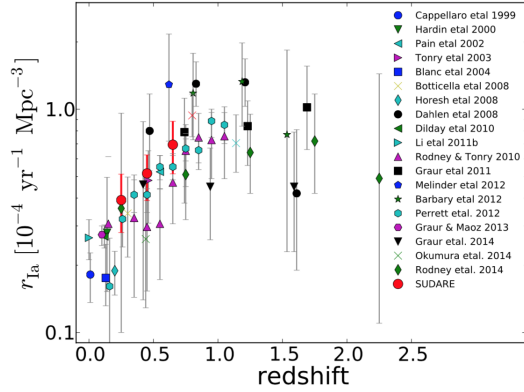
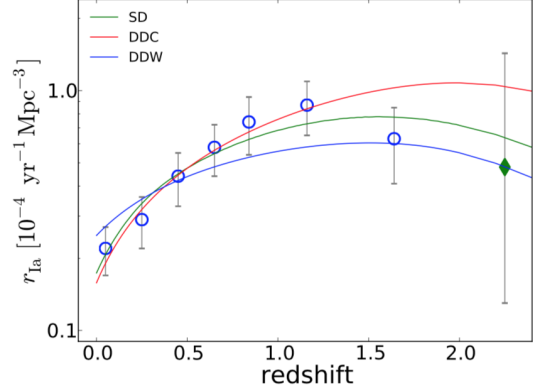


Figure 3.4: Supernova rates (solid symbols) are plotted against galaxy type. Image from Li et al. (2011a).

limited sample of local galaxies. They used a generalized control time method to account for a luminosity function family and shape for each supernova subtype (Li et al., 2011b). A major result from the LOSS survey is a rate-size relation, which points out that the SN rate per unit of mass decreases with the increasing of galaxy mass. Beside the former relation, it is important to mention the morphology relation with the SN rate (Cappellaro et al., 1999; Cappellaro et al., 1997b), that can account for some trend for a stellar population to produce SNe of a certain type (see Fig. 3.4). The rate of SN Ia in galaxies of late-type galaxies is composed by a significant fraction of SN Ia coming from rather young (10^8 years) populations. The morphology relation suggests an empirical proof that the SN Ia rate is related to the star formation history (SFH) of the parent population. As already mentioned in chapter 2, the link between the SN Ia rate with the SFH is represented by the specific DTD, i.e. the fraction of SNe as function of time that would follow a hypothetical instantaneous burst of star formation.



(a) In the figure various estimates of the SN Ia rate from the literature are compared. The rate of Blanc et al. (2004); Cappellaro et al. (1999); Hardin et al. (2000); Madgwick et al. (2003) is given per unit luminosity. They are converted in rate per unit volume using the following relation of the luminosity density as a function of redshift: $j_B(z) = (1.03 + 1.76z) \times 10^8 L_{\odot}^B \text{ Mpc}^{-3}$ (Botticella et al.). The measurements of Perrett et al. (2012) are scaled up by 15% to account for the fact that they not include the faint SN 1991bg-like events.



(b) Average SN rate measurements compared to the theoretical SN Ia rate considering DTD from a SD, DD in close or wide progenitor system, (DDC or DDW; see Cappellaro et al., 2015, for details).

Figure 3.5

The nature of DTD depend on the progenitor system (see Greggio, 2005, 2010, for details), thus the comparison with the data could help us to figure out which is the most probable channel for a binary system two end its evolution as a Type Ia SN, but the dispersion of SN Ia rate estimates and the marginal differences for the evolution with cosmic time of the volumetric SN rate does not allow to discriminate between SD and DD progenitor scenarios (see figure 3.5). Because of the growing interest in using the evolution of the SN rate over cosmic time to constrain the progenitor systems of SNe, recent studies have derived SN rates at moderate to high redshifts (Blanc et al., 2004; Botticella et al.; Hardin et al., 2000; Madgwick et al., 2003; Strolger et al., 2004, e.g.). Many of these investigations were conducted with systematic rolling searches using large ground-based telescopes or the Hubble Space Telescope, yielding rates that have precisions comparable or superior to those of the published nearby SN rates. Thus, it is critical to improve the precision of the nearby SN rates before they become the bottleneck for studies of the cosmic evolution of SN rates.

Chapter 4

SUPernova Diversity And Rate Evolution

The SUPernova Diversity And Rate Evolution (SUDARE) survey aims to obtain accurate measurements of the SN rate for both CC and Type Ia SNe in order to constraint their progenitors by analysing the dependence of the rates on the properties of the parent stellar population averaging over a population of galaxies with different ages in a cosmic volume and in a galaxy sample. In this chapter I present the survey's strategy and pipeline and the results from the data analysis.

4.1 SUDARE

The SUDARE survey is performed using the VLT Survey Telescope (VST, Capaccioli et al., 2012) equipped with the OmegaCAM camera, placed at ESO Paranal (Chile) and operating since October 2011. VST is a 2.6 m class telescope with f/5.5 modified Ritchey-Chretien optical layout designed to deliver a large, uniform focal plane. The camera is equipped with a mosaic of 32 CCDs, each with 4000×2000 pixels, covering $1 \times 1 \text{ deg}^2$ with a pixel scale of $0.21 \text{ arcsec pix}^{-1}$.

Most of the observing time at VST has committed to ESO public surveys but a fraction of time has been dedicated to the Guaranteed Time Observations (GTO) made available to the telescope and instrument teams in rewards of their investments in the construction and installation of instruments. The VST has been involved in

Table 4.1: Field coordinates and compact log of the observations

Field	RA(2000.0)	DEC(2000.0)	Field size deg^2	Observing	Epochs			Seeing
	hh:mm:ss	dd:mm:ss		season	r	g	i	range [median]
CDFS1	03 : 33 : 34.506	-27 : 34 : 10.78	1.15	Aug.2012-Jan.2013	29	7	11	0.51-1.44 [0.89]
CDFS2	03 : 29 : 02.654	-27 : 34 : 00.70	1.15	Oct.2011-Jan.2012	23	6	4	0.51-1.46 [0.82]
CDFS3	03 : 29 : 00.270	-28 : 34 : 29.40	1.15	Jan.2013-Dec.2014	30	10	14	0.52-1.20 [0.84]
CDFS4	03 : 33 : 34.240	-28 : 34 : 45.20	1.15	Oct.2013-Feb.2015	30	8	18	0.65-1.19 [0.85]
COSMOS	10 : 00 : 28.600	+02 : 12 : 21.00	1.15	Dec.2011-Apr.2015	49	25	15	0.50-1.28 [0.86]

three large public programs: the Kilo Degree Survey (KIDS), VST ATLAS, and the VST Photometric H-alpha Survey of the Southern Galactic Plane (VPHAS+). These surveys complemented other surveys carried out with VISTA, working in the infrared, and investigated a wide range of topics ranging from studies of the Milky Way to exploring the nature of dark matter. The time allocated to the SUDARE survey was from the VST and OmegaCAM GTO and Chilean GTO time. VST covering a wide sky field at very faint magnitudes (the 3σ mag limits for the deep images are 26.2, 25.6, 24.9 mag for r, g, and i bands, respectively) allows us to monitor a large volume for searching SNe and to improve the SN statistics in the rate measurement. SUDARE monitored for four years (2011-2015) two extragalactic fields (Fig 4.1): the *Chandra Deep Field South* (CDF-S) and the *Cosmos Evolution Survey* (COSMOS) field (see table 4.1).

CDF-S is one of the fields which held the deepest observations obtained with the X-ray Chandra satellite, it observed at the same path of the sky for 11 days. After these observations, the CDF-S has become the center of one the most comprehensive multi-wavelength campaign ever carried out with ground-based and space telescopes (see https://www.eso.org/~vmainier/cdfs_pub/ for details on the project). COSMOS is an astronomical survey designed to probe the formation and evolution of galaxies as a function of both cosmic time and the local galaxy environment. The survey covered a 2 square degree equatorial field with spectroscopy and X-ray to radio imaging by most of the major space-based telescopes and a number of large ground based telescopes (see <http://cosmos.astro.caltech.edu/> for details on the project).

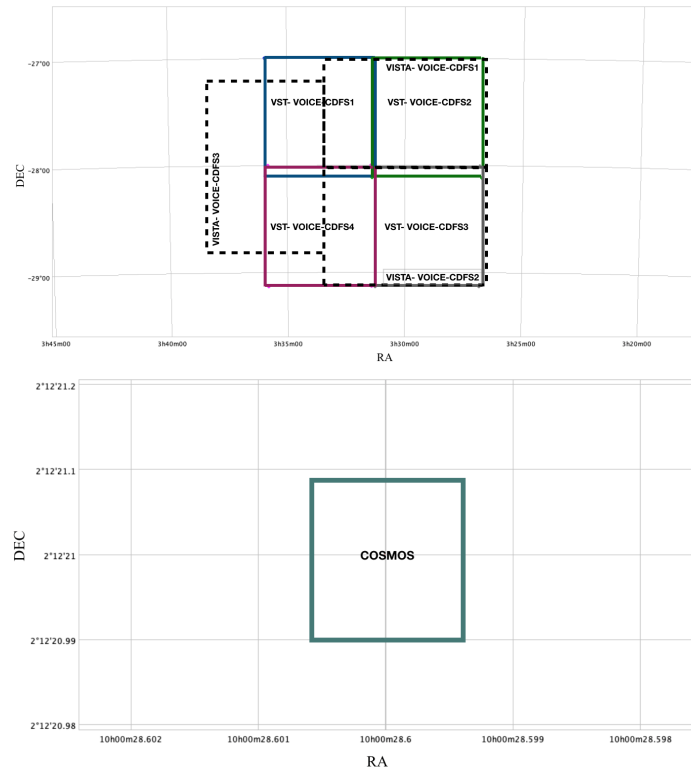


Figure 4.1: The top panel shows the area of each of the single pointing for the CDF-S field. It shows also the overlapped area for the VISTA-VIDEO survey. The bottom panel shows the area for the pointing in the COSMOS field.

Table 4.2: The table shows, for each of the VST pointing, the epochs of the observations and the seeing of each observation.

VOICE-CDFS1		VOICE-CDFS2		VOICE-CDFS3		VOICE-CDFS4		COSMOS			
EPOCH	SEEING	EPOCH	SEEING	EPOCH	SEEING	EPOCH	SEEING	EPOCH	SEEING	EPOCH	SEEING
2012-08-05	1.31	2011-10-20	1.17	20130106	0.81	20140731	0.67	2011-12-18	0.65	20131227	0.72
2012-08-13	0.69	2011-10-25	0.56	20130802	0.73	20140803	0.71	2011-12-22	0.92	20131230	1.01
2012-09-02	1.02	2011-10-28	0.92	20130805	0.83	20140807	1.19	2011-12-27	1.03	20140103	0.86
2012-09-05	1.28	2011-10-30	1.06	20130815	0.68	20140817	0.96	2011-12-31	1.14	20140105	0.81
2012-09-08	1.00	2011-11-02	0.78	20130817	0.69	20140902	0.96	2012-01-02	0.63	20140112	0.73
2012-09-14	0.55	2011-11-04	0.62	20130827	0.87	20140925	0.82	2012-01-06	0.58	20140121	1.18
2012-09-17	1.06	2011-11-15	0.61	20130830	0.79	20140927	0.82	2012-01-18	0.63	20140124	0.80
2012-09-20	0.87	2011-11-18	0.90	20130905	0.87	20140930	1.02	2012-01-20	0.87	20140127	1.09
2012-09-22	0.89	2011-11-21	0.68	20130909	1.02	20141002	0.65	2012-01-22	0.77	20140202	1.21
2012-09-24	1.44	2011-11-23	0.90	20130913	0.79	20141013	0.87	2012-01-24	0.68	20140209	1.28
2012-10-07	0.93	2011-11-26	0.64	20130925	0.82	20141020	0.80	2012-01-27	0.92	20140219	0.89
2012-10-08	0.93	2011-11-28	1.04	20130928	1.01	20141023	0.90	2012-01-29	0.86	20140221	0.93
2012-10-11	0.92	2011-12-01	0.82	20131003	0.94	20141026	1.08	2012-02-02	0.88	20140223	0.81
2012-10-14	1.07	2011-12-03	0.52	20131005	1.16	20141029	0.73	2012-02-16	0.50	20140226	0.81
2012-10-17	0.92	2011-12-14	0.88	20131007	0.87	20141110	0.78	2012-02-19	0.97	20140228	0.77
2012-10-21	0.51	2011-12-17	0.88	20131012	0.70	20141202	0.84	2012-02-21	0.77	20140304	1.11
2012-10-25	0.86	2012-01-14	0.77	20131021	0.71	20141205	0.74	2012-02-23	0.74	20140308	0.91
2012-11-04	0.67	2012-01-18	0.57	20131024	1.15	20141211	0.99	2012-02-26	0.84	20140321	0.96
2012-11-06	0.83	2012-01-20	1.00	20131025	1.01	20141213	0.87	2012-02-29	0.89	20140323	0.92
2012-11-08	0.88	2012-01-23	0.59	20131026	0.62	20141216	1.07	2012-03-03	0.93	20140325	0.66
2012-11-10	0.76	2012-01-25	0.90	20131027	0.56	20141218	0.77	2012-03-06	0.80	20140329	0.89
2012-11-20	0.78	2012-01-29	0.67	20131028	0.52	20141222	0.91	2012-03-13	0.68	20140404	0.58
2012-12-03	0.71	2012-02-02	1.46	20131030	0.87	20141224	0.65	2012-03-15	1.11	20140407	0.61
2012-12-07	0.81			20131107	0.88	20150109	0.85			20141203	1.00
2012-12-13	0.55			20131110	1.01	20150113	0.67			20141230	1.04
2012-12-20	0.96			20131222	0.83	20150117	0.72			20150111	0.71
2013-01-03	0.68			20131224	0.64	20150121	1.00			20150128	0.90
2013-01-06	0.91			20131230	1.20	20150130	0.85			20150131	0.73
2013-01-10	0.89			20140102	0.72	20150201	0.94			20150215	0.70
				20140106	0.87					20150310	0.80
				20140108	1.01					20150314	0.84
				20141215	0.68					20150319	1.00

The SUDARE strategy consists in observing each field every three days in r-band, excluding only ± 5 days around the full moon, in table 4.2 a list of the observation epochs is provided. The choice of the r-band was made considering that in the redshift range $[0, 1]$ the SN luminosity peaks in this band due to the shift of the rest frame SED at longer wavelengths.

The images are taken with an exposure time of 30 min to reach a magnitude limit of 25 mag in average condition sky. Each observation is split in 6 min exposures with a dithering pattern designed to fill the gap between the chips (the dithering range is from 25 *arcsec* to 85 *arcsec*).

Exposures in the g and i bands have been acquired to measure the colours of the transients, which are crucial ingredients to obtain an accurate photometric classification. The cadence in these bands is more relaxed respect to the r-band, one observation every week. Deep stacked images in the u g r i bands from the SUDARE and the VOICE (VST Optical Imaging of CDFS and ES1 Fields) surveys (Vaccari et al., 2016) with deep stacked image in the JHK bands from the VISTA Deep Extragalactic Observation (VIDEO, Jarvis et al., 2012) survey have been exploited to measure the spectral energy distribution (SED) of galaxies. These observations have been used to estimate galaxies' photometric redshift, z_{phot} , an important ingredient in SN classification and SN rate measurement, and the galaxy mass e star formation history (SFH) required for SN rate normalization and analysis.

The procedure for searching SN candidates in the images is composed by four steps:

- images reduction for each single epoch;
- difference between images at different epochs;
- transient detection in difference images;
- transient classification from the light curve analysis.

The flowchart in figure 4.2 shows in more details the procedure applied for the SN search and classification.

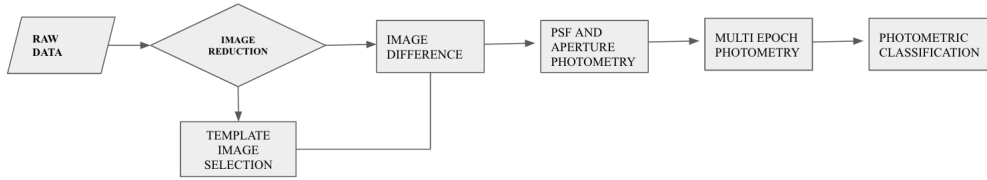


Figure 4.2: The flowchart shows the steps for the analysis of the images and the transient detection and classification. The raw images are reduced through the VST-Tube pipeline, which co-adds single epoch images and produces stacked images. Between the single epoch images, within the analysed epochs range, the one with the best seeing is selected as template for the difference. For each of the other images, hotpants is used to obtain the difference images. These are analysed using SExtractor to detect all the residual sources. A visual analysis of all the images has been performed to check the presence of the transients. For the transients selected as possible SN, light curves are obtained in g, r and i bands. The light curves are used to classify the transients through the comparison with light curve templates with two different tools (an ad hoc python code to fit the light curve with the templates and SNANA).

4.2 Image reduction and difference image analysis

Single epoch images were reduced combining the dithered exposures using the VST-Tube pipeline (Grado et al., 2012). The reduction process is composed of the following steps:

1. instrument’s signature (overscan, flat-field, CCD gain, illumination correction, master bias);
2. astrometry and photometric calibration;
3. the dithered exposures;

The overscan correction, measured over the overscan region, is applied by subtracting the median bias value. Along with this, also a master bias correction is applied to take into account the effects of electronic noise on the physical pixels in the image. The master-bias image is obtained as a sigma-clipped average of bias frames and then subtracted from each image.

The master-flat is a combination of a master twilight flat, to correct for a pixel-to-pixel sensitivity variation, and a super sky-flat, made from a combination of science images, accounting for a low spatial frequency gain variation. The master twilight and master sky-flat are produced using a robust sigma clipped average of overscan and

bias corrected twilight frames and science frames, respectively. Wherever possible, the master frames are produced independently for each epoch. Along with the flat field correction, the effect due to a large-scale gradient in the quotient of the flat field at different wavelengths is considered, since the color of the morning sky (where the sky flats are taken) and of the night sky is different.

The absolute photometric calibration is computed comparing the observed magnitudes of stars in standard fields with SDSS photometry. The extinction coefficient was taken from the extinction curve M.OMEGACAM.2011-12-01T16:15:04.474 provided by ESO.

The relative photometric correction among the exposures was obtained by minimizing the quadratic sum of differences in magnitude between overlapping detections. The r.m.s. of the magnitude residuals taking only the sources with a high (≥ 90) signal-to-noise ratio (S/N) takes into account is 0.039 mag.

The absolute astrometric accuracy compared to the reference 2MASS (Skrutskie et al., 2006) catalog is 0.28 *arcsec*, while the relative astrometric accuracy, computed as the quadratic sum of the errors along RA and Dec, is 0.06 *arcsec*; the tool used for these tasks is SCAMP (Bertin, 2006).

The tool SWARP (Bertin et al., 2002) is used for the image resampling in order to apply the astrometric solution and produce the combined single-epoch and stacked multi epoch images.

4.3 Transient detection

The transients search is performed through a python based tool. I exploit r band images to search SNe because in the redshift range of interest ($0 \leq z \leq 1$) the SED of an higher number of SNe is expected to peak in that band.

To optimize the SN search, it is important to properly choose the images that would be used for the subtraction. There are two requirements:

1. the seeing of the two images does not have to be very different;
2. the time gap between the images acquisition has to be the longest possible.

If the time gap between the image and the reference is too close, the SN can

appear in both images, thus the subtraction would let the SN to remain undetected in the difference image.

As outcome from the images reduction steps it is obtained a mask image for saturated stars that is combined with the weighted map produced by VST tube. This allow to build a bad pixel mask for each single epoch image.

I need to mask the saturated stars to prevent their use for the search, and to remove all the detections in the difference images at their positions.

To perform the images' difference it has been used *hotpants* (High Order Transform of PSF And Template Subtraction), developed by Andrew Backer as an implementation of Alard (1999) algorithm.

The algorithm takes into account two issues with image difference:

- the alignment of the images frames;
- the matching of the point spread functions (PSFs).

The first step can be done registering the two images, a process that matches the coordinate system of the two images.

The second step is the atmospheric conditions and visual response from the telescope are different at any time an image is acquired. The idea of Alard and Lupton (1998) is to adopt the best seeing image as reference and to match the seeing by convolving the reference to the seeing of the new image:

$$Ref(x, y) \otimes K(u, v) = I(x, y) \tag{4.1}$$

where $Ref(x, y)$ is the reference image convolved with the kernel, $K(u, v)$, and $I(x, y)$ is the image to be aligned. In principle, solving this equation is a nonlinear problem; however the kernel can be decomposed using basic functions:

$$K(u, v) = \sum_i a_i \times B_i(u, v). \tag{4.2}$$

With this decomposition, the problem is changed in finding the a_i parameters, that can be done solving the inverse problem

$$M\mathbf{a} = \mathbf{V}, \tag{4.3}$$

where $M_{ij} = \int C_i(x, y) \frac{C_j(x, y)}{\sigma^2(x, y)} dx dy$, $V_i = \int Ref(x, y) \frac{C_i(x, y)}{\sigma^2(x, y)} dx dy$ and $C_i(x, y) = I(x, y) \otimes B(x, y)$; $\sigma(x, y)$ takes into account the fluctuation of the Poisson statistic.

By default the kernel is chosen to be decomposed on a basis of three Gaussian functions with polynomial order from 2 to 6.

The difference images are analysed with SExtractor (Bertin and Arnouts, 1996a) to detect all positive sources that are transient and variable sources, but also artefacts that result from poorly masked CCD defects, poorly removed cosmic rays, residual from the subtraction of bright sources, reflection ghosts from bright sources. This software characterises each source detected on an image with a series of parameters related to the tomography and the brightness of the source itself. I applied an algorithm that assigns a score to each sources to the catalog obtained with SExtractor. The algorithm uses a number of parameters measured by SExtractor for each source: the FWHM, flux_ratio, isoarea and magnitude within different apertures. This allows to distinguish the sources that fall into the selected regions of the parameters space, which are considered as *true* detections. If the score is below a given threshold (30) the source is labelled as an artefact. The ranking scores and the threshold are selected and calibrated through extensive artificial star experiments.

Each source detected in the difference image with a score higher than 30 is stored in a web archive and a stamp is created with a series of images at different epochs of a small region centered at the position of the source (see Fig.4.3)

About 100 sources per field and epoch pass the selection process, are validated by visual inspection and are labeled as: supernova (SN), possible SN (PSN), active galactic nucleus (AGN), variable star (VAR), bad subtraction (BADSUB), or moving object (MOV). The final selection of the SN candidates is done by taking into account the photometric evolution of the source.

The archive allows to keep track of the light curves, preliminary and final classification, spectroscopic classification, and host galaxy photometric redshift for each SN candidate.

To identify the host galaxy for each SN in the sample, I measured the separation of the SN from each candidate host galaxy in term of an elliptical radius, R , defined by SExtractor as:

$$CX(x_{SN} - x_C)^2 + CY(y_{SN} - y_C)^2 + CXY(x_{SN} - x_C)(y_{SN} - y_C)^2 = R^2, \quad (4.4)$$

```

#30 RA= 3:27:44.643 DEC=-28:29:13.57 score=60.0
      xc      yc    fwhm fluxrad isoarea mag auto  aper  cl star phmag
dif 13925.93 11077.71  2.86  2.05  82.00  20.48  20.44  0.98  20.29
                                     18.69 ref
                                     18.32 new
dist= nan  z= nan

```

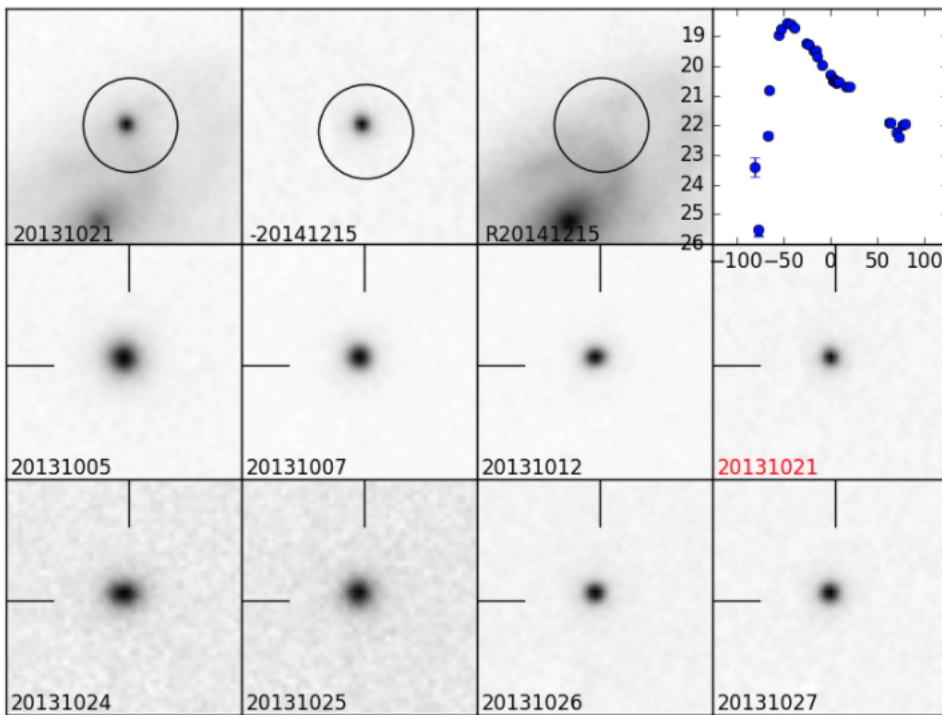


Figure 4.3: Example of a stamp produced by the SUDARE pipeline. In the first line of the stamp (from left to right), we show the search difference and the template images and a preliminary light curve. The second and third lines show a series of images at different epochs centered at the position of the source.

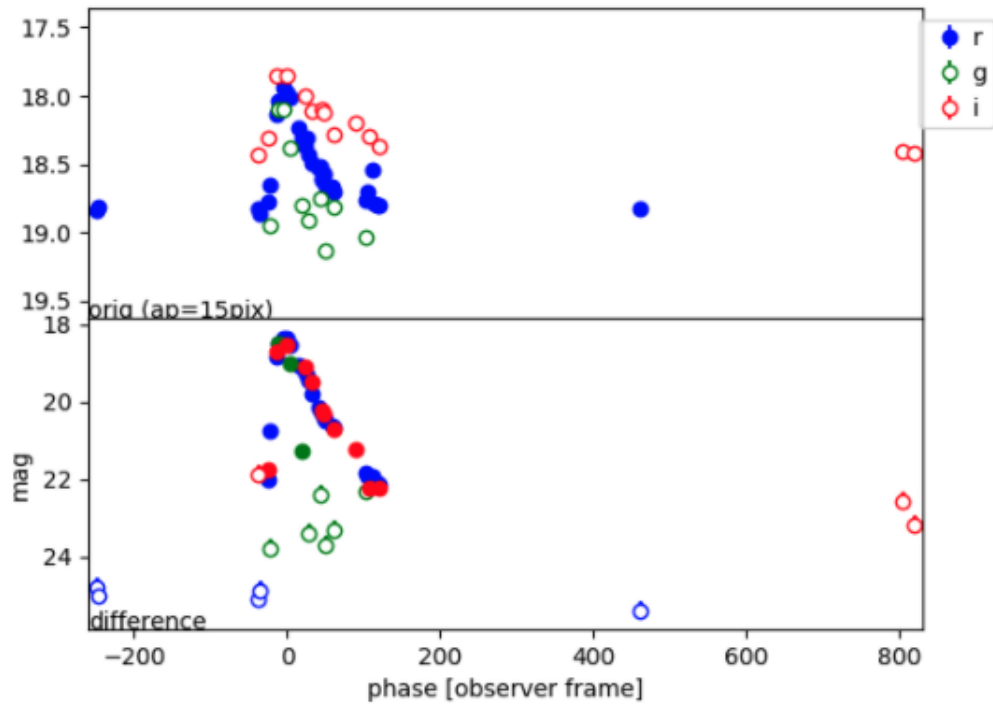


Figure 4.4: Example of a light curve obtained with forced photometry in g,r and i bands: in the upper panel, the photometry from the original image takes into account for the flux contribution of the host galaxy to the light curve. In the bottom panel, the force photometry is performed on the difference images.

where (x_{SN}, y_{SN}) are the coordinates of the SN and (x_C, y_C) are the coordinates of the galaxy centre. I assume that the isophotal limit of a given galaxy corresponds to $R = 3$. The host galaxy is selected as the nearest in terms of R , and it is verified through visual inspection. The light curves (LC) in r, g and i bands are obtained for all the SN by performing forced photometry at the position of the source in the r-band images (an example of light curve is in Fig.4.4). I performed PSF-fit photometry for each SN candidate both on search images and on difference images for all available epochs.

Table 4.3: List of supernovae.

candidate	$z(\text{host})$	err	Source	z_{sn}	Template	$T_{MAX}[MJD]$	AV	$\Delta\mu$	Type	χ^2	N_{pt}	P_{χ^2}
cdfs3_g_20130817_20131030_68B	0,139		spec	0,14					II	2,30E+02	41	1,50E-27
cdfs3_g_20130830_20131030_43C				0,44					II	3,40E+01	39	7,00E-01
cdfs3_g_20131110_20130817_3C	0,265		spec	0,26					Ia	6,00E+01	26	1,80E-04
cdfs3_i_20130815_20151121_170C	0,142	[0.047,0.275]	phot	0,49					Ia	6,60E+01	42	1,10E-02
cdfs3_r_20130802_20141215_12D				0,28					Ia	3.1E1	39	8.9E-1
cdfs3_r_20130802_20141215_230D				0,22					II	1.4E1	32	1.0E-1
cdfs3_r_20130802_20141215_231D				0,31					II	3.0E1	39	8.6E-1
cdfs3_r_20130802_20141215_244D				0,53					II	5.9E1	42	4.0E-2
cdfs3_r_20130802_20141215_8D	0,665	[0.511,0.786]	phot	0,47					Ia	1.E1	38	1.0E-1
cdfs3_r_20130805_20130106_2A	0,35		spec	0,30	1998S	56531.3	0.5	0.3	IIIn	2.8E2	40	3.4E-37
cdfs3_r_20130805_20141215_247B	0,05		spec	0.074					II	1.9E1	42	1.0E-1
cdfs3_r_20130805_20141215_3C	0,39	[0.32,0.46]	phot	0.553					Ia	2.8E1	36	8.2E-1
cdfs3_r_20130805_20141215_6C	0,17		spec	0,24					Ia	2.2E1	30	8.7E-1
cdfs3_r_20130815_20141215_25D	0,15	[0.17,0.22]	phot	0,25	1991T	56531.3	0.9	0.3	Ia	8.1E1	42	2.9E-4
cdfs3_r_20130815_20141215_31D	0,44		spec	0,62					Ia	5.1E1	39	9.0E-2
cdfs3_r_20130817_20141215_247C	0,24		spec	0,34					Ibc	7.4E1	41	8.6E-4
cdfs3_r_20130905_20130106_11E	0,19	[0.06,0.25]	phot	0,28	1994D	56531.3	-0.3	-0.3	Ia	9.0E1	42	2.7E-5
cdfs3_r_20130905_20130106_6F	0,23		spec	0,33					Ia	4.6E1	42	3.1E-1
cdfs3_r_20131007_20130106_59C				0,39					IIIn	3.2E1	34	5.9E-1
cdfs3_r_20131012_20141215_36D	0,10	[0.05,0.29]	phot	0,34	2010jl	56540.3	1.8	0.3	II	2.9E2	36	5.2E-54
cdfs3_r_20131021_20141215_13B	0,38	[0.21,0.49]	phot	0,49					Ibc	4.6E1	32	5.6E-2
cdfs3_r_20131021_20141215_25B	0,34		spec	0,49	2005gj	56546.3	0.3	0.3	Ia	5.0E2	34	4.0E-84
cdfs3_r_20131021_20141215_30B	0,05	[0.01,0.10]	phot	0,08	1991T	56540.3	0.6	0.3	Ia	1.9E2	38	2.2E-21
cdfs3_r_20131021_20141215_3B	0,17	[0.13,0.24]	phot	0,24					Ia	3.7E1	34	3.5E-1
cdfs3_r_20131021_20141215_5B				0,27	1998S	56577.2	0.3	0.3	Ia	3.5E1	31	2.9E-1
cdfs3_r_20131026_20141215_139A				0,23					II	2.5E1	31	7.7E-1
cdfs3_r_20131027_20141215_51B	0,157	[0.07,0.29]	phot	0,08					II	2.6E1	30	6.9E-1

cdfs3_r_20131030_20130106_20C				0.04	1998S	56606.2	0.3	0.3	Ibc	7.6E1	30	6.5E-6
cdfs3_r_20131107_20130106_35B	0,66	[0.54,0.17]	phot	0.28					II	6.0E1	27	2.8E-4
cdfs3_r_20131110_20130106_3E	0,29		spec	0.42					Ibc	5.2E1	29	1.1E-1
cdfs3_r_20131222_20130103_13B	0,28		spec	0.40					Ia	6.3E0	10	7.9E-1
cdfs3_r_20131222_20130103_87B	0,40	[0.27,0.49]	phot	0.58					Ia	1.7E1	10	7.4E-2
cdfs3_r_20131222_20130103_92C	0,45	[0.36,0.52]	phot	0.65					Ia	6.6E0	10	7.6E-1
cdfs3_r_20131224_20130106_33A	0,967	[0.762,1.222]	phot	0.47					IIIn	7.2E1	13	4.0E-10
cdfs3_r_20140102_20130106_16B	0,696	[0.548,0.815]	phot	0,09					II	3.5E1	30	2.4E-1
cdfs3_r_20140108_20130106_4E	0,29		spec	0.42					Ia	5.3	10	87E1
cdfs3_r_20130103_20140106_54C	0,05		spec	0.06	1999br	56291.1	-0.3	0.1	FAIL	0		
cdfs4_r_20140731_20131010_52B	0.889		spec	0.07	2005gj	56876.3	0.9	0.3	II	2.7E1	22	2.0E-1
cdfs4_r_20140731_20131010_63B	0.252	[0.130,0.364]	phot	0.25					IIIn	5.0	22	1.00
cdfs4_r_20140803_20131010_202B	0.533	[0.360,0.742]	phot	0.47					Ia	1.5E1	22	8.6E-1
cdfs4_r_20140803_20131010_4B	0.499	[0.344,0.647]	phot	0.39					Ia	2.3E1	22	4.0E-1
cdfs4_r_20140803_20131010_69B	2.324		spec	0.32	2005gj	56886.3	0.4	0.3	IIIn	3.7E1	20	1.1E-2
cdfs4_r_20140803_20150113_111A	0.382		spec	0.37					II	1.0E1	21	0.8E-1
cdfs4_r_20140803_20150113_73A	2.080	[1.934,2.242]	phot	0.16	2005gj	56902	0.6	0.3	IIIn	1.9E1	23	6.8E-1
cdfs4_r_20140807_20131010_8B	0.268		spec	0.29	2005gj	566866.3	1.5	0.3	IIIn	8.0E1	24	5.8E-8
cdfs4_r_20140902_20131010_185B	1.254	[1.046,1.512]	phot	0.26	1991T	56902.3	0.8	0.3	Ia	8.3	23	1.0E-1
cdfs4_r_20140902_20131010_2B				0.42	1992H	56902.3	0.3	0.3	Ia	1.5E1	25	9.5E-1
cdfs4_r_20140925_20131010_122B				0.14					Ia	3.7E1	27	8.9E-2
cdfs4_r_20140925_20131010_185B	0.668	[0.483,0.788]	phot	0.67	1998S	56927.3	1.5	0.3	Ia	4.1E1	28	4.9E-2
cdfs4_r_20140925_20131010_189B	0.782		spec	0.24	1998S	56869.4	0.3	0.3	Ia	1.5E1	19	6.9E-1
cdfs4_r_20140925_20131010_28B	0.727		spec	0.70					Ia	4.8E1	29	1.6E-2
cdfs4_r_20140925_20131010_35B				1.0					Ia	1.5E1	26	9.4E-1
cdfs4_r_20140925_20150113_40A	0.686		spec	0.67					Ia	5.2E1	27	3.0E-3
cdfs4_r_20140927_20131010_4B	0.338		spec	0.33					Ia	3.9E1	29	1.1E-1
cdfs4_r_20140927_20150113_139A	0.738		spec	0.73					Ia	2.2E1	27	7.3E1
cdfs4_r_20140930_20131010_55B	0.380		spec	0.37					Ia	3.0E1	30	4.6E-1
cdfs4_r_20141002_20131010_157B	-1.0			0.12					Ic	1.3E1	28	9.9E-1

cdfs4_r_20141002_20131010_97B	0.801		spec	0.78	2005gj	56927.3	0.3	0.3	Ia	3.7E1	28	1.2E-1
cdfs4_r_20141020_20131010_1B				0.13					Ibc	3.1E1	30	4.3E-1
cdfs4_r_20141020_20131010_4B				0.39					Ia	2.6E1	30	8.9E-6
cdfs4_r_20141029_20131010_180B	0.585	[0.452,0.733]	phot	0.58					Ia	2.9E1	30	5.4E1
cdfs4_r_20141110_20131010_3B				0.45					Ia	2.5E1	22	3.0E-1
cdfs4_r_20141205_20140731_63A	0.334		spec	0.33					Ia	2.5E1	24	4.3E-1
cdfs4_r_20141213_20131010_4B	0.568		spec	0.55					Ia	1.0E1	22	9.8E-1
cdfs4_r_20141213_20131010_9B	0.409	[0.275,0.572]	phot	0.40					Ia	9.9	22	3.1E-1
cdfs4_r_20141218_20131010_163B	0.595		spec	0.58					Ia	2.7E1	22	2.0E-1
cdfs4_r_20141218_20131010_31B				0.07	1991T	57015.3	0.9	0.3	Ibc	3.7E1	20	2.4E1
cdfs4_r_20141218_20131010_50B	0.520	[0.412,0.568]	phot	0.42	2009bw	57008.1	1.02	-1.5	IIn	4.3E1	22	4.3E-3
cdfs4_r_20141218_20140731_150A	0.701		spec	0.70	1992A	57020.57	0.45	-1.5	Ia	3.8E1	22	1.9E-2
cdfs4_r_20141222_20131010_249B	0.875		spec	0.85	2005gj	57007.0	0.4	0.3	Ia	3.8E1	22	2.1E-2
cdfs4_r_20150109_20131010_17B				0.13					Ibc	3.7E1	13	4.9E-4
cdfs4_r_20150109_20131010_27B	-1.0			0.19					Ia	1.4E1	13	3.7E-1
cdfs4_r_20150109_20131010_2B				0.17					Ia	3.8E1	24	3.1E-2
cdfs4_r_20150109_20131010_4B	0.354		spec	0.34	1991T	57042.42	0.56	0.00	Ia	1.4E1	13	3.7E-1
cdfs4_r_20150113_20131010_188B	0.367		spec	0.36					Ia	9.6	14	7.9E-1
cdfs4_r_20150113_20131010_56B	0.531		spec	0.47	1998S	57035.1	0.3	0.3	Ia	2.2E1	14	8.9E-2
cdfs4_r_20150113_20131010_85B				0.06					Ibc	1.0E1	9	3.2E-1
cdfs4_r_20150117_20131010_55B	0.354	[0.228,0.497]	phot	0.36					IIn	1.9E1	15	2.4E-1
cdfs4_r_20150117_20131010_74B				0.22	1993J	57045.37	-0.3	-0.9	II	9.0	13	7.7E-1
cdfs4_r_20150117_20131010_86B	0.535	[0.388,0.701]	phot	0.53					Ia	6.2	10	7.8E-1
cdfs4_r_20150117_20131010_8B	0.286	[0.115,0.578]	phot	0.27					IIn	1.7E1	13	0.27
cdfs4_r_20150117_20140731_80A	0.328	[0.177,0.506]	phot	0.36					II	5.1E1	14	3.7E-6
cdfs4_r_20150121_20131010_100B				0.26					II	5.5E1	22	3.6E-5
cosmos_r_20131225_20111222_103B	0.312	[0.278,0.352]	phot	0.22					II	4.5E1	32	7.0E-2
cosmos_r_20131227_20111222_106B	0.132	[0.101,0.155]	phot	0.13					IIn	2.3E1	32	8.7E-1
cosmos_r_20131227_20111222_7B	0.159	[0.036,0.250]	phot	0.18					Ia	2.7E1	38	9.1E-1
cosmos_r_20131227_20111222_88B	0.479	[0.434,0.528]	phot	0.47					Ia	4.9E1	40	1.5E-1

cosmos_r_20131227_20111222_90B	0.250		spec	0.24						Ia	3.1E1	38	7.9E-1
cosmos_r_20131230_20111222_129B	0.367	[0.320,0.409]	phot	0.35						Ia	4.7	9	8.6E-1
cosmos_r_20131230_20111222_47B	1.041	[0.966,1.115]	phot	0.09	2005gj	56656.3	0.3	0.3		II	3.9E1	34	2.7e-1
cosmos_r_20131230_20120102_255A	0.187		spec	0.18						Ia	3.9E1	43	6.3E-1
cosmos_r_20140103_20111222_124B	1.759	[1.695,1.823]	phot	0.45						II	1.8E1	23	7.3E-1
cosmos_r_20140105_20111222_91B	0.970	[0.904,1.048]	phot	0.42	2005gj	56656.2	-0.3	0.3		II	2.4E1	35	9.1E-1
cosmos_r_20140112_20111222_5B	0.220		spec	0.22						Ia	5.1E1	36	5.5E-2
cosmos_r_20140124_20111222_45C	0.112	[0.079,0.154]	phot	0.08	1999em	56691	0.3	0.3		IIIn	3.8E1	15	5.9E-3
cosmos_r_20140124_20111222_54C	0.186	[0.146,0.226]	phot	0.18						Ia	6.9E1	40	2.9E-3
cosmos_r_20140221_20111222_124B				0.12						Ibc	1.6E1	27	9.5E-1
cosmos_r_20140221_20111222_141B	0.671	[0.616,0.720]	phot	0.67						Ia	2.3E1	29	7.7E-1
cosmos_r_20140221_20111222_1C	0.097	[0.073,0.136]	phot	0.09						II	1.5E1	29	1.5E-1
cosmos_r_20140221_20111222_48C	0.615	[0.530,0.680]	phot	0.60						Ia	5.1E1	27	3.1E-3
cosmos_r_20140223_20111222_88A	0.217		spec	0.21						Ia	1.4E1	19	7.9E-1
cosmos_r_20140226_20111222_87B	0.359		spec	0.34						II	9.7E1	27	8.2E-10
cosmos_r_20140226_20120102_55A	0.187		spec	0.18	1990N	56681.2	0.5	0.3		Ia	2.1E2	46	3.5E-23
cosmos_r_20140308_20111222_66B	0.741	[0.687,0.805]	phot	0.47	1990N	56734.0	0.2	0.3		Ia	2.4E1	19	2.1E-1
cosmos_r_20140308_20111222_6B	0.380	[0.321,0.427]	phot	0.39						Ia	2.5E1	25	4.4E-1
cosmos_r_20140308_20111222_83B	0.524	[0.484,0.565]	phot	0.39						Ia	5.0E1	27	4.4E-3
cosmos_r_20140308_20111222_99B	0.222	[0.188,0.258]	phot	0.22						II	6.5E1	37	6.0E-5
cosmos_r_20140407_20111218_137A	1.3016	[1.122,1.436]	phot	0.91	2005gj	56697.1	-0.3	-0.3		II	4.7E1	17	1.1E-4
cosmos_r_20141203_20111222_2B	0.186		spec	0.18						Ia	8.7	16	9.3E-1
cosmos_r_20141203_20111222_3B	0.310		spec	0.31						Ia	5.2	16	9.8E-1
cosmos_r_20141203_20120102_110A	0.383	[0.334,0.428]	phot	0.37						Ia	6.7	16	9.8E-1
cosmos_r_20141230_20120102_116A	0.096	[0.061,0.135]	phot	0.07						Ia	3.2E1	21	5.8E-2
cosmos_r_20150111_20111222_158B	0.521	[0.344,0.638]	phot	0.28	2005gj	56753	0.3	0.3		IIIn	1.7E1	19	5.9E-1
cosmos_r_20150111_20111222_250B	0.355	[0.306,0.405]	phot	0.34						II	3.7E1	20	1.2E-2
cosmos_r_20150111_20111222_42B	0.655	[0.574,0.736]	phot	0.61	1998S	57015.7	-0.3	-0.3		Ia	2.3E2	21	4.8E-37
cosmos_r_20150111_20111222_46B	0.572		spec	0.53						Ia	2.2E2	9	1.6E-41
cosmos_r_20150125_20120102_5A	0.575	[0.511,0.649]	phot	0.55	1991T	57053.6	-0.3	0.3		Ia	1.1E2	20	4.4E-15

cosmos_r_20150215_20111218_92A	3.448	[3.385,3.513]	phot	0.27					II	7.1E1	18	2.7E-8
cosmos_r_20150219_20120102_202A	0.371	[0.329,0.415]	phot	0.32					II	1.3E1	15	6.0E-1
cosmos_r_20150310_20111222_31A	0.370		spec	0.36					Ia	3.6	8	8.9E-1
cosmos_r_20150310_20111222_67A	0.238	[0.206,0.274]	phot	0.24					Ia	1.1E1	9	2.9E-1
cosmos_r_20150314_20111222_260B	0.832	[0.773,0.891]	phot	0.82					Ia	6.6	9	6.8E-1
cosmos_r_20150314_20111222_5B	0.341	[0.315,0.386]	spec	0.33					Ia	9.6	8	2.9E-1
cosmos_r_20150314_20111222_95B	0.420	[0.374,0.463]	spec	0.40					Ia	9.6	8	3.0E-1
cosmos_r_20150319_20120102_149A				0.18	2005gj	57093.2	1.5	0.3	II	9.9E1	6	9.9E-1

4.4 Detection efficiency

The detection efficiency (DE) is estimated through the so-called *artificial stars experiment*. I perform a Monte Carlo simulation by injecting artificial stars on the images and then running the SUDARE pipeline to estimate the number of artificial stars retrieved. For each single-epoch image, 100 artificial stars with a fixed magnitude are injected in the image. The experiment is repeated five times for each magnitude in the range [20, 25], with a step of 0.5 mag. Adding a large number of fake stars could bias the computation of the convolution kernel.

To reproduce better the properties of the real sources, three criteria to position fake stars are adopted:

- events associated with galaxies. I pick a random sample of galaxies from the catalog, placing one fake star in each of them.
- events that coincide with persistent, point-like sources. I add fake stars to the same position of existing sources in the field: in the nucleus of compact host galaxies, variable AGNs, and variable stars.
- events with no counterpart in the template image. These are placed at random positions across the image, irrespective of existing sources or the possible coincidence with CCD defects or gaps.

Once the fake stars are placed, the difference procedure is applied as described before, and using SExtractor it is possible to analyse the number of retrieved sources. The distribution in magnitude of the fraction of retrieved sources gives the DE for a given single-epoch image. Finally, I fit the DE function $\epsilon(m) = \frac{A}{\pi}(\arctan(\beta(m_{50} - m) + \frac{\pi}{2}))$, where A and β are scaling factors and m_{50} is the magnitude for which the detection efficiency drops to 50% (an example can be seen in Fig.4.5). The former parameter determines the limiting magnitude for a straightforward detection of a transient. An important argument has to be pointed out: looking at the DE function, the maximum DE is $\approx 95\%$, even at the bright magnitude end. This happens because a few artificial stars are injected on pixels flagged in the bad pixel mask (5 – 10% of the image area) and are rejected in the detection process, and indeed the bad pixel mask flags 5 – 10% of the image area. In figure 4.5 is shown the DE fit for a selected

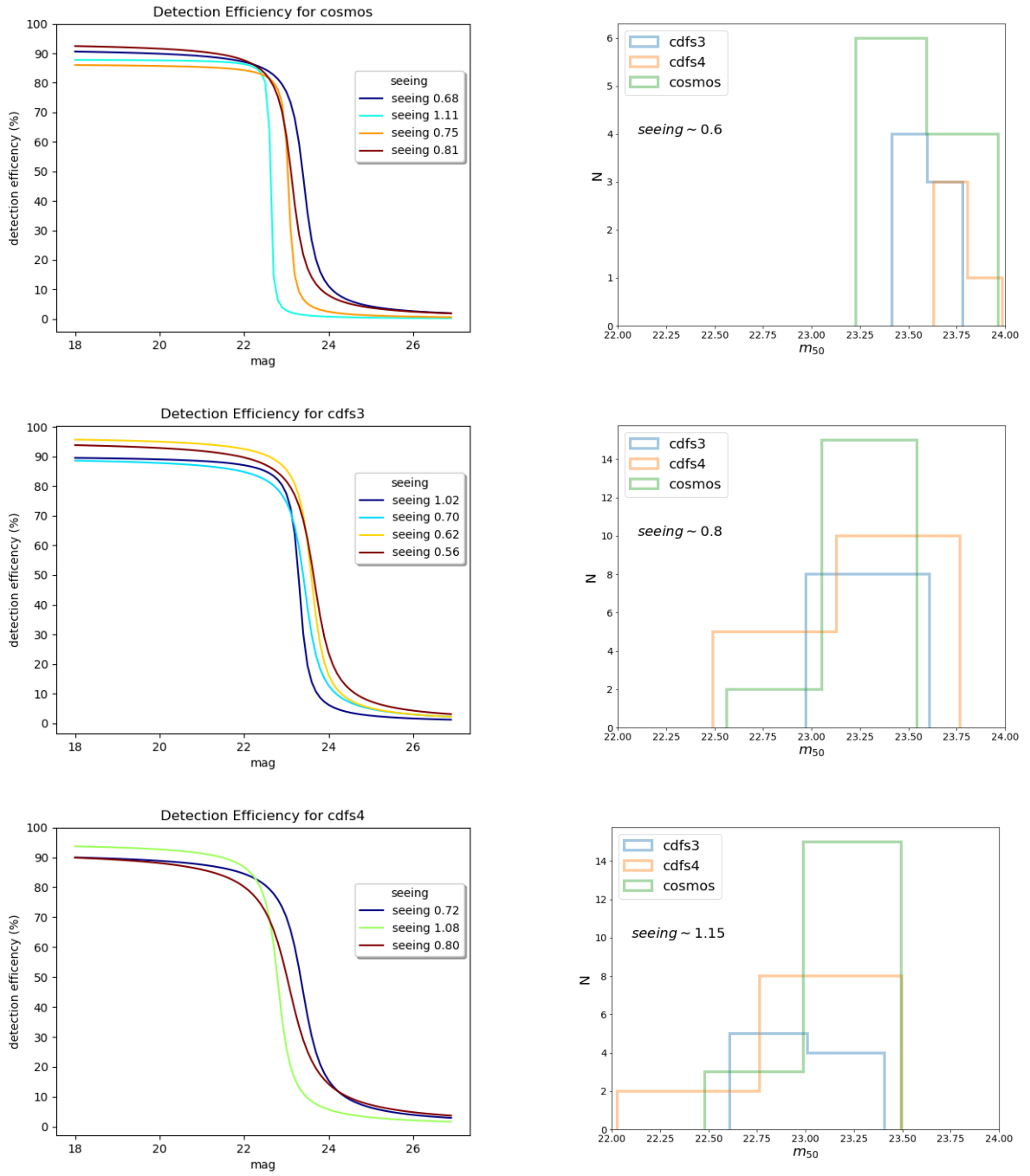
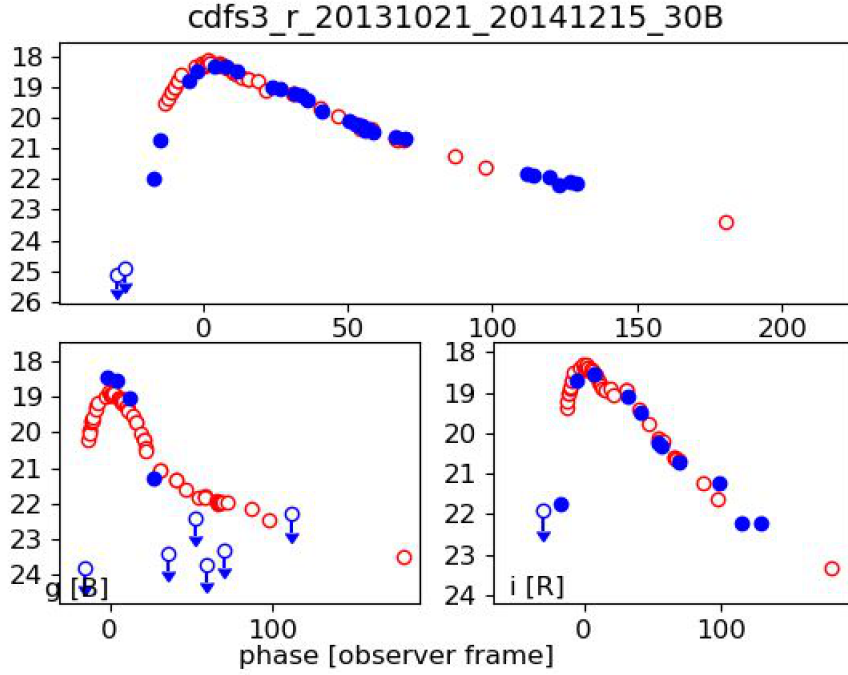


Figure 4.5: I investigated the correlation between the detection efficiency and the the seeing for the SUDARE fields. The panels on the left show how the DE curve reach earlier the 50% threshold with a worse seeing. To confirm this trend the panels on the right show that the observations with the faintest DE threshold are the ones with better seeing.



1991T Ia z=0.04 max=56536.3 AV=2.1 dm=-0.3 chi=23.53 P=5.2e-08

Figure 4.6: Example of a result from the fitting procedure developed by Enrico Cappellaro.

sample of single epoch images to analyse the trend of m_{50} with the seeing. The main result points out that the DE depends on the image seeing (a better seeing allows to detect fainter sources), and for a given seeing it is comparable in different sky fields (see Fig. 4.5).

4.5 Transient classification

The photometric classification is obtained by fitting the observed light curves of SN candidates with a set of templates light curves (see table 4.4) in the phase, redshift, distance modulus and extinction hyperspace with a code developed for SUDARE data. The set of parameters that gives the maximum probability between all the possible configurations and templates determines the class for the SN candidate (see Fig. 4.6).

The procedure to type the candidates can be summarized in five steps:

Table 4.4: List of the template SNe used for the SUDARE classification tool (Cappellaro et al., 2015).

SN	type	vel [$km s^{-1}$]	m-M reference
1990N	Ia	998	31.73 Lira et al. (1998); Mazzali et al. (1993)
1992A	Ia	1854	31.14 Altavilla et al. (2004); Kirshner et al. (1993)
1994D	Ia	450	30.92 Patat et al. (1996); Richmond et al. (1995)
2002bo	Ia	1289	31.77 Benetti et al. (2004)
1999ee	Ia bright	3407	33.42 Hamuy et al. (2002); Maximilian et al. (2002)
1991T	Ia bright	1732	30.74 Altavilla et al. (2004); Lira et al. (1998); Ruiz-Lapuente et al. (1992)
1991bg	Ia faint	913	31.44 Filippenko et al. (1992); Leibundgut et al. (1993); Turatto et al. (1996)
2000cx	Ia pec	2421	32.39 Candia et al. (2003); Matheson et al. (2008)
2002cx	Ia pec	7183	35.09 Li et al. (2003)
1987A	II	320	18.48 Catchpole et al. (1989); Hamuy et al. (1990); ESO/Asiago Archive
1992H	IIL	1021	30.97 Clocchiatti et al. (1996a)
2009bw	IIP	1155	31.45 Inserra et al. (2012)
1999em	IIP	710	29.47 Elmhamdi et al. (2003); Hamuy et al. (2001); Leonard et al. (2001)
2004et	IIP	40	28.85 Maguire et al. (2010)
1999br	II faint	1021	30.97 Pastorello et al. (2004)
1999gi	II faint	592	29.80 Leonard et al. (2002)
2005cs	II faint	600	29.26 Pastorello et al. (2006, 2009a)
1993J	I Ib	-35	27.80 Barbon et al. (1995); Filippenko et al. (1992); Richmond et al. (1994)
2008ax	I Ib	579	29.92 Pastorello et al. (2008); Taubenberger (2011)
1997cy	II pec	17700	37.03 Turatto (2000)
1998S	I In	895	31.18 Fassia et al. (2000)
2010jl	I In	13207	34.92 Pozzo et al. (2004)
2005gj	I In (Ia)	17988	37.15 Aldering et al. (2006)
2008es	SLSN-II	0.202*	39.70 Gezari et al. (2008b)
2009jf	Ib	2379	32.65 Valenti (2011)
2008D	Ib (XRF)	1955	32.29 Mazzali et al. (2008)
1994I	Ic	461	29.60 Clocchiatti et al. (1996b); Wheeler et al. (1994)
1998bw	Ic (GRB)	2550	32.76 Galama et al. (1998); Patat et al. (2001)
2004aw	Ic	4742	34.17 Taubenberger et al. (2006)
2007gr	Ic	492	29.84 Hunter et al. (2009); Valenti et al. (2008)

*redshift instead of velocity

1. for each template, K-correction is derived as a function of the phase from maximum and redshift, as the difference of the synthetic photometry on the rest frame spectrum and the same spectrum properly shifted;
2. The K-corrected templates are compared with the observed LC of the SN candidates estimating the χ^2 . Minimizing it, we are able to select the set of parameters which reproduce the observed light curve in the *gri*-bands;
3. To record the SN type from the best fitting template along with the best fit parameters corresponding to the minimum χ^2 .

To select the best fitting template, a Bayesian model selection is applied. The Bayesian evidence is computed for each SN type:

$$E_{type} = \sum_{template} \int_{pars.range} P(z) e^{-\chi^2/2} dz dA_V dT_{max} d\delta(\mu).$$

The fitting parameters are the photometric redshift z with its probability distribution ($P(z)$), the extinction A_V , the time of maximum T_{max} and the flux scaling factor $\delta(\mu)$. The photometric classification is more reliable if the redshift of the host galaxy is available. When the transient is not associated with a host galaxy or when the host redshift is not available, the redshift is left as free parameter in the transient light curve fitting (Cappellaro et al., 2015). In this case, however, for photometric redshift a normal distribution for $P(z)$ is assumed with the σ provided by the photometric redshift code. A flat probability distribution is considered as prior for the relative rate of each template within a given class and for the relative rates of the different SN types. The Bayesian probability for each of the main SN types is obtained as:

$$P_{type} = \frac{E_{type}}{E_{Ia} + E_{Ib/c} + E_{II} + E_{SLSN}}$$

Type II and type II_n templates are merged in the type II group. However, in the subsequent analysis, I indicate when the best fitting template is a type II_n. This is done to allow a direct comparison with PSNID, a software for the photometric classification available in SuperNova ANALysis (SNANA) package (Kessler et al., 2009). For the fit with PSNID, I also set the host-galaxy redshift as a prior with the same range of uncertainty as in our procedure. Despite the discrepancy in the classification of individual events of specific sub-types (see Table 4.3), there is an excellent agreement of the number of SNe in each class.

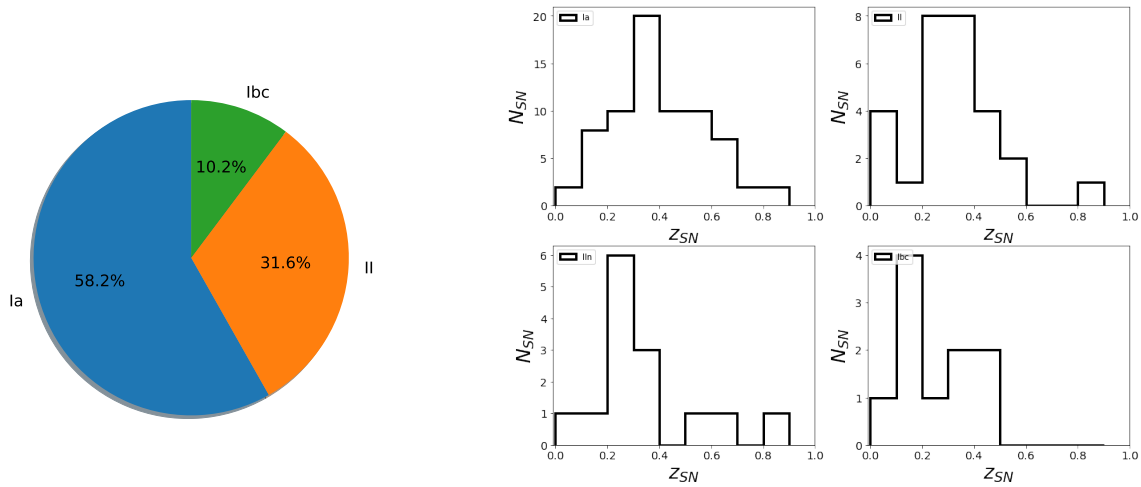


Figure 4.7: Fraction of classified SNe per type, in our sample, and their redshift distribution.

4.6 SN sample

The total number of SNe discovered in the four years of the SUDARE campaign are 241, divided in 117 SNe discovered in the first two years, and 124 SNe in the last two years. The final sample, though, is augmented of 50% with respect to the sample analysed in Botticella et al. (2017).

The overall sample has 58.2% Type Ia, 31.6% Type II and 10.2% Type Ib/c (see left panel of Fig. 4.7).

The host galaxies of 15 SNe are not detected in the K_S stack used to obtain the galaxy catalog, the VST and VISTA images do not completely overlap (see Figs. 4.1 and 4.10). The host galaxies of 2 SNe are fainter than our selection limit ($K_S = 23.5$ mag). I detected these host galaxies in r band stacks and measured their photometric redshift by using only optical bands. The redshift distribution for the different SN types is shown in the right panel of Fig. 4.7.

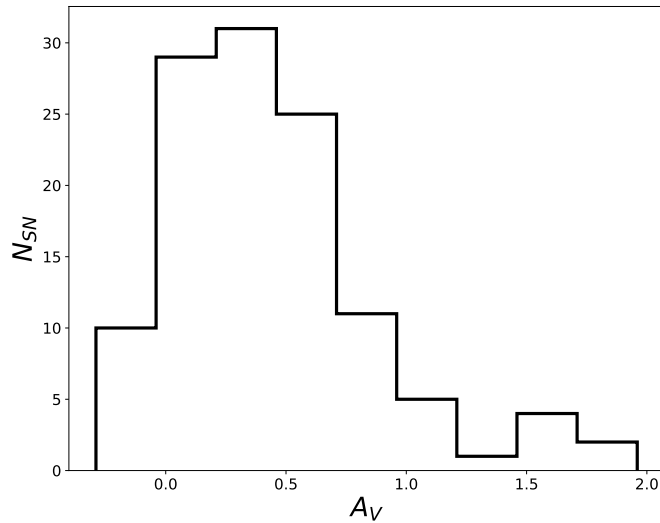


Figure 4.8: The figure shows the distribution of the extinction of the SNe from the fit procedure for the classification.

4.7 Galaxy sample

For a complete analysis of the SN rate as function of galaxy mass and sSFR, the galaxy sample monitored by SUDARE is selected and analysed. For CDFS, near infrared photometry is obtained from the VIDEO survey. The VIDEO survey is a 12 deg^2 , Z,Y,J,H,Ks survey specifically designed to enable galaxy and cluster/structure evolution to be traced as a function of both epoch and environment from the present day out to $z = 4$, and AGN and the most massive galaxies up to and into the epoch of re-ionization (Jarvis et al., 2012). VIDEO images were processed at the Cambridge Astronomical Survey Unit (CASU) using the pipeline specifically developed for the reduction of VIRCAM data as part of the VISTA Data Flow System (VDFS, Irwin et al., 2004)

The VIDEO images are registered onto the same astrometric grid and resampled to r-image, using the SWarp package (Bertin, 2010). The optical-NIR photometry is complemented with data from SPITZER and IRAC bands, for all source in common between these and our catalog.

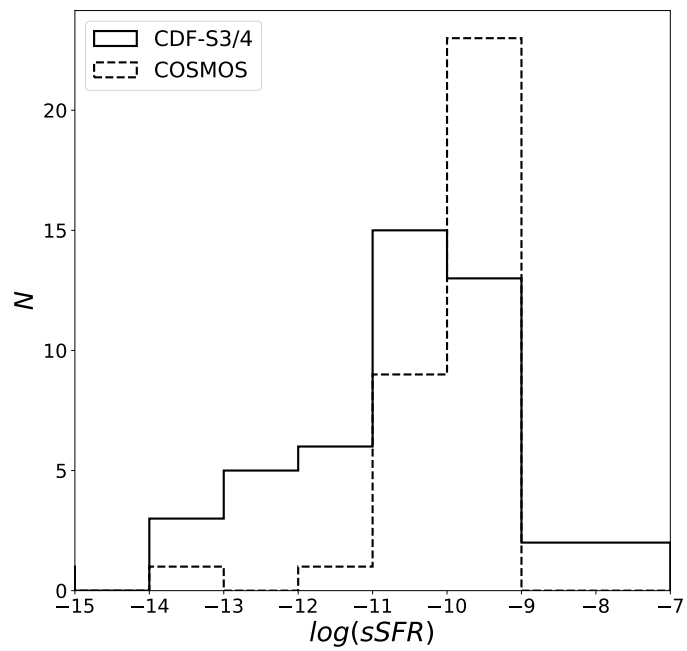


Figure 4.9: Distribution of sSFR for the host galaxies of classified SNe. More than half of the total sample of classified SNe are associated with galaxies with high sSFR.

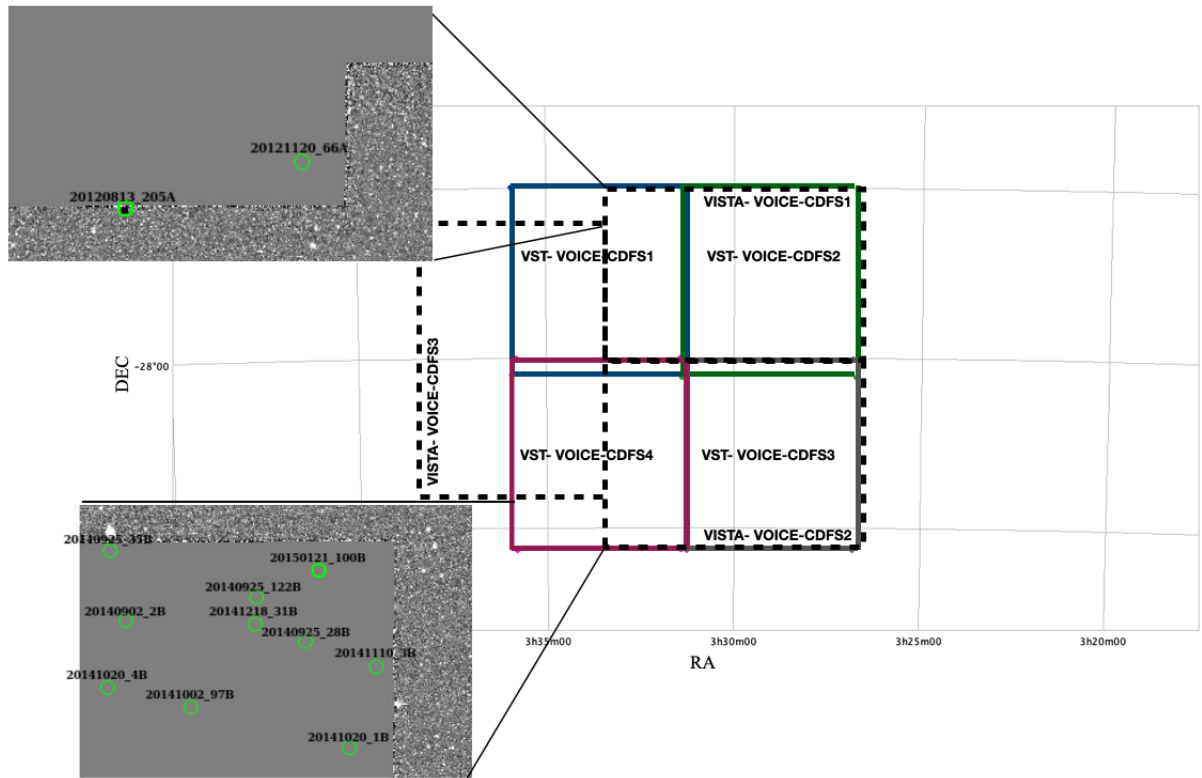


Figure 4.10: Blow up of the Ks stack which does not overlap the VST-CDF-S 4 field. The green points identify the SNe detected in the VST r images that fall outside the region where the analysis of the galaxy sample was performed.

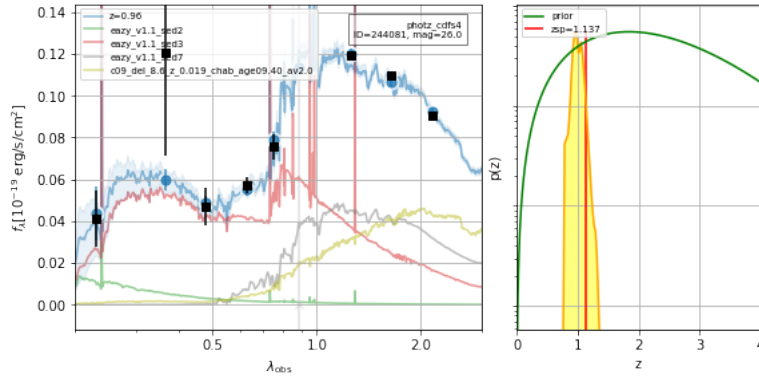


Figure 4.11: The panel on the left shows how each component of the templates sample contributes to the empirical SED. The right panel shows the posterior z_{phot} probability distribution from which estimation of the redshift is derived.

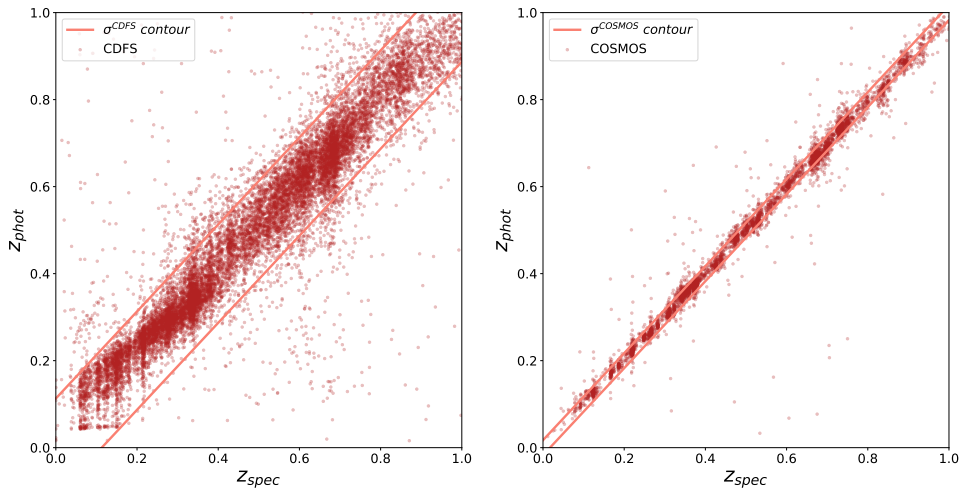


Figure 4.12: The figure shows the comparison between the spectroscopic redshift of the galaxy for which it was available with the photometric redshift for CDFS (left panel) and COSMOS (right panel). The dashed lines are the 68% confidence region produced considering the statistical error on the photometric redshift.

The sources on the resampled images are detected with SExtractor (Bertin and Arnouts, 1996b) in dual mode using the K_s band image as reference. The dual mode

allows to measure the photometry in the position of all the sources detected on the K_s on the images observed with the other bands using the same photometric aperture, which is set as that on the K_s image. The photometric aperture is obtained through an estimate of the “total flux” by integrating pixel values within an adaptively scaled aperture. SExtractor automatic aperture photometry routine derives from Kron’s “first moment” algorithm (Kron, 1980):

$$r_{Kron} = \frac{\sum_{i \in \epsilon} r_i p_i}{\sum_{i \in \epsilon} p_i} \quad (4.5)$$

where p_i is the pixel value in the detection image, and r_i is the *reduced pseudo-radius* at pixel i :

$$r_i \equiv \sqrt{CXXIMAGE \times \Delta x_i^2 + CXYIMAGE \times \Delta y_i^2 + CXYIMAGE \times \Delta x_i^2 \Delta y_i^2} \quad (4.6)$$

where Δx and Δy account for the pixel coordinates relative to the detection centroid. Eventually, the total flux is the sum of the pixel values from the detection image, subtracted from the local background inside the Krone ellipse. The total flux is the sum of pixel values from the measurement image, subtracted from the local background, inside the Kron ellipse.

$$FLUX_AUTO = \sum_{i \in K} p_i \quad (4.7)$$

The ellipse, K , is defined by the second order moment of the light distribution of the object multiplied by 6 (which roughly corresponds to twice the size of the isophotal footprint on each axis).

From the $FLUX_AUTO$ measurements, MAG_AUTO is defined as:

$$MAG_AUTO = MAG_{ZEROPOINT} - 2.5 \log_{10} FLUX_AUTO. \quad (4.8)$$

Photometric redshifts are based on the detection of strong spectral features, such as the 4000 Å break, the Balmer break, the Lyman decrement or strong emission lines. In general, broad-band filters allow us to detect only breaks, and they are not sensitive to the presence of emission lines, except when their contribution to the total flux in a given filter is higher or of the same order of photometric errors, as it happens

in the case of AGNs or SNe IIn (Kitsionas et al., 2005). The photometric redshift for our galaxy sample is estimated with the SED fitting technique using the EAZY code (see Brammer et al., 2008, for details). I use the same approach as in Muzzin et al. (2008), so I first apply the extinction correction for each filter in the given field, and imposing a magnitude cut of $K_s = 23.5$ mag (at 5σ in a $2''$ diameter aperture). I selected as galaxies all sources in the region of the $J - K_s$ vs $u - J$ diagram defined by:

$$\begin{aligned} J - K_s &> 0.18 \times (u - J) - 0.75 \quad \text{if } u - J < 3.0 \\ J - K_s &> 0.08 \times (u - J) - 0.45 \quad \text{if } u - J > 3.0 \end{aligned}$$

This technique allows to retrieve from the broad band photometry an empirical SED that can be compared with the synthetic SEDs (or a set of well sampled SED templates; an example is shown in Fig 4.11). Through the χ^2 test, the best fit parameters determine the best value for the redshift:

$$\chi^2(z) = \sum_i^{N_{points}} \left[\frac{F_{obs,i} - b \cdot F_{temp,i}(z)}{\sigma_i} \right]^2, \quad (4.9)$$

where $F_{obs,i}$, $F_{temp,i}(z)$ and σ_i are the observed and template fluxes and their uncertainty in the i filter, respectively, and b is a normalization constant. For the COSMOS field, I exploited the data analysis from deep multi-band surveys published by Muzzin et al. (2013) retrieving, for the galaxies monitored by SUDARE (1.15 deg^2), photometric redshifts from their catalogs. The measure of the quality of the photometric redshift relies on the σ_{NMAD} defined as:

$$\sigma_{NMAD} = 1.48 \times \text{median} \left(\frac{|\Delta z - \text{median}(\Delta z)|}{1 + z_{spec}} \right). \quad (4.10)$$

For CDFS, I find $\sigma_{NMAD} = 0.02$, which is comparable to that found in other surveys with a similar number of filters whereas, for COSMOS, $\sigma_{NMAD} = 0.005$. Another estimate for the quality of photometric redshift is the fraction of catastrophic redshifts, which measures the number of galaxies for which $\frac{|z_{phot} - z_{soec}|}{(1 + z_{spec})} \geq 5\sigma_{NMAD}$. In the sample, we find a fraction of catastrophic redshifts of less than 2% for CDFS, and less than 0.4% for COSMOS. The difference between the COSMOS and the CDFS fields

consists in the number of filters available for the analysis, i.e. a maximum of 12 filters for CDFS and 30 for COSMOS, that results in different quality of the photometric redshifts (see figure 4.12). The figure 4.13 shows the distribution in redshift of the galaxies in two different sky fields.

I selected the galaxies with $Q_z < 1$, K_s magnitude ≤ 23.5 mag and $0.15 \leq z \leq 0.75$. Q_z is a quality parameter provided by EAZY¹ for the reliability of the redshift measurement from the SED fit.

The final catalogue consists of 281823 galaxies from CDFS, and 67418 galaxies from COSMOS, for a total sample of 349241 galaxies. From the SED fitting, we are able to estimate the rest frame galaxy colors. As shown in Muzzin et al. (2013), the distribution of the U-V vs V-J color-color diagram allows for a simple separation of star-forming from passive galaxies: the U-V colour covers the Balmer break and therefore it is a good measure for relatively unobscured recent star formation (Baldry et al., 2004; Blanton et al., 2003), while V-J allows to empirically separate "red" passively evolving galaxies from "red" dusty star-forming galaxies, since dust-free quiescence galaxies are relatively blue in V-J. The distribution in figure 4.14 outlines a bimodal distribution, where the passive galaxies are those in the region of the color-color diagram for which:

$$\begin{cases} U - V > 1.3 & \text{for all redshifts} \\ V - J < 1.5 & \text{for all redshifts} \\ U - V > (V - J) \times 0.88 + 0.69 & \text{for } 0 \leq z \leq 1 \end{cases} \quad (4.11)$$

To estimate the galaxy mass, SFR and sSFR, we use FAST (Fitting and Assessment of Synthetic Templates), an IDL-based code that fits stellar population synthesis templates to broadband photometry and spectra, originally developed by Mariska Kriek (Kriek et al., 2009). The software selects the best fit parameters using a simple χ^2 - test. FAST runs over all the hyperspace cube of the model fluxes for the full stellar population grid, the filters and the spectral element. It estimates the best fit for all the points to avoid multiple minimum the usual minimum search algorithm for the χ^2 function. The code takes into account also the possible contribution of

¹ $Q_z = \frac{\chi^2}{N_{filt}-3} \frac{u^{99}-l^{99}}{p_{\Delta z=0.2}}$, where N_{filt} is the number of photometric measurement used in the fit, the numerator of the second fraction represent the 99% confidence intervals and $p_{\Delta z=0.2}$ is the fractional probability that the redshift lies within ± 0.2 of the nominal value

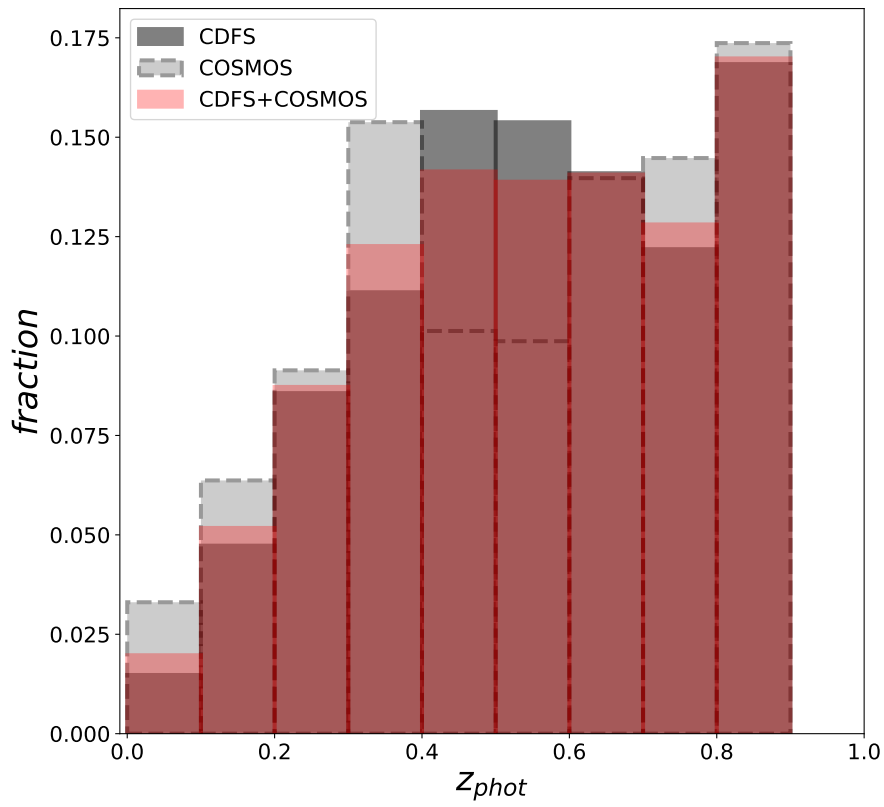


Figure 4.13: Distribution of z_{phot} for galaxies in CDF-S (black line), COSMOS (dashed line) and the overall sample (red line).

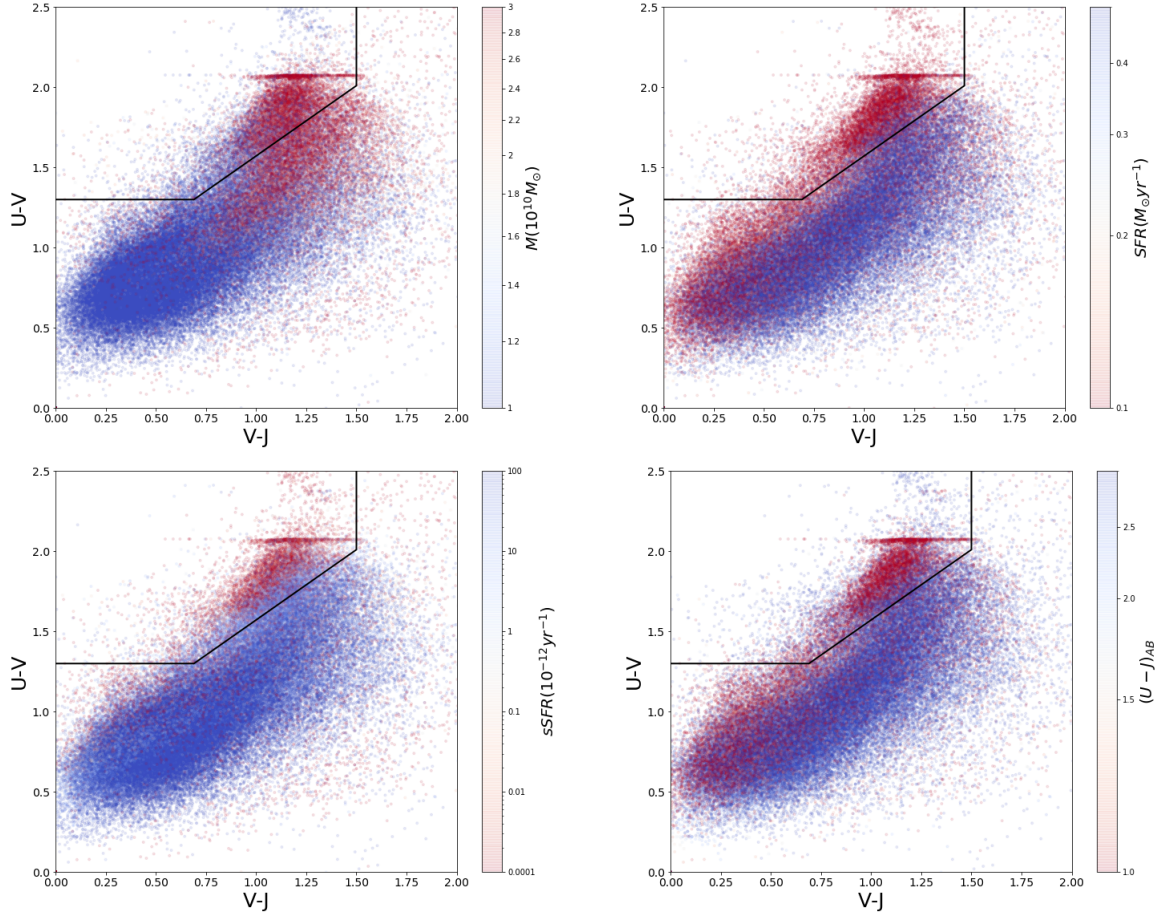


Figure 4.14: Rest-frame U - V vs V - J color-color plot for galaxies in the global sample, color coded by galaxy mass (top left), SFR (top right) and sSFR (bottom left), as derived from the SED fitting. In the bottom right panel, the color encoding traces the rest frame dereddened U - J colour.

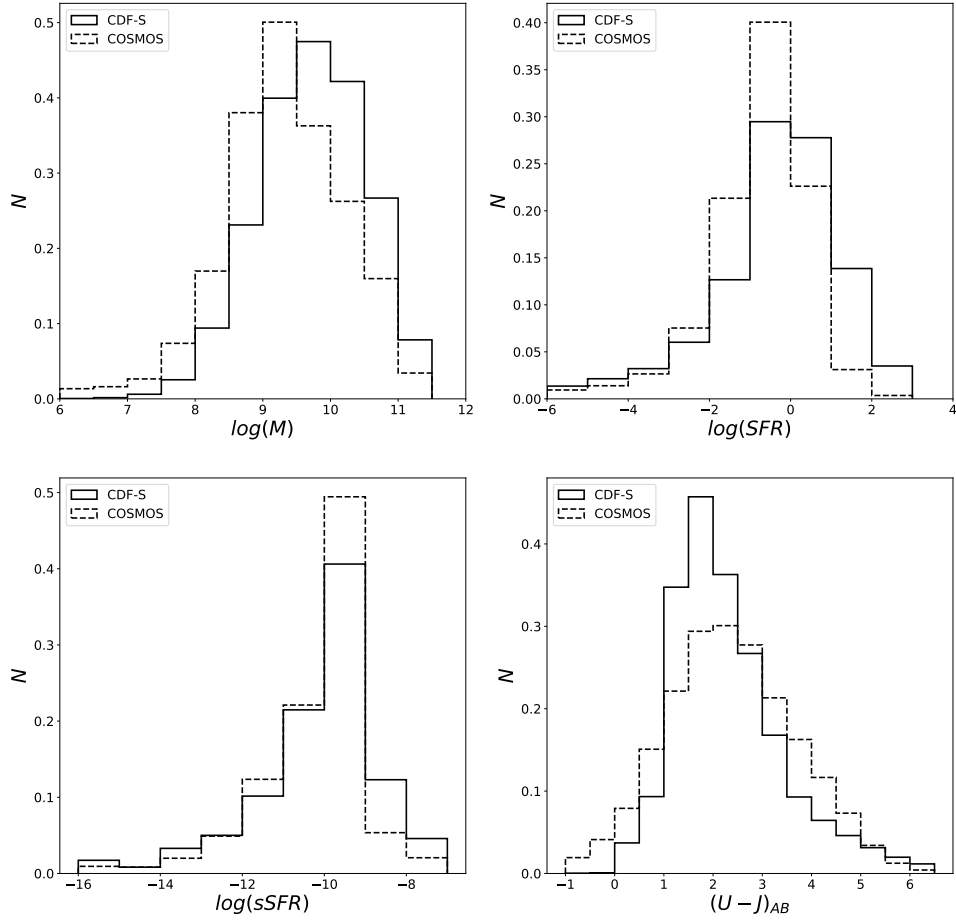


Figure 4.15: The distribution of stellar masses (top-left panel), SFR (top right panel) and sSFR (bottom-left panel) estimated with FAST for the global sample. In the bottom-right panel, the distribution of the rest frame color $U - J$ in AB magnitude is shown, with the same line symbols as described above.

AGNs in the galaxy luminosity. The confidence levels are calibrated using Monte Carlo simulations. The observed fluxes are modified according to their photometric errors, and these modified fluxes are fitted as well. The 68% (95% or 99%) confidence intervals are defined by the χ^2 value in the original grid that encloses 68% (95% or 99%) of these simulations. Thus, the confidence intervals on all properties are the minimum and maximum values allowed by this χ^2 threshold.

To construct the set of template SEDs, I adopt the Bruzual and Charlot (2003) stellar population synthesis model library; a Salpeter IMF; solar metallicity; an exponentially declining SFR, which follows the $\Psi(t) \sim e^{-\frac{t}{\tau}}$ relation, where t is the time since the onset of the star formation and τ is the e-folding star formation timescale, ranging in $10^7 - 10^{10}$ Gyr; we also adopt the Calzetti et al. (2000) dust attenuation law. For all galaxies, I restrict t to be less than the age of the Universe at the redshift of the galaxy and allow for a luminosity attenuation in the $0 - 4$ mag range. Redshifts are fixed to the values derived by EAZY. FAST does not account for the gas recycling and the mass of gas processed by the stars and returned to the interstellar medium during the evolution. Due to this lack in the models, FAST slightly overestimates the stellar masses. In the upper-left panel in Fig. 4.15, I show the distribution of stellar masses for both COSMOS and CDFS samples. The COSMOS sample appears to include a larger fraction of low mass galaxies, compared to the CDFS sample.

The SFRs are more uncertain when they are derived solely from optical-NIR photometry. The lack of FUV and MIR data, that probe respectively unobscured and obscured star formation has an important effect on the estimate of SFR for galaxies experiencing a recent star formation burst.

Looking at the SFR histogram in Fig 4.15, COSMOS galaxies are found systematically lower than CDF-S galaxies. Interestingly, the distribution of the sSFR, i.e., the ratio between the current SFR and the galaxy mass, is the same for the two samples, even though the distributions in mass and SFR are slightly different (Fig. 4.15 bottom left panel). The sSFR is less sensitive to the choice of IMF, and input SPS models since the total SFR and mass both exhibit a similar dependence on these parameters (Williams et al., 2010).

4.8 SN rate measurements

To calculate the SN rates, an estimate of the time of the effective surveillance of the sample is needed, the *control time* (CT), already introduced in Section 3.2. To evaluate the total CT of SUDARE survey it is followed the method described in Cappellaro et al. (1997a). Then the SN rate is computed as the number of events detected in the survey divided by the total CT.

To compute the CT a template light curve is selected (templates are listed in Table 4.4) that is representative of a given SN subtype in a given redshift range ($0 \leq z \leq 1$) and an extinction value in the range $0 \leq A_V \leq 2$ in the host galaxy rest frame. To take into account the diversity of photometric evolution of different types, the templates in Table 4.4 are used, and simulate a number of N events that explore the possible epochs of explosion, in the interval $[t_0 - 365d, t_K]$. Then we can compute:

$$CT_{SNi,E_{BK}}(z) = (t_K - t_0 + 365) \frac{\sum_{j=1}^N p(x_j)}{N} \quad (4.12)$$

with the following meaning for the symbols: SNi is the template SN subtype, $p(x_j)$ is the detection probability given by the detection efficiency for the expected magnitude, t_0 and t_K are the Julian date of the first and last observation of the field, N is the number of simulated events. Finally the CT fro each of the main SN type is:

$$CT_{SN}(z) = \sum_{SNi} \sum_{E_{BV}} f_{SNi} g_{E_{BV}} CT_{SNi,E_{BK}}(z) \quad (4.13)$$

where f_{SNi} is the fraction of SN subtypes and, $g_{E_{BV}}$ is the distribution of $E(B - V)$ color excess. We adopt the following subtype distribution:

- type Ia: 70% normal, 10% bright 1991T-like, 15% faint 1991bg-like, and 5% 2002cx-like;
- type II: 60% IIP, 10% 2005cs-like, 10% 1987A-like, 10% IIL, and 10% II
- type Ib/c: 27% Ib, 68% Ic, and 5% 1998bw-like
- type IIn: 45% 1998S-like, 45% 2010jl-like, 10% 2005gj-like.

SN type	z_{bin}	SNe	rate	stat.
Ia	0.01-0.1	5.2	0.41	-0.18+0.25
	0.1-0.26	37.5	0.52	-0.09+0.09
	0.26-0.46	46.9	0.48	-0.08+0.07
	0.46-0.63	30.7	0.64	-0.13+0.12
	0.63-0.80	6.0	0.87	-0.35+0.52
II	0.01-0.1	11.5	0.95	-0.31+0.32
	0.1-0.25	24.3	0.60	-0.13+0.14
	0.25-0.46	8.8	0.43	-0.18+0.15
Ib/c	0.01-0.1	10.0	0.86	-0.34+0.27
	0.1-0.25	12.5	0.30	± 0.10
	0.25-0.44	6.4	0.43	-0.12+0.21
IIIn	0.01-0.1	1.0	0.04	-0.03 +0.10
	0.1-0.27	7.1	0.04	-0.01 +0.02
	0.27-0.46	3.0	0.008	-0.004 +0.01
	0.46-0.65	1.0	0.003	-0.002 +0.006
	0.65-0.88	0.5	0.001	± 0.003

Table 4.5: SN rates per unit volume [$10^{-4}yr^{-1}Mpc^{-3}$].

4.8.1 SN rate per unit volume

The volumetric SN rates at a given redshift z is given by:

$$r_{SN}(z) = \frac{1+z}{V(z)} \frac{N_{SN}(z)}{CT_{SN}(z)} \quad (4.14)$$

where $N_{SN}(z)$ is the number of SNe of a given type in the specific redshift bin, $CT_{SN}(z)$ is the control time, $V(z)$ is the comoving volume for the given redshift bin, as described in Section 3.3.

The volumetric rates estimate is based on the SNe exploded within the volume set by $0.15 < z < 0.7$ for CC SNe and $0.15 < z < 0.85$ for SNe Ia. The results of the analysis on the overall SN sample is shown in figure 4.16 and table 4.5.

Figure 4.17 shows the comparison of the measure I obtain for the rate of CC SNe in this thesis with all measurements available in the literature. The CC SN rate is obtained cumulating the type II, Ibc and IIn events. As mentioned in Section 2.3.1, the evolution of the CC SN rates with redshift is a tracer of the cosmic SFH. Conversely, existing estimates of the SFH can be used to compute the expected CC SN rate, assuming a mass range for CC SN progenitors.

Stellar evolution models suggest a typical range for CC SNe progenitors of 8-40 M_{\odot} . For the upper limit, there are strong uncertainties because of its dependence on metallicity, rotation, binarity or other factors. With a mass range of 8 – 40 M_{\odot} for the SN CC progenitors, I obtain a scale factor $K_{CC} = 6.7 \times 10^{-3} M_{\odot}^{-1}$ for a standard Salpeter IMF, similar to Hopkins and Beacom (2006). With reference to Fig. 4.17 the model from Hopkins Beacom follows very well the majority of the published data with some discrepancy at low redshift, overpredicting the number of SNe in the range $z = 0$ to 0.45. Horiuchi et al. (2011) argue that this indicates a “supernova rate problem”, for which they propose some possible explanations: either many CC SNe are missed in the optical searches because of heavy dust-obscuration, or there is a significant fraction of intrinsically very faint (or dark) SNe, whose ejecta falls back onto the black hole.

Finally the measurements of the rate of SN Ia obtained in this thesis are shown in Fig. 4.18, along with all those available from the literature. The results appear in agreement with other measurements within the statistical errors. However, the estimates obtained in this thesis seem to be on the high side compared with the bulk

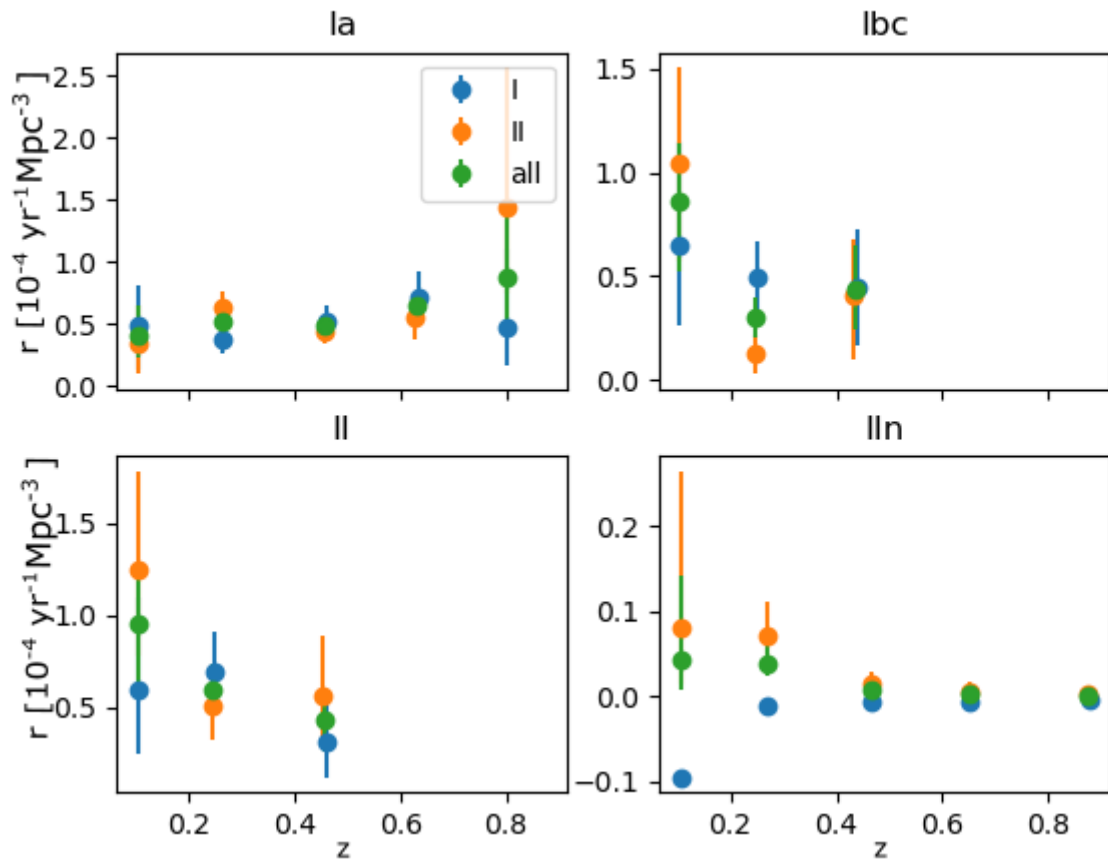


Figure 4.16: Comparison between the SN rate for unit volume in the two observation seasons of the SUDARE survey (points in blue and orange) and for the overall survey (points in green). For all SN types we have agreements within the statistical errors on the SN rate measurements.

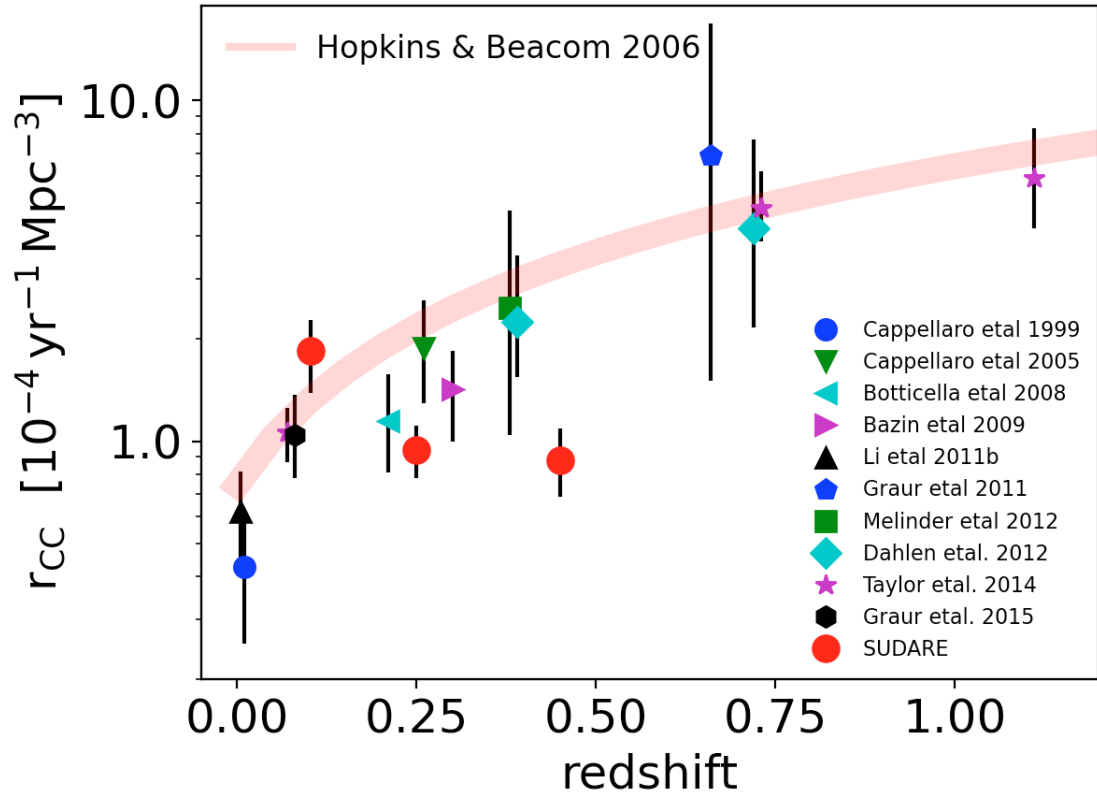


Figure 4.17: CC SN rate per unit volume. All measurements do not account for the correction for hidden SNe. To obtain the predicted SN rate from the measured SFR, we adopt $8 - 40 M_{\odot}$ as the lower and upper mass limits for CC SN progenitors and the proper IMF, Salpeter for Hopkins and Beacom (2006).

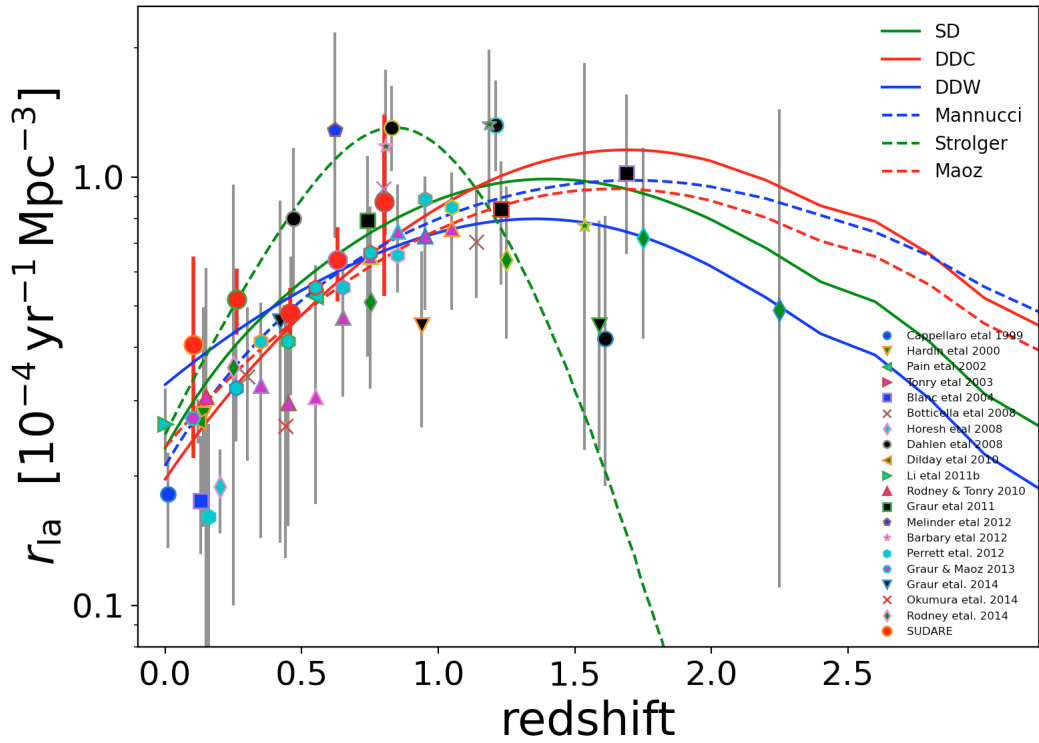


Figure 4.18: Our estimates of the SN Ia rate at $z = 0.25, 0.45, 0.65$ are compared with the other values from literature. The rate of Cappellaro et al. (1999), Hardin et al. (2000), Madgwick et al. (2003), Blanc et al. (2004) are given per unit luminosity. They are converted in rate per unit volume using the following relation of the luminosity density as a function of redshift: $jB(z) = (1.03 + 1.76z) \times 10^8 L_{\odot}^B Mpc^{-3}$ (Botticella et al.). The measurements of Perrett et al. (2012) are scaled up by 15% to account for the fact that they not include faint SN 1991bg-like events.

of published measurements in the two first redshift bins. Six DTD models are selected and their predictions for the cosmic SN Ia rate are compared to the measured ones. The models include a single SD, and two flavours of the double degenerates, either with a close binary separation (DDC), or wide (DDW), which predict a steep and a mildly decreasing distribution of the delay times, respectively (see Greggio, 2005, 2010, for more details). The selected models correspond to a very different time evolution following a burst of star formation. For the DDC, SD, and DDW models, 50% of the explosions occur within the first 0.45, 1, and 1.6 Gyr, respectively, while the fraction of events within 500 Myr is 0.55, 0.3, and 0.18 of the total. The late epoch declines are also different, the rate scaling by $t \sim 1.3$ and $t \sim 0.8$ for the DDC and DDW models, respectively. The comparison with the models does not allow to discriminate between progenitors scenarios. In figure 4.17, all models with the exception of Strolger et al. (2004) match the data distribution with the major discrepancy towards the end of the data sample range.

Eventually the sparsity of the measurements is too large to constraint the models, scarce statistics and high uncertainties do not allow to infer unique conclusion on the progenitors. Thus, more precise data and the possibility to observe and classify an higher number of SNe at different redshifts are needed to constrain the progenitor scenarios.

Figure 4.16 shows the result of our analysis for each subtypes: for type Ibc I found there are $40 \pm 8\%$ of CC SNe at a mean redshift $z = 0.25$. This result agrees within the statistical errors with the estimates of Li et al. (2011b) for the Local Universe. The author measured a fraction of SNe Ib/c that ranges from $46 \pm 17\%$ in early spiral galaxies to $20 \pm 5\%$ in late spirals, with an average value of 33.9% . The interpretation of the intrinsic difference in CC SN population could be somehow related to a metallicity effect (Li et al., 2011b).

About the estimate of the rate of type IIn SNe, there are high uncertainties mainly because SNe IIn are rare and the event statistics is very poor, but also because the variety in luminosity and light curve evolution, that in some cases mimic those of other SNe (e.g. SN, IIL or SLSN), jeopardizing the photometric classification. However, because of the intrinsically bright and slowly evolving luminosity, type IIn SNe are detected in a redshfit range comparable to that of SN Ia. In the 0.1-0.4 redshift bin, I estimate that SNe IIn are $12 \pm 12\%$ of all CC SNe. This value is much greater then

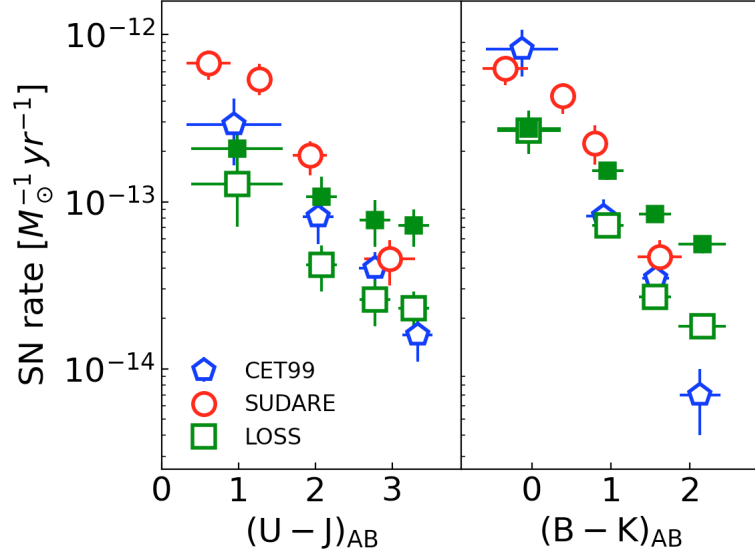


Figure 4.19: Observed correlations between the SNIa rate and the parent galaxy U-J (left) and B-K (right) colour in the SUDARE, Cappellaro et al. (1999), labeled as CET99 in the figure, and LOSS surveys. For the LOSS survey we also show as filled symbols the rate normalized to the mass derived from the Bell and de Jong (2001) relation. Colours are shown in the AB magnitude system. The horizontal error bars show the 1σ width of the galaxy distribution within each colour bin; the vertical error bars show the uncertainty on the rate from the statistics of the events.

the $6 \pm 2\%$ value measured in the Local Universe (Li et al., 2011b). However because of the even greater uncertainties, it is compatible with the reference values in the literature. On the other hand, the apparent decrease in the rate at higher redshift (a factor ~ 2.5 in the redshift bin 0.4–0.9, compared with the nearest bin) appears at odds, considering that the overall CC SN rate in the same redshift interval increases by about the same factor. This result confirms what was highlighted in Cappellaro et al. (2015). The authors consider this diversity due to a strong evolution of the type IIIn rate with redshift or, in this search, the fact that we missed (or mis-classified) of the two-thirds of the distant type IIIn SNe.

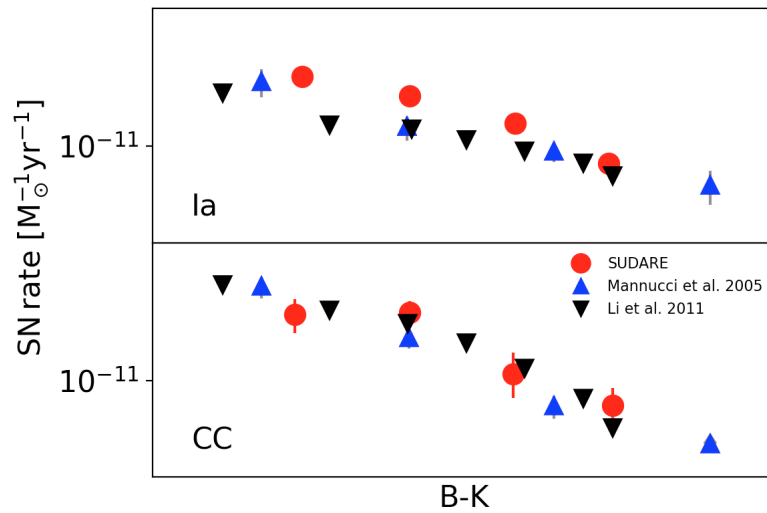


Figure 4.20: SN rates as a function of the B-K galaxy color for SNe Ia (top panel) and CC SNe (bottom panel). For comparison, we report the same measurements obtained in the Local Universe by Mannucci et al. (2005) and Li et al. (2011b). The mass estimates for the galaxies by Mannucci et al. (2005) and Li et al. (2011b) are converted to a Salpeter IMF, and B-K colors are in AB mag.

4.8.2 SN rate as function of galaxy colour

SN Ia rate shows a value for "blue" galaxies 30 times larger than that of "red" galaxies, and confirmed the earlier suggestion that a significant fraction of SNe Ia in late spirals/irregulars originates in a relatively young stellar component. Moreover, Greggio and Cappellaro (2019) pointed out that the U-J color and the SN Ia rate traces the SFH of the average age of the parent stellar population. The efficiency of "blue" galaxies in producing SN Ia events was interpreted as due to a DTD being more populated at short delay times ($\leq 1 \text{ Gyr}$) already by Oemler and Tinsley (1979) and Greggio and Renzini (1983). The rate of CC SNe in the early type galaxies is close to zero, it is small in the reddest galaxies, and in general becomes progressively higher in bluer galaxies.

Figure 4.19 shows the measured rates per unit mass versus the galaxy colours for three independent surveys Cappellaro et al. (1999), the Lick Observatory Supernova Search (LOSS) and SUDARE. The galaxy mass for the normalization is estimated using two different relations, as described in Greggio and Cappellaro (2019): a piece-wise relation tailored to the log-normal SFH models and a regression from Bell and de Jong (2001) used in Mannucci et al. (2005) to convert the K-band luminosity into stellar mass. For the LOSS survey, we show the effect of adopting different relations to evaluate the mass-to-light ratio at a given B-K color: filled symbols assume the relation regression to convert the K-band luminosity into stellar mass, while empty symbols are derived with the piece-wise relation. It turns out that the slope of the observed correlation is very sensitive to the adopted scaling of the mass-to-light ratio with the galaxy color. For the two local surveys, the rates per unit mass as functions of U-J are consistent within the statistical errors when the same mass-to-light ratio regression is used; the same is true for the rates as a functions of B-K but for galaxies in the bluest and the reddest bins.

In figure 4.20 the SN rate measurements are shown as a function of $B - K_s$. The measurements are in agreement in all color bins and suggest that there is no evolution of the dependence on galaxy colours for both SN CC and Ia rates with cosmic time.

The connection between a color sequence and a sequence in the SFR is not straightforward because the colors trace the global SFH in a galaxy, while the SFR refers to only the more recent past. The existence of an analytical expressions for the SFH in the SED fitting supports a relation between the global colors and the recent SFR.

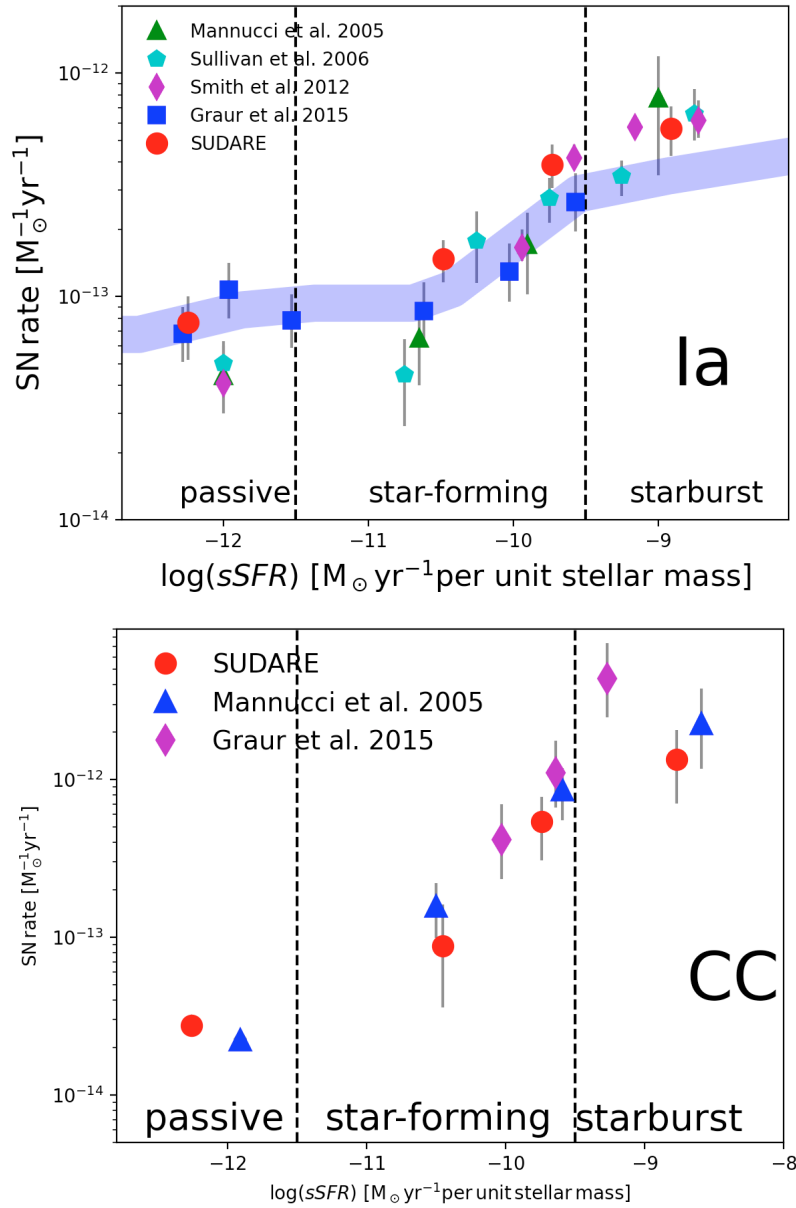


Figure 4.21: SN rates in SNum vs sSFR for Type Ia (top panel) and CC SNe (bottom panel), in three different groups of galaxies based on their sSFR: the first group of passive galaxies with a zero mean SFR; the second group of galaxies with $-12.0 \leq \log(sSFR) \leq -9.5$; the third group of galaxies with $\log(sSFR) \geq -9.5$. In both panels, the circles are from SUDARE, the triangles from Mannucci et al. (2005), the pentagons from Sullivan et al. (2006), the diamond are from Smith et al. (2012) and the squares from Graur et al. (2015). The literature values have been corrected to a Salpeter IMF.

Table 4.6: SN rate per unit mass [$10^{-3} \text{ SNe yr}^{-1} 10^{-10} \text{ M}$] in different bins of sSFR and galaxy mass as measured by FAST. The Type Ia SN rate has been measured in the redshift range $0.15 < z < 0.75$, while the CC SN rate in the range $0.15 < z < 0.35$.

SN type	N_{gal}	$\log(\langle \text{sSFR} \rangle)$	N_{SN}	rate
Ia	16832	-12.2	12.6	$0.76^{+0.24}_{-0.24}$
	38996	-10.5	25.5	$1.47^{+0.32}_{-0.32}$
	33083	-9.7	24.4	$3.9^{+1.1}_{-1.1}$
	31132	-9.0	19.4	$5.6^{+1.5}_{-1.4}$
CC	15561	-12.2	1.0	< 0.6
	30573	-10.5	3.9	$0.8^{+0.7}_{-0.5}$
	27576	-9.7	9.1	$5.4^{+2.3}_{-2.3}$
	8638	-8.8	4.7	$9.05^{+4.3}_{-5.7}$

Moreover, the dust content and the presence of recent mergers can make extremely complex the relations between SFR and the galaxy colors (see figure 4.14).

4.8.3 SN rate as function of sSFR

The sSFR is a good approximation for the SFH and the evolutionary stage of the galaxy. In particular the inverse of the sSFR defines a timescale for the formation of the stellar population of a galaxy. To compare results from this thesis to previous works it is adopted the same criteria to separate passive and star-forming galaxies as in Sullivan et al. (2006), defining three galaxy groups based on the nature of star formation: the first group of passive galaxies with a zero mean SFR; the second group of galaxies with a small or moderate sSFR ($-12.0 \leq \log(\text{sSFR}) \leq -9.5$); the third group of galaxies with a large sSFR ($\log(\text{sSFR}) \geq -9.5$). We stress that the $\log(\text{sSFR}) \geq -9.5$ condition as division between highly and moderately star-forming is arbitrary. The results (see figure 4.21 and table 4.6) confirm that the rates per unit stellar mass grow with increasing the galaxy sSFR with approximately the same trend in the Local Universe and at intermediate redshifts. The enhancement of

both SN Ia and CC SN rate from star-forming to starburst galaxies is steeper for CC SNe: we find an increase of about a factor of 5 for Type Ia and 15 for CC SNe. The difference between the SN Ia rate in passive galaxies and starburst galaxies is about a factor of 13 for our measurements, very close to Sullivan et al. (2006) estimates in an almost identical range of redshift. A similar trend between the SN Ia rate per unit mass and the sSFR is reported by Graur et al. (2015) in the redshift range $0.04 \leq z \leq 0.2$, while Smith et al. (2012) found a steeper increase from star-forming to starburst galaxies in the same range of redshift ($0.05 \leq z \leq 0.25$). The trend of SN Ia rate with the sSFR reflects the fact that the higher the SFR over the past 0.5 Gyr, the higher the SN Ia rate (Greggio, 2010). The similar scaling of the SN Ia rate with sSFR found at the different redshifts supports the notion that the ability of the stellar populations to produce SN Ia events does not vary with cosmic time. The dependence of CC SN rate per unit mass on the sSFR is expected to be linear since the CC SN rate is proportional to the recent SFR and the trend from SUDARE data is very similar to that observed in the Local Universe (Mannucci et al., 2005) and in the redshift range $0.04 \leq z \leq 0.2$ (Graur et al., 2015).

4.9 Conclusion

The aim of the SUDARE survey is to constrain the SN progenitors analysing the dependence of the SN rate on the properties of the parent stellar population. The uncertainties in both SN rate and SFH measurements prevent an analysis based on individual galaxies. Therefore I averaged over a population of galaxies with different ages and SFR following two different approaches: measuring SN rate in large volume as a function of redshift and measuring the SN rates in a sample of galaxies as a function of the galaxy colours or SFR, both tracers of galaxy age. The main findings are: the trend of the SN rates as a function of the B-K colour of the parent galaxy from SUDARE data is consistent with that observed in the Local Universe. Both CC and type Ia SN rates become progressively higher for bluer galaxies but CC SNe with a steeper slope. The SN Ia rate per unit mass is about a factor of five higher in the star-forming with respect to the passive galaxies identified as such on the U-V vs V-J color-color diagram. Only a lower limit for CC SN rate has been estimated in passive galaxies. This is expected given the short lifetimes of CC SN progenitors

which imply that the CC SN rate is proportional to the recent SFR. Moreover, the results confirm that the higher the sSFR the higher the SN Ia rate per unit mass, suggesting a DTD declining with delay time. The fact that this trend is similar at the different redshifts suggests that the ability of the stellar populations to produce SN Ia events does not vary with cosmic time. From the observed correlations between the SN rates and properties of the parent galaxies that, according to the expectations of stellar evolution, the minimum mass for CC SN progenitors is between $8 - 10 M_{\odot}$ and the DTD of SN Ia progenitors is skewed at the short delay times ($\leq 1Gyr$). However, the uncertainties on both CC and type Ia SN rates are still too high to constrain the mass range of CC SN progenitors with sufficient accuracy and to discriminate between SD and DD progenitor scenarios.

Chapter 5

Transient searches with large synoptic surveys

In the past century, there has been a profound change in the observational approach of studying astrophysical phenomena, from an object oriented point of view to a large scale sky field perspective, due to the the instrument and telescopes technologies. The Sloan Digital Sky Survey (SDSS Donald et al., 2000), the Two Micron All Sky Survey (2MASS Skrutskie et al., 2006), the Galaxy Evolution Explorer (GALEX Martin et al., 2005), and Gaia (Gaia Collaboration, 2016), just to mention some of the sensitive surveys over a large fraction of the sky, enabled an extremely broad range of new scientific investigations that impacted nearly all fields of astronomy and several areas of fundamental physics. Because of the evident progresses enabled by large sky surveys, three nationally-endorsed reports by the U.S. National Academy of Sciences (National Research Council, 2001, 2003a,b, 2010) decided to implement a dedicated ground-based wide-field imaging telescope with an effective aperture of 6-8 meters: the Vera C. Rubin Observatory. This new technology can potentially improve the number of detected SNe, allowing a more accurate measurement of the SN rate, that ultimately can help constraining SN progenitors, as showed in the previews chapter.

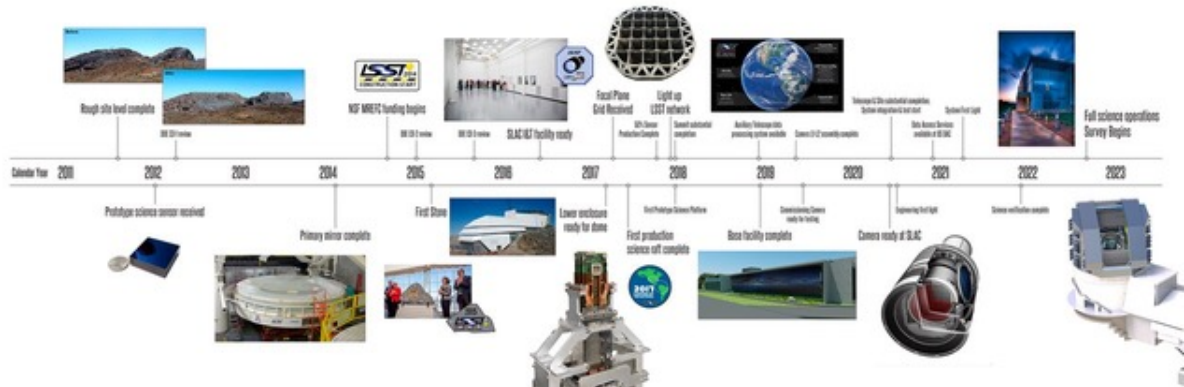


Figure 5.1: The timeline of the project.

5.1 The Vera C. Rubin Observatory

The Vera C. Rubin Observatory project is an astronomical observatory currently under construction in Chile. Its main task will be a 10-year astronomical survey, the Legacy Survey of Space and Time (LSST), that will deliver almost 500 petabyte of images and data products exploited for the following science topics:

- Understanding Dark Matter and Dark Energy;
- Inventory Solar System;
- The Transient Optical Sky;
- The Formation and Structure of the Milky Way.

LSST will cover an enormous area of sky with a frequency that enables images of every part of the visible sky to be obtained every few nights for ten years, to achieve astronomical catalogs thousands of times larger than those previously compiled. The details of the survey cadence are still under discussion; the project is expected to start in 2023 (see figure 5.1). Finally the Vera Rubin Observatory will develop *the Science Platform*, which allows for the creation of User Generated data products and enable science cases that greatly benefit from the collocation of user processing data within the LSST Archive Center.

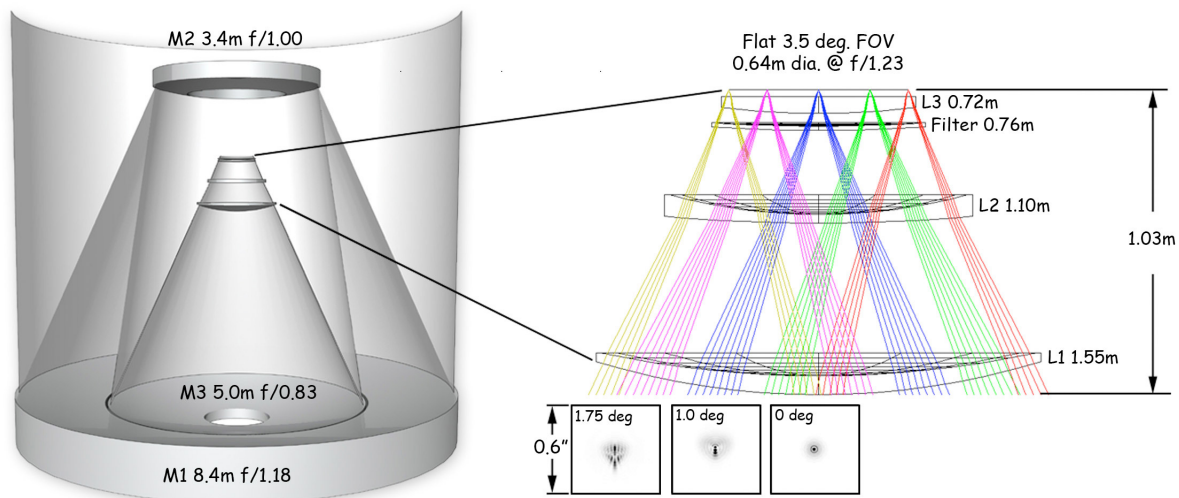


Figure 5.2: A schematic view of the LSST optics.

5.1.1 The Simonyi Survey Telescope

The Simonyi Survey Telescope is an 8 m-class telescope with a field of view of 9.6 deg^2 , unique in its design among large telescopes. Combined with its large aperture, and thus light-collecting ability, this will give it a spectacularly large étendue¹. For LSST the estimated étendue is $\sim 320 \text{ m}^2 \text{ deg}^2$ (Ivezić et al., 2019). This is more than three times the étendue of the best existing telescopes, the Subaru Telescope with its Hyper Suprime Camera, and Pan-STARRS.

With reference to figure 5.2, the telescope’s primary mirror (M1) is 8.4 meters in diameter, the secondary mirror (M2) is 3.4 meters in diameter, and the tertiary mirror (M3), inside the ring-like primary, is 5.0 meters in diameter. The primary and tertiary mirrors (M1 and M3) are designed as a single piece of glass, the *M1M3 monolith*. Placing the two mirrors in the same location minimizes the overall length of the telescope, making easier to reorient it quickly, contributing to a rapid settling after motion. The secondary mirror is expected to be the largest convex mirror in any operating telescope by the time of the writing. The second and third mirrors reduce the primary mirror’s light-collecting area to 35 m^2 , equivalent to a 6.68 m diameter

¹The étendue is a parameter that characterizes how “spread out” the light is in area and angle. It corresponds to the beam parameter product (BPP) in Gaussian beam optics.

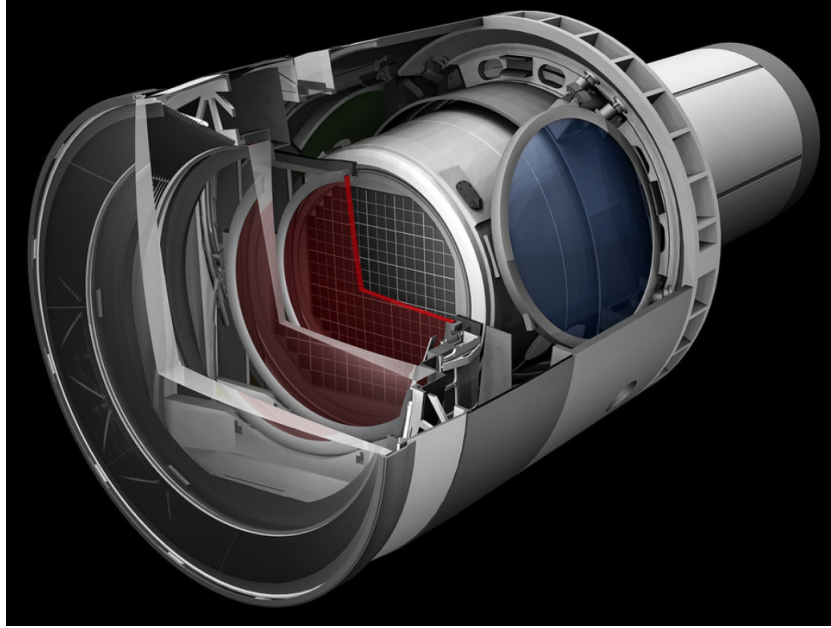


Figure 5.3: A schematic of the LSST Camera.

telescope (Ivezić et al., 2019).

The optics include three corrector lenses to reduce aberrations. All the light collected by the optics is then focused on a 3.2-gigapixel prime focus digital camera. The LSST Camera is designed to provide a 3.5-degree field of view, with its $10 \mu\text{m}$ pixels capable of an 0.2 arcsecond sampling for optimized pixel sensitivity vs. pixel resolution. The image surface is flat with a diameter of approximately 25.2 inches (64 cm). The detector format employs a mosaic of 189 16-megapixel silicon detectors arranged on 21 "rafts" to provide a total of about 3.2 gigapixels. It is positioned in the middle of the telescope, where the cross sectional area is constrained by optical vignetting (edge darkening) and heat dissipation must be controlled to limit lens-deforming thermal gradients in the incoming light. The camera includes a filter located between the second and third lenses (see figure 5.3), and an automatic filter-changing mechanism. Although the camera has six filters (ugrizy) covering 330 to 1080 nm in wavelengths, the camera's position between the secondary and tertiary mirrors limits the size of its filter changer. It can only hold five filters at a time, so each day one of the six must be omitted for the following night. The image quality is better than 0.3 *arcsec* for all bands, as measured by the 80% encircled energy of



Figure 5.4: Construction progress of the Vera C. Rubin Observatory building at Cerro Pachón in September 2019. Credit: "LSSTProject/NSF/Aura"

the image of a point source, which is a standard measure in optics of how well the optical system focuses the gathered light. For longer wavelengths corresponding to the r, i, z and y spectral bands, the 80% encircled energy is ~ 0.2 arcsec, or better. Typically imaging will be limited by the atmosphere, around 0.7 arcsec (Riot et al., 2012). The LSST camera will take a 15 s exposure every 20 s, and repositioning such a large telescope (including settling time) within 5 seconds requires an exceptionally short and stiff structure. This in turn implies a very small focal ratio, which requires very precise focusing of the camera. The 15 second exposures are a compromise to spot both faint and moving sources. Longer exposures would reduce the overhead of camera readout and telescope re-positioning, allowing deeper imaging, but then fast moving objects such as near-Earth objects, would move significantly during an exposure.

5.1.2 Legacy Survey of Space and Time

The LSST consists of different surveys in selected areas of the sky with different observational with different observational strategies: the "Wide, Fast, Deep" (WFD), the "Deep Drilling Fields" (DDF) and the "Mini surveys" (MS). The 90% of the total

	ELAIS S1	XMM-LSS	Extended CDFS	COSMOS
RA 2000	00 37 48	02 22 50	03 32 30	10 00 24
DEC 2000	-44 00 00	-04 45 00	-28 06 00	+02 10 55
Galactic l	311.30	171.20	224.07	236.83
Galactic b	-72.90	-58.77	-54.47	42.09
Ecliptic l	345.97	31.04	40.29	150.70
Ecliptic b	-43.18	-17.90	-45.47	-9.39

Table 5.1: List of the four DDFs, with approximate field center positions (see <https://www.lsst.org/scientists/survey-design/ddf> for details).

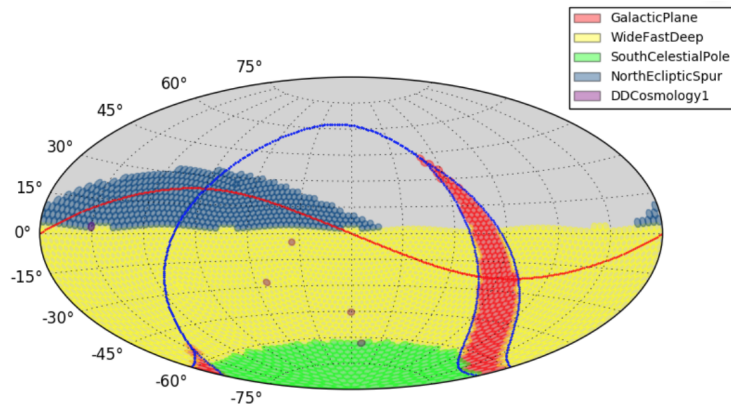


Figure 5.5: The different areas WFD, DD and MS.

time will be constrained to the WFD survey, which will observe every night the all-sky footprint (18000 deg^2 away from the Galactic plane to avoid the zone of high extinction) in all the filters (u,g,r,i,z,y) within a given cadence, the claimed median depth in r will be ~ 24.5 mag for each visit (LSST Science Collaboration, 2009). From 10 to 20% of the observing time will be dedicated to DDF and other MS programs. The DDF are four sky fields (see table 5.1) of limited areas with deeper coverage and more frequent temporal sampling (in at least some of the ugrizy filters). The MS will be focused on the Galactic plane, and they will cover different areas of this region:

1. the central portion of the Galactic plane that is not included in the main survey, it is centered around $|l| = 0$ and covers $\sim 1860 deg^2$. It is observed at a much reduced rate compared to the main survey, and with a smaller total number of observations per field (30 visits per field and per filter, in ugrizy), so as to provide astrometry and photometry of stars towards the Galactic center, but without reaching the confusion limit in the coadded images;
2. the South Celestial Pole, that covers the southern region of the main survey; it will cover $\sim 2315 deg^2$, including the Magellanic Clouds. This mini survey is observed with a strategy similar to the Galactic Plane mini survey, with 30 visits per field per filter in ugrizy, and without requiring pairs of visits. This provides coverage of the Magellanic clouds, but without committing extensive time as these fields are at high airmasses from the LSST site;
3. the North Ecliptic Spur, that covers the northern area of the Ecliptic plane, it is intended to observe the entire Ecliptic plane for the purpose of inventorying the minor bodies in the Solar System. This area ($\sim 4160 deg^2$) is observed on a schedule similar to the main survey, although with a smaller total number of visits per field and only in filters griz;

5.2 Transient searches

The characteristics of the LSST rise the possibility to foster the detection and characterization of transients and stellar variability. Every single visit image acquired with LSST will be immediately reduced, calibrated and processed through the Difference

Image Analysis (DIA). LSST will release survey data in real-time and will spread alerts on new discoveries within seconds. Indeed, an alert packet is produced for each source on the difference image with a $SNR \sim 5$. The alert will be produced within 60 s of the end of the image readout and will deliver the location, fluxes, derived parameters, and $\sim 6 \text{ arcsec} \times 6 \text{ arcsec}$ cutouts of the source. The outcome of the alerts will be delivered within 24 hours on the Science Platform, which is designed to be run at the Data Access Center (DAC) in Tucson, AZ, USA. This platform allows to perform searching and visualization of the database contents and provides a Jupyter notebook aspect to code interactively by remote. Due to the very high bandwidth of the LSST Alert Stream, it will be delivered in real-time to 4-7 Alert Brokers (Bellm et al., 2018). The Alert Brokers are the intermediaries between the LSST data and the scientific community. Four kind of data products will be delivered to the community:

- forced photometry in the position of a source detected in the difference image in the last ~ 30 days before the discovery, to look for faint precursors;
- forced photometry in the position of a source detected in the difference image in the past ~ 12 months, to monitor the evolution of the source;
- a catalog which will contain some light curve characterization parameters of all sources detected in the difference image;
- the association of all sources detected in the difference image with the nearest static sky objects to provide the potential host galaxies for the transients.

There will be about 10^4 detections ($SNR \geq 5$) at each read-out. The astronomical community will be responsible for the analysis and the science with these alerts. This includes classification, complex filtering, and the organization of follow-up observations. In many cases it will not be possible to classify variables or new objects based on the LSST photometry only. Other observations, especially spectroscopic observations, will be required, on very short time after the initial discovery.

Table 5.2: Opsim v1.5 databases.

Family	Name
agn	agnddf
alt	alt_dust
	alt_roll_mod2_dust_sdf_0.20
baseline operation	baseline_2snaps
	baseline
bulges	bulges_bs
	bulges_bulge_wfd
	bulges_cadence_bs
	bulges_cadence_bulge_wfd
	bulges_cadence_i_heavy
daily	bulges_i_heavy
	daily_ddf
dcr	dcr_nham1_ug
	dcr_nham1_ugr
	dcr_nham1_ugri
	dcr_nham2_ug
	dcr_nham2_ugr
	dcr_nham2_ugri
descddf	descddf
filterdist	filterdist_indx1
	filterdist_indx2
	filterdist_indx3
	filterdist_indx4
	filterdist_indx5
	filterdist_indx6
	filterdist_indx7
	filterdist_indx8
footprint	footprint_add_mag_clouds
	footprint_big_sky_dust
	footprint_big_sky_nouiy

	footprint_big_sky
	footprint_big_wfd
	footprint_bluer_footprint
	footprint_gp_smooth
	footprint_newA
	footprint_newB
	footprint_no_gp_north
	footprint_standard_goals
	footprint_stuck_rolling
	goodseeing_gi
goodseeing	goodseeing_gri
	goodseeing_griz
	goodseeing_gz
	goodseeing_i
greedy	greedy_footprint
	roll_mod2_dust_sdf_0.20
	rolling_mod2_sdf_0.10
roolling	rolling_mod2_sdf_0.20
	rolling_mod3_sdf_0.10
	rolling_mod3_sdf_0.20
	rolling_mod6_sdf_0.10
	rolling_mod6_sdf_0.20
	short_exp_2ns_1expt
short	short_exp_2ns_5expt
	short_exp_5ns_1expt
	short_exp_5ns_5expt
spider	spiders
	third_obs_pt120
	third_obs_pt15
third	third_obs_pt30
	third_obs_pt45
	third_obs_pt60
	third_obs_pt90

	twilight_neo_mod1
twilight neo	twilight_neo_mod2
	twilight_neo_mod3
	twilight_neo_mod4
u60	u60
var	var_expt
	wfd_depth_scale0.65_noddf
	wfd_depth_scale0.65
	wfd_depth_scale0.70_noddf
	wfd_depth_scale0.70
	wfd_depth_scale0.75_noddf
	wfd_depth_scale0.75
	wfd_depth_scale0.80_noddf
wfd	wfd_depth_scale0.80
	wfd_depth_scale0.85_noddf
	wfd_depth_scale0.85
	wfd_depth_scale0.90_noddf
	wfd_depth_scale0.90
	wfd_depth_scale0.95_noddf
	wfd_depth_scale0.95
	wfd_depth_scale0.99_noddf
	wfd_depth_scale0.99

5.3 Operation simulator, OpSim

The Rubin Observatory asks to the scientific community to contribute in the process of finalizing the survey design by contributing startegy suggestions and metrics to evaluate the success of a strategy to achieve specific scientific goals². The project team

²See <https://www.lsst.org/call-whitepaper-2018> and <https://www.lsst.org/submitted-whitepaper-2018>

led by Lynne Jones & Peter Yoachim at the University of Washington, has developed a dedicated Metrics Analysis Framework (MAF: Jones et al. 2014)³, an extensive simulations framework shared with the scientific community at a very high level of detail, including: detailed hardware specifications, facility operations models, atmospheric transmission, and astrophysical populations. Standard metrics run on all `OpSims` by the project fall under the main `sims_maf` package,⁴ while community-contributed metrics are curated at the `maf-contrib` project.⁵ The Rubin Observatory Project team has shared its extensive simulations framework with the scientific community at a very high level of detail, including: detailed hardware specifications, facility operations models, atmospheric transmission, and astrophysical populations (Connolly et al., 2014). For most users in the scientific community, the metadata of the predicted observing strategies (*e.g.* observing time, expected seeing, instantaneous depth to 5σ photometric precision) are the most relevant to the evaluation of survey strategies. The Operations Simulator⁶, (Delgado et al., 2014), generates the metadata for a full ten-year period of operation under specified desiderata for the run characteristics. For brevity, we refer to a simulated 10-year survey as an `OpSim`, all the most recent simulation available are listed in Tab 5.2. The `MAF` API is a software package to facilitate the evaluation of simulated LSST cadence to achieve specific science goals as measured by the strategy’s ability to obtain observations with specified characteristics. The `MAF` interacts with databases. The `MAF` has been made public upon its creation to facilitate community input in the strategy design. The `MAF` enables selections observations within an `OpSim` primarily through: `sqlconstrain` which allows the user to select, for example, filters or time ranges (*e.g.* the first year of the survey). Further, the choice of `slicers` allows the user to group observations.

In the following, I present two metrics designed to deliver a Figure of Merit (*FoM*) aimed to compare the performance on a given science case of different observation strategies on two scientific cases: the measurements of SN rates and the discovery of True Novelties.

³Also available at <https://www.lsst.org/content/lsst-metrics-analysis-framework-maf>

⁴https://github.com/lsst/sims_maf

⁵https://github.com/LSST-nonproject/sims_maf_contrib

⁶The description of these `OpSims` can be found in the release note of `OpSim run v1.5` <https://community.lsst.org/t/fbs-1-5-release-may-update-bonus-fbs-1-5-release/4139>

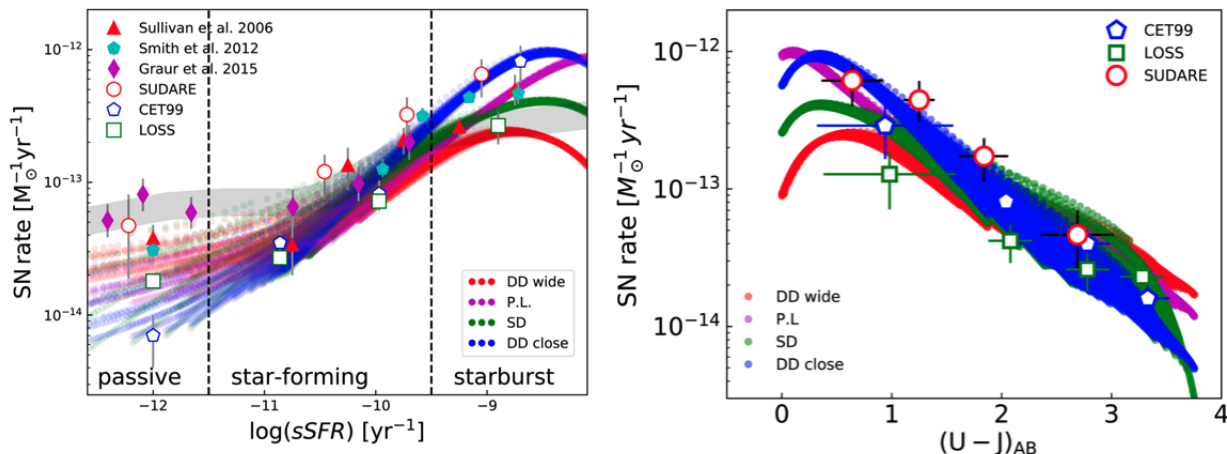


Figure 5.6: SN Ia rate as a function of sSFR and parent galaxy color. The curves show the expected rate for the progenitor models related to four options for the SFH: a SD, two kind of DD, and a power law (see Greggio, 2005, 2010, for more details). The sparse distribution of the measurement does not allow us to discriminate between the different scenarios. Figures credit: Cappellaro et al. (2015); Greggio and Cappellaro (2019)

5.4 SN rates with LSST

The insufficient statistics and systematic uncertainties, make hard to draw straight-forwards conclusions on the SN progenitor problem (see figure 5.6). The possibility to span a large range of stellar population ages with the unprecedented number of galaxies the LSST survey will provide, will strongly improve both the statistical and the systematic uncertainties on the determination of the intrinsic properties of the parent stellar populations. The analysis of the SN rates as a function of both the cosmic time and the parent galaxy properties (mass, colours, SFR, metallicity, e.g. Greggio and Cappellaro, 2019) will set important constraints on the progenitors of all SN types. The measurement of the rate of CC SNe as a function of the cosmic time and galaxy mass from the LSST survey will allow us to check how well this rate traces the global sSFR in the Universe, as derived from other measurements of the production of massive stars.

With the improved statistics from LSST, it will be possible to constrain the mass

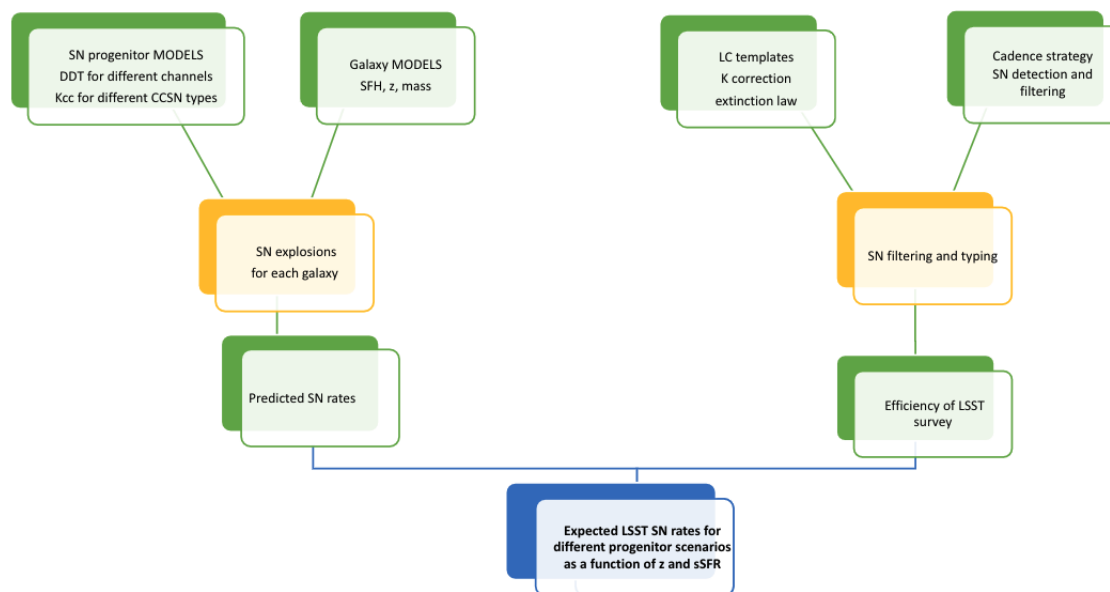


Figure 5.7: The flow chart shows the two stages of the simulation: on the left it illustrates how we will estimate theoretical expectation values of the SN rate for different progenitor scenarios; on the right, instead, it illustrates how we estimate the detection efficiency of the search. These two outcomes will be combined to estimate an expected SN rate measurement as a function of different progenitor scenarios.

ranges of the different CC SN subtypes, and derive the dependence on metallicity. On the other side, the rate of type Ia SNe depends on both the SFH and the distribution of the delay times (see 2.3.2). The trend of the type Ia SN rate with redshift and with galaxy colours measured with LSST data will then be a useful tool to derive information on the distribution of the delay times and the efficiency of type Ia SN production from stellar populations. Eventually, the comparison of the SN rate measurements with our theoretical predictions will allow to discriminate different progenitor scenarios (e.g. Greggio and Cappellaro, 2019). The detailed analysis of the observed rates and the host galaxies properties will also help to shed light on the origin of the SN diversity. In this scenario I developed a metric to optimize the measurement of the SN rates with the Vera Rubin Observatory (see figure 5.7), and a FoM to evaluate the cadence strategy that leads to the higher accuracy in the SN photometric classification. To estimate the detections efficiency and typing for different LSST observing

cadence strategies for each SN type, the following steps have been performed:

1. rest frame light curves template are collected;
2. a grid of light curves simulated at different redshifts applying the proper K-correction, time dilution and extinction are obtained;
3. SNe of each type with simulated light curves have been injected uniformly in the sky and in survey time (in the WFD or DD fields) and time;
4. the number of detections for each event are collected to obtain the observed light curve;
5. the number of simulated SNe meeting criteria for photometric typing are measured.

The survey strategy that maximises the fraction of correctly classified SNe is the best survey cadence for our science case. We adopted 30 templates light curves of SNe with spectroscopic classification and well sampled lightcurve in several bands. The template population is divided into 9 type Ia, 6 type Ibc and 15 type II SNe, that include different light curve morphological and spectroscopic subtypes (IIIn, SLSN, IIL, IIb). The full list of templates is in section 4.5, Table 4.4. The lightcurves have been properly corrected for the time dilution and K-correction in each redshift bin. K-corrections as a function of phase from maximum and redshift (in the range $0 < z < 1$) were obtained as the difference of the synthetic photometry measured on the rest frame spectra and on the redshifted spectra. At the moment, any dust extinction distribution is not considered, even though the metric considers the possibility to inject a proper distribution to simulate the luminosity attenuation leaded by the dust.

The light curves obtained are injected in the **MAF**, and using the proper **OpSim**, it evaluates what is the number of detections for the same simulated SN for the time of the survey, the filters used for the observations and the SNR for each filter. I adopted as detection criterium a $SNR > 5$ in all filters. Furthermore, filtering criteria have been adopted to select the observed SNe for photometric typing:

- at least 10 points on the lightcurve with a $SNR > 5$;

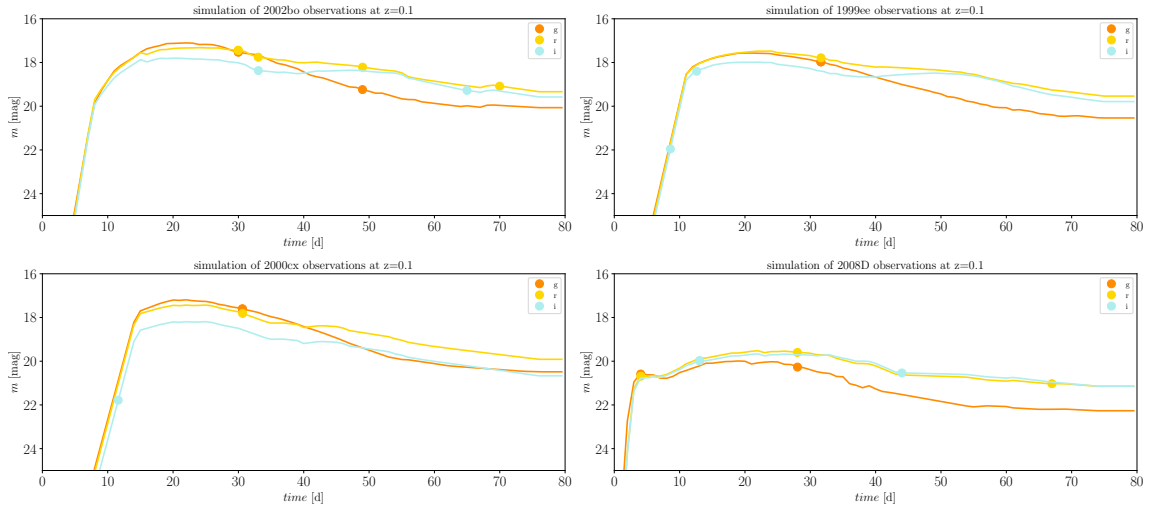


Figure 5.8: Four different examples of simulated light curves.

- detections in a minimum of 3 filters.

The simulated lightcurves (see figure 5.8) are then processed by a classification algorithm, PSNID (Sako et al., 2011). I illustrate as an example the results for the *baseline_v1.5* strategy. I simulated the listed templates in the redshift range $[0,1]$, with an explosion time uniformly distributed within the first year of survey in locations through the WFD field footprint.

For each LSST pointing 9000 SNe were produced with lightcurves in the g, r and i bands. The results are shown in figure 5.9. The fraction of SNe with a correct classification is 70% for type Ia SNe, thus we are still far from an optimal scenario for the photometric classification.

5.5 True novelties

In section 5.2 it is highlighted that the most promising achievement of LSST will be to discover sources unprecedentedly observed. But how can we assure a strategy decisions will maximize the ability to discover astrophysical novelties? Although many metrics have been designed to assess how well a proposed strategy would discover planets, or exploding stars, and allow us to extract their physical properties, designing a metric to evaluate LSST ability to discover true novelties is a conceptually and

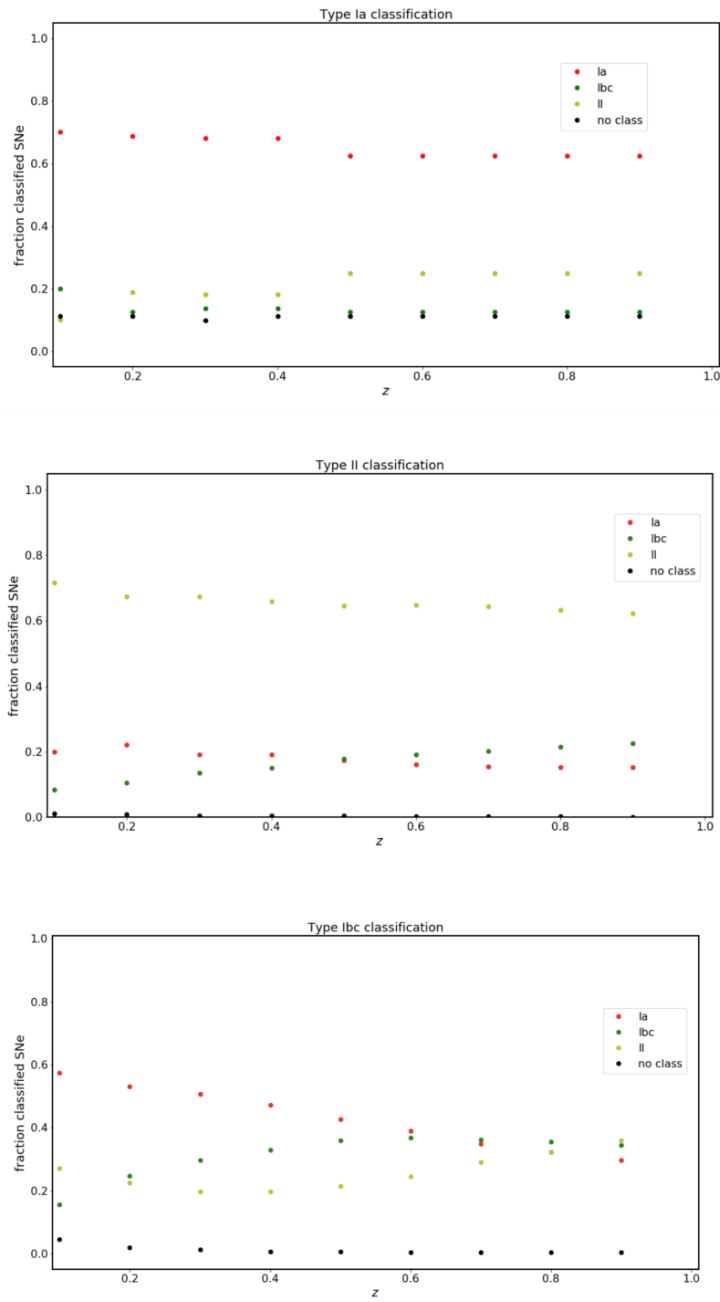


Figure 5.9: Each panel shows the fraction of classified SNe for a given type and the fraction of mis-classified ones as a function of the redshift. From top to bottom type Ia, type II and type Ibc are illustrated.

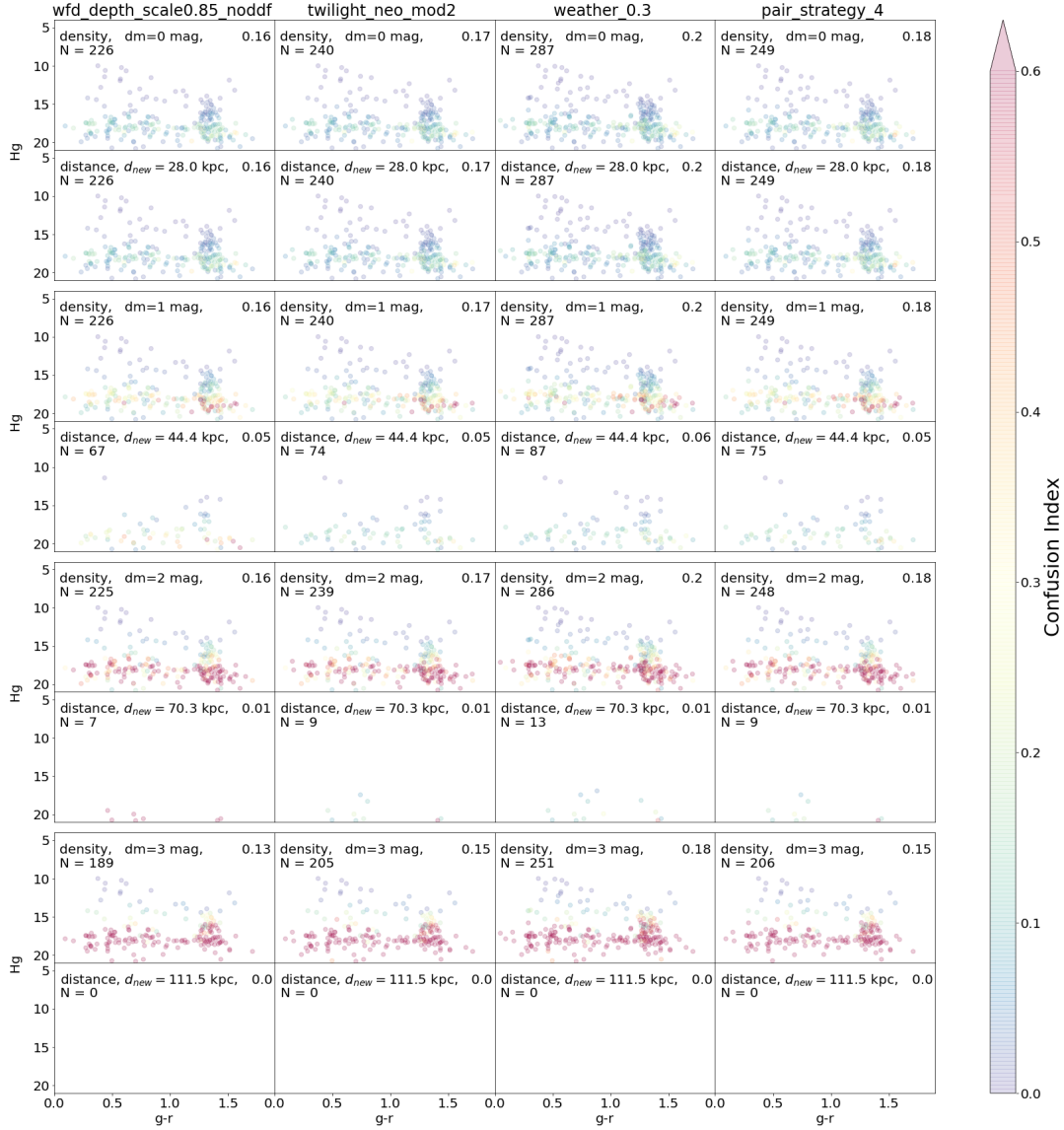


Figure 5.10: Proper Motion Diagram (PMD) showing $H_g = g + 5 \log \mu + 5$ versus $g - r$ color. This figure presents the Confusion Index-based analysis of the first two years of LSST for four different OpSims as indicated on top of each plot column, showing the OpSim's ability to reproduce the PMD in Carlin et al. (2012). We simulate LSST detections based on the properties of Sag A but changing its density or distance. From the top to the bottom we increase the magnitude to simulate either a fainter (*i.e.*, less dense, top row of each row pair) or more distant (bottom row) Sgr A-like stellar structure; the specific mode of each simulation is conveyed in the top left of each panel. At the top right of each panel, the fraction of detected stars is indicated. The color represents a star confusion index **CI**: the number of stars that are measured to have the same proper-motion based on the assumption that the proper motion is measured with uncertainty as expressed in eq. 5.2. N is the number of the detected stars we can associate with the main dynamic structure in the Sag A trail.

practically challenging task that no one had yet attempted. The characteristics and the results of a LSST metrics for true novelties will be presented, by mapping planned LSST observations to a phase space defined by the brightness, color, and the change of those features and exploring the completeness in this phase space, considering the extent of and magnitude depth on the proposed survey footprint, and the ability to identify anomalously moving objects and structures. We measure the ability of 86 currently simulated surveys to discover anomalies including anomalies in color, light curve evolution, association, and proper motion. The results allow the Rubin Observatory to design a survey that maximizes our chances to discover true novelties. Astronomical objects are characterized by brightness, brightness ratio in different portions of the energy spectrum (color), position, shape, and the rate and direction of change in any of those features. This leads to a multidimensional phase space which can be explored. Different categories of phenomena lie in different regions of the phase space (see Figure 5.11). Accordingly, the following features are identified that can be measured in the Rubin Observatory data:

- Color
- Time evolution
- Motion
- Morphology
- Association

Morphology is set aside, as largely the power of the survey to measure morphological anomalies does not depend on the survey strategy, but rather on the image system design (*e.g.*, resolution and depth). Measuring anomalous associations it is assumed depends on the accuracy in measuring the properties of each object.

Having identified features that can be extracted from the Rubin Observatory data, such as color information or light curve evolution, we measure the completeness of the survey in a hypercube in the feature space as a model-independent measure of the power to detect *novel transients* or novel modes of variability. Generally, transients are defined as objects whose observational *and physical* properties are changed by some event, usually as the result of some kind of eruptions, explosions or collisions, whereas

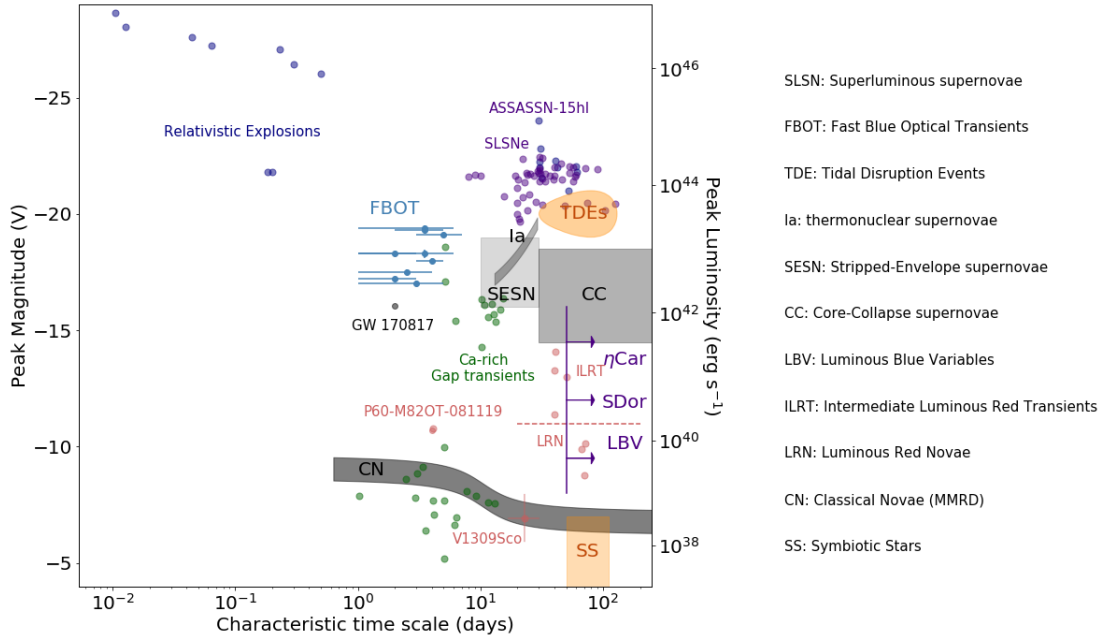


Figure 5.11: The phase space of transients, reproduced with modifications and permission from Ivezić et al. (2019): the intrinsic brightness is plotted against the characteristic time scale of evolution. Shaded areas indicate the region of this phase-space occupied by various classes of objects and individual objects are indicated for less numerous classes. The notable gap at all intrinsic magnitudes fainter than -20 is likely due, at least in part, to an observational bias as surveys are typically not able to probe large volumes of the Universe at short time down to faint brightnesses. Data for Superluminous supernovae (SLSNe) and Fast Blue Optical Transients (FBOTs) that were not included in the original plot are collected from Drout et al. (2014); Inserra (2019), respectively.

variables are objects whose nature is not altered significantly by the event (*e.g.*, flaring stars). Furthermore, some objects vary not because they are intrinsically variable, but because some aspect of their geometry causes them to vary (*e.g.*, eclipsing binaries).

To measure dynamical anomalies in a completely model-independent way proves to be more difficult. Considering objects in the Galaxy when the proper motion of an object is measured in the sky, the ability to understand if it is anomalous depends on the accuracy in the motion measurement, and to the ability to associate that object

to a known galactic component with known proper motion distribution, given its coordinates, color, and brightness. Thus, to measure the ability to identify anomalous proper motions, the photometric accuracy and the time gap between observations of the same field have to be considered. One final parameter that influences the ability to detect anomalies is the sky footprint. Trivially, a larger sky footprint will lead to a higher event rate for anomalies. If one wants to maximise the chance of detecting extragalactic anomalies, then a larger footprint would be favorable, while the probability of detecting Galactic anomalies will scale with density of objects in the sky. Both will scale with the depth of the observations over which the footprint is observed. Ultimately, we define a set of metrics that can simply be summed to generate a *FoM* for *true novelties*:

$$FoM = \sum_{i=c,s,d,\mu,A_{\text{sky}},D_{\text{Star}}} w_i \text{MAF}_i \quad (5.1)$$

where c , s , d , μ , A_{sky} , D_{Star} , represent the color, light curve shape, magnitude depth, proper motion, footprint, and star density respectively, and w are weights that can be assigned to favor the discovery of, for example, transients over non-evolving objects, or Galactic over extragalactic transients. We refrain from assigning weights and we normalize each **MAF** to the best of our ability in a 0-1 range, where 1 is optimal and 0 is pessimal, to provide a “neutral” comparison of the existing LSST simulations.

The Vera C. Rubin Observatory will conduct extensive observations of the Galaxy which can lead to the discovering of new Galactic objects. In addition to transients and variables, the survey may discover objects with unusual proper motions within our Galaxy, or peculiar kinematic structures, such as streams. We consider both cases in this section. Besides, unusual kinematic structures may appear anywhere in the sky, thus we evaluate an **OpSim**’s ability to detect unusual proper motion objects and components in the WFD.

To measure the LSST potential to discover new objects with peculiar motions, we use three different approaches: we begin considering existing structures and the ability of a survey to discover them. We start by taking an exemplary Galactic structure, Sagittarius A, and make it fainter, and move it farther away to test the limits of different **OpSims**. This is not an approach that tells us about true novelties, but it is a starting point to measure the power of the survey to detect unusual kinematic

structures. Next, we generate synthetic objects in a Monte Carlo simulation within a proper motion distribution unlike that of any known Galactic component. Finally, we generate moving transients and assess their detectability. Our figure of merit FoM_{PM} is the sum of the MAFs for these three approaches.

To detect motion we assume that the proper motion μ has to be greater of the 5% of the point-spread-function (PSF) full width half maximum (W_{PSF}). As Kuijken and Rich (2002) showed, the uncertainties on the position of a moving star can be estimated as: $\sigma_{\Delta x} = \frac{0.67 W_{PSF}}{\frac{S}{N}}$. The error on the proper motion μ is:

$$\sigma_{\mu} = \frac{0.67 \cdot W_{PSF}}{\Delta t \cdot \frac{S}{N}}, \quad (5.2)$$

since the uncertainties on the time $\sigma_{\Delta x}$ is negligible, and σ_{μ} depends on the `OpSim` characteristics via Δt , $\frac{S}{N}$, and W_{PSF} . To measure these `OpSim` features, we use the time gaps metric described in the Section 5.5.2 and we extract the PSF directly from the `OpSim` catalog, as well as the signal-to-noise ratio $\frac{S}{N}$ of the measurement of a given star, which is derived from the 5- σ magnitude limit of the image as reported in the `OpSim`.

5.5.1 True anomalies proper motion

Within this project I analyse the ability in detecting unusual motion and structures we implemented to different simulations, thus I perform a simulation that produces stellar objects in structures and studies the ability to recognise all the component of the structure itself; and one that analyses the probability for a single object detection to be unusual. Thus, I used the Sgr A structure as a toy model to analyze the ability of an `OpSim` to discover streams. I reproduced the analysis from Carlin et al. 2012 on the proper motion of the Sgr A trail tidal debris and we ask two questions: if the stream was fainter, could we still detect it? And could we still detect it was farther away?

1. To answer the first question, I decrease the magnitude of all stars in the dataset used in Carlin et al. (2012). This can be interpreted as a probing if the stream could be detected using main sequence stars, instead of stars in the Giant branch. While observationally this produces an overall fainter stream, phys-

ically this corresponds to a stream of a lower star density (assuming the same star mass distribution);

2. to answer to the second question, I decrease the magnitude *and the proper motion* of all stars in the data set used in Carlin et al. 2012, which corresponds to moving the stream farther away.

In item 1, I drop the stars magnitude by Δm in [0, 1, 2, 3] mag steps; in item 2 I move Sgr A within a distance range [28, 111] kpc in four steps to reproduce the same Δm drops, and change the proper motion of the sources according to $\mu_{new} = \frac{\mu_{old}}{10^{\frac{\Delta m}{5}}}$. In both scenarios, we measure:

- the fraction α of detections we lose as they exceed the magnitude limit of the survey.
- the fraction of stars that cannot be detected without being confused with nearby stars, which we call *Confusion Index (CI)*.

The **MAF** for the Sag A simulations is defined as follow:

$$MAF_{CI} = \frac{1 - \mathbf{CI}}{\alpha}. \quad (5.3)$$

CI is estimated as the fraction of objects that falls into the error area on the proper motion diagram (PMD): a phase space of $H_g = g + 5 \log \mu + 5$ versus $g - r$ color. The simulated changes in the structure's properties affect the precision on the proper motion measurement (eq. 5.2). Figure 5.10 shows a PMD for four **OpSims** under the four Δm and distance scenarios. For all **OpSims**, we note that, with reference to Figure 5.10, we rapidly reach the 50% limit in the confusion index. This means that for structures dimmer by two magnitudes than Sgr A we are able to use only the 50% of the stars in the stream, while for a Sgr A-like structure farther away by 111 kpc we will be able to detect only $\sim 20\%$ of the stellar objects.

Finally, I note that to assess if the structure can be detected, I should further investigate our ability to distinguish the main dynamic structure from the background by following the Carlin et al. (2012) methodology.

Looking at the heliocentric velocity distribution from Carlin et al. (2012), I note that they needed ~ 68 stars to recognize the main dynamic structure in the Sgr A

trail. To classify the main and the secondary kinematic structure in the Sgr A stream, we use the Gaussian mixture model technique. The sample can be modeled as a sum of $(k = 1, 2, \dots, K)$ Gaussian components, with mixture weight α_k such that $\sum_{k=1}^K \alpha_k = 1$ estimated by treating the unknown component identification of each object as a latent variable, fitting the mixture-model components θ_k iteratively along with the mixture weights, using the expectation maximization algorithm or a variant thereof.

This technique helps setting the number of stars there would have needed to highlight the second stream in Sgr A in Carlin et al. (2012). Thus, we have a value to the number of stars in the dynamic structure we are able to detect in each simulation. The results (see Fig. 5.10) show that, for all the `OpSim`, when moving the structure by about 44 kpc (corresponding to $\Delta m = 1$), we generally already reach the limit at which Carlin et al. (2012) can distinguish the structure from the background.

Then, I use a Monte Carlo simulation to estimate the LSST ability to distinguish unusual proper motion distributions for stars in different part of the sky, considering the kinematics features of the known stellar Galactic components (the bulge, the disk, and the stellar halo) as described in Binney and Tremaine (2008). Stars in the Galaxy have a characteristic color, luminosity, and proper motions which relate to their position and the probability to belong to one of the known Galactic components. From the color, luminosity, and coordinates, the expected proper motion can be estimated.

For each pointing in the `OpSim`, the algorithm proceeds as follows.

1. I generate a set of $N = 500000$ distances d for stars within a distance range $d \sim [0, 120]$ kpc, according to the distance distribution in Binney and Tremaine (2008).
2. I generate a set of m_g for each object simulated in step (1) by assigning to each object an absolute magnitude following a simplistic single-age distribution from Percival et al. (2008) with stellar age ~ 6 Gyr (which is between the typical age of stars in the bulge and those in the disk as claimed in Tawny and Ness (2020)). Stars in the magnitude range $m_g \sim [15, 25]$ are retained;
3. I select only the 1% dimmer population of the entire simulated sample;

4. I associate each selected object with a Galactic component assigning them in proportion to the relative density of object in each component at distance d ;
5. I assign a velocity \vec{v} to each selected object drawing either from the assigned Galactic component velocity distribution or from an *unusual* distribution;
6. Finally, I calculate the tangential velocity v_{tan} , which represents the projection of the velocity vector on the sky plane, *i.e.*, its proper motion, as:

$$\mu = \frac{v_{\text{tan}}}{4.74 d} / \text{yr}. \quad (5.4)$$

The velocity distribution of the *known* objects is parametrized following the approach of Binney (2010): the action angles (J_θ, J_ϕ, J_z) describe the constants of motion of the orbits in axisymmetric Hamiltonian. For each simulated object in the disk, in the bulge or in the halo, I used the proper velocity distribution function Baushev (2012); Binney (2010); Kuijken (1995):

$$\begin{aligned} f_{DF}^{DISK}(J_z, J_r, L_z) &= \frac{\int_0^{\tau_m} d\tau e^{\frac{\tau}{t_0}} f_{\sigma_r}(J_r, L_z) f_{\sigma_z}(J_z)}{t_0(e^{\frac{\tau_m}{t_0}} - 1)} \\ f_{DF}^{BULGE}(v) &= \frac{1}{\sqrt{2\pi}\sigma_{disp}} e^{-\frac{v^2}{2\sigma_{disp}^2}}, \\ f_{DF}^{HALO}(v) &= \frac{4N}{\sqrt{\pi}v_\odot} \left(\frac{v}{v_\odot}\right)^2 e^{-\frac{v^2}{v_\odot^2}}. \end{aligned}$$

(5.5)

To model the kinematics of *unusual* objects I propose two different paths: first I assumed a known distribution for unusual object from Carlin et al. (2012), the same Sag A stream we used in; then to answer the more general questions about the ability of the LSST to discover never-before-seen novelties, I use an uniform velocity distribution in the range $[-5000, 5000]$ km/s . While this is not a non-parametric approach, as no simulation can be, the uniform distribution is minimally informative because it does not influence the posterior distribution such as others probability distributions (Lemoine, 2019).

v_{\odot} [$\frac{km}{s}$]	N	v_{disp} [$\frac{km}{s}$]	k	q	R_d [kpc]	$\sigma_{z,0}$ [$\frac{km}{s}$]	$\sigma_{r,0}$ [$\frac{km}{s}$]	β	L_0 [$\frac{km}{s}$]	Σ [$\frac{M_{\odot}}{kpc^2}$]	τ_1 [Gyr]	τ_m [Gyr]	t_0 [Gyr]
187.5	1.003	140 $\frac{km}{s}$	0.25	0.45	3.2	19	33.5	0.33	10	$300 \cdot 10^{-6}$	0.11	10	8

Table 5.3: Parameters for the velocity distribution functions, as described in Baushev (2012); Binney (2010); Kuijken (1995)

When I measure the time gap between two observations of a field in g band to measure Δt , I consider only the observations in the first 2-years of the survey in order to explore the potential of LSST to *promptly* detect kinematic anomalies.

To understand which strategy will perform better in detecting unusual objects, I measure what fraction of unusual objects has a proper motion beyond the $5 - \sigma$ limit of the known objects' proper motion distribution.

To each simulated object we associate a proper motion likelihood $\mathcal{L}(\mu)$; the likelihood function is described as follow:

$$\mathcal{L}(\mu_i | \mathbf{X}, m_g, \Delta t) = \left(\sum_{k=1}^3 \mathcal{L}_{k,i} \right) \otimes P(\mu_i | m_{g,i}, \Delta t_i), \quad (5.6)$$

where the first term of the product is the likelihood of the proper motion measurement due to its location in the Galaxy, I considered the distribution of the measured proper motion, where I selected as measured all simulated proper motion which verify two main criteria:

- 1) the apparent magnitude of the star related to the simulated proper motion has a SNR greater then 5;
- 2) the motion performed by the star related to the simulated proper motion is greater then the 5% of the W_{PSF} .

where v_{\odot} is the Sun's velocity, σ_{disp} is the central velocity dispersion of the Galaxy, and the τ -dependent part in the velocity distribution function of the disk takes into account the realistic distribution that must consider the thin disc to be a superposition of pseudo-isothermal cohorts of different ages and chemical compositions (Binney, 2010). The parameters are shown in Table 5.3.

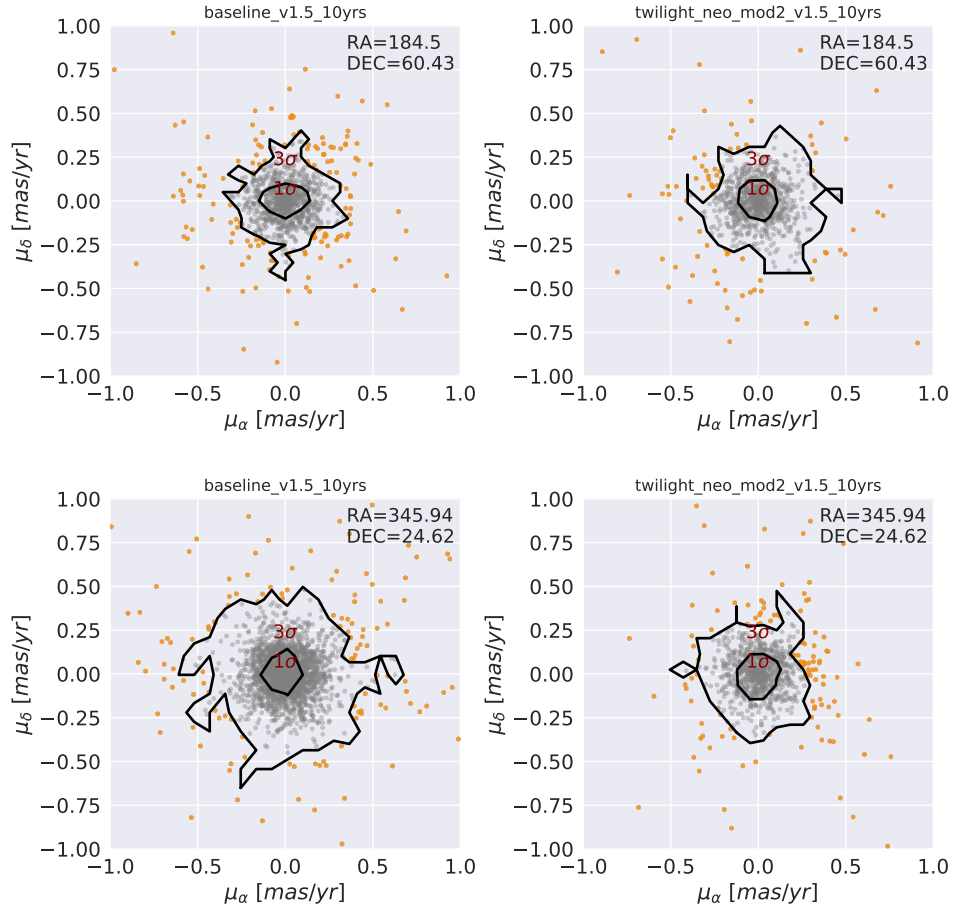


Figure 5.12: The bold line in the figure shows the 3σ contours of the usual proper motion distribution, the fraction of unusual object detected as outliers is represented by the number of points outside the contour. Two pointings for two different observing strategies, at a first glimpse they work very similarly, suggesting that at least these two strategies will detect the same fraction of unusual objects. It is also clear from the point distribution that the kind of detected unusual objects are quite different, highlighting the potential of a certain strategy to work better in a certain region of the parameters space.

$P(\mu|m_g, \Delta t)$ is the probability to measure a certain proper motion for an object with a magnitude m_g in a given time interval Δt . Given the uncertainty on the proper motion (eq. 5.2), the probability $P(\mu|m_g, \Delta t)$ can be written as:

$$P(\mu|m_g, \Delta t) \approx e^{-\left(\frac{0.05W_{\text{PSF}} - \mu\Delta t \frac{S}{N}}{0.67W_{\text{PSF}}}\right)^2}, \quad (5.7)$$

where the term $0.05W_{\text{PSF}}$ is the threshold for a motion to be detected, μ is the simulated proper motion, $\frac{S}{N}$ is the signal to noise ratio, and Δt is the time gap between two g observations.

I present the simulations for the baseline and one of the **OpSim**, twilight neo mod2, for the unusual distribution. What I need to highlight is the ability of a given observation strategy to detect as many objects as possible that lay outside the inter-quartile interval (the black lines show the 3σ limit of the usual distribution). With reference to Fig. 5.12 the unusual proper motion distribution spread outside the range when generated from a uniform velocity distribution. This allows to assume that these strategies will be able to discriminate the unusual population from the usual ones when the unusual population comes from a different origin.

It is expected that some objects' unusual proper motion should lay in the tails of the distribution of usual objects. This fraction of objects can be still detected as usual if the error lets them be comprised in the usual object distribuiton. Therefore our proper motion MAF is:

$$\text{MAF}_{\mathcal{L},i} = \sum_{i=0}^{N_{\text{stars}}^{\text{tails}}} \frac{\mathbf{is\ unusual}}{N_{\text{stars}}^{\text{tail}}}. \quad (5.8)$$

where

$$\mathbf{is\ unusual} = \begin{cases} 0, & \text{if } (\mu_{\text{unusual}} \pm \delta\mu_{\text{unusual}}) - \bar{\mu}_{\text{usual}} > 5\sigma_{\mu_{\text{usual}}} \\ 1, & \text{otherwise} \end{cases} \quad (5.9)$$

As a last component of our proper motion figure of merit FoM_{PM} , we investigate the **OpSims** ability to measure the proper motion of transients and variable objects. Unusual proper motion could impair the identification of a transients or a variable by hiding the time dependent features of the source, *e.g.*, the variability could work on timescales shorter than the ones of the motion, causing an object to appear different

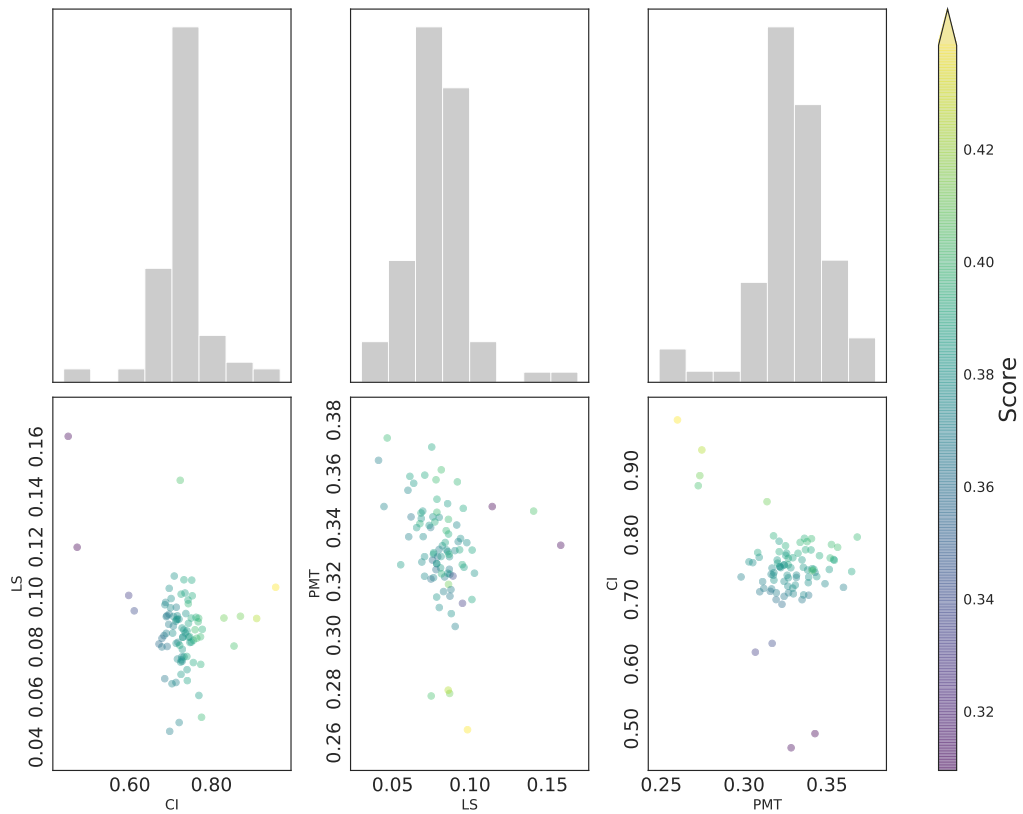


Figure 5.13: The distribution and correlation of the three proper motion MAFs, over all the OpSims examined. The scatter plots do not show a high correlation, indicating that all three MAFs can contribute to the design of an optimal proper motion anomaly detection OpSim.

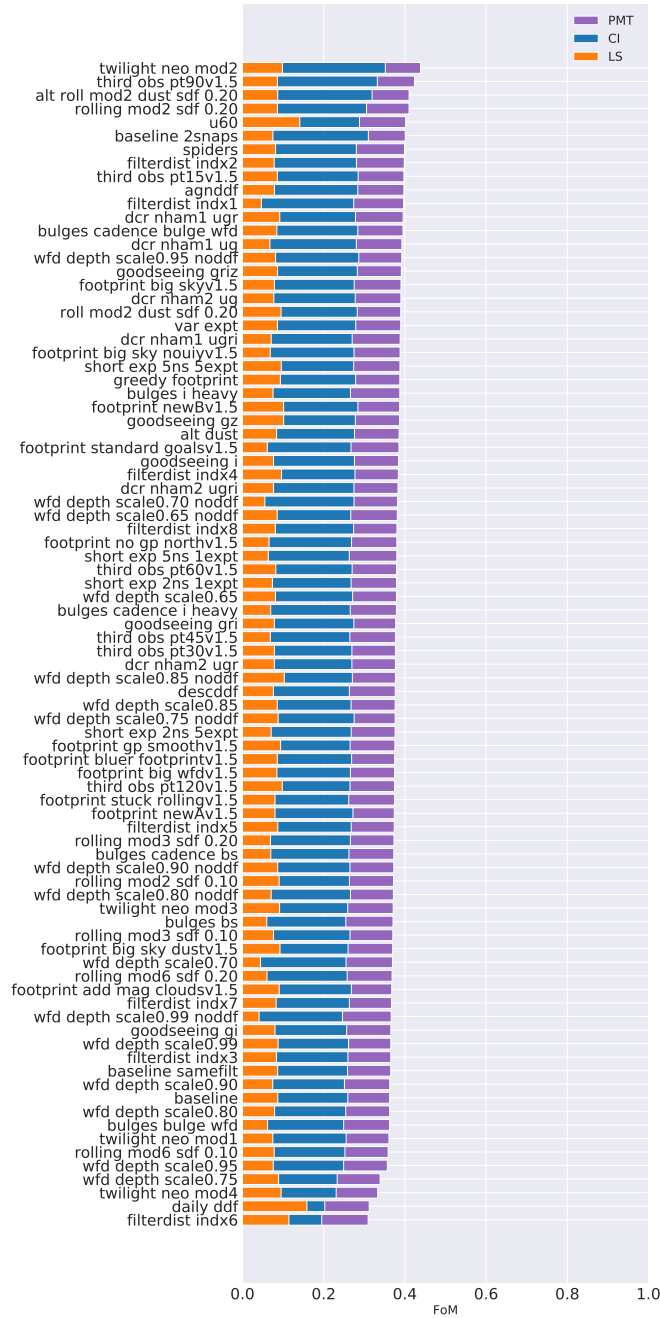


Figure 5.14: Values of the Figure of Merit for the three metrics about the Likelihood Score MAF_{LS} , the Confusion Index MAF_{CI} , and the Transients fraction $MAF_{transients}$. The three metrics are normalized so that the distributions change in the same range.

and at a different location in two images, rendering its identification difficult; or the proper motion can be correlated to atypical transient events providing phenomenological information that should be included in models. To analyze the ability to retrieve both the astrometric and the variability features, I simulate light curves that go on and off during the survey duration, such that the transients can be observed at least twice, and its motion can be detected as well. I use a Monte Carlo simulation to reproduce transients with a different cadence, within the range from few days to few months duration, with a magnitude at peak in the range [17, 25] mag. Among all simulated transients, we measured the fraction of detected light curves with at least two detections that enable the measurement of the proper motion. The related MAF is then the detected fraction:

$$\text{MAF}_{\text{transient}} = \sum_{i=0}^{N_{\text{transients}}} \frac{\text{is detected}}{N_{\text{transients}}}. \quad (5.10)$$

This MAF a modified version of the TransientMetric⁷ **is detected** is 1 if the object has at least two detections in the g band separated by Δt such that $\sigma_{\mu} < 3\mu$, 0 otherwise.

The described metrics allow us to determine, from the astrometric point of view, the best strategy to detect anomalies in the proper motion. The True Anomalies Proper Motion figure of merit FoM_{PM} for an OpSim is defined as:

$$FoM_{\text{PM}} = A_{\text{CI}} \frac{\sum_i \text{MAF}_{\text{CI},i} \cdot w_i}{\sum_i w_i} + \quad (5.11)$$

$$A_S \frac{\sum_i \text{MAF}_{\mathcal{L},i} \cdot w_i}{\sum_i w_i} + \quad (5.12)$$

$$A_{\text{transients}} \frac{\sum_i \text{MAF}_{\text{transients},i} \cdot w_i}{\sum_i w_i} \quad (5.13)$$

where MAF_i is the outcome of the metric for the i -th field; A_S , A_{CI} , $A_{\text{transients}}$ are the normalization factors that we set so that each piece contributes similarly. The last term to discuss, w_i , is a weighting factor that weight different fields differently. We considere as a weight the star density in each field estimated using the star-density metric⁸.

⁷<https://sims-maf.lsst.io/lsst.sims.maf.metrics.html#lsst.sims.maf.metrics.transientMetrics.TransientMetric>

⁸<https://sims-maf.lsst.io/lsst.sims.maf.metrics.html?highlight=star%20density#module-lsst.sims.maf.metrics.starDensity>

I further investigate the interplay of these MAFs (see Fig. 5.13). From a first glimpse, the three MAFs are slightly correlated; this assure they can be used independently to highlight features of a given observation strategy. Indeed, for each MAF, the scatter of the values cluster the best performing from the others in a separated region of the parameters' space.

This *FoM* is plotted in Fig. 5.14. The major interplay into the estimation of the best *OpSim* is due to the Likelihood and the ConfusionIndex metrics, the ProperMotionTransient metric contributes uniformly. This is related to the fact that I analyze the transients only in the g band, so the number of transients is limited to these which vary in g. The single band approach is not the best in reproducing the number of detectable transients, it allows us to show that not all the *OpSim*s perform the same in detecting transients, as shown in the histogram on the right of Fig. 5.13. Generally for these metrics are advantaged *OpSim*s with higher footprint area and with a more uniform time gaps distribution, while rolling cadences appear to be higher sensitive to the discovery of novelties but with a lower performance on the ability to distinguish between different structures.

5.5.2 Color and time evolution

The LSST characteristics in photometric sensibility and footprint extension an opportunity to for new transient phenomena. The LSST capability to discover novel transients then largely depends⁴ on its observation cadence.

Different transients will benefit from different observation strategies because of the different phenomenological expression of their intrinsic physics. To make sure that the observation strategies under design maximize our chances to discover *any* novel transient, we created the *filterTGapsMetric*. This MAF evaluates the ability of LSST's observation strategies to capture information about color and its time evolution at multiple time scales.

Rubin LSST will image the sky in six filter bands u, g, r, i, z, y . The *filterTGapsMetric* measures all time gaps between two filters in an *OpSim*, *i.e.*, ug, gr, ri and so on. The *filterTGapsMetric FoM* evaluates the coverage of time gaps for each filter-pair. We prefer an observation strategy that minimizes uncovered gaps within a relevant time interval.

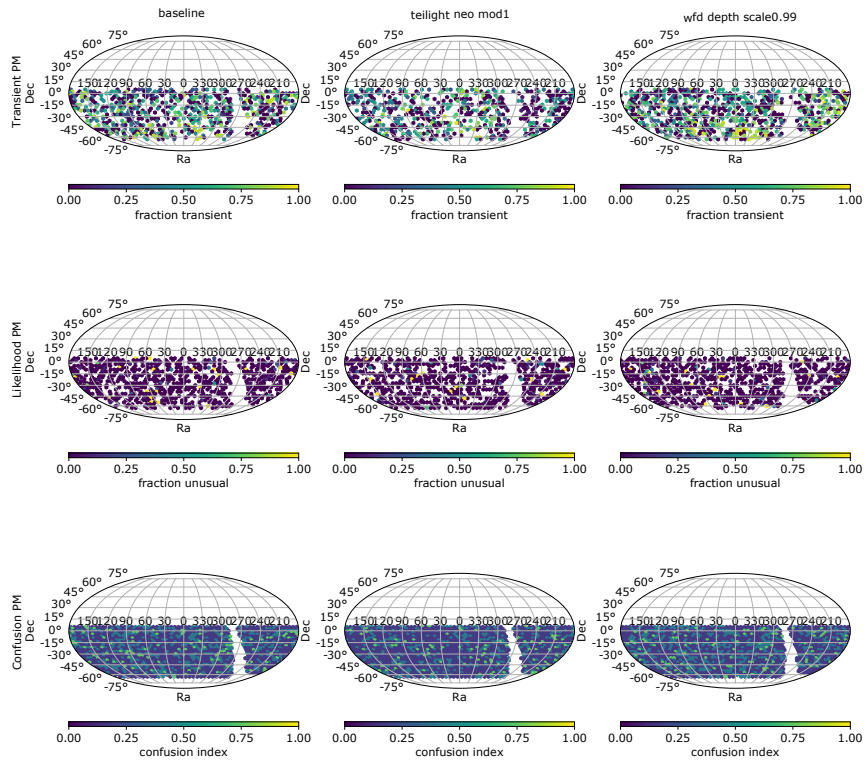


Figure 5.15: In the figure is shown the sky map distribution for the metrics described in the previews sections for three different OpSims. The spatial trend suggests that typically all the strategies has the same probability to detected unusual objects with similar accuracy.

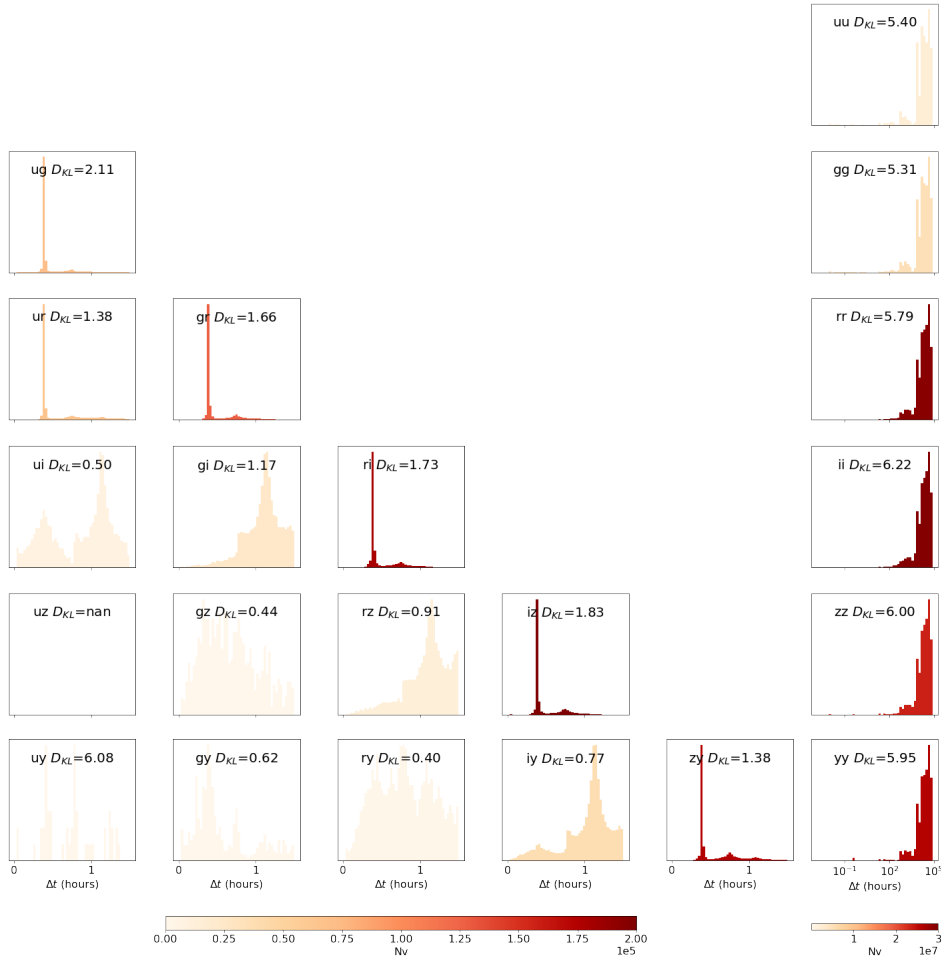


Figure 5.16: The distribution of all time gaps for the **baseline v1.5 OpSim**. The triangle of plots on the left shows all time gaps between different filters (which enable the measurement of color) within 1.5 hours. The column of plots on the right shows the distribution of time gaps in the same filters for the 10-year survey, which enables the measurement of brightness changes. The filters are indicated in each quadrant, from u to y from top to bottom and left to right. All histograms are normalized but the intensity of the color is proportional to the total number of observations in that filter-pair, as indicated by the color bar. In each quadrant the value of D_{KL} is reported. We note that the majority of observations are taken with adjacent filters, which give a narrow leverage on the spectral energy distribution (SED), and less possibility to measure color. Color is in fact better measured with filters that are more separated in wavelength such as $g-i$ or $r-z$, as described in Bianco et al. (2019).

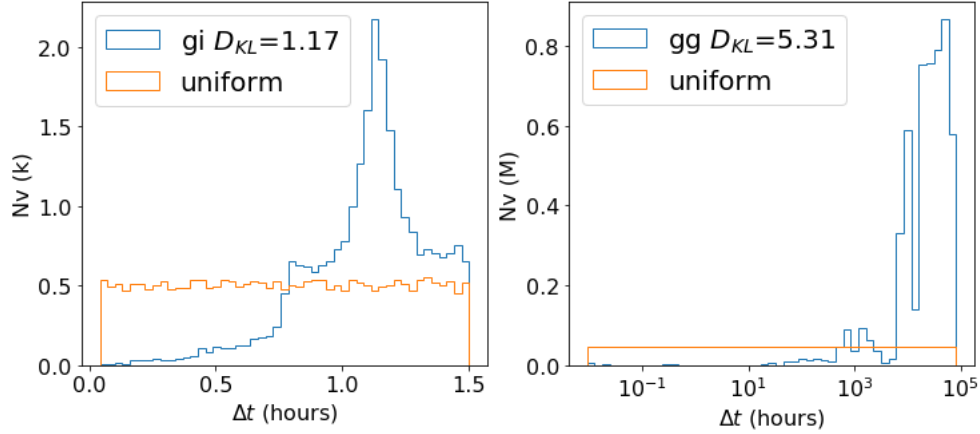


Figure 5.17: Time gaps in $g-i$ (left) and $g-g$ (right) from **baseline v1.5** compared to the "ideal" distribution, plotted in orange: a uniform distribution for the colors (left, with the y -axis in units of 1000 observations) and a uniform distribution in log space for the lightcurve shape (right, with the y -axis in units of 1 million observations).

On a field-by-field basis, for each filter pair, the metric and FoM are evaluated as follows:

- selecting the survey (*e.g.* WFD in this paper) and the observation time range using `sqlconstraint` and slice the sky with `HealpixelSlicer`;
- fetching the observation times for each field, for all visit in either of the two filters;
- performing an element-wise subtraction to get all time gaps.

Fig. 5.16 shows the distribution of time gaps for all filters pairs for the **baseline v1.5**.

The basic output from **MAF** for this metric is a field-by-field time-gap distributions, the FoM for the entire candidate survey strategy is then computed by measuring how well the distribution of time gaps matches an ideal distribution, which we set to be a uniform distribution between 0 and 1.5 hours. Bianco et al. (2019) has shown that color can be measured reliably even for rapid explosive transients within 1.5 hours. Of course this is not necessarily true for novel phenomena, but we will use this as a fiducial time interval. We use the Kullback-Leibler (KL) divergence (or relative entropy S .

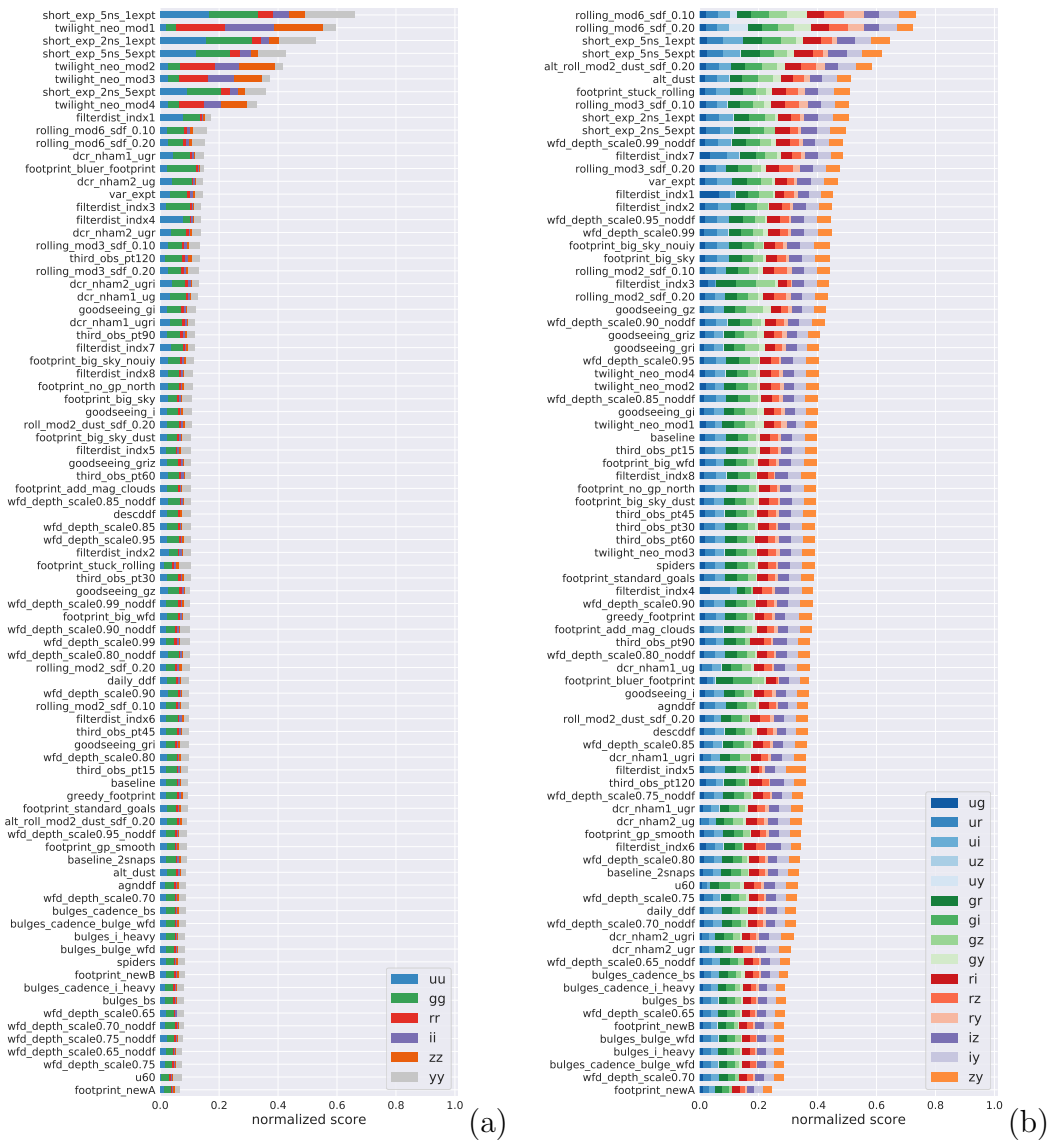


Figure 5.18: Figures of merit $FoMtGaps$ for the OpSim v1.5 runs based on the distribution of time gaps. The $FoMtGaps$ is calculated as described in 5.15. The plot on the *left* shows the FoM for repeat visits in the same filter. The plot on the *right* shows the value for observations in pairs of different filters. Each OpSim is presented as a bar whose length corresponds to the value of the FoM . For each OpSim $FoMs$ for different filters are concatenated horizontally. For example: on the left the different color bars represent the time gap FoM for different filters from u to y and the OpSims are sorted by the total FoM , i.e. the sum of the $FoMs$, for that color (a) and shape (b) “diagnostics”.

and A., 1951) to measure the discrepancy between the ideal and observed distribution. The KL divergence provides an information-criteria based measure of the difference between two distributions: the KL divergence from Q to P is defined as $D_{KL}(P||Q) = \sum P \log(\frac{P}{Q})$. The KL divergence is not a distance, in the sense that it does not satisfy the triangle inequality, its not symmetric, and it is not normalized. To derive a normalized quantity from D_{KL} we use $e^{-D_{KL}}$, where two identical distributions, with $D_{KL} = 0$ would contribute 1 to the sum, while $D_{KL} > 0$ would contribute < 1 . Thus a larger FoM indicates a preferable simulation. This FoM is naturally normalized between 0 and 1 for each field. To probe light curve shapes, instead, we want to measure the evolution at all time scales: repeated observations in the same filter at different Δt , covering small time gaps to recover information about rapidly varying transients, or rapid evolution phases of transients, but also large time gaps to cover long time scales. We measure how similar a distribution of Δt is to a logarithmic distribution by measuring $e^{-D_{KL}}$ between the observed distribution and a uniform distribution in $\log_{10}(\Delta t)$ for the entire 10-year survey.

The steps of the FoM calculation then are:

- to compute the discrepancy-measure $e^{-D_{KL}}$ between the distribution of time gaps and an “ideal” distribution, for each filter-pair. This step is shown in figure 5.17.
- to sum the discrepancy measures over the filter pairs, weighted by the number of visit pairs over the whole sky in each filter pair N_k , and by a “scientific” weight factor w that allows certain filter-pairs to be (de)-emphasized.

This weighted sum is the FoM for the OpSim of interest. The process is summarized in the relation:

$$FoM_{tGaps} = \sum_i^N \sum_{k=ug,gr,\dots} w_{k,i} N_{k,i} e^{-D_{KL,k,i}}, \quad (5.14)$$

where $0 \leq w_k \leq 1.0$, N_k stands for the number of visits, and the index i runs through the `healpixels`. In fact, we use a simplified version of the above relationship where the KL divergence is calculated directly for all of the sky since we will embed preferences in the pointint with subsequent components of the FoM :

$$FoM_{t\text{Gaps}} = \sum_{k=ug,gr,\dots} w_k N_k e^{-D_{KL,k}} \quad (5.15)$$

As indicated earlier, we do not choose any weights: the value of w_k is always set to 1 in our calculations. Some filters and filter combinations may well be more useful than others to discover anomalies. Trivially, the value of w_k could be set by the limiting magnitude for the shallowest filter in a filter pair.

Fig. 5.18 shows the $FoM_{t\text{Gaps}}$ calculated in eq. 5.15 for all **OpSim** runs in **OpSim** v1.5. At the top of the list ranked by $FoM_{t\text{Gaps}}$ rise two families of **OpSims** for the color diagnostics: *short* and *twilight* (Fig. 5.18, (left)). This can be explained by the fact that these **OpSims** contain short exposures that fill in the distributions at short time scales. While higher cadence is useful to discover rapidly evolving astrophysical novelties, a largely unexplored regime, one needs to assure that the observations reach a sufficient magnitude to penetrate an unexplored *volume* of Universe. The depth of the observations will be added at the next step. While short and twilight overperform all other **OpSims**, after a significant performance step we see *filterdist*, *rolling*, and *dcr* families as next best options.

The light curve shape $FoM_{t\text{Gaps}}$ (Figure 5.18, (right)), shows the *rolling* family of **OpSims** rising among the top performers: a rolling strategy naturally provides a log-like coverage which supports the discovery and study of transients at multiple scales. All top 10 performing surveys, from the point of view of the lightcurve-shape characterization, are *rolling* or *short* cadence **OpSims** although we see a smooth performance decline with no sharp transition.

Because our time-gaps, metrics are essentially based on the number of images that meet some criteria in an **OpSim**, it is important to assure that the counted images all meet quality standards. In particular, we need to include information about the image depth (*i.e.*, limiting magnitude), so that we compare the discovery potential within the same volume of the Universe. Some simulations augment the WFD survey with short exposures. In fact, we noted in the $FoM_{t\text{Gaps}}$ analysis that **OpSims** include short exposures rise to the top of the ranked list of **OpSims**: while these **OpSims** meet the nominal criteria and provide valuable image pairs at short time gaps, they may fail to extend the explored volume of the Universe to unexplored regions, which is the most important contribution LSST will make in the anomaly discovery space. To account

for this, we add a metric component that measures the depth of the images collected by an **OpSim**.

We inspect the depth distribution of an **OpSims** for each filter and compare it with the survey expectations as laid out in Ivezić, and the LSST Science Collaboration (2013) table 6.

Short exposures are typically designed for specific purposes, such as the detection of Near Earth Objects (NEOs) (*e.g.*, the *twilight_neo* family) or decreasing the saturation limit to enable calibrations with shallower surveys (John, 2019). We want to penalize surveys where these short exposures come at a cost of deeper images. In Fig. 5.19 we consider three **OpSims**: the baseline (blue filled histogram), *twilight_neo_mod1*, and *short_exp_2ns_1expt*. *twilight_neo_mod1*, *short_exp_2ns_1expt* have a bimodal distribution of ($5\text{-}\sigma$) limiting magnitude. The short exposures contribute to a cluster that peaks at a magnitude fainter than 21 in all bands ($u=20.45$, $g=20.95$, $r=20.95$, $i=20.95$, $z=20.75$, $y=19.95$ for *short_2ns* and $r=20.95$, $i=20.85$, $z=20.25$, $y=20.95$ for *twilight_neo_mod1*). However, while for *short_exp_2ns_1expt* the distribution of faint (≥ 21.5 mag) images is not substantially different from the baseline's one, *twilight_neo_mod1* has fewer faint images in the r , i , and z band, and more in the y band.

The related *FoM* is then the difference between the median of the distribution and the survey specification:

$$MAF_{depth} = \frac{\sum_{u,g,r,i,z,y} m_{median, i} - m_{goal, i}}{6}, \quad (5.16)$$

where the sum extends to the 6 filters. This leads to a ranking of the **OpSims** shown in Fig. 5.20; the short exposure family ranks low, compensating for the high rank in the time-gap metric *FoM* due to the higher number of images. Aside from the *u60*, *short*, and *twilight* families, all other **OpSims** have a similar score, between ~ 0.8 and ~ 0.9 . *u60*, which produces 60-second u -band exposure instead of the standard 30-second, ranks at the top. We also note that the *rolling* and *footprint - big sky* families are penalized in this metric. This may be a consequence of the added constraints on pointing competing with the constraints on image quality (related to weather, airmass, *etc...*).

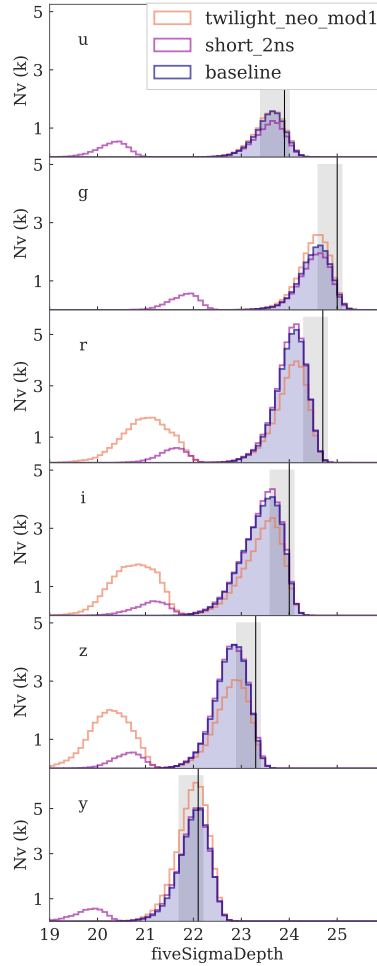


Figure 5.19: Distribution of depth for images in three different OpSims. The survey specification are indicated as a gray band (minimum requirement to stretch goal) and a vertical line (design specification) as per Ivezić, and the LSST Science Collaboration (2013) table 6 for each filter (as indicated in the top left of each panel). Some OpSims are designed to include in the WFD short exposures and may perform well in metrics based on number of exposures taken. But shallower images generate lower SNR measurements and only allow the exploration of a smaller volume of the Universe: this would have negative impact on the discovery of anomalies if it came at the cost of long exposures.

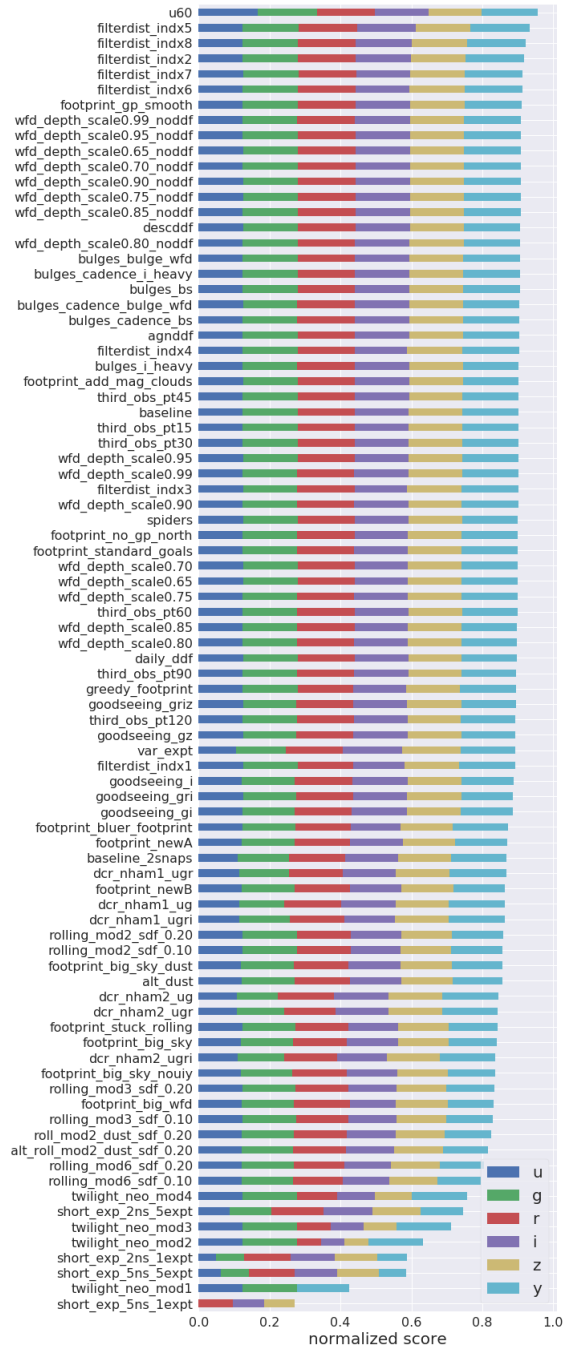


Figure 5.20: Ranking of OpSims based on the depth of the exposure. *u60*, which produces 60-second *u*-band exposure instead of the standard 30-second, extends the observed volume slightly, but performs poorly in both FoM_{tGaps} (Fig. 5.18, a and b). Otherwise, for the most part, family of OpSims are clustered together in this diagram, all with a similar FoM_{depth} score: 90% of the OpSims generate values within 10% of each other in this metric.

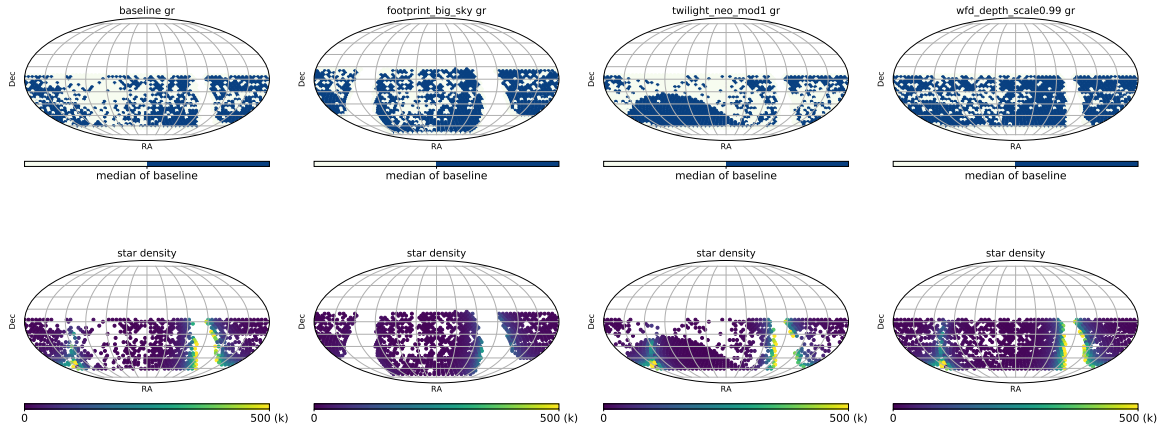


Figure 5.21: The WFD footprint.

5.5.3 Footprint and Minisurveys

The footprint coverage is another important factor which plays a crucial role in determining the LSST ability to discover anomalous and unusual phenomena.

We evaluate what fraction of the sky is covered by an observing strategy for each filter pair. Although an object may have an anomalous color which could be detected in a single visit pair, here we focus on transients and proper motions and we want to observe a field repeatedly to detect changes. We use the median number of visits N_{median} in `baseline v1.4` as a fiducial threshold: a field is considered well observed if it has more observations than N_{median} . To do this, we perform the follow steps for each field:

- we count number of visits within 1.5 hours for each filter pair;
- we check if $N > N_{median}$;
- we sum over all fields that pass the requirement.

However, depending on whether a scientist focus is on extragalactic or galactic anomalies, the preferred footprint would be different: for extragalactic anomalies one would simply maximize the sky coverage, whereas for Galactic science the probability of discovering an anomalous object or phenomenon would scale with the number of objects in the Galaxy in that observed field. Therefore, in addition to this

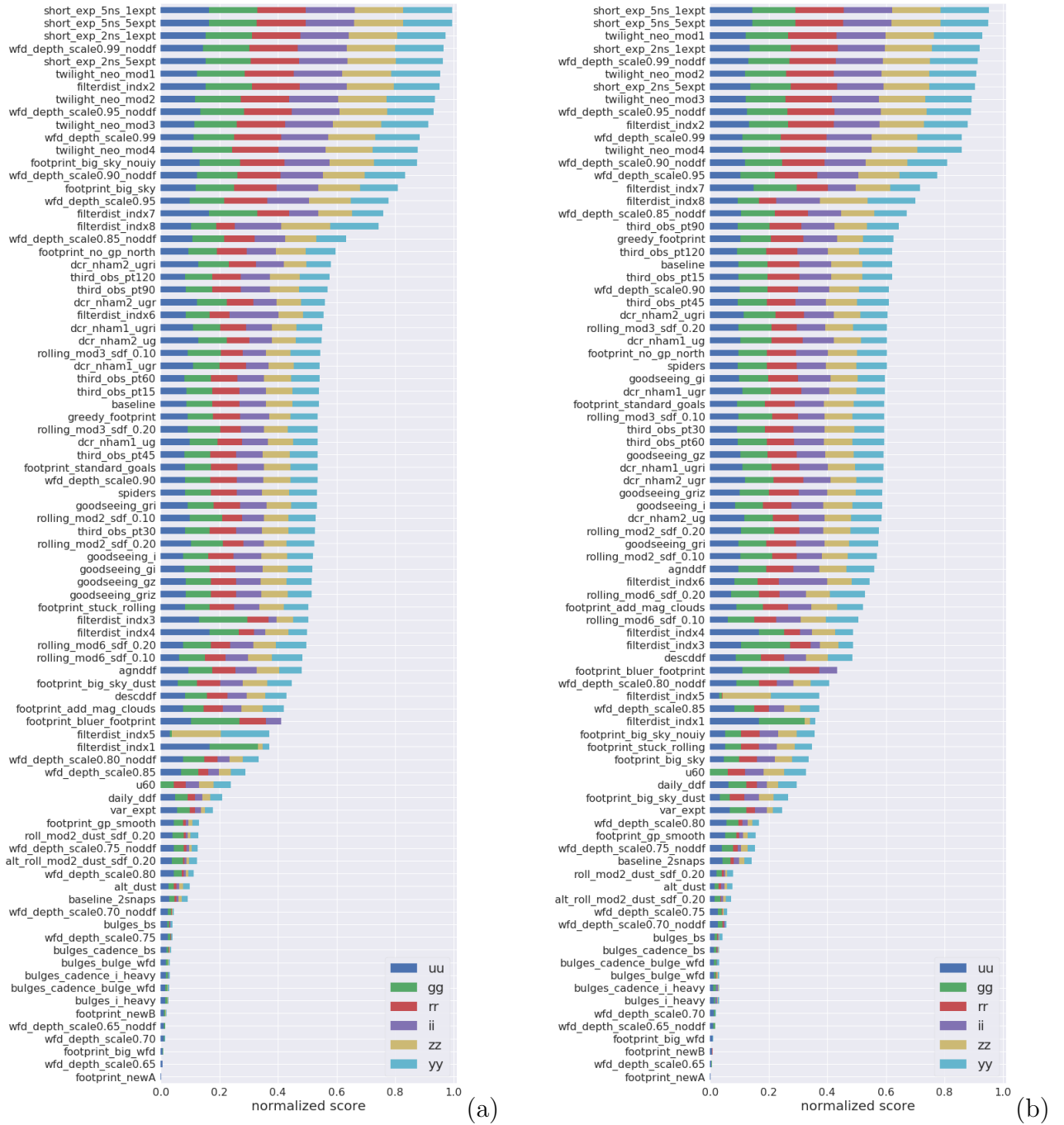


Figure 5.22: The FoM_{EG} (a) and FoM_{Gal} (b) figure of merit for all `OpSim` runs (for the WFD surveys) based on footprint coverage and star density with image pairs in the same filters (measuring color) as described in Section 5.5.3 (expression 5.17). Compared to the same figure for the same-filter pairs, we see *rolling* surveys performing well. Colors and symbols denote filter-combinations using the same conventions as in Figure 5.18.

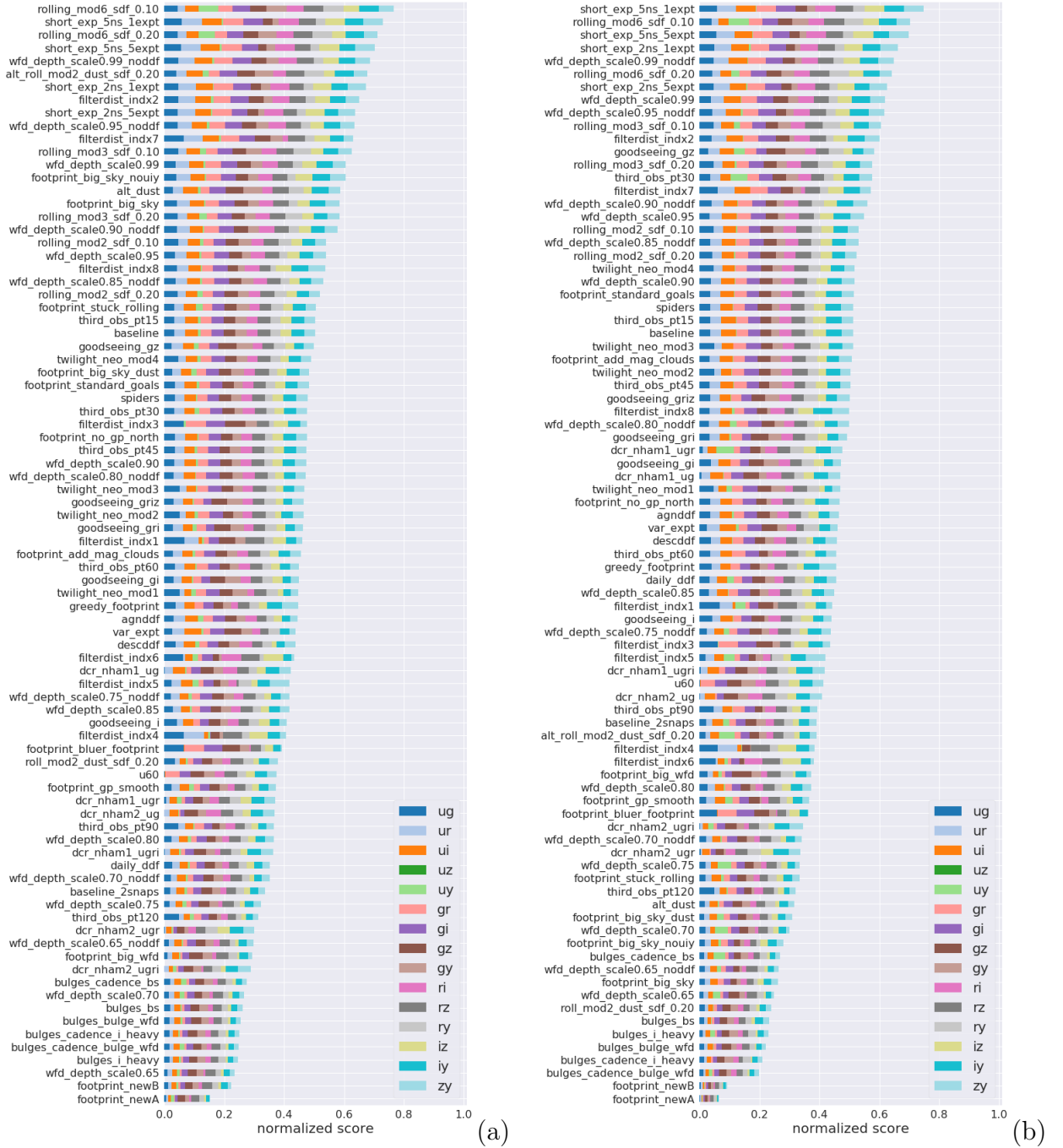


Figure 5.23: FoM_{EC} (a) and FoM_{Gal} (b) figure of merit for all OpSim runs (for the WFD surveys) based on footprint coverage and star density with image pairs in different filters (measuring lightcurve shape), as described in Section 5.5.3 (equation 5.17). Colors and symbols denote filter-combinations using the same conventions as in Figure 5.18. *Short* and *twilight* exposures performs highly, but note, that some of the images produced are shallower exploring a smaller volume (Fig. 5.19).

FoM (FoM_{EG} hereafter), which focuses on extragalactic science, we include footprint FoM , FoM_{Gal} , that scales with the field star density: FoM_{Gal} , which is the sum of each field that meets the requirements as described above, multiplied by the number of stars in that field.

For an `OpSim`, these $FoMs$ are therefore defined as:

$$\begin{aligned}
 p_i &= 1 \text{ if } N > N_{\text{median}} \text{ else } 0 \\
 FoM_{\text{EG}} &= \sum_i p_i, \\
 FoM_{\text{Gal}} &= \sum_i s_i p_i.
 \end{aligned} \tag{5.17}$$

where, as usual, i is an index that ranges over all observed fields; s_i is the star density (which is obtained from existing MAF functions) for the i th field; and p equals to 1 or 0 depending on whether the field meet the minimum requirement.

These $FoMs$ of merit for all 86 simulations are plotted in Figs. 5.22 and 5.23.

Some `OpSims` designed to cover a large footprint (*e.g.* `footprint_bigsky`), rank highly `OpSim`, however others perform even better even if they cover a smaller area. The advantage is given by the acquisition of image pairs in the short 1.5 hour time gap that was identified as optimal to measure color (Bianco et al., 2019). So we see again the short and rolling cadenced rising to the top.

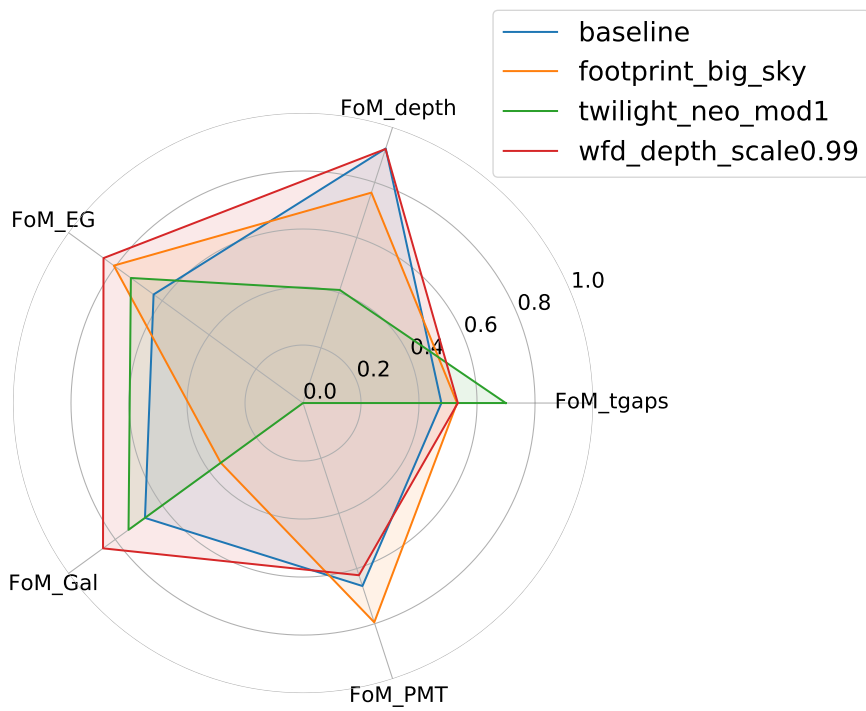


Figure 5.24: The radar plot for all the opsims, renormalized between $[0, 1]$.

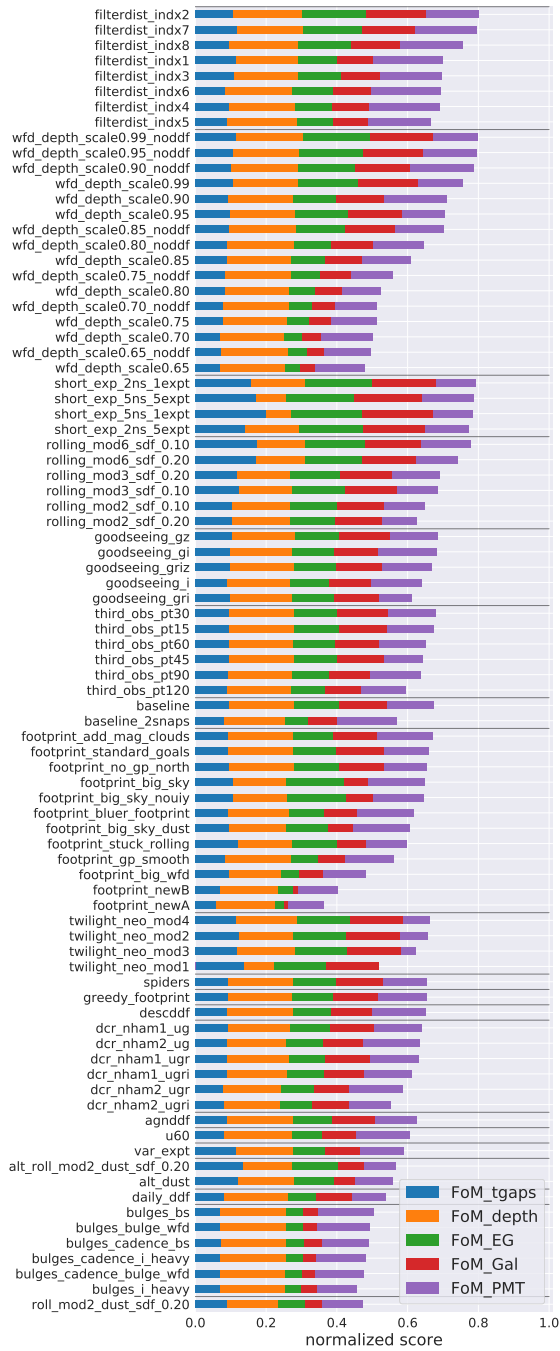


Figure 5.25: The bar plot with all *FoMs* divided by OpSim families.

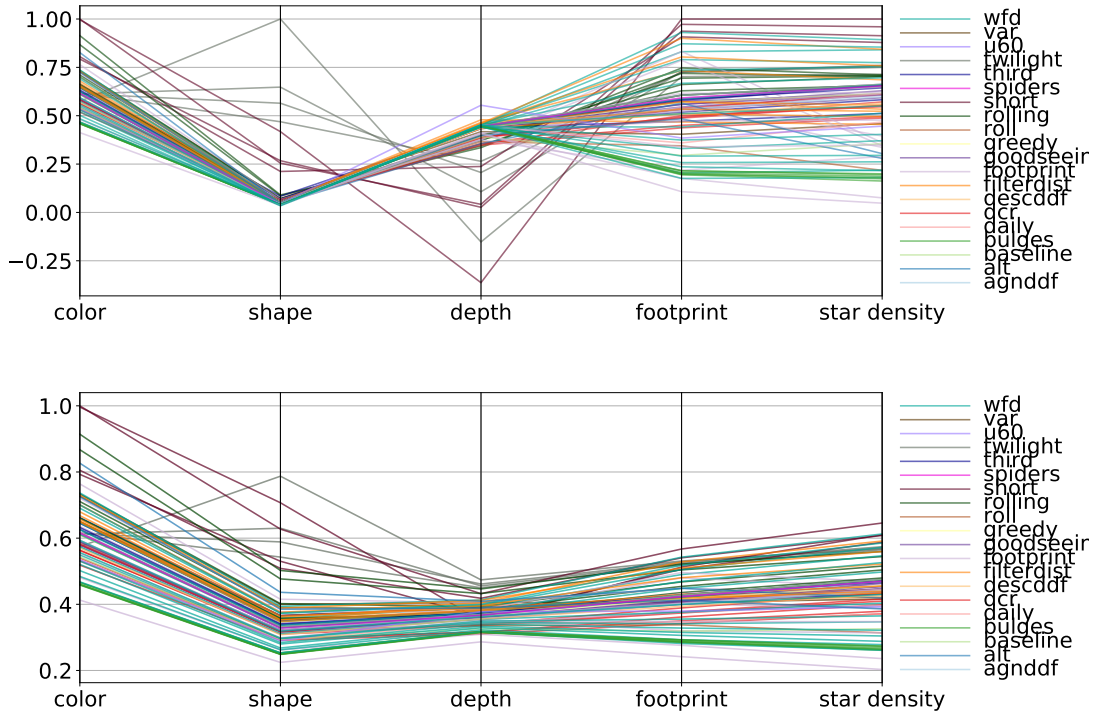


Figure 5.26: The result of the four FoM for all available OpSims. Different FoM s are shown along the x axis, for all OpSims. Different families of OpSims are shown in different colors. On the top each, FoM is shown individually, at the bottom their cumulative sum (normalized) is shown. The FoM “color”, which measures how regularly time gaps are collected within 1.5 hours, generally leads to smaller values.

5.6 Conclusion

In this chapter, a comprehensive description of the work developed within the Transient and Variable Stars anomalies group for SN rate simulations, and the detection of individual objects of interest in a multidimensional feature space that includes time coverage, filter coverage, and footprints have been illustrated. The simulations in Section 5.4 show that the baseline strategy is not the best one for the SN rate science case and we need further inspections of different cadence strategies to state what the best strategy is. Furthermore, the simulations have to be implemented:

- to consider other classification tools;

- to consider different dust extinction distributions;
- to build a more comprehensive set of templates to be referred to the wide SN taxonomy.

Finally we need to estimate the SN rate for each SN progenitor model.

The results of the simulations on true novelties show that LSST will give a great opportunity to improve the knowledge and the number of discoveries in the future, but the effect of the selected strategy for a given science case is a very important issue to be taken into account. Both exercises will be used together with all the simulations produced by the LSST community to infer the best observational strategy for the majority of the science cases.

Chapter 6

Transient studies in the multimessenger Astronomy era

Transient events are detectable in a wide range of wavelengths and the analysis of the photometric evolution at different wavelengths allows to shed light on the progenitor and explosion mechanism. Some transient events originate from a violent explosion caused by esoenenergetic phenomena. The radiation that we observe strictly depends on what kind of physical process undergoes (see figure 6.1). Nuclear interactions or dynamical effects due to the gravitational potential of very dense configurations can produce: electromagnetic radiation in the UV-Optical-IR (UVOIR) range of the spectrum; X-ray emission, related to friction of the plasma in a magnetic field that give rise to synchrotron radiation; γ - ray or neutrinos, related to relativistic processes such as Compton or inverse-Compton scatter, electron capture or fusion reactions. Finally, the strong gravitational potential from the collapse of a massive star or the merging of a binary system also generates another messenger, the Gravitational Waves emission. In a single explosive event, a few processes may enter into play, and more than one messenger can be generated and detected (see Apel et al., 2009; Scholberg, 2012, and reference therein). The simultaneous analysis of piece of information carried out by different messengers is fundamental to derive the physical properties of the explosion and to make relevant progress in time-domain Astronomy. In this chapter I present transient events that produce other messenger than electron-magnetic radiation, the methods and the results of the analysis of their electro-magnetic counterpart.

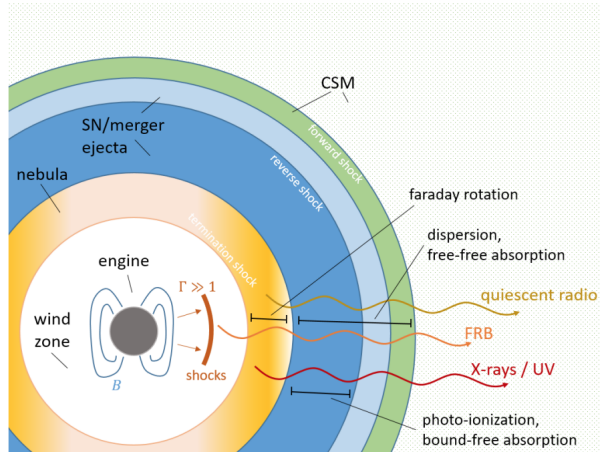


Figure 6.1: Schematic view of the CC SN explosion, the different stages of the explosion are characterized by different physical phenomena which can be detected at a wide range of wavelengths.

6.1 Gamma Ray Bursts

Gamma Ray Bursts (GRBs) are extremely energetic explosions that have been observed at cosmological distances. They are characterized by a collimated relativistic outflow, pushing through the interstellar medium powered by a central engine. This prompt phase is followed by a fading afterglow emission at longer wavelength (X-ray, UV, optical, IR, microwave and radio), powered in part by the expanding outflow, and in part by continuous energy injection from the central engine. Bursts peaking in the gamma-ray domain can last from ten milliseconds to several hours (Gendre et al., 2013; Kouveliotou et al., 1993). The observed distribution of GRB durations is bimodal, with peaks at $T_{90} \sim 20$ sec and $T_{90} \sim 0.2$ sec (Kouveliotou et al., 1993). These two classes of long (LGRBs) and short GRBs (SGRBs) show substantial evidences for different origins: SGRBs appear to originate from the merger of binary neutron stars while LGRBs originate from the explosion of massive stars. ¹ A different origin for SGRBs is supported by the detection of a SGRB in coincidence with the gravitational wave (GW 170817) detection (Abbott et al., 2017a) and the detection of underlying SN features in the light curves and

¹ T_{90} is defined as the time during which the cumulative counts increase from 5% to 95% above background, adding up to 90% of the total GRB counts.

spectra of the LGRB optical afterglows. SN features have been observed in the spectra of several LGRB afterglows. Examples of spectroscopic SN-GRB connection include SN1998/GRB980425 (Galama et al., 1998), SN2003dh/GRB030329 (Hjorth et al., 2003; Stanek et al., 2003), SN2003lw/GRB031203 (Malesani et al., 2004) and SN2006aj/GRB060218 (Campana et al., 2006; Masetti et al., 2006; Modjaz et al., 2006).

SNe connected with GRBs have very large explosion energy, mass production of ^{56}Ni and high ejecta velocity compared to normal Ib/c SNe (Deng et al., 2005; Iwamoto et al., 1998; Mazzali et al., 2006b; Nakamura et al., 2001).

Although emission of γ -rays at even higher energies (teraelectronvolt, TeV) by other radiation mechanisms in LGRBs are theoretically predicted, it has not been observed (Fan and Piran, 2008; Inoue et al., 2013; Mé et al., 2004; Nava, 2018) until the case of the GRB190114C, detected by the MAGIC collaboration. An extensive follow up was conducted of this event from the optic to the radio bands, to construct a comprehensive description of the transient.

6.2 MAGIC

The Major Atmospheric Gamma Imaging Cherenkov² (MAGIC) telescopes is a system of two telescopes with a diameter of 17 meters situated at the Roque de los Muchachos Observatory on La Palma, see figure 6.2). The first telescope was built in 2004 and operated for five years in a stand-alone mode. A second MAGIC telescope (MAGIC-II), at a distance of 85 m from the first one, started taking data in July 2009. Together, they integrate the MAGIC telescope stereoscopic system (Juan et al., 2009).

MAGIC belongs to a class of telescopes named Imaging Atmospheric Cherenkov Telescopes³ (IACT) that can detect very-high-energy gamma ray photons in the photon energy range of 50 GeV to 50 TeV. Ground-based γ -ray telescopes typically observe gamma energies above 200 - 300 GeV. Satellite-based detectors find γ -rays in the energy range from keV up to several GeV. There are four operating IACT

²Cherenkov radiation is electromagnetic radiation emitted when a charged particle (such as an electron) passes through a dielectric medium at a speed greater than the phase velocity (speed of propagation of a wave in a medium) of light in that medium.

³For a more detailed description, visit <http://magic.mppmu.mpg.de>

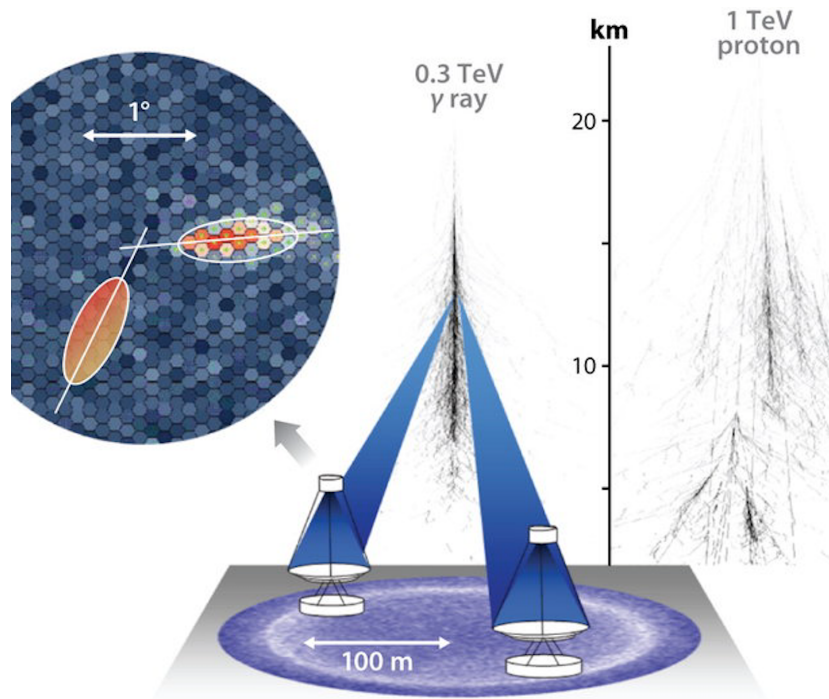


Figure 6.2: Top panel: the two Cherenkov telescopes of the MAGIC system. Bottom panel: a scheme of the detection, in the zoomed area the reconstruction of the detection is shown, where the intersection of the streams gives the localization of the source (credits Hinton and Hofmann, 2009).

systems: High Energy Stereoscopic System (H.E.S.S. Hofmann), MAGIC, First G-APD Cherenkov Telescope (FACT), and Very Energetic Radiation Imaging Telescope Array System (VERITAS). Set to be the largest telescope at the highest altitude in the world, the Major Atmospheric Cherenkov Experiment Telescope (MACE) is built at Hanle, Ladakh, India. The Cherenkov Telescope Array (CTA) is also under design. The CTA is the next-generation ground-based observatory for γ -ray astronomy. With more than 100 telescopes located in the northern and southern hemispheres, CTA will be the largest and most sensitive high-energy γ -ray observatory in the world.

An IACT works by imaging the very short flash of Cherenkov radiation generated by the cascade of relativistic charged particles produced when a very-high-energy gamma ray strikes the atmosphere. This shower of charged particles, known as an Extensive Air Shower (EAS), initiates at an altitude of 10- 20 km. The incoming gamma-ray photon undergoes pair production in the proximity of the nucleus of an atmospheric molecule. The electron-positron pairs produced have extremely high energy and immediately produce Bremsstrahlung or "Braking Radiation". This radiation produced is itself extremely energetic, with many of the photons undergoing further pair production. A cascade of charged particles ensues which, due to its extreme energy, produces a flash of Cherenkov radiation lasting between 5 and 20 ns. The total area on the ground illuminated by this flash corresponds to many hundreds square meters, this is why the effective area of IACT telescopes is so large.

The most effective mode of operation is to use an array of such telescopes, which can be typically located 70 to 120 meters apart. The primary advantage of this mode of operation is that the energy threshold (the peak sensitivity) of the telescope can be lowered as local muons produced by induced cosmic ray showers can be eliminated. This is because the narrow Cherenkov light cone produced by local muons will only be recorded by a single telescope. The shower reconstruction and background rejection offered by an array of telescopes provides an order of magnitude increase in sensitivity and improved angular and energy resolution as compared to a single telescope.

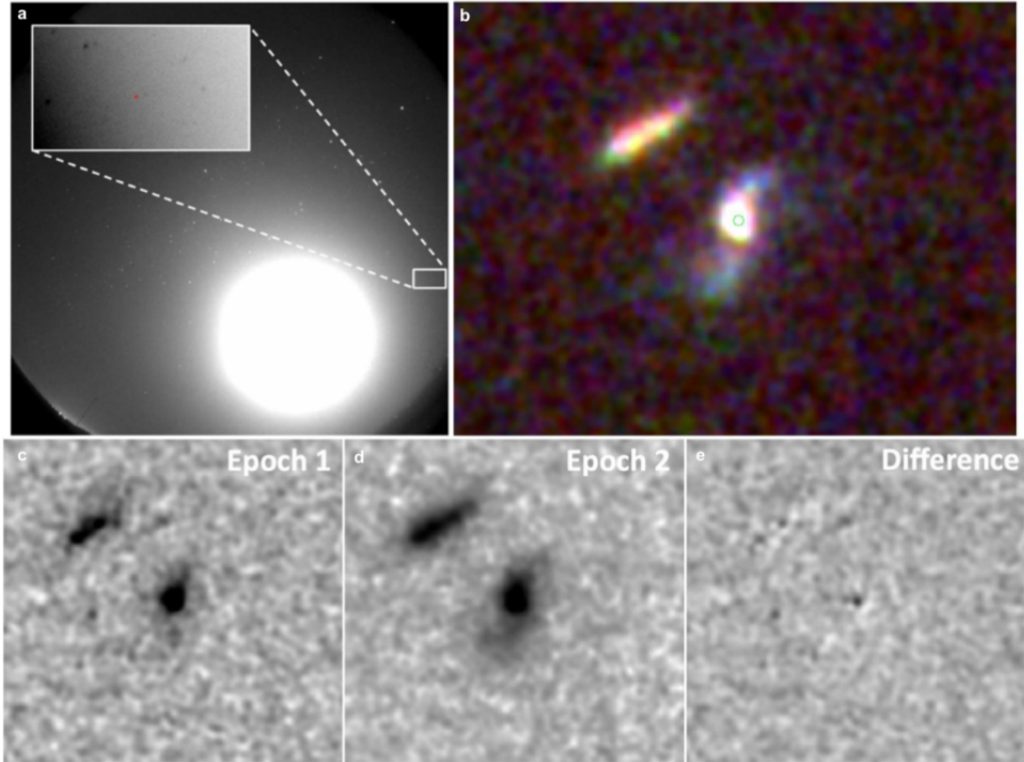


Figure 6.3: Localisation region of GRB190114C. In panel a, the CASANDRA-2 at the BOOTES-2 station all-sky image is shown, with no optical emission detected at the GRB 190114C location (red circle). Panel b displays a three-colour image of the host of GRB 190114C taken with the HST. The host galaxy is a spiral, and the green circle indicates the location of the transient close to the host nucleus. The image F.o.v. is 8 arcsec across, north is up and east to the left. Panels c, d and e show F850LP imaging of GRB 190114C taken with the HST. Two epochs are shown (images are 4" across), as well as the result of the difference image. A faint transient is visible close to the nucleus of the galaxy, later identified as the late-time afterglow of the burst. The image credits are MAGIC Collaboration et al. (2019).

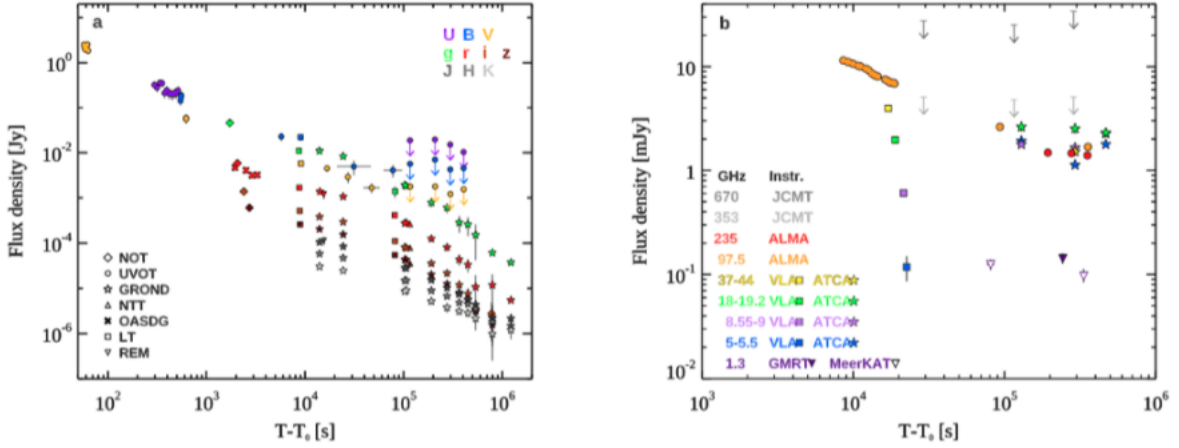


Figure 6.4: Afterglow light curve of GRB190114C, with the flux density as a function of time since the initial burst T_0 . In panel a, the NIR/Optical/UV bands are shown with the flux corrected for the extinction of the host galaxy and the Milky Way. In the panel b, the Radio and sub-mm observations from 1.3GHz to 670GHz, are shown.

6.3 GRB190114C

GRB190114C was detected in 2014 as one of the most energetic GRB (Gropp et al., GCN Circ. 23688), few of the detection images are shown in figure 6.3. For the first time, γ -rays in the energy range 0.2–1 TeV are observed with MAGIC from about 1 minute after the burst (MAGIC Collaboration et al., 2019). I observed on 2019-01-16 (i.e. about 1.32 days from the burst) the optical counterpart of this transient on behalf of the ePESSTO collaboration (extended Public ESO Spectroscopic Survey for Transient Objects Smartt et al., 2015) in the g, r, i, z gunn filters using the EFOSC2 instrument in imaging mode. Due to its distance ($D \sim 2.3 \text{ Gpc}$) it was possible a prompt follow up of the transient. Indeed, the signal was observed by several space missions (*Fermi*/GBM³¹, *Fermi*/LAT³², *Swift*/BAT³³, *Swift*/UVOT, *Super-AGILE*³⁴, *AGILE*/MCAL³⁴, *KONUS*/Wind³⁵, *INTEGRAL*/SPI-ACS³⁶, and *Insight*/HXMT, *HST*, *Swift*/XRT, *XMM-Newton* and *NuSTAR*) and ground based telescopes (MAGIC, GROND, GTC, LT, NTT, OASDG, NOT,

VLT, REM)⁴, collecting data in the spectral range from 8 keV to ~ 100 GeV. The overall light curve from γ -ray to optical and radio shows a complex temporal structure with several emission peaks with a total duration of ~ 25 s and total radiated energy of $E_{\gamma,iso} = (2.5 \pm 0.1) \times 10^{53}$ ergs (see figure 6.4).

The observation of TeV emission reveals a new emission component in the afterglow of a GRB, whose power is comparable to that of the synchrotron component. The similarity of the radiated power and temporal decay slopes in the TeV and X-ray bands suggests that this component is intimately related to the electron synchrotron emission and points to processes such as inverse Compton radiation as the mechanism of the TeV emission, while processes such as synchrotron emission by ultrahigh-energy protons are disfavoured due to their low radiative efficiency (MAGIC Collaboration et al., 2019). The discovery of an energetically important emission component beyond electron synchrotron emission that possibly be common in GRB afterglows, offers important new insights into the physics of GRBs (MAGIC Collaboration, 2019).

6.4 Gravitational Waves

First detection of a Gravitational Wave (GW) was on 2015 September 14th, on that date another window on the understanding of the transient phenomena was opened. Through the GWs observations independent and accurate measurement of mass and distance for GW sources become possible. In 1916, the year after the final formulation of the field equations of General Relativity (GR), Albert Einstein predicted the existence of GWs. The underline assumption of the GR is that mass and energy produce a curvature of the four-dimensional space-time, in response of this change of the geometry the matter moves. GWs interact very weakly with the matter and are intrinsically non linear, because the wave energy density itself generates addi-

⁴Gamma-ray burst Optical/NIR Detector (GROND) is a telescope at La Silla Observatory in the southern part of the Atacama desert; LT is a 2m robotic telescope in Tenerife, Spain; GTC is a 10m telescope in La Palma in Canaries Island; NTT is a telescope with a diameter ~ 4 m equipped with a spectrograph and a NIR camera in La Silla Observatory; OASDG a 0.5 remote telescope of the Osservatorio Astronomico "S. DiGiacomo" , located in Agerola (Italy); NOT an astronomical system of 4 m telescopes located at the Roque de los Muchachos Observatory, La Palma in the Canary Islands; VLT is a 8.2 m telescope operated by the European Southern Observatory on Cerro Paranal; REM is a fully automatic, 60 cm aperture telescope located at ESO's La Silla Observatory.

tional curvature of space-time, beside the very weak intensity with respect to the Electromagnetic waves (EWs) counterpart. This means that GWs can propagate practically unhampered from their source to detectors on the Earth. Finally, the frequency band, f , of relevance to gravitational-wave astronomy is far different from the band of relevance to electromagnetic astronomy: $10^{-18}Hz < f_{GW} < 10^4Hz$, whereas $10^7Hz < f_{EM} < 10^{24}Hz$. The typical model for the binaries GW sources can be divided in three phases:

1. Inspiral. This phase, the bodies are widely separated, and the system's evolution is adiabatic - the time scale τ_{RR} when radiation reaction changes the binary's orbit is greater than the orbital period. Thus, the binary spends many orbital cycles near some particular point in its evolutionary phase space.
2. Merger. As the bodies in the binary spiral close together, the radiation reaction timescale gets progressively smaller, decreasing at a rate faster than the orbital period. Eventually, the radiation reaction timescale becomes roughly equal to the orbital period, and the evolution of the system cannot be described in an adiabatic manner. At roughly the same time, the orbit of the binary system may become dynamically unstable, so that the compact bodies will violently plunge and collide, eventually settling down to some quiescent final state.
3. Ringdown waves. If the final state of the system contains a single black hole, then the tail end of the merger epoch will be dominated by ringdown waves. This is certainly be the case in the merger of binary black holes, and it is quite likely to be the case in the merger of binary neutron stars as well.

Binary systems are not the only one that can produce GWs. Indeed, theoretically it is plausible to detect GW signals from stars which end their evolution as CC SNe. During a CC event, a number of processes are ongoing: fluid instabilities in the proto-neutron star, neutrino-driven convection beneath the SN shock wave, the standing accretion shock instability (SASI), deceleration in an aspherical shock, and an aspherical neutrino emission. As consequence, no viable CC SNe explosion is spherical. Hence, due to time-changing quadrupolar motions, CC SNe are classic sources of gravitational waves (GWs), with most of the gravitational-wave energy ($\approx 10^8 M.c^2$) coming out at 10^{-2} to 10^{-3} Hz. The same multi-step evolution of the

GW signal can be considered also for the GW from CC SNe, but assuming different physical process (Melson et al., 2015; Morozova et al., 2018; Murphy et al., 2009):

1. the prompt convection signal: an initial and relatively weak signal that starts at bounce and ends between 50 and 75 ms after bounce;
2. the quiescent phase: a quiescent stage that immediately follows the prompt signal, and ends sometimes between 125 ms and 175 ms after bounce;
3. the neutrino convection/SASI driven phase: a strong signal, which follows the quiescent stage and is the most energetic part of the GW signal. This stage ends sometimes between 350 ms and 450 ms after bounce;
4. the explosion phase: a tail, which starts before the end of the strong signal, at about 300 ms after bounce.

These models are the baseline for the template database to detect and analyse the observations. *"On August 17, 2017 at 12 : 41 : 04 UTC the Advanced LIGO and Advanced Virgo gravitational -wave detectors made their first observation of a binary neutron star inspiral"* (see p.1 Abbott et al., 2017a). The incipit of the abstract in Abbott et al. (2017a) marked the beginning of the multi-messenger astronomy. On the one hand, this was another confirmation of the Einstein's General Relativity prediction, on the other hand this new observable signal finally allowed to add to the EW information train the GW's ones on the analysis of transient events. With reference to figure 6.5 is used O1, O2, O3, O4 and O5, for the different observational runs. Data for O3, measured using the Advanced LIGO and Virgo detectors, were collected from April to October of 2019. During this time, 39 new mergers were observed: one binary neutron star, 36 confident binary black holes, and two possible neutron star-black hole candidates. Including the 11 mergers from Gravitational Wave Transient Catalog 1 (GWTC-1) (Abbott et al., 2019d), that makes 50 detected events in GWTC-2 (Abbott et al., 2020), all with a false-alarm-rate of less than two per year. Remarkable cases are:

- GW150914: the first ever detection of gravitational waves from the merger of two black holes, more than a billion light years away;

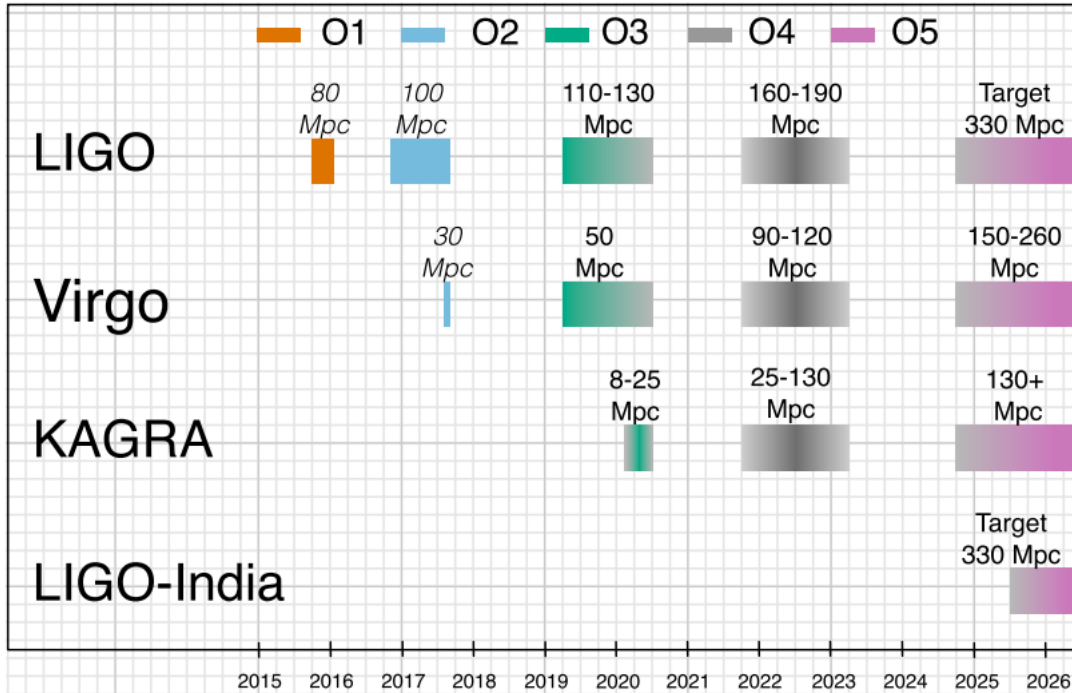


Figure 6.5: The planned sensitivity evolution and observing runs of the aLIGO, AdV and KAGRA detectors over the coming years. The colored bars show the observing runs, with achieved sensitivities in O1, O2 and O3, and the expected sensitivities for future runs. The O4 observing run is projected not to begin before June 2022, due to both key procurement delays and COVID-related delays.

- GW170814: the first GW signal measured by the three-detector network, also from a binary black hole (BBH) merger;
- GW170817: the first GW signal measured from a binary neutron star (BNS) merger — and also the first event observed in light, by dozens of telescopes across the entire electromagnetic spectrum.
- GW190412: the first BBH with definitively asymmetric component masses, which also shows evidence for higher harmonics
- GW190425: the second gravitational-wave event consistent with a BNS
- GW190426: a low-mass event consistent with either an NSBH or BBH
- GW190521: a BBH with total mass over 150 times the mass of the Sun
- GW190814: a highly asymmetric system of ambiguous nature, corresponding to the merger of a 23 solar mass black hole with a 2.6 solar mass compact object, making the latter either the lightest black hole or heaviest neutron star observed in a compact binary
- GW190924: likely the lowest-mass BBH, with both black holes exceeding 3 solar masses

Using the observation of GW170817, a BNS event rate of $110 - 3840 \text{ Gpc}^{-3}\text{year}^{-1}$ and $9.7 - 101 \text{ Gpc}^{-3}\text{year}^{-1}$ for BBH (Abbott et al., 2019a) were estimates. This rate is obtained by combining the results over different search pipelines and two different astrophysical populations, which assume a uniform mass distribution in the $1M_{\odot} - 2M_{\odot}$ range for the NSs, as described in Abbott et al. (2020). From the observations of BBHs during O1 and O2, it was inferred that the rate of these systems is $53.2^{+55.8}_{-28.2} \text{ Gpc}^{-3}\text{year}^{-1}$ (Abbott et al., 2019b). This rate is the result from the outcome of different search pipelines and two astrophysical populations:

1. a population of BBHs with primary mass following a power law distribution with $\alpha = 1.3$ index;
2. a population of BBHs with primary mass distribution uniform in the log.

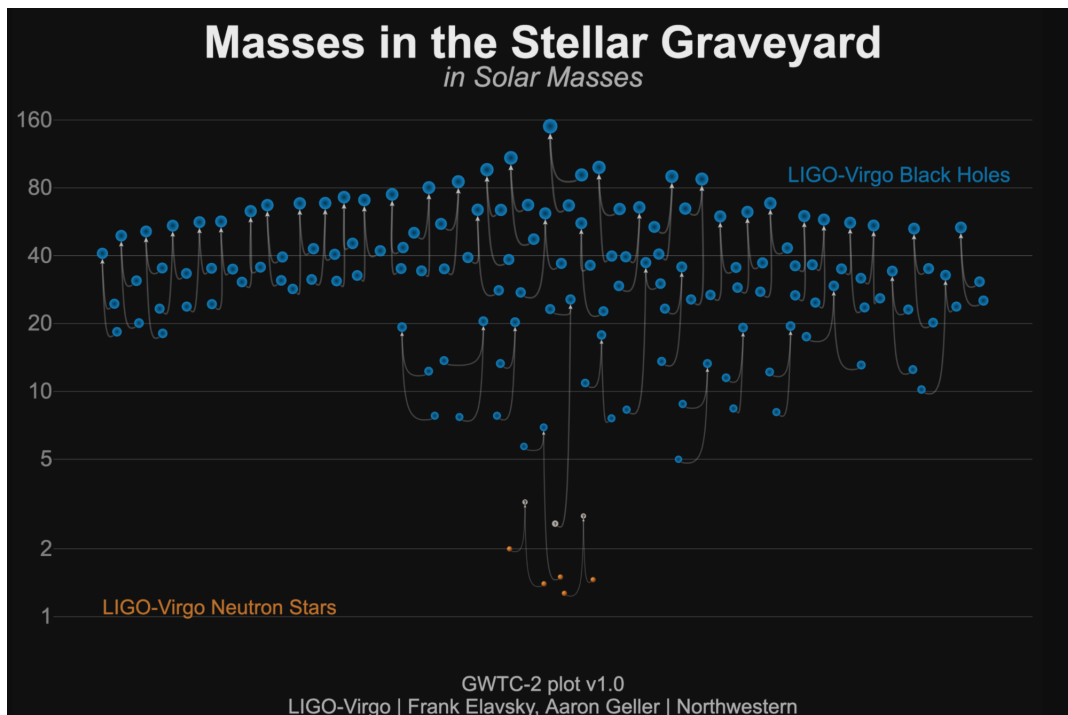


Figure 6.6: Masses of the binary component objects for the merger events observed in O1, O2 and O3a that were used to infer population properties in this paper. Selected individual events have been highlighted (Credit: LIGO-Virgo Collaboration / IGFAE / Thomas Dent).

Both populations were constrained with a mass cut off (see figure 6.6) at a lower mass of $5M_{\odot}$ and at a maximum mass of $50M_{\odot}$ (Abbott et al., 2019a,b). Using a power law mass distribution with flexible values for the power law index, and the minimum and maximum masses (Abbott et al., 2019a, model B in), the BBH rate is estimated to be $25 - 109 \text{ Gpc}^{-3}\text{year}^{-1}$. The non-detection of NSBHs in O1 and O2 allows us to place a 90% upper limit of the merger rate of $610 \text{ Gpc}^{-3}\text{year}^{-1}$ (Abbott et al., 2019b).

6.5 LIGO/VIRGO interferometers

The LIGO/VIRGO Collaboration is a scientific collaboration of international physics institutes and research groups dedicated to the detection and analysis of GWs. LIGO and VIRGO are two modified Michelson-Morley interferometers: VIRGO has two arms that are three kilometers long and located in Santo Stefano a Macerata, near the city of Pisa, Italy; LIGO uses three specialized Michelson interferometers, located at two sites: an observatory on the Hanford site in Washington houses two interferometers, the 4 km-long H1 and 2 km-long H2 detectors; and an observatory in Livingston Parish, Louisiana, houses the 4 km-long L1 detector (see figure 6.7).

Both LIGO and VIRGO are powered by recycling Fabry-Perot cavity. This is a improvement of the original Michelson interferometer.

Beside the arms length the LIGO and VIRGO structures are very similar (see figure 6.8). They have two orthogonal arms divided by a beam splitter, which is a semi transparent mirror. The two arms are provided by a mirror to compose the Fabry-Perot cavity; this allows to expand the light path through the arms to let the interferometer to be more sensible to the GW signal. The increasing of the path length introduces a light loss in the system which is used to grow the power of the laser with a recycling mirrors' system. This light is sent back to the instrument in phase with the incident beam, thus increasing the light power that can reach several tens of kilowatt in the Fabry-Perot resonant cavities. The LIGO and VIRGO system works as a light trap; if no GW reaches the Earth no diffraction image appears on the detector, because the relative distance of the detectors' arms are such that the light travelling through them disruptive interference. When a GW interact with the Earth it changes the geometry of the space-time, changing the relative distance of the arms,



Figure 6.7: Areal view of LIGO facility in Washington (top image), LIGO facility in Livingston (central image) and VIRGO (bottom image) interferometers. Credits: LIGO and VIRGO collaborations.

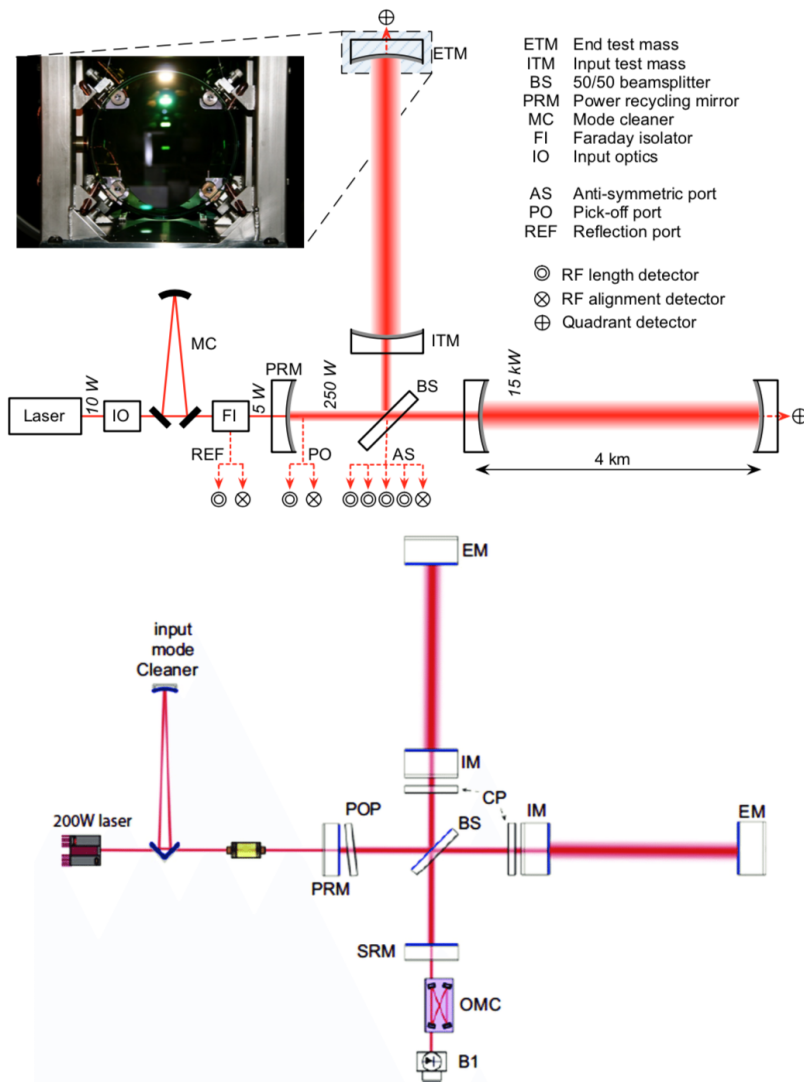


Figure 6.8: A schematic view of the two interferometers system (LIGO at top figure, VIRGO at the bottom). The IO block for LIGO includes laser frequency and amplitude stabilization, and electro-optic phase modulators. The power recycling cavity is formed between the PRM and the two ITMs, and contains the BS. The inset photo shows an input test mass mirror in its pendulum suspension. The near face has a highly reflective coating for the infrared laser light, but transmits visible light. For VIRGO there is a very similar configuration with the recycling mirror between the beamsplitter, and the laser and the cavities with the same configuration as LIGO's. Credits: LIGO and VIRGO collaborations.

thus a diffraction image appears because of the GW.

The nominal VIRGO sensitivity ranges from 10 to 10000 Hz, as for LIGO, and allows the detection of gravitational signal from the coalescence of binary systems (stars or black holes).

The Fabry-Perot cavity and the recycling mirrors are the essential ingredients for the high sensitivity of the instruments, to reach those results the total length of each cavity must be held to an integer multiple of the laser wavelength, so that newly introduced carrier light interferes constructively with light from previous round trips. With this scheme, the light inside the cavities are in resonance. Another important condition is that the Michelson phase must be controlled to ensure that the photodiode does not intercept any light from the instrument, implying for the LIGO setting that the AS port remains on the dark fringe.

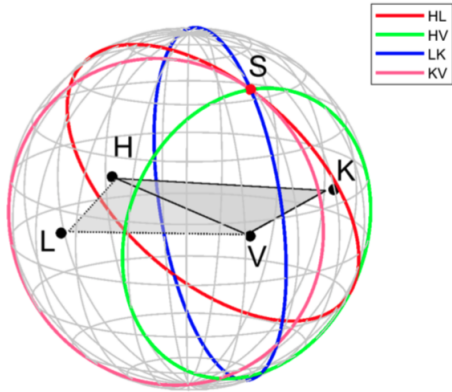
The instruments, as described, can detect signals from a well-defined range in distance. These signals can be produced by different sources, some are noise from the Earth activities (such as earthquakes, low seismic activities, etc...), others are related to the background noise or to actual GW candidates.

For unmodeled short-duration (≤ 1 s) signals or bursts, an approximate sensitive luminosity distance is evaluated as the combination of the contribution of the total energy E_{GW} emitted by GWs, the central frequency f_0 of the burst, the detector noise power spectral density $S(f_0)$, and the single-detector SNR threshold ρ_{det} (Sutton, 2013):

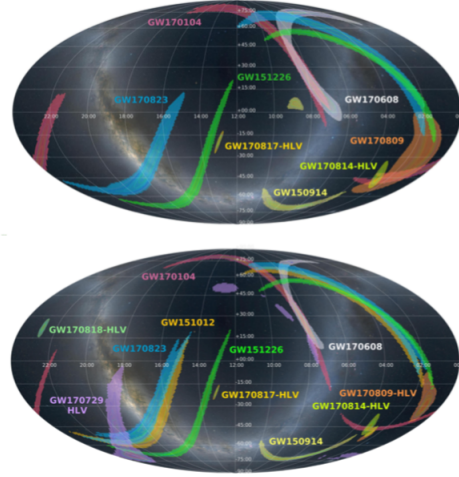
$$D \approx \left(\frac{G}{2\pi^2 c^3} \frac{E_{GW}}{S(f_0) f_0^2 \rho_{det}^2} \right)^{\frac{1}{2}},$$

following the detection, a posterior probability distribution of the distance and position is estimated through a bayesian framework. The localization make use of the triangulation of the time delay between the different sites of the instruments, this set the localization scale. The effective single-time visit accuracy is $\sigma_t = (2\pi\rho\sigma_f)^{-1}$, where ρ is the SNR of the instrument and σ_f is the effective bandwidth of the signal in the detector (typical value for $\sigma_f \approx 100$ Hz and $\sigma_t \approx 10^{-4}$ s).

The simple model for the localization does not take into account some ancillary informations carried by the signal (such as the phase and the amplitude across the detector network, the instrumental calibration accuracy), the actual source Sky location of the Compact Binary Coalescence (CBC) signal is evaluated by introducing the



(a) Source localization by timing triangulation for the aLIGO-AdV-KAGRA network (KAGRA is a Japanese interferometer that started to work in cooperation with LIGO and VIRGO from February 2020). The locations of the four detectors are indicated by black dots, with LIGO Hanford labeled H, LIGO Livingston as L, Virgo as V and KAGRA as K. The locus of constant time delay (with associated timing uncertainty) between two detectors forms an annulus on the sky concentric about the baseline between the two sites (labeled by the two detectors). For clarity we omit the HK and LV combinations. For four or more detectors there is a unique intersection region (Figure from Chatterji et al. (2006)).



(b) The image shows the localization region for the observed GW confidently detected in the operations O1 and O2; the top panel shows the initial sky location released in low-latency to the astronomers (Abbott et al., 2016), while the bottom panel shows the refined sky location including updated calibration and final choice of waveform models (Abbott et al., 2019c)

Figure 6.9

requirement of phase and amplitude consistency between detectors (Fairhurst, 2018; Grover et al., 2014). A Bayesian inference algorithm constructs posterior probability distributions for the system parameters (such as location, mass, distance, orientation, etc.) by matching GW models to the detector strain of three detectors. The time delays restrict the source to two sky regions which are mirror images with respect to the plane passing through the three sites. Requiring consistent amplitudes and phase in all the detectors usually eliminates one of these regions (Fairhurst, 2018). This typically yields regions with areas of several tens to hundreds of square degrees (see Fig. 6.10).

Upgrading the existing instruments, will enable LIGO and Virgo to increase their range with respect to the aLIGO and AdV detector design sensitivities (figure 6.5). The upgrade to the aLIGO instruments will include higher power, frequency-dependent squeezing and, crucially, new test masses with improved coating thermal noise. Facilities modifications to incorporate the filter cavity required for frequency dependent squeezing will begin after O3. The full configuration, adding improved test masses and balanced homodyne readout, is expected to be in place for O5. The AdV upgrade will occur in two phases. Phase 1 installation will begin after O3 and will involve adding signal recycling, frequency-dependent squeezing, higher input laser power (to 50 W from 20 W currently) and cancellation of Newtonian noise (Abbott et al., 2020).

Providing a prompt localization of the source increase the chance to detect an electromagnetic counterpart. GW170817 was associated to a SGRB and kilonova emission. In the next paragraph is described the discovery and observational strategy and follow up of the optical counterpart.

6.6 GW170817

The signal from GW170817 was initially found by the LIGO-Hanford detector; the localization algorithm pointed the source in a region of 31 deg^2 with a combined SNR of 32.4 (Abbott et al., 2017b). The region of interest for the source was further limited using the VIRGO data to an area of 28 deg^2 . Nearly simultaneously, the Fermi and INTEGRAL telescopes detected a γ -ray transient, GRB 170817A. However, the Fermi/INTEGRAL localization area was larger than the LIGO/Virgo localization

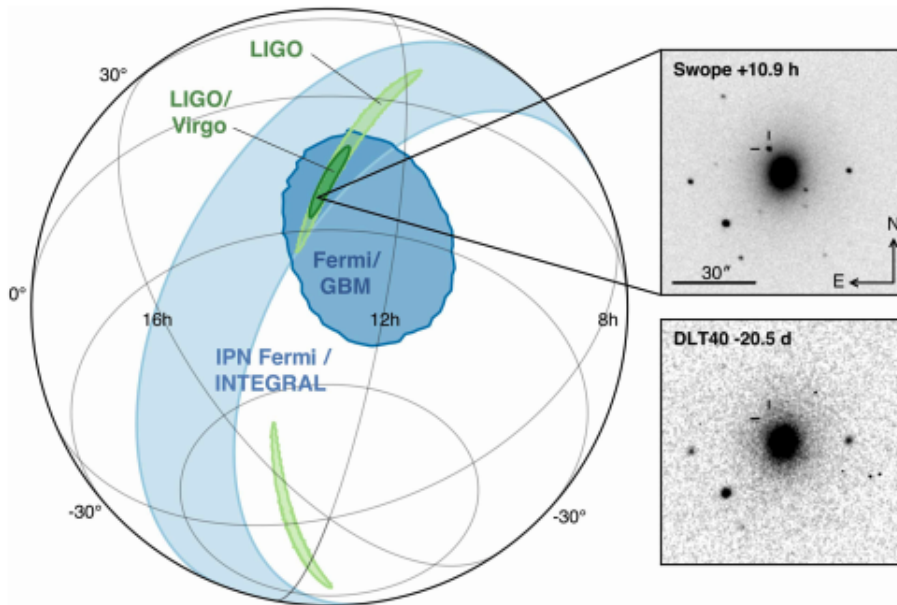


Figure 6.10: Localization of the gravitational-wave, gamma-ray, and optical signals from GW170817. The left panel shows an orthographic projection of the 90% credible regions from LIGO (190 deg^2 ; light green), the initial LIGO-Virgo localization (31 deg^2 ; dark green), IPN triangulation from the time delay between Fermi and INTEGRAL (lightblue), and Fermi-GBM (dark blue). The inset shows the location of the apparent host galaxy NGC 4993 in the Swope optical discovery image at 10.9 hr after the merger (top right) and the DLT40 pre-discovery image from 20.5 days prior to merger (bottom right). The reticle marks the position of the transient in both images.

area. The γ -ray emission from a binary neutron star (BNS) merger progenitor is predicted to happen in a few seconds after the merger. The EM signal and the GW are expected to travel at the same velocity.

The progenitor of the GW was expected to be a NS-NS binary and the presence of a SGRB few minute later the GW event was a huge hint for the hypothesis. Models describe that NS-NS merger ejects small amount of mass with low electron fraction at a very high velocity, and the ejecta undergoes rapid neutron capture (r-process) nucleosynthesis which forms radioactive elements. They release energy as they decay, powering electromagnetic transient called kilonova, visible in the optical and NIR and radio bands.

The limited area (figure 6.10) for the position of the source allowed by the combination of LIGO-VIRGO data, triggered a world-wide follow up campaign for the search of the optical counterpart of the GW source with different facilities (among all: the European Southern Observatory,ESO, the Las Cumbres Observatory,LCO, and the Cerro Tololo Inter-American Observatory in Chile, the Siding Spring Observatory in Australia, the South African Astronomical Observatory in Cape Town, the Lick Observatory in California and the Swope Telescope in Las Campanas).

A transient designated AT 2017gfo (originally, SSS 17a) was found, with the Swope telescope 11 hours after the gravitational wave signal, in the galaxy NGC 4993. Spectroscopic observations were performed by McCully et al. (2017) roughly after 12 hours, showing a blue and featureless continuum. This supported the idea that AT 2017gfo was discovered young, although a blue and featureless continuum is also common to young SNe II and GRB afterglows. The fast cooling (and hence the small ejected mass) became evident as more spectra were collected. Over the subsequent two weeks, a network of ground-based telescopes and space observatories followed the initial detections, from the UVOIR wavelengths. These observations carefully monitored the SED, revealing that this exceptional electromagnetic counterpart was a kilonova (see figure 6.12). These observation firmly connected kilonovae with the SGRBs and BNS mergers, providing evidence supporting the idea that kilonovae result from the radioactive decay of the heavy elements formed by neutron capture during a BNS merger.

The ePESSTO collaboration observed the optical transient ~ 35 hours after GW170817, reporting a featureless spectrum, with a much redder continuum than that observed

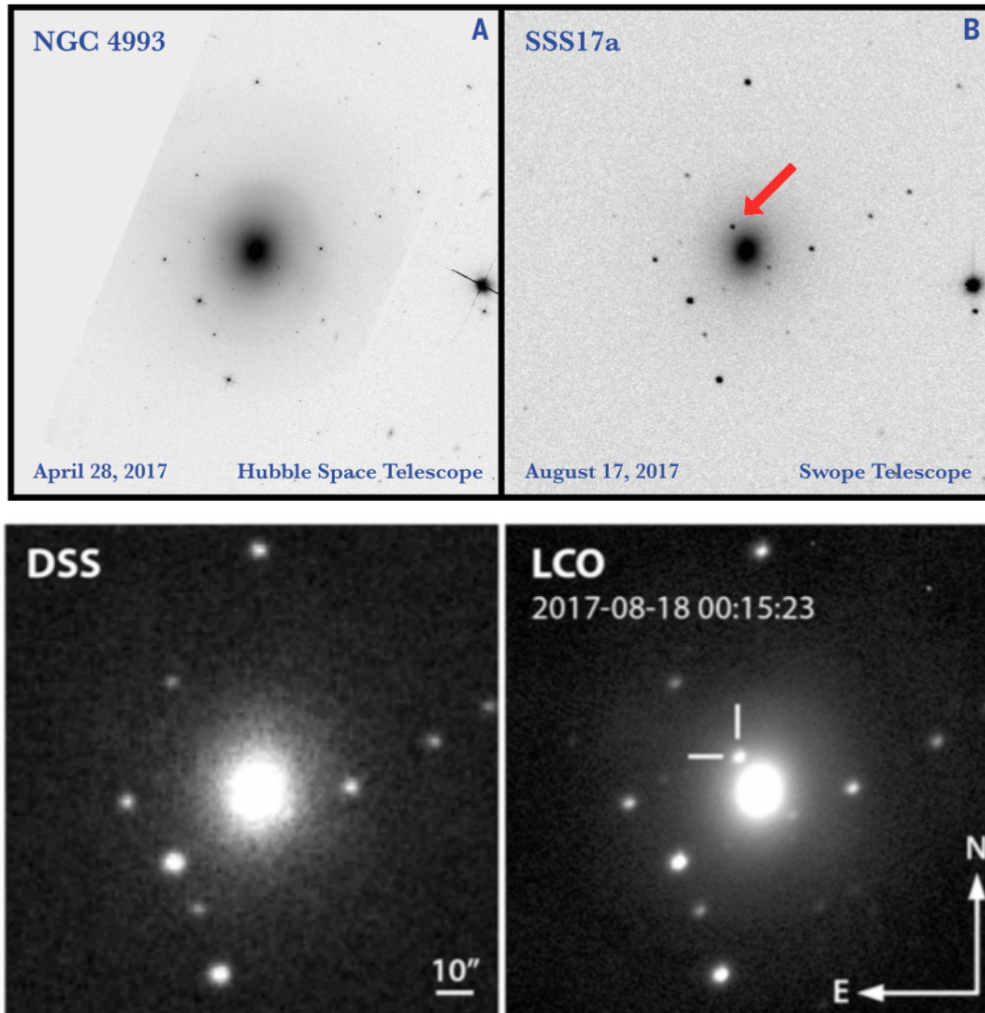
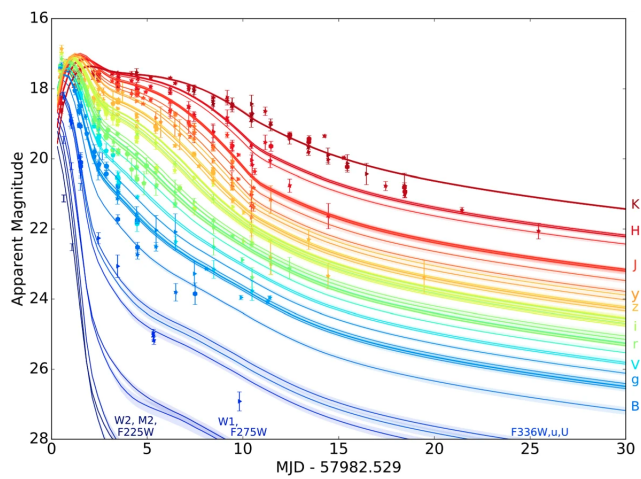
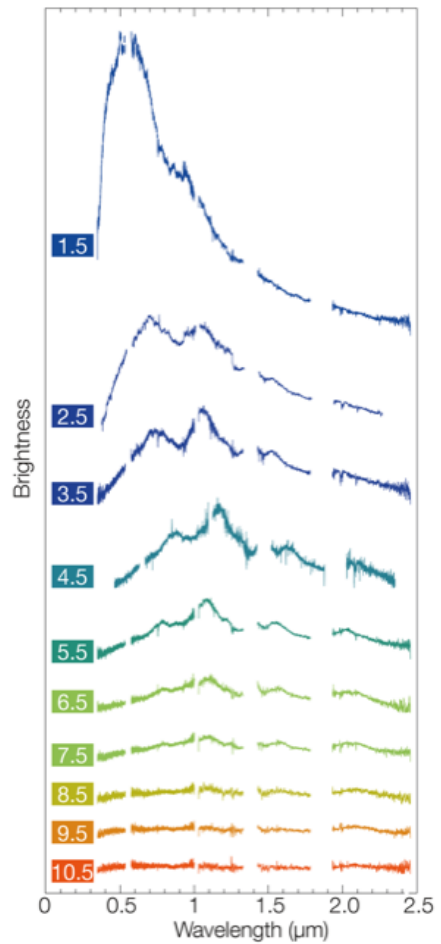


Figure 6.11: The NG4993 galaxy in V band (top right) from the Hubble Space (HST) and w band (bottom right) from the LCO. Both the bands reveal the presence of a transient in a location comparable to the site of the GW.



(a) UVOIR light curves of AT2017gfo, from Metzger (2019)



(b) Evolution of the spectrum of AT2017gfo. Credit: Eso/E. Pian et al./S. Smartt e ePessto

Figure 6.12

in SN spectra at similar phases (Lyman et al., 2017). A black-body fit to the spectrum revealed a temperature of $\sim 5200K$. Considering a spherically symmetric explosion and a black body emission, the radius of the kilonova should have expanded from the radius of a neutron star (few tenth 10^5 cm) to $\sim 7.3 \times 10^{14}$ cm. Following the success of the GW170817 follow up campaign, a large fraction of the EW/GW community in member states of the European Southern Observatory have formed the Electromagnetic counterparts of gravitational wave sources at the Very Large Telescope (ENGRAVE)⁵ international collaboration to exploit ESO powerful resources during the future LIGO-Virgo observing runs.

6.7 GW190814

On 2019 August 14, a GW signal was detected by the LIGO-VIRGO collaboration. The analysis of the GW signal constrained the progenitor mass of the binary system, to be $23M_{\odot}$ for the heavier compact object in the system a $22.2 - 24.3M_{\odot}$ black hole and a compact object with a mass of $2.50 - 2.67M_{\odot}$ (all measurements quoted at the 90% credible level Abbott et al., 2020), consistent with the population of black holes observed by LIGO and Virgo so far (see figure 6.6). The asymmetry of the larger and smaller masses helps to measure the source properties more precisely. The greater the asymmetry the stronger is the signature of higher “harmonics” of the fundamental frequency in the gravitational wave signal. As in the case of the unequal-mass black hole merger GW190412 (The LIGO Scientific Collaboration et al., 2020), the ambiguity between the distance and the inclination of the system is partially broken by the extra information contained in the higher harmonics. This is the best localized source up to now, the localization area was limited to 5 deg^2 at 50% confidence and 23 deg^2 at 90% (see figure 6.16). The source distance was inferred by the GW observation to be $D \approx 267 \pm 52$ Mpc. No γ -ray or neutrino signal related to the event were detected. Compact objects like neutron stars and black holes are expected to be spinning. Although their spins do not affect the gravitational wave signal as strongly as their masses, and hence are more difficult to measure, GW190814 was a long signal. It was also possible to determine that the system was likely not precessing. Because the very limited region of interest for the event the follow up effort

⁵<http://www.engrave-eso.org/>

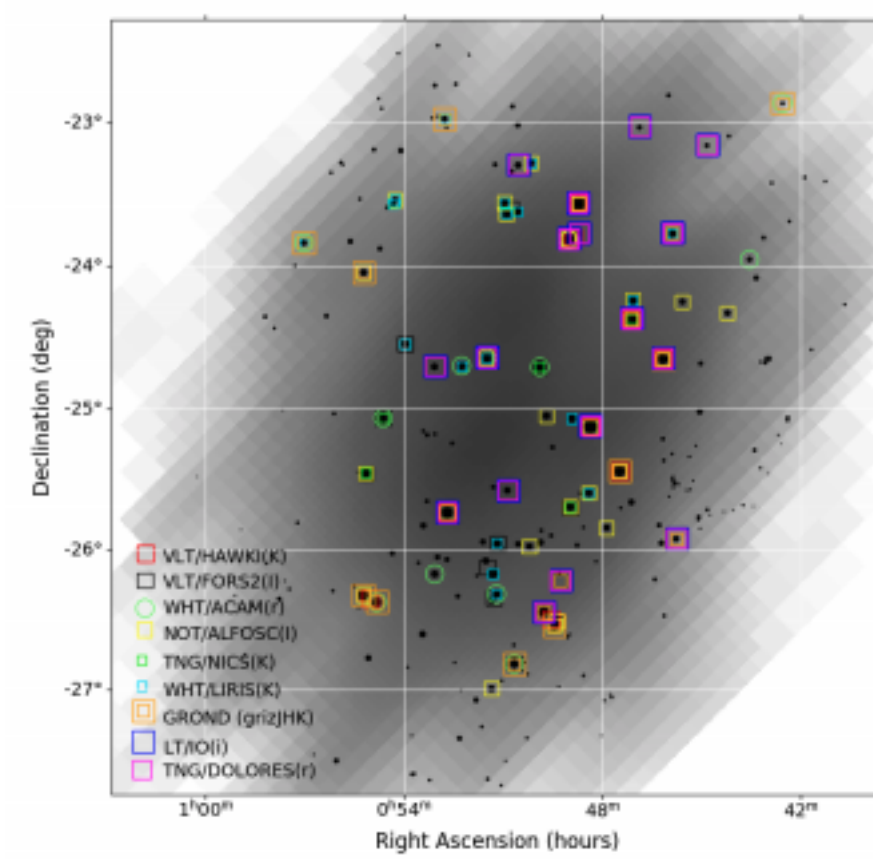


Figure 6.13: The LVC skymap of GW190814 in greyscale, with galaxies over-plotted (black dots) selected through HOGWARTS. Only the higher probability northern region of the skymap is included, since the southern region was not followed up by ENGRAVE. The size of the symbol of each galaxy (i.e. the black dots) is proportional to the probability of hosting the GW event.

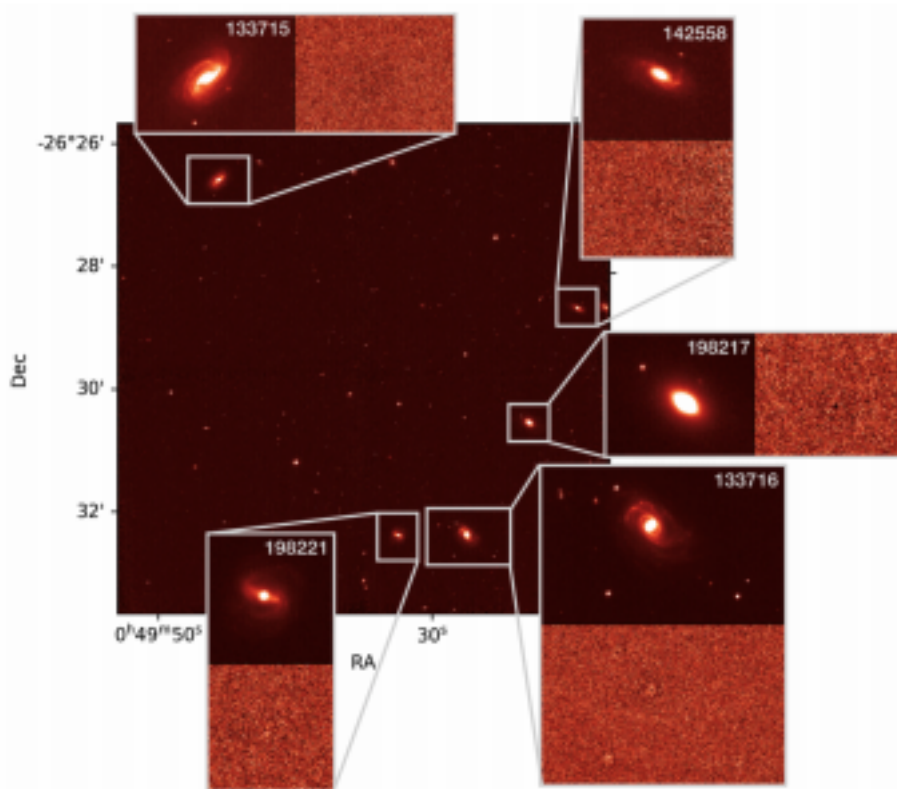


Figure 6.14: A VLT/HAWK-I image of a galaxy targeted field. A number of catalogued galaxies (and at least one uncatalogued galaxy likely at the same redshift) are visible in the field. The insets show each galaxy as well as the resulting subtraction, demonstrating the absence of variable sources to the limits of the data hosted in all these galaxies.

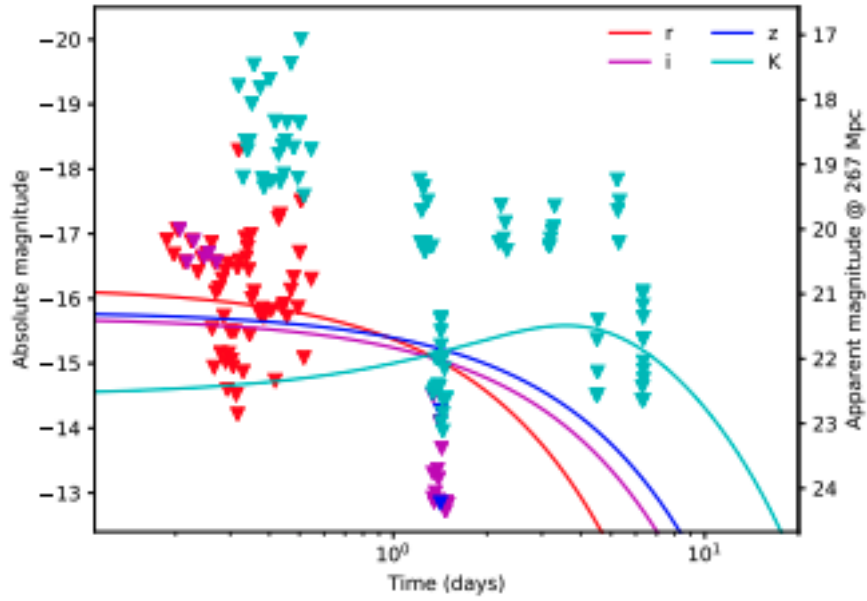


Figure 6.15: Galaxy targeted limits for GW190814, alongside the equivalent AT2017gfo KN models. Due to the different distances of the observed galaxies, the data and models are presented in absolute magnitudes. For limits below the model lines, the observations would have uncovered a transient comparable to AT2017gfo. The apparent magnitude of the data and models are also reported when shifted to the luminosity distance of GW190814 (267 Mpc). Foreground extinction is not considered

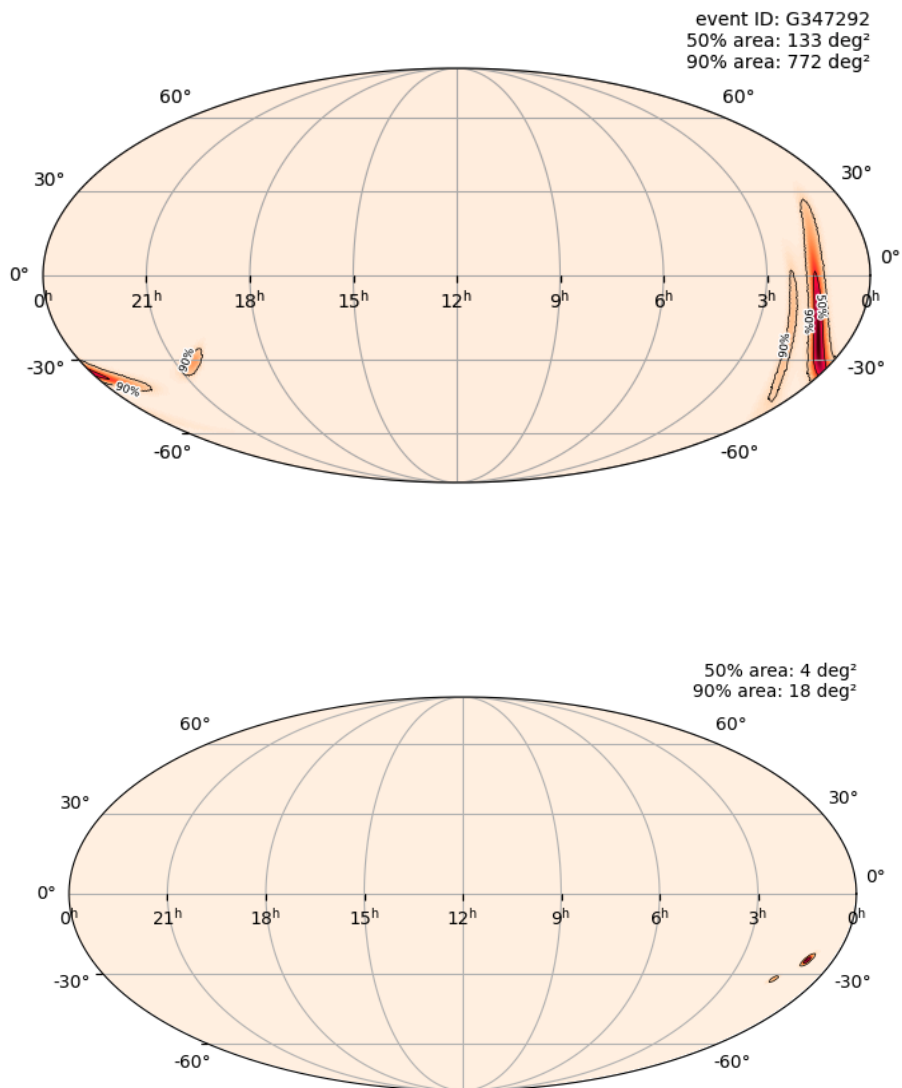


Figure 6.16: The wider area was the estimated location area for the GW source in the initial report (top panel), reduced then in the 90% and 50% confidence regions shown as red shaded color in the image (bottom panel).

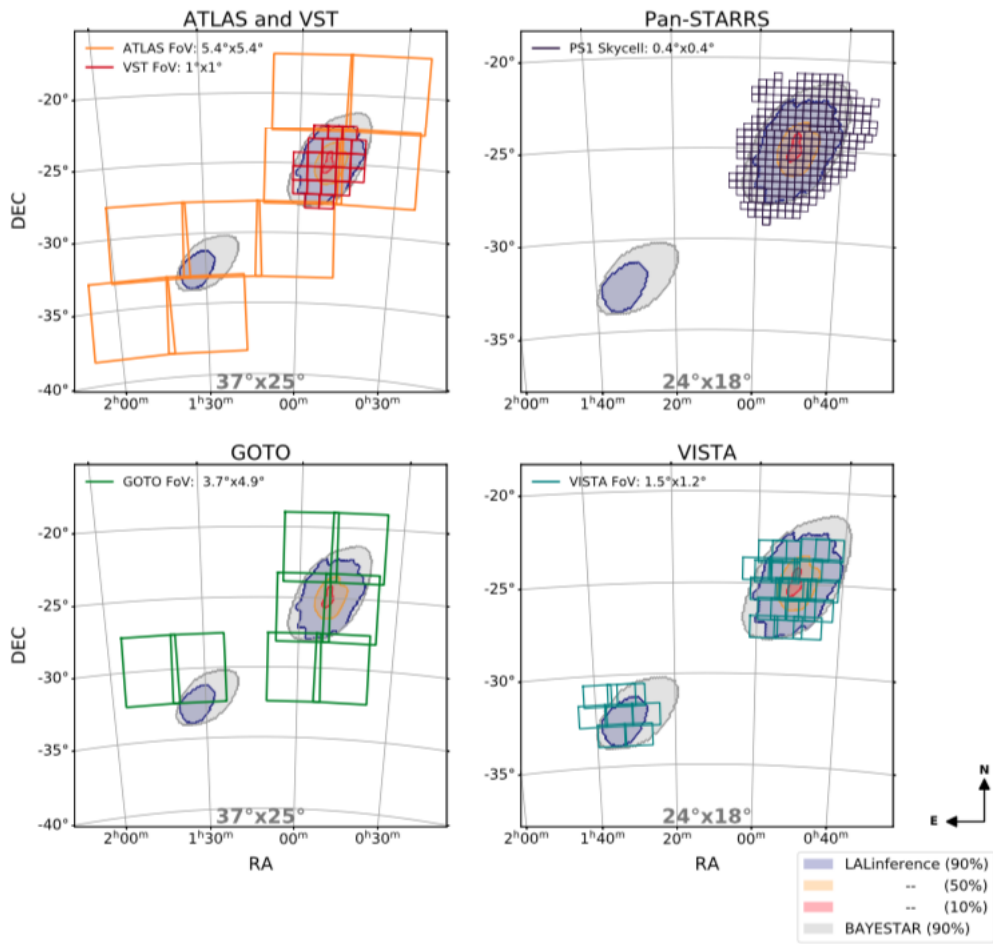


Figure 6.17: Coverage maps from the wide-field surveys with the probability contour maps.

to look for an EM counterpart was world wide. Beside the ENGRAVE consortium other programs triggered their facilities for this event: GOTO, ATLAS, GRAWITA-VST, Pan-STARRS and VINROUGE. The overlap of pointings of these programs and the GW localization area is in Fig. 6.17.

Two different approaches to search for an optical or NIR counterpart to GW190814 were employed. A number of wide-field facilities (with FoV, of 1 deg^2 or more) were used to tile the LVC GW skymap with the aim of covering as much of the 2D probability of GW190814 localisation as possible. These telescopes (with apertures of 0.4m to 4m) were situated in La Palma, Chile and Hawaii, giving a spread of latitude and temporal coverage. The second approach was to target specific galaxies in the 3D sky region with larger aperture (2m to 8m) telescopes and smaller FoV cameras. In the following, we present the observing campaign for the search as described in Ackley et al. (2020).

The GOTO (GW Optical Transient Observer) wide field search used a tiling strategy derived from the initial skymap, for which the 90% localisation probability area was 772 deg^2 . Each tile was observed using sequences of 60s or 90s exposures in the GOTO-L filter, which is a wide filter covering the region from 400 – 700 nm (slightly wider than combined Sloan g+r).

The survey area monitored by VST is about 23 deg^2 covering a maximum of 87.7% of the localisation probability of GW190814. This search discovered 27 transients out of these 21 objects already discovered by other surveys. All these transients show a slow evolution in the two weeks of the observing campaign, and we exclude that are associated with the GW event.

The VISTA search under VINROUGE program, observing the area at three epochs: the first over several nights after-merging, the second around a week later, and the final epoch at roughly seven weeks post-merger which was used as our primary reference template. No new sources were found in the search, with the exception of a transient unrelated to GW190814.

The Asteroid Terrestrial-impact Last Alert System (ATLAS)- with two telescopes located on two separate sites in Hawaii of 0.5 m aperture with a FoV of 29.2 deg^2 (Tonry et al., 2018)- was serendipitously observing the GW190814 skymap region several hours before its detection. Hence, any young and bright transients would have been identified. Seven pointings of ATLAS covered entirely the LALInference

skymap for three nights. In none of the three post-event epochs new transients were detected within the GW localisation area of ATLAS.

The Pan-STARRS system typically observes in a quad sequence similar to ATLAS, with a set of 4×45 s exposures taken across a time span of 1 hour to identify moving sources. None of these surveys were able to identify a optical or NIR candidate as counterpart of the GW event.

Galaxy targeted searches, although they cannot cover the entire 2D skymap, offer significantly improvement of the depth of the wide field surveys for a select number of high luminosity galaxies.

To build a catalog of the highest probability galaxies of hosting the GW event the HOGWARTS code (Salmon et al., 2020) was utilized that ranked galaxies in the Galaxy List for the Advanced Detector Era (GLADE; Dályá et al., 2018) catalogue according to their probability of containing the GW source (see figure 6.13) given the 3D localization probability density (Singer et al., 2014), and based on the expectation that NS-BH merger rates follow the galaxy mass distribution (Arcavi et al., 2017). Coordinated observations were obtained with GROND telescope LT, the Nordic Optical Telescope (NOT), the Telescopio Nazionale Galileo (TNG), the Very Large Telescope (VLT) and the William Herschel Telescope (WHT). In total, over 400 multi-wavelength (grizJHK) images of the 67 most probable galaxies within the 3D volume were acquired in the ten days following the merger (see figure 6.14 for an example image). The VLT images were obtained in the *i* and *z* band with the FOcal Reducer and low dispersion Spectrograph (FORS, Appenzeller et al., 1998) in one epoch, and HAWK-I in the *Ks* band in three epochs. Given the likely slow rise time of kilonovae in the NIR bands, the first two HAWK-I *Ks*-band epochs were intended to be sensitive to the peak of the KN a few days after the merging time. This complemented the FORS optical imaging within the first 24–48 hours, which are more sensitive to the early emission. These images reached significantly deeper limiting magnitudes across the field than those obtained by smaller aperture telescope searches, with typical depths of $i \sim 23 - 24$ mag.

The WHT obtained a series of optical and NIR observations of 16 galaxies of the sample in the *r* band, using the Auxiliary-port CAMera (ACAM), while NIR observations of 12 galaxies were taken in the *Ks* band using the Long-slit Intermediate Resolution Infrared Spectrograph (LIRIS). Moreover, optical and NIR images of a

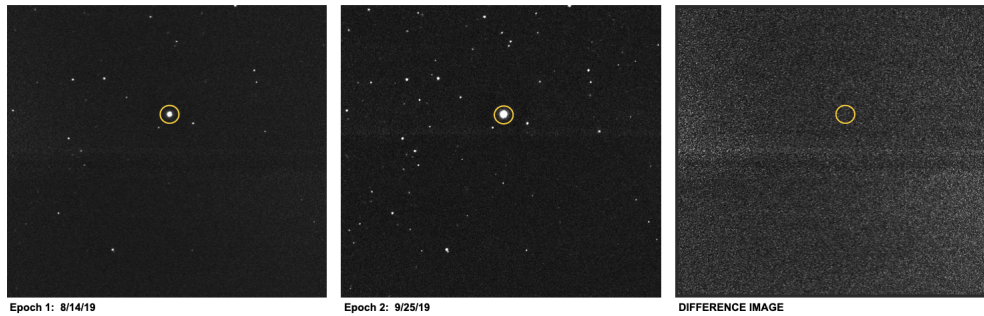
subset of 16 galaxies were carried out with the Italian 3.6-m TNG telescope, situated on La Palma, using the DOLoRes (optical) and NICS (NIR) instruments. The typical upper limit was $K_s \sim 19.7 - 20.9$ (3σ detection limit). GROND obtained observations of 36 galaxies simultaneously in g' , r' , i' , z' , J, H, K, reaching typical 3σ detection limits of $20 - 22$ mag in the r band and $17.5 - 19.5$ mag in K. Finally, a total of 19 galaxies were observed using the IO:O imaging camera of the LT (Steele et al., 2004). We derive 3σ limiting magnitudes, with the calibration tied to the Pan-STARRS photometric standards in each field (magnitude limit in r ~ 21.8 mag).

Within the ENGRAVE collaboration attempt to find the EM counterpart of the GWs source I inspected the images from GROND. For each galaxy I obtained an average exposure of 2.1 minuter in the optical bands, and 3.9 minutes, in the NIR bands. The data were reduced using the GROND pipeline. I used hotpans to perform images' difference to show the possible presence of a source in the selected galaxies. For each galaxy detected with GROND, I analysed those undetected in K band with other telescopes, and those not observed by VST in the r band. No transients have been identified in the difference images. I measured the limiting magnitude to define an upper limit on the transient luminosity by injecting fake stars with a range of magnitudes on the images in different positions, within the galaxy search radius (see figure 6.18). I obtained the difference image with the same template of the search and estimated the recovery of the artificial stars in our difference images. I assumed as a limiting magnitude the average magnitude of the fainter fake star that can be visually identified. The observations reached typical 3σ detection limits of $20 - 22$ mag in the r band, and $17.5 - 19.5$ mag in K.

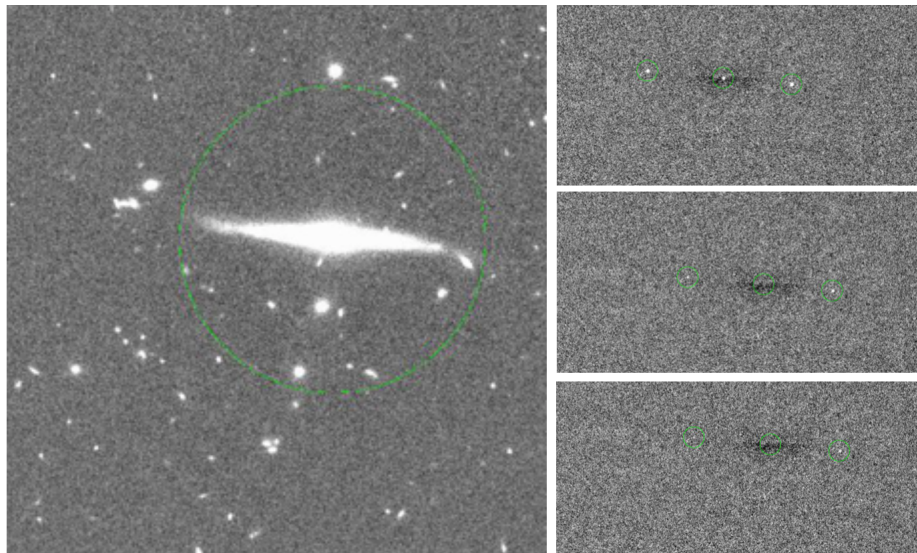
A similar procedure was applied for the VLT, LT, WHT, TNG observations, and all the searches gave the same outcome: fake stars revealed up to a magnitude limits of 20.9 mag in the K_S band, 24 mag in the i band and 22.8 mag in the r band.

With respect to the GW170817 the galaxy targeted search was less effective because of the higher distance (267 ± 52 Mpc compared to ≈ 40 Mpc for GW170817).

The missing chance to detect an EM counterpart, the galaxy-targeted observations were able to set limits over a fraction of the error box. Early observations with $r \geq 22$ mag, were below the expected brightness of an AT2017gfo-like KN (comparison was made with the model from the KN shifted to the skymap distance). Data taken in the IR on timescales of 5 - 10 days reaching $K_S \geq 21$ mag were also useful to set a



(a) Result of the procedure for obtaining difference image by the galaxy targeted search. ESO474-026 is the galaxy in the example. We derive the difference image using the HOTPANTS software and a configuration file. As for all the other difference images from other galaxies in the area of interest, no optical transient is detectable to the visual inspection



(b) Procedure for the magnitude limit estimate. We inject artificial stars into the image in a specific position of the galaxy. In doing this within the magnitude range between 20 mag and 24 mag for the Ks images, and 16 mag and 20 mag for the r band images with step of 0.5 mag, we check whether the injected stars are detected or not in the difference image. The magnitude limit is set to the lower magnitude which the stars are no longer detectable.

Figure 6.18: An example of the procedure applied in the galaxy targeted search.

limit of the magnitude of the possible event (Ackley et al., 2020, see figure 10 in). Although the majority of observations were above the depth at which the kilonova would have been seen, early observations from the WHT and TNG in the r band, and later observations in the IR from HAWK-I are most constraining as these would have revealed a kilonova similar to AT2017gfo if visible (see figure 6.15). In order to assess more quantitatively the ability of our observations to uncover a putative kilonova transient as for GW170817, we can combine our wide-field and galaxy-targeted observations. For the few, highest probability galaxies the most constraining limit arises from our galaxy-targeted search, but for the majority of the localisation volume the most constraining limits are through wide field search, in particular from VST, PS1 and VISTA. Our search is therefore sensitive to a kilonova over 40% of the localisation probability, and over 80% to a transient with the same temporal behaviour, but brighter by a factor of 2. The most constraining observations (due to both depth and coverage) are those in the r and Ks bands. The worldwide intensive efforts to identify a counterpart to GW190814 had led to the identification of multiple transients within the error localisation. In part this is due to the deep observations that were capable of identifying transient sources fainter than 22 mag. In addition to the transients identified here through our searches, additional counterparts were found by other groups (Andreoni et al., 2020; Dobie et al., 2019; Gomez et al., 2019). In total approximately 75 optical transients were identified. In principle, each of these should be considered a potential counterpart unless it can be ruled out through follow-up observations. All these transients were ruled out as EM counterpart for several reasons: the SN spectrum, their distance inconsistent with the GW distance, a light curve similar to a SN, the nuclear position in host galaxy with AGN activity, no obvious underlying host galaxy. Based on the results of Veitch et al. (2015) the probable progenitor of GW190814 could be a neutron star-black hole (NS-BH) system or a binary black holes (BBH) system. The NS classification of the companion was just based on the mass constrain, $M_1 \leq 3M_\odot$, and a low mass BH could not be ruled out. For a BBH progenitor system, no EM counterpart was expected. Hence, we searched for a kilonova event a EM counterpart of the GW signal from a NS-SH progenitor system. NS-BHs have both a larger total mass and a larger chirp mass (this is an indicative parameter linked to the amplitude of the GW) than NS-NS systems. Thus they are expected to produce a stronger GW signal that can be observed out to greater distances. Models

predict that the last phase of the NS-BH coalescence can lead to two ends:

1. the NS is partially or totally disrupted by the BH tidal field;
2. the NS is swallowed directly by the BH without any significant mass left outside the merger remnant (Lattimer and Schramm, 1974).

EM emission is expected when the disruption occurs before the NS reaches the innermost stable circular orbit (ISCO) of the BH. The location of the ISCO with respect to the tidal disruption radius depends on the mass ratio of the two compact objects, the BH spin, and the NS equation of State (EoS) (Foucart, 2012; Foucart et al., 2018; Kyutoku et al., 2011; Shibata and Taniguchi, 2011). The expected EM emission from a NS-BH merger event are constrained by less extreme values for the NS-BH mass ratio, larger BH spin, and stiffer NS EoS favors the disruption of the NS before the ISCO, enabling the formation of the accretion disk, tidal tails, and unbound ejecta. This material forms different components from which EM signals can originate. The KN emission for a given merger is a function of the mass deposited in the various components of the KN, including neutrino- and viscosity-driven neutron-rich winds (Fernández and Metzger, 2013; Just et al., 2015) and low-electron-fraction tidal tails (Foucart et al., 2014; Kiuchi et al., 2015; Kyutoku et al., 2018; Roberts et al., 2016). It is therefore relevant to compare the observational limits on a kilonova emission from GW190814 with the expectations of NS-BH models. The representative limits on the disk and tidal ejecta masses are $M_{disk} \leq 0.3M_{\odot}$ and $M_t \leq 102 M_{\odot}$, respectively. Based on this, large amount of ejecta as product of the NS-BH binary progenitor can be excluded, this indicates that most likely the NS was not disrupted by the tidal forces during the final part of the inspiral towards its BH companion, which disfavors high (aligned) BH spins and small mass ratio (or both).

6.8 Conclusion

The missed chance to find an electromagnetic counterpart for GW190814 signal suggests that the current generation of wide-field facilities are not optimised for the majority of future candidates, as observations may need to reach $r \geq 23$ mag to probe a reasonable fraction of kilonova parameter space. While some wide-field facilities may be able to attain sufficient depth over a significant fraction of future events

(e.g., DECam, BlackGEM, LSST); events at $\approx 300\text{Mpc}$ may only be detectable by 8 m class telescopes. The requirement to observe such events will depend sensitively on where the true event rate of NS-NS and NS-BH lies. At the higher end, optical/IR observers can focus on nearby events. However, ELT-like resources are required for their follow-up. Effort should be expended on extending the GW detector network such that the 3D probability volumes for the GW events can become tractable for such observations .

Nonetheless, in O4 we predict a BNS search volume VT of $1.6 \times 10^7 \text{ Mpc}^3 \text{ year}$, and 10_{-10}^{52} expected detections with a median 90% credible region for the localization area (volume) of BNS is 33_{-5}^5 deg^2 ($52_{-9}^{10} \times 10^3 \text{ Mpc}^3$). A percentage of 38–44% (12– 16%) of the events are expected to have a 90% credible region smaller than 20 deg^2 (5 deg^2). For BBH the VT searched is $1.5 \text{ Gpc}^3 \text{ year}$ with 79_{-44}^{89} expected detections. The median 90% credible region for the localization area (volume) of BBH is 41_{-6}^7 deg^2 ($7700_{-920}^{1500} \times 10^3 \text{ Mpc}^3$). A percentage of 35–39% (11–14%) of the events are expected to have a 90% credible area smaller than 20 deg^2 (5 deg^2) (Abbott et al., 2020). Identifying multimessenger sources is a fundamental challenge. Poor source localization by gravitational-wave detectors and the often short available time window for follow-up observations requires a new level of cooperation between new and old forms of astronomy. Cooperative ventures between different facilities and survey programs have created an integrated network of observatories that can react rapidly to discoveries of cosmic events. The expansion of observational capacity with the new generation instruments and the enhanced cooperation between collaborations and instruments are expected to augment the number and type of observable events, while at later stages the available large number of discoveries will enable deeper, detailed explorations of these phenomena.

Chapter 7

Conclusion and perspectives

The aim of this thesis is to study transient events in the multi-messenger era. I measured SN rates as function of cosmic volume and parent galaxy color, mass and sSFR. This allows to constrain progenitor parameters comparing the measured SN rates with the expected values from the theoretical models. I found that according to the expectations of stellar evolution, the minimum mass for CC SN progenitors is between $8 - 10 M_{\odot}$ and the DTD of SN Ia progenitors is skewed at the short delay times ($\leq 1Gyr$). However, the uncertainties on both CC and type Ia SN rates are still too high to constrain the mass range of CC SN progenitors with sufficient accuracy and to discriminate between SD and DD progenitor scenarios. Hence, to explore the improvement that we can obtain in the SN rate measurements with the next LSST survey, I performed a simulation to analyse the impact of different observational strategies on the statistic and systematic uncertainties of SN rate measurements. Next synoptic surveys will also improve our ability to detect other transient events in regions of the phase space still uncovered. I performed simulations aimed to exploit the detection of unknown transients as function of LSST cadences. The results suggest that whereas some OpSims designed to cover a large footprint (*e.g. footprint_bigsky*), rank highly OpSim, however others perform even better even if they cover a smaller area. The advantage is given by the acquisition of image pairs in the short 1.5 hour time gap that was identified as optimal to measure color (Bianco et al., 2019).

Further analysis will be dedicated to the new synoptic surveys such as those of the Vera Rubin Observatory with LSST, and new simulations on the transients detection and classification will include dust distributions, a wider set of SN templates for the

simulations of the SN population and different classification tool to compare their performances. Specifically to the SN rate simulation, eventually, the ultimate outcome will be the estimation of the SN rate as function of the progenitor models; this can be compared to the future measurements of the SN rate from the analysis of the LSST data, the accuracy expected from the next generation surveys will be able to disentangle the degeneracy between SNe and their progenitor. The expertises acquired on SN search can be also extended to the search for the EM counterpart of GWs or high energy events (such as GRB). Indeed, difference image process has been used in the case of the search for the EM counterpart of GW190814, and artificial experiment algorithm has been used to study the limiting magnitude of the search. Moreover, the study of the photometry evolution has been shown as an important tool to study features of the high energetic GRB190114C. Indeed, the overall light curve from γ -ray to optical and radio shows a complex temporal structure with several emission peaks. The observation of TeV emission reveals a new emission component in the afterglow of a GRB, whose power is comparable to that of the synchrotron component. Multimessenger observations of transients are an emerging branch of astronomy, fundamental for our understanding of the most energetic cosmic events, the evolution of the Universe and possibly some of the cardinal laws of physics. The detectors' sensitivity to these new messengers, is expected to expand rapidly. This will highly impact the search and follow up in the optical regime of transient events such as GW170817 and GW190814 and will help disclosing new features of these phenomena.

Bibliography

- B. P. Abbott et al. Observation of Gravitational Waves from a Binary Black Hole Merger,. *Phys. Rev. Lett.*, 116:061102, Feb 2016. doi: 10.1103/PhysRevLett.116.061102. URL <https://link.aps.org/doi/10.1103/PhysRevLett.116.061102>.
- B. P. Abbott et al. Prospects for observing and localizing gravitational-wave transients with Advanced LIGO, Advanced Virgo and KAGRA,. *Living Reviews in Relativity*, 21(1):3, April 2018. doi: 10.1007/s41114-018-0012-9.
- B. P. Abbott et al. GWTC-1: A Gravitational-Wave Transient Catalog of Compact Binary Mergers Observed by LIGO and Virgo during the First and Second Observing Runs. *Physical Review X*, 9(3):031040, July 2019a. doi: 10.1103/PhysRevX.9.031040.
- B. P. Abbott et al. Binary Black Hole Population Properties Inferred from the First and Second Observing Runs of Advanced LIGO and Advanced Virgo. , 882(2):L24, September 2019b. doi: 10.3847/2041-8213/ab3800.
- B. P. Abbott et al. GWTC-1: A Gravitational-Wave Transient Catalog of Compact Binary Mergers Observed by LIGO and Virgo during the First and Second Observing Runs,. *Physical Review X*, 9(3):031040, July 2019c. doi: 10.1103/PhysRevX.9.031040.
- B. P. Abbott et al. Tests of general relativity with the binary black hole signals from the LIGO-Virgo catalog GWTC-1. , 100(10):104036, November 2019d. doi: 10.1103/PhysRevD.100.104036.
- B. P. Abbott et al. Prospects for observing and localizing gravitational-wave transients with advanced ligo, advanced virgo and kagra. *Living Reviews in Relativity*, 23

- (1):3, 2020. doi: 10.1007/s41114-020-00026-9. URL <https://doi.org/10.1007/s41114-020-00026-9>.
- B.P. Abbott et al. Gw170817: Observation of gravitational waves from a binary neutron star inspiral. *Physical Review Letters*, 119(16), Oct 2017a. ISSN 1079-7114. doi: 10.1103/physrevlett.119.161101. URL <http://dx.doi.org/10.1103/PhysRevLett.119.161101>.
- B.P. Abbott et al. Gravitational Waves and Gamma-Rays from a Binary Neutron Star Merger: GW170817 and GRB 170817A,. *The Astrophysical Journal*, 848(2): L13, oct 2017b. doi: 10.3847/2041-8213/aa920c. URL <https://doi.org/10.3847/2041-8213/aa920c>.
- R. Abbott et al. GWTC-2: Compact Binary Coalescences Observed by LIGO and Virgo During the First Half of the Third Observing Run. *arXiv e-prints*, art. arXiv:2010.14527, October 2020.
- F. Acero et al. Prospects for cherenkov telescope array observations of the young supernova remnant RX, j1713.7-3946. *The Astrophysical Journal*, 840(2):74, may 2017. doi: 10.3847/1538-4357/aa6d67. URL <https://doi.org/10.3847/1538-4357/aa6d67>.
- K. Ackley et al. Observational constraints on the optical and near-infrared emission from the neutron star-black hole binary merger candidate S190814bv,. , 643:A113, November 2020. doi: 10.1051/0004-6361/202037669.
- S. M Adam and CS Kochanek. Loss's first supernova? new limits on the 'impostor'sn 1997bs. *Monthly Notices of the Royal Astronomical Society*, 452(2):2195–2207, 2015.
- C. Alard. Image subtraction with non-constant kernel solutions,. *arXiv e-prints*, art. astro-ph/9903111, March 1999.
- C. Alard and R. H. Lupton. A Method for Optimal Image Subtraction,. , 503(1): 325–331, August 1998. doi: 10.1086/305984.

- G. Aldering et al. Nearby Supernova Factory Observations of SN 2005gj: Another Type Ia Supernova in a Massive Circumstellar Envelope, , 650(1):510–527, October 2006. doi: 10.1086/507020.
- Greg Aldering, Roberta M Humphreys, and Michael Richmond. Sn 1993j: the optical properties of its progenitor. *The Astronomical Journal*, 107:662–672, 1994.
- G. Altavilla et al. Cepheid calibration of Type Ia supernovae and the Hubble constant, , 349(4):1344–1352, April 2004. doi: 10.1111/j.1365-2966.2004.07616.x.
- R. Amanullah et al. The Peculiar Extinction Law of SN 2014J Measured with the Hubble Space Telescope. , 788(2):L21, June 2014. doi: 10.1088/2041-8205/788/2/L21.
- I. Andreoni et al. GROWTH on s190814bv: Deep synoptic limits on the optical/near-infrared counterpart to a neutron star–black hole merger. *The Astrophysical Journal*, 890(2):131, feb 2020. doi: 10.3847/1538-4357/ab6a1b. URL <https://doi.org/10.3847/1538-4357/ab6a1b>.
- W.D. Apel et al. Energy spectra of elemental groups of cosmic rays: Update on the cascade unfolding analysis. *Astroparticle Physics*, 31(2):86 – 91, 2009. ISSN 0927-6505. doi: <https://doi.org/10.1016/j.astropartphys.2008.11.008>. URL <http://www.sciencedirect.com/science/article/pii/S0927650508001783>.
- I. Appenzeller et al. Successful commissioning of FORS1 - the first optical instrument on the VLT. *The Messenger*, 94:1–6, December 1998.
- I. Arcavi et al. Optical follow-up of gravitational-wave events with las cumbres observatory. *The Astrophysical Journal*, 848:L33, 10 2017. doi: 10.3847/2041-8213/aa910f.
- W. Baade and F. Zwicky. On super-novae. *Proceedings of the National Academy of Sciences*, 20(5):254–259, 1934. ISSN 0027-8424. doi: 10.1073/pnas.20.5.254. URL <https://www.pnas.org/content/20/5/254>.
- P. V. Baklanov, S. I. Blinnikov, and N. N. Pavlyuk. Parameters of the classical type-iip supernova sn 1999em. *Astronomy Letters*, 31(7):429–441, 2005. doi: 10.1134/1.1958107. URL <https://doi.org/10.1134/1.1958107>.

- I. K. Baldry et al. Quantifying the Bimodal Color-Magnitude Distribution of Galaxies. , 600(2):681–694, January 2004. doi: 10.1086/380092.
- C. Barbarino et al. SN 2012ec: mass of the progenitor from PESSTO follow-up of the photospheric phase. *Monthly Notices of the Royal Astronomical Society*, 448(3):2312–2331, 02 2015. ISSN 0035-8711. doi: 10.1093/mnras/stv106. URL <https://doi.org/10.1093/mnras/stv106>.
- R. Barbon, F. Ciatti, and L. Rosino. Photometric properties of type II supernovae. , 72:287–292, February 1979.
- R. Barbon, S. Benetti, E Cappellaro, F Patat, M. Turatto, and T. Iijima. Sn 1993j in m 81: One year of observations at asiago. *Astronomy and Astrophysics Supplement Series*, 110:513, 1995.
- A. Barth et al. The environments of supernovae in archival hubble space telescope images. *The Astronomical Journal*, 111:2047, 1996.
- A.N. Baushev. Principal properties of the velocity distribution of dark matter particles near the solar system. *Journal of Physics: Conference Series*, 375(1):012048, jul 2012. doi: 10.1088/1742-6596/375/1/012048. URL <https://doi.org/10.1088/1742-6596/375/1/012048>.
- L. R. Bedin et al. Improved Hubble Space Telescope proper motions for Tycho-G and other stars in the remnant of Tycho’s Supernova 1572. *Monthly Notices of the Royal Astronomical Society*, 439(1):354–371, 02 2014. ISSN 0035-8711. doi: 10.1093/mnras/stt2460. URL <https://doi.org/10.1093/mnras/stt2460>.
- E. F. Bell and R. S. de Jong. Stellar Mass-to-Light Ratios and the Tully-Fisher Relation. , 550(1):212–229, March 2001. doi: 10.1086/319728.
- E.C. Bellm et al. Plans and Policies for LSST Alert Distribution,, jan 2018. URL [ls.st/LDM-612](https://lsst.st/LDM-612).
- S. Benetti et al. Supernova 2002bo: inadequacy of the single parameter description,. , 348(1):261–278, February 2004. doi: 10.1111/j.1365-2966.2004.07357.x.

- S. Benetti et al. The spectacular evolution of supernova 1996al over 15 yr: a low-energy explosion of a stripped massive star in a highly structured environment. *Monthly Notices of the Royal Astronomical Society*, 456(3):3296–3317, 2016.
- M.C. Bersten, O. Benvenuto, and M. Hamuy. Hydrodynamica models of type ii plateau supernovae. *The Astrophysical Journal*, 729(1):61, feb 2011. doi: 10.1088/0004-637x/729/1/61. URL <https://doi.org/10.1088/0004-637x/729/1/61>.
- E. Bertin. Automatic Astrometric and Photometric Calibration with SCAMP. In C. Gabriel, C. Arviset, D. Ponz, and S. Enrique, editors, *Astronomical Data Analysis Software and Systems XV*, volume 351 of *Astronomical Society of the Pacific Conference Series*, page 112, July 2006.
- E. Bertin. Swarp: Resampling and co-adding fits images together. *Astrophysics Source Code Library*, pages 10068–, 10 2010.
- E. Bertin and S. Arnouts. SExtractor: Software for source extraction. , 117:393–404, June 1996a. doi: 10.1051/aas:1996164.
- E. Bertin and S. Arnouts. SExtractor: Software for source extraction. *Astron. Astrophys. Suppl. Ser.*, 117(2):393–404, 1996b. doi: 10.1051/aas:1996164. URL <https://doi.org/10.1051/aas:1996164>.
- E. Bertin et al. The TERAPIX Pipeline. In David A. Bohlender, Daniel Durand, and Thomas H. Handley, editors, *Astronomical Data Analysis Software and Systems XI*, volume 281 of *Astronomical Society of the Pacific Conference Series*, page 228, January 2002.
- F Bertola. The supernovae in ngc 1073 and ngc 1058. In *Annales d’Astrophysique*, volume 27, page 319, 1964.
- F.B. Bianco et al. Presto-color: A photometric survey cadence for explosive physics and fast transients. *Publications of the Astronomical Society of the Pacific*, 131(1000):068002, apr 2019. doi: 10.1088/1538-3873/ab121a. URL <https://doi.org/10.1088/1538-3873/ab121a>.

- J. Binney. Distribution functions for the Milky Way,. *Monthly Notices of the Royal Astronomical Society*, 401(4):2318–2330, 01 2010. ISSN 0035-8711. doi: 10.1111/j.1365-2966.2009.15845.x. URL <https://doi.org/10.1111/j.1365-2966.2009.15845.x>.
- J. Binney and S. Tremaine. *Galactic Dynamics: Second Edition*,. 2008.
- W. P. Blair et al. An expanded hst/wfc3 survey of m83: Project overview and targeted supernova remnant search. *The Astrophysical Journal*, 788(1):55, 2014.
- G. Blanc et al. Type Ia supernova rate at a redshift of ~ 0.1 . , 423:881–894, September 2004. doi: 10.1051/0004-6361:20035948.
- M. Blanton et al. The Galaxy Luminosity Function and Luminosity Density at Redshift $z = 0.1$. , 592(2):819–838, August 2003. doi: 10.1086/375776.
- S. Bose et al. Supernova 2012aw – a high-energy clone of archetypal Type IIP SN 1999em. *Monthly Notices of the Royal Astronomical Society*, 433(3):1871–1891, 06 2013. ISSN 0035-8711. doi: 10.1093/mnras/stt864. URL <https://doi.org/10.1093/mnras/stt864>.
- S. Bose et al. SN 2013ab: a normal Type IIP supernova in NGC 5669. *Monthly Notices of the Royal Astronomical Society*, 450(3):2373–2392, 05 2015. ISSN 0035-8711. doi: 10.1093/mnras/stv759. URL <https://doi.org/10.1093/mnras/stv759>.
- M. T. Botticella et al. *A&A*, (1):49. doi: 10.1051/0004-6361=20078011.
- M. T. Botticella et al. A comparison between star formation rate diagnostics and rate of core collapse supernovae within 11 mpc. , 537:A132, January 2012. doi: 10.1051/0004-6361/201117343.
- M. T. Botticella et al. Supernova rates from the SUDARE VST-Omegacam search II. Rates in a galaxy sample,. , 598:A50, February 2017. doi: 10.1051/0004-6361/201629432.
- G. B. Brammer, P.G. van Dokkum, and P. Coppi. EAZY: A Fast, Public Photometric Redshift Code,. , 686(2):1503–1513, October 2008. doi: 10.1086/591786.

- D Branch and J. C Wheeler. *Supernova Explosions*. 2017. doi: 10.1007/978-3-662-55054-0.
- E. Bravo and D. García-Senz. Pulsating reverse detonation models of type ia supernovae. i. detonation ignition. *The Astrophysical Journal*, 695(2):1244–1256, apr 2009. doi: 10.1088/0004-637x/695/2/1244. URL <https://doi.org/10.1088/0004-637x/695/2/1244>.
- P.J. Brown et al. Swidultraviolet observations of supernova 2014j in m82: large extinction from interstellar dust. *The Astrophysical Journal*, 805(1):74, may 2015. doi: 10.1088/0004-637x/805/1/74. URL <https://doi.org/10.1088/0004-637x/805/1/74>.
- G. Bruzual and S. Charlot. Stellar population synthesis at the resolution of 2003,. , 344(4):1000–1028, October 2003. doi: 10.1046/j.1365-8711.2003.06897.x.
- D. Calzetti et al. The Dust Content and Opacity of Actively Star-forming Galaxies,. *The Astrophysical Journal*, 533(2):682–695, April 2000. doi: 10.1086/308692.
- S. Campana et al. The association of GRB 060218 with a supernova and the evolution of the shock wave. , 442(7106):1008–1010, August 2006. doi: 10.1038/nature04892.
- P. Candia et al. Optical and Infrared Photometry of the Unusual Type Ia Supernova 2000cx,. , 115(805):277–294, March 2003. doi: 10.1086/368229.
- Yi Cao et al. Discovery, progenitor and early evolution of a stripped envelope supernova iptf13bvn. *The Astrophysical Journal Letters*, 775(1):L7, 2013.
- M. Capaccioli et al. VST: the VLT Survey Telescope. VST: An Overview. In *Science from the Next Generation Imaging and Spectroscopic Surveys*, page 1, October 2012.
- E. Cappellaro and M. Turatto. The Frequency of Supernovae in External Galaxies. In R. S. Roger and T. L. Landecker, editors, *IAU Colloq. 101: Supernova Remnants and the Interstellar Medium*, page 489, January 1988.
- E. Cappellaro, M. Turatto, S. Benetti, D. Yu. Tsvetkov, O. S. Bartunov, and I. N. Makarova. The rate of supernovae. II. The selection effects and the frequencies per unit blue luminosity. , 273:383–392, June 1993b.

- E Cappellaro, R Evans, and M Turatto. A new determination of supernova rates and a comparison with indicators for galactic star formation. *arXiv preprint astro-ph/9904225*, 1999.
- E. Cappellaro et al. The rate of supernovae. I. The data base, the recipe and the uncertainties. , 268:472–482, February 1993a.
- E. Cappellaro et al. The rate of supernovae from the combined sample of five searches., , 322:431–441, June 1997a.
- E. Cappellaro et al. The rate of supernovae from the combined sample of five searches. , 322:431–441, June 1997b.
- E. Cappellaro et al. Supernova rates from the sudare vst-omegacam search - i. rates per unit volume. *A&A*, 584:A62, 2015. doi: 10.1051/0004-6361/201526712. URL <https://doi.org/10.1051/0004-6361/201526712>.
- J. L. Carlin et al. Kinematics and Chemistry of Stars along the Sagittarius Trailing Tidal Tail and Constraints on the Milky Way Mass Distribution,. *The Astrophysical Journal*, 744(1):25, January 2012. doi: 10.1088/0004-637X/744/1/25.
- S. Carroll. page Guidebook Part 2 page 44. The Teaching Company, 2007.
- R. M. Catchpole et al. Spectroscopic and photometric observations of SN 1987A- V. Days 386-616., , 237:55P–68, March 1989. doi: 10.1093/mnras/237.1.55P.
- S. Chandrasekhar. *An introduction to the study of stellar structure*, volume 2. Courier Corporation, 1957.
- S. Chatterji et al. Coherent network analysis technique for discriminating gravitational-wave bursts from instrumental noise,. *Phys. Rev. D*, 74:082005, Oct 2006. doi: 10.1103/PhysRevD.74.082005. URL <https://link.aps.org/doi/10.1103/PhysRevD.74.082005>.
- J. S. W. Claeys, S. E. de Mink, O. R. Pols, J. J. Eldridge, and M. Baes. Binary progenitor models of type IIb supernovae. , 528:A131, April 2011. doi: 10.1051/0004-6361/201015410.

- A. Clocchiatti et al. A Study of SN 1992H in NGC 5377,. , 111:1286, March 1996a. doi: 10.1086/117874.
- A. Clocchiatti et al. SN 1994I: Disentangling He i Lines in Type IC Supernovae,. , 462:462, May 1996b. doi: 10.1086/177165.
- J. G Cohen, J. Darling, and A. Porter. The nonvariability of the progenitor of supernova 1993j in m81. *Astronomical Journal*, 110(1):308–311, 1995.
- S.A. Colgate and R. H. White. The Hydrodynamic Behavior of Supernovae Explosions,. , 143:626, March 1966. doi: 10.1086/148549.
- A. J. Connolly et al. An end-to-end simulation framework for the Large Synoptic Survey Telescope,. In George Z. Angeli and Philippe Dierickx, editors, *Modeling, Systems Engineering, and Project Management for Astronomy VI*, volume 9150 of *Society of Photo-Optical Instrumentation Engineers (SPIE) Conference Series*, page 14, 2014. doi: 10.1117/12.2054953.
- R. M. Crockett et al. The birth place of the type ic supernova 2007gr. *The Astrophysical Journal Letters*, 672(2):L99, 2007a.
- RM Crockett et al. A deeper search for the progenitor of the type ic supernova 2002ap. *Monthly Notices of the Royal Astronomical Society*, 381(2):835–850, 2007b.
- RM Crockett et al. The type iib sn 2008ax: the nature of the progenitor. *Monthly Notices of the Royal Astronomical Society: Letters*, 391(1):L5–L9, 2008.
- RM Crockett et al. On the nature of the progenitors of three type ii-p supernovae: 2004et, 2006my and 2006ov. *Monthly Notices of the Royal Astronomical Society*, 410(4):2767–2786, 2011.
- G. Dályá et al. GLADE: A galaxy catalogue for multimessenger searches in the advanced gravitational-wave detector era. , 479(2):2374–2381, September 2018. doi: 10.1093/mnras/sty1703.
- T. DeLaney et al. The density and mass of unshocked ejecta in cassiopea a though low frequency radio absorption. *The Astrophysical Journal*, 785(1):7, mar 2014.

doi: 10.1088/0004-637x/785/1/7. URL <https://doi.org/10.1088/0004-637x/785/1/7>.

F. Delgado et al. The LSST operations simulator,. In , volume 9150 of *Society of Photo-Optical Instrumentation Engineers (SPIE) Conference Series*, page 915015, August 2014. doi: 10.1117/12.2056898.

M. Della Valle et al. Why Are Radio Galaxies Prolific Producers of Type Ia Supernovae? , 629(2):750–756, August 2005. doi: 10.1086/430433.

J. Deng, N. Tominaga, P. A. Mazzali, K. Maeda, and K. Nomoto. On the Light Curve and Spectrum of SN 2003dh Separated from the Optical Afterglow of GRB 030329. , 624(2):898–905, May 2005. doi: 10.1086/429284.

D. Dobie et al. An ASKAP search for a radio counterpart to the first high-significance neutron star–black hole merger LIGO/virgo s190814bv. *The Astrophysical Journal*, 887(1):L13, dec 2019. doi: 10.3847/2041-8213/ab59db. URL <https://doi.org/10.3847/2041-8213/ab59db>.

J. B. Doggett and D. Branch. A comparative study of supernova light curves,.. , 90: 2303–2311, November 1985. doi: 10.1086/113934.

I. Domínguez et al. Type Ia supernovae: influence of the progenitor on the explosion. 9 1998.

G. York Donald et al. The Sloan Digital Sky Survey: Technical Summary,. *The Astronomical Journal*, 120(3):1579–1587, sep 2000. doi: 10.1086/301513. URL <https://doi.org/10.1086/301513>.

C. L. Douglas et al. A study of the type II-plateau supernova 1999[CLC]gi[/CLC] and the distance to its host galaxy, NGC 3184. *The Astronomical Journal*, 124(5):2490–2505, nov 2002. doi: 10.1086/343771. URL <https://doi.org/10.1086/343771>.

M. R. Drout et al. Rapidly Evolving and Luminous Transients from Pan-STARRS1,. , 794:23, October 2014. doi: 10.1088/0004-637X/794/1/23.

- M.R. Drout et al. The first systematic study of type ibc supernova multi-band light curves. *The Astrophysical Journal*, 741(2):97, oct 2011. doi: 10.1088/0004-637x/741/2/97. URL <https://doi.org/10.1088/0004-637x/741/2/97>.
- Schuyler D. Van Dyk, Peter M. Garnavich, Alexei V. Filippenko, Peter Höflich, Robert P. Kirshner, Robert L. Kurucz, and Peter Challis. The progenitor of supernova 1993j revisited. *Publications of the Astronomical Society of the Pacific*, 114(802):1322–1332, dec 2002. doi: 10.1086/344382. URL <https://doi.org/10.1086/344382>.
- J. J. Eldridge and J. R. Maund. The disappearance of the helium-giant progenitor of the Type Ib supernova iPTF13bvn and constraints on its companion. *Monthly Notices of the Royal Astronomical Society: Letters*, 461(1):L117–L121, 05 2016. ISSN 1745-3925. doi: 10.1093/mnrasl/slw099. URL <https://doi.org/10.1093/mnrasl/slw099>.
- J. J. Eldridge et al. Possible binary progenitors for the Type Ib supernova iPTF13bvn. *Monthly Notices of the Royal Astronomical Society*, 446(3):2689–2695, 11 2014. ISSN 0035-8711. doi: 10.1093/mnras/stu2197. URL <https://doi.org/10.1093/mnras/stu2197>.
- John J Eldridge, Morgan Fraser, Stephen J Smartt, Justyn R Maund, and R Mark Crockett. The death of massive stars–ii. observational constraints on the progenitors of type ibc supernovae. *Monthly Notices of the Royal Astronomical Society*, 436(1):774–795, 2013.
- J. H. Elias et al. Type I supernovae in the infrared and their use as distance indicators. , 296:379–389, September 1985. doi: 10.1086/163456.
- N. Elias-Rosa et al. On the progenitor of the type ii-plateau sn 2008cn in ngc 4603. *The Astrophysical Journal*, 706(2):1174, 2009.
- N. Elias-Rosa et al. The massive progenitor of the type ii-linear supernova 2009kr. *The Astrophysical Journal Letters*, 714(2):L254, 2010.
- N. Elias-Rosa et al. The massive progenitor of the possible type ii-linear supernova 2009hd in messier 66. *The Astrophysical Journal*, 742(1):6, 2011.

- N. Elias-Rosa et al. On the progenitor of the Type Ic SN 2013dk in the Antennae galaxies. *Monthly Notices of the Royal Astronomical Society: Letters*, 436(1):L109–L113, 09 2013. ISSN 1745-3925. doi: 10.1093/mnrasl/slt124. URL <https://doi.org/10.1093/mnrasl/slt124>.
- N Elias-Rosa et al. Dead or alive? long-term evolution of sn 2015bh (snhunt275). *Monthly Notices of the Royal Astronomical Society*, 463(4):3894–3920, 2016.
- A. Elmhamdi et al. Photometry and spectroscopy of the Type IIP SN 1999em from outburst to dust formation,. , 338(4):939–956, February 2003. doi: 10.1046/j.1365-8711.2003.06150.x.
- S. Fairhurst. Localization of transient gravitational wave sources: beyond triangulation,. *Classical and Quantum Gravity*, 35(10):105002, May 2018. doi: 10.1088/1361-6382/aab675.
- D. Falta, R. Fisher, and G. Khanna. Gravitational Wave Emission from the Single-Degenerate Channel of Type Ia Supernovae. , 106(20):201103, May 2011. doi: 10.1103/PhysRevLett.106.201103.
- Yi-Zhong Fan and T. Piran. High-energy γ , ν -ray emission from gamma-ray bursts —, before GLAST,. *Frontiers of Physics in China*, 3(3):306–330, sep 2008. doi: 10.1007/s11467-008-0033-z.
- A. Fassia et al. Optical and infrared photometry of the Type IIn SN 1998S: days 11–146,. , 318(4):1093–1104, November 2000. doi: 10.1046/j.1365-8711.2000.03797.x.
- R. Fernández and B. D. Metzger. Delayed outflows from black hole accretion tori following neutron star binary coalescence,. *Monthly Notices of the Royal Astronomical Society*, 435(1):502–517, 08 2013. ISSN 0035-8711. doi: 10.1093/mnras/stt1312. URL <https://doi.org/10.1093/mnras/stt1312>.
- A. Filippenko et al. The Subluminous, Spectroscopically Peculiar Type Ia Supernova 1991bg in the Elliptical Galaxy NGC 4374,. , 104:1543, October 1992. doi: 10.1086/116339.
- A. V. Filippenko. Supernova 1987K: Type II in Youth, Type Ib in Old Age,. , 96: 1941, December 1988. doi: 10.1086/114940.

- Alexei V. Filippenko. Optical Spectra of Supernovae. , 35:309–355, January 1997. doi: 10.1146/annurev.astro.35.1.309.
- Alexei V. Filippenko, Thomas Matheson, and Luis C. Ho. The “Type IIb” Supernova 1993J in M81: A Close Relative of Type Ib Supernovae. , 415:L103, October 1993. doi: 10.1086/187043.
- R. J Foley et al. The diversity of massive star outbursts. i. observations of sn2009ip, ugc 2773 ot2009-1, and their progenitors. *The Astrophysical Journal*, 732(1):32, 2011.
- S. J. Fossey et al. Supernova 2014J in M82 = Psn J09554214+6940260. *Central Bureau Electronic Telegrams*, 3792:1, January 2014.
- F. Foucart. Black hole neutron star mergers: Disk mass predictions. *Phys. Rev. D*, 86:124007, Dec 2012. doi: 10.1103/PhysRevD.86.124007. URL <https://link.aps.org/doi/10.1103/PhysRevD.86.124007>.
- F. Foucart, T. Hinderer, and S. Nissanke. Remnant baryon mass in neutron star-black hole mergers: Predictions for binary neutron star mimickers and rapidly spinning black holes,. , 98(8):081501, October 2018. doi: 10.1103/PhysRevD.98.081501.
- F. Foucart et al. Neutron star-black hole mergers with a nuclear equation of state and neutrino cooling: Dependence in the binary parameters. *Phys. Rev. D*, 90:024026, Jul 2014. doi: 10.1103/PhysRevD.90.024026. URL <https://link.aps.org/doi/10.1103/PhysRevD.90.024026>.
- M Fraser et al. On the progenitor and early evolution of the type ii supernova 2009kr. *The Astrophysical Journal Letters*, 714(2):L280, 2010.
- M. Fraser et al. Red and dead: the progenitor of sn 2012aw in m95. *The Astrophysical Journal Letters*, 759(1):L13, 2012.
- M. Fraser et al. On the progenitor of the type iip sn 2013ej in m74. *Monthly Notices of the Royal Astronomical Society: Letters*, 439(1):L56–L60, 2014.
- M others Fraser. Sn 2009md: another faint supernova from a low-mass progenitor. *Monthly Notices of the Royal Astronomical Society*, 417(2):1417–1433, 2011.

- C. Fremling et al. PTF12os and iPTF13bvn. Two stripped-envelope supernovae from low-mass progenitors in NGC 5806. , 593:A68, September 2016. doi: 10.1051/0004-6361/201628275.
- Gaia Collaboration. Gaia Data Release 1. Summary of the astrometric, photometric, and survey properties,. , 595:A2, November 2016. doi: 10.1051/0004-6361/201629512.
- A. Gal-Yam. Luminous Supernovae. *Science*, 337(6097):927, August 2012. doi: 10.1126/science.1203601.
- A. Gal-Yam. *Observational and Physical Classification of Supernovae*, page 195. 2017. doi: 10.1007/978-3-319-21846-5_35.
- A. Gal-Yam and L. DC. A massive hypergiant star as the progenitor of the supernova sn 2005gl. *Nature*, 458(7240):865–867, 2009.
- A Gal-Yam et al. A high angular resolution search for the progenitor of the type ic supernova 2004gt. *The Astrophysical Journal Letters*, 630(1):L29, 2005.
- A. Gal-Yam et al. On the progenitor of sn 2005gl and the nature of type iin supernovae. *The Astrophysical Journal*, 656(1):372, 2007.
- T.J. Galama et al. An unusual supernova in the error box of the γ -ray burst of 25 april 1998. *Nature*, 395(6703):670–672, 1998.
- B. Gendre et al. The Ultra-Long Gamma-Ray burst 111209A: the collapse of a blue supergiant?,. *The Astrophysical Journal*, 766(1):30, mar 2013. doi: 10.1088/0004-637x/766/1/30. URL <https://doi.org/10.1088/0004-637x/766/1/30>.
- C. Georgy, G. Meynet, R. Walder, D. Folini, and A. Maeder. The different progenitors of type Ib, Ic SNe, and of GRB,. , 502(2):611–622, aug 2009. doi: 10.1051/0004-6361/200811339.
- S. Gezari et al. Probing shock breakout with serendipitous galex detections of two snls type ii-p supernovae. *The Astrophysical Journal Letters*, 683(2):L131, 2008a.

- S. Gezari et al. Discovery of the ultra-bright type ii-l supernova 2008es. *The Astrophysical Journal*, 690(2):1313, 2008b.
- R. Gilmozzi et al., 1987a.
- R Gilmozzi et al. The progenitor of sn1987a. *Nature*, 328(6128):318–320, 1987b.
- H. L. Gomez et al. Dust in historical Galactic Type Ia supernova remnants with Herschel*. *Monthly Notices of the Royal Astronomical Society*, 420(4):3557–3573, 03 2012. ISSN 0035-8711. doi: 10.1111/j.1365-2966.2011.20272.x. URL <https://doi.org/10.1111/j.1365-2966.2011.20272.x>.
- S. Gomez et al. A galaxy-targeted search for the optical counterpart of the candidate NS–BH merger s190814bv with magellan. *The Astrophysical Journal*, 884(2):L55, oct 2019. doi: 10.3847/2041-8213/ab4ad5. URL <https://doi.org/10.3847/2041-8213/ab4ad5>.
- A. Goobar et al. Constraints on the origin of the first light from sn 2014j. *The Astrophysical Journal*, 799(1):106, jan 2015. doi: 10.1088/0004-637x/799/1/106. URL <https://doi.org/10.1088/0004-637x/799/1/106>.
- A. Grado, M. Capaccioli, L. Limatola, and F. Getman. VST processing facility: first astronomical applications,. *Memorie della Societa Astronomica Italiana Supplementi*, 19:362, January 2012.
- Or Graur, Federica B., and M. Modjaz. A unified explanation for the supernova rate-galaxy mass dependence based on supernovae detected in Sloan galaxy spectra. *Monthly Notices of the Royal Astronomical Society*, 450(1):905–925, 04 2015. ISSN 0035-8711. doi: 10.1093/mnras/stv713. URL <https://doi.org/10.1093/mnras/stv713>.
- L. Greggio. The rates of type Ia supernovae - I. Analytical formulations,. *A&A*, 441(3):1055–1078, 2005. doi: 10.1051/0004-6361:20052926. URL <https://doi.org/10.1051/0004-6361:20052926>.
- L. Greggio. The rates of type Ia supernovae – II. Diversity of events at low and high redshifts,. *Monthly Notices of the Royal Astronomical Society*, 406(1):22–42,

- 07 2010. ISSN 0035-8711. doi: 10.1111/j.1365-2966.2010.16371.x. URL <https://doi.org/10.1111/j.1365-2966.2010.16371.x>.
- L. Greggio and E. Cappellaro. Correlation of the rate of Type Ia supernovae with the parent galaxy properties: Light and shadows. , 625:A113, May 2019. doi: 10.1051/0004-6361/201834932.
- L. Greggio and A. Renzini. The binary model for type I supernovae - Theoretical rates. , 118(2):217–222, February 1983.
- L. Greggio and A. Renzini. *Supernovae*, chapter 7, pages 171–206. John Wiley Sons, Ltd, 2011. ISBN 9783527636617. doi: <https://doi.org/10.1002/9783527636617.ch7>. URL <https://onlinelibrary.wiley.com/doi/abs/10.1002/9783527636617.ch7>.
- J. H. Groh, C. Georgy, and S. Ekström. Progenitors of supernova Ibc: a single Wolf-Rayet star as the possible progenitor of the SN Ib iPTF13bvn. , 558:L1, October 2013. doi: 10.1051/0004-6361/201322369.
- K. Grover et al. Comparison of gravitational wave detector network sky localization approximations,. *Phys. Rev. D*, 89:042004, Feb 2014. doi: 10.1103/PhysRevD.89.042004. URL <https://link.aps.org/doi/10.1103/PhysRevD.89.042004>.
- M. Hamuy, N. B. Suntzeff, J. Bravo, and M. M. Phillips. SN 1987A in the Large Magellanic Cloud. IV. Photometry from the Spectrophotometry,. , 102:888, August 1990. doi: 10.1086/132713.
- M. Hamuy et al. The distance to sn 1999em from the expanding photosphere method. *The Astrophysical Journal*, 558(2):615, 2001.
- M. Hamuy et al. Optical and infrared spectroscopy of sn 1999ee and sn 1999ex. *The Astronomical Journal*, 124(1):417, 2002.
- D. Hardin et al. Type Ia supernova rate at $z \sim 0.1$. , 362:419–425, October 2000.
- R. P. Harkness et al. The Early Spectral Phase of Type Ib Supernovae: Evidence for Helium. , 317:355, June 1987. doi: 10.1086/165283.

- MA Hendry et al. Sn 2004a: another type ii-p supernova with a red supergiant progenitor. *Monthly Notices of the Royal Astronomical Society*, 369(3):1303–1320, 2006.
- J.A. Hinton and W. Hofmann. Teraelectronvolt Astronomy,. *Annual Review of Astronomy and Astrophysics*, 47(1):523–565, 2009. doi: 10.1146/annurev-astro-082708-101816. URL <https://doi.org/10.1146/annurev-astro-082708-101816>.
- Jens Hjorth et al. A very energetic supernova associated with the γ -ray burst of 29 March 2003. , 423(6942):847–850, June 2003. doi: 10.1038/nature01750.
- W. Hofmann. The H.E.S.S. Telescopes,. URL <https://www.mpi-hd.mpg.de/hfm/HESS/pages/about/telescopes/>.
- A. M. Hopkins and J. F. Beacom. On the normalization of the cosmic star formation history. *The Astrophysical Journal*, 651(1):142–154, 2006. doi: 10.1086/506610.
- S. Horiuchi, K. Nakamura, T. Takiwaki, K. Kotake, and M. Tanaka. The red supergiant and supernova rate problems= implications for core-collapse supernova physics. *Monthly Notices of the Royal Astronomical Society= Letters*, 445(1):L99–L103, 09 2014. ISSN 1745-3925. doi: 10.1093/mnrasl/slu146. URL <https://doi.org/10.1093/mnrasl/slu146>.
- S. Horiuchi et al. The Cosmic Core-collapse Supernova Rate Does Not Match the Massive-star Formation Rate,. *The Astrophysical Journal*,, 738(2):154, sep 2011. doi: 10.1088/0004-637X/738/2/154.
- D. J. Hunter et al. Extensive optical and near-infrared observations of the nearby, narrow-lined type Ic <ASTROBJ>SN 2007gr</ASTROBJ>: days 5 to 415,. , 508(1):371–389, December 2009. doi: 10.1051/0004-6361/200912896.
- M. Ilkov and N. Soker. Type Ia supernovae from very long delayed explosion of core-white dwarf merger. , 419(2):1695–1700, January 2012. doi: 10.1111/j.1365-2966.2011.19833.x.

- S. Inoue et al. Gamma-ray burst science in the era of the Cherenkov Telescope Array,. *Astroparticle Physics*, 43:252–275, mar 2013. doi: 10.1016/j.astropartphys.2013.01.004.
- C. Inserra. Observational properties of extreme supernovae,. *Nature Astronomy*, 3: 697–705, August 2019. doi: 10.1038/s41550-019-0854-4.
- C. Inserra et al. The bright type iip sn 2009bw, showing signs of interaction. *Monthly Notices of the Royal Astronomical Society*, 422(2):1122–1139, 2012.
- Mike J. Irwin, Jim Lewis, Simon Hodgkin, Peter Bunclark, Dafydd Evans, Richard McMahan, James P. Emerson, Malcolm Stewart, and Steven Beard. VISTA data flow system: pipeline processing for WFCAM and VISTA. In Peter J. Quinn and Alan Bridger, editors, *Optimizing Scientific Return for Astronomy through Information Technologies*, volume 5493 of *Society of Photo-Optical Instrumentation Engineers (SPIE) Conference Series*, pages 411–422, September 2004. doi: 10.1117/12.551449.
- . Ivezić,, Ž and the LSST Science Collaboration. Lsst science requirements document. 2013.
- Ž Ivezić et al. LSST: From Science Drivers to Reference Design and Anticipated Data Products,. *The Astrophysical Journal*, 873(2):111, March 2019. doi: 10.3847/1538-4357/ab042c.
- K. Iwamoto, K. Nomoto, P. Garnavich, and R. Kirshner. Light Curve Modeling of the Type Ib/ic Supernova 1997EF. In Wolfgang Hillebrandt and Ewald Muller, editors, *Nuclear Astrophysics*, page 138, January 1998.
- Matt J. Jarvis, D. G. Bonfield, V. A. Bruce, J. E. Geach, K. McAlpine, R. J. McLure, E. González-Solares, M. Irwin, J. Lewis, A. Kupcu Yoldas, S. Andreon, N. J. G. Cross, J. P. Emerson, G. Dalton, J. S. Dunlop, S. T. Hodgkin, Fèvre O. Le, M. Karouzos, K. Meisenheimer, S. Oliver, S. Rawlings, C. Simpson, I. Smail, D. J. B. Smith, M. Sullivan, W. Sutherland, S. V. White, and J. T. L. Zwart. The VISTA Deep Extragalactic Observations (VIDEO) survey. *Monthly Notices of the Royal Astronomical Society*, 428(2):1281–1295, 10 2012. ISSN 0035-8711. doi: 10.1093/mnras/sts118. URL <https://doi.org/10.1093/mnras/sts118>.

- A. Jerkstrand et al. The progenitor mass of the Type IIP supernova SN 2004et from late-time spectral modeling,. , 546:A28, oct 2012. doi: 10.1051/0004-6361/201219528.
- G. John. Calibrating Milky Way Maps: An LSST Bright(ish),. 2019.
- R. L. Jones et al. The LSST metrics analysis framework (MAF),. In , volume 9149 of *Society of Photo-Optical Instrumentation Engineers (SPIE) Conference Series*, page 91490B, July 2014. doi: 10.1117/12.2056835.
- C. Juan, G. Florian, and S. Thomas. Technical Performance of the MAGIC Telescopes,, 2009.
- O. Just, A. Bauswein, R. Ardevol Pulpillo, S. Goriely, and H.T. Janka. Comprehensive nucleosynthesis analysis for ejecta of compact binary mergers,. , 448(1):541–567, March 2015. doi: 10.1093/mnras/stv009.
- E. Kankare et al. The nature of supernovae 2010o and 2010p in arp 299–i. near-infrared and optical evolution. *Monthly Notices of the Royal Astronomical Society*, 440(2):1052–1066, 2014.
- I. Karl et al. Nucleosynthetic layers in the shocked ejecta of cassiopea a. *The Astrophysical Journal*, 757(2):126, sep 2012. doi: 10.1088/0004-637x/757/2/126. URL <https://doi.org/10.1088/0004-637x/757/2/126>.
- K. S. Kawabata et al. Optical and Near-infrared Polarimetry of Highly Reddened Type Ia Supernova 2014J: Peculiar Properties of Dust in M82. , 795(1):L4, November 2014. doi: 10.1088/2041-8205/795/1/L4.
- P. L. Kelly et al. Constraints on the Progenitor System of the Type Ia Supernova 2014J from Pre-explosion Hubble Space Telescope Imaging. , 790(1):3, July 2014. doi: 10.1088/0004-637X/790/1/3.
- R. Kessler et al. Snana: A public software package for supernova analysis. *Publications of the Astronomical Society of the Pacific*, 121(883):1028–1035, Sep 2009. ISSN 1538-3873. doi: 10.1086/605984. URL <http://dx.doi.org/10.1086/605984>.

- C. D Kilpatrick et al. On the progenitor of the type iib supernova 2016gkg. *Monthly Notices of the Royal Astronomical Society*, 465(4):4650–4657, 2017.
- R. Kirshner et al. Sn 1992a: ultraviolet and optical studies based on hst, iue and ctio observations. *The Astrophysical journal. Chicago. Vol. 415, no. 2, pt. 1 (Oct. 1993)*, p. 589-615, 1993.
- R. et al Kirshner. Supernova 1987A in the Large Magellanic Cloud,. , 4435:1, August 1987.
- S. Kitsionas, E. Hatziminaoglou, A. Georgakakis, and I. Georgantopoulos. On the use of photometric redshifts for X-ray selected AGNs,. , 434(2):475–482, May 2005. doi: 10.1051/0004-6361:20041916.
- K. Kiuchi et al. Efficient magnetic-field amplification due to the kelvin-helmholtz instability in binary neutron star mergers. *Phys. Rev. D*, 92:124034, Dec 2015. doi: 10.1103/PhysRevD.92.124034. URL <https://link.aps.org/doi/10.1103/PhysRevD.92.124034>.
- C. S. Kochanek, D. M. Szczygiel, and K. Z. Stanek. The Supernova Impostor Impostor SN 1961V: Spitzer Shows That Zwicky Was Right (Again),. , 737(2):76, August 2011. doi: 10.1088/0004-637X/737/2/76.
- C. S. Kochanek et al. Supernova progenitors, their variability and the Type IIP Supernova ASASSN-16fq in M66. *Monthly Notices of the Royal Astronomical Society*, 467(3):3347–3360, 02 2017. ISSN 0035-8711. doi: 10.1093/mnras/stx291. URL <https://doi.org/10.1093/mnras/stx291>.
- C. Kouveliotou et al. Identification of Two Classes of Gamma-Ray Bursts. , 413: L101, August 1993. doi: 10.1086/186969.
- O. Krause et al. Tycho brahe’s 1572 supernova as a standard type ia as revealed by its light-echo spectrum. *Nature*, 456(7222):617–619, 2008.
- M. Kriek et al. An Ultra-Deep Near-Infrared Spectrum of a Compact Quiescent Galaxy at $z = 2.2$. , 700(1):221–231, July 2009. doi: 10.1088/0004-637X/700/1/221.

- R. G. Kron. Photometry of a complete sample of faint galaxies.,. *The Astrophysical Journal Supplement Series*, 43:305–325, June 1980. doi: 10.1086/190669.
- K. Kuijken. An Axisymmetric Distribution Function for the Galactic Bulge.,. *The Astrophysical Journal*, 446:194, June 1995. doi: 10.1086/175778.
- K. Kuijken and R. M. Rich. Hubble Space Telescope WFPC2 Proper Motions in Two Bulge Fields: Kinematics and Stellar Population of the Galactic Bulge.,. , 124(4): 2054–2066, October 2002. doi: 10.1086/342540.
- K. Kyutoku, H. Okawa, M. Shibata, and K. Taniguchi. Gravitational waves from spinning black hole-neutron star binaries: dependence on black hole spins and on neutron star equations of state.,. , 84(6):064018, September 2011. doi: 10.1103/PhysRevD.84.064018.
- K. Kyutoku et al. Neutrino transport in black hole-neutron star binaries: Neutrino emission and dynamical mass ejection. *Phys. Rev. D*, 97:023009, Jan 2018. doi: 10.1103/PhysRevD.97.023009. URL <https://link.aps.org/doi/10.1103/PhysRevD.97.023009>.
- J. M. Lattimer and D. N. Schramm. Black-Hole-Neutron-Star Collisions.,. , 192:L145, September 1974. doi: 10.1086/181612.
- B. Leibundgut et al. Sn 1991bg-a type ia supernova with a difference. *The Astrophysical journal. Chicago. Vol. 415, no. 2, pt. 1 (Oct. 1993), p. 589-615*, 1993.
- N. P. Lemoine. Moving beyond noninformative priors: why and how to choose weakly informative priors in bayesian analyses. *Oikos*, 128(7):912–928, 2019. doi: 10.1111/oik.05985. URL <https://onlinelibrary.wiley.com/doi/abs/10.1111/oik.05985>.
- D. Leonard et al. The distance to sn 1999em in ngc 1637 from the expanding photosphere method. *Publications of the Astronomical Society of the Pacific*, 114(791): 35, 2001.
- D. Leonard et al. A study of the type ii-plateau supernova 1999gi and the distance to its host galaxy, ngc 3184. *The Astronomical Journal*, 124(5):2490, 2002.

- D.C Leonard et al. An upper mass limit on a red supergiant progenitor for the type ii-plateau supernova sn 2006my. *Publications of the Astronomical Society of the Pacific*, 120(874):1259, 2008.
- W. Li. On the progenitors of two type ii-p supernovae in the virgo cluster. *The Astrophysical Journal*, 661(2):1013, 2007.
- W. Li et al. Sn 2002cx: the most peculiar known type ia supernova. *Publications of the Astronomical Society of the Pacific*, 115(806):453, 2003.
- W. Li et al. On the progenitor of the type ii supernova 2004et in ngc 6946. *Publications of the Astronomical Society of the Pacific*, 117(828):121, 2005.
- W. Li et al. Identification of the Red Supergiant Progenitor of Supernova 2005cs: Do the Progenitors of Type II-P Supernovae Have Low Mass?., , 641(2):1060–1070, April 2006a. doi: 10.1086/499916.
- W. Li et al. Identification of the red supergiant progenitor of supernova 2005cs: Do the progenitors of type ii-p supernovae have low mass? *The Astrophysical Journal*, 641(2):1060, 2006b.
- W. Li et al. Nearby supernova rates from the Lick Observatory Supernova Search - III. The rate-size relation, and the rates as a function of galaxy Hubble type and colour. , 412(3):1473–1507, April 2011a. doi: 10.1111/j.1365-2966.2011.18162.x.
- W. D. Li. Supernova 1999em in NGC 1637. , 7294:1, October 1999.
- Weidong Li et al. Nearby supernova rates from the Lick Observatory Supernova Search - II. The observed luminosity functions and fractions of supernovae in a complete sample. , 412(3):1441–1472, April 2011b. doi: 10.1111/j.1365-2966.2011.18160.x.
- M. Limongi and A. Chieffi. The Chemical Yields Produced by a Zero M and others Generation of Core Collapse Supernovae and Their Comparison with the Chemical Composition of Extremely M and others Poor Stars,. In Hillebrandt W. and Leibundgut B., editors, *From Twilight to Highlight: The Physics of Supernovae*, page 367, January 2003. doi: 10.1007/10828549_49.

- P. Lira et al. Optical light curves of the type ia supernovae sn 1990n and sn 1991t. *The Astronomical Journal*, 115(1):234, 1998.
- LSST Science Collaboration. LSST Science Book, Version 2.0,. *arXiv e-prints*, art. arXiv:0912.0201, December 2009.
- P. Lundqvist et al. No trace of a single-degenerate companion in late spectra of supernovae 2011fe and 2014J. , 577:A39, May 2015. doi: 10.1051/0004-6361/201525719.
- J. Lyman et al. Ligo/virgo g298048: epesto optical spectra of the candidate optical/nir counterpart of the gravitational wave g298048 in ngc4993. *GRB Coordinates Network*, 21582:1, 2017.
- P. Madau and M. Dickinson. Cosmic star-formation history. *Annual Review of Astronomy and Astrophysics*, 52(1):415–486, 2014. doi: 10.1146/annurev-astro-081811-125615. URL <https://doi.org/10.1146/annurev-astro-081811-125615>.
- D. S. Madgwick et al. Spectroscopic Detection of Type Ia Supernovae in the Sloan Digital Sky Survey. , 599(1):L33–L36, December 2003. doi: 10.1086/381081.
- MAGIC Collaboration. Teraelectronvolt emission from the γ -ray burst GRB 190114C. , 575(7783):455–458, November 2019. doi: 10.1038/s41586-019-1750-x.
- MAGIC Collaboration, V. A. Acciari, et al. Observation of inverse Compton emission from a long γ -ray burst. , 575(7783):459–463, November 2019. doi: 10.1038/s41586-019-1754-6.
- K. Maguire et al. Optical and near-infrared coverage of SN 2004et: physical parameters and comparison with other Type IIP supernovae. , 404(2):981–1004, May 2010. doi: 10.1111/j.1365-2966.2010.16332.x.
- K. Maguire et al. Optical and near-infrared coverage of SN 2004et: physical parameters and comparison with other Type IIP supernovae. *Monthly Notices of the Royal Astronomical Society*, 404(2):981–1004, 05 2010. ISSN 0035-8711. doi: 10.1111/j.1365-2966.2010.16332.x. URL <https://doi.org/10.1111/j.1365-2966.2010.16332.x>.

- J. Maíz-Apellániz et al. The progenitor of the type II-p SN 2004dj in NGC 2403. *The Astrophysical Journal*, 615(2):L113–L116, oct 2004. doi: 10.1086/426120. URL <https://doi.org/10.1086/426120>.
- D. Malesani et al. SN 2003lw and GRB 031203: A Bright Supernova for a Faint Gamma-Ray Burst. , 609(1):L5–L8, July 2004. doi: 10.1086/422684.
- F. Mannucci, G. Cresci, R. Maiolino, and M. Della Valle. The Infrared Supernova Rate. *arXiv e-prints*, art. astro-ph/0310210, October 2003.
- F. Mannucci et al. The supernova rate per unit mass. *A&A*, 433(3):807–814, 2005. doi: 10.1051/0004-6361:20041411. URL <https://doi.org/10.1051/0004-6361:20041411>.
- F. Mannucci et al. The supernova rate in local galaxy clusters. , 383(3):1121–1130, January 2008. doi: 10.1111/j.1365-2966.2007.12603.x.
- D. Maoz and O. Graur. Star formation, supernovae, iron, and α : consistent cosmic and galactic histories. *The Astrophysical Journal*, 848(1):25, October 2017. doi: 10.3847/1538-4357/aa8b6e.
- D.C. Martin et al. The galaxy evolution explorer: A space ultraviolet survey mission. *The Astrophysical Journal*, 619(1):L1–L6, jan 2005. doi: 10.1086/426387. URL <https://doi.org/10.1086/426387>.
- N. Masetti, A. Malizia, A. J. Dean, A. Bazzano, and R. Walter. Optical spectroscopic identification of candidate counterparts to four INTEGRAL sources. *The Astronomer’s Telegram*, 957:1, December 2006.
- T. Matheson et al. Optical Spectroscopy of Type ia Supernovae,. , 135(4):1598–1615, April 2008. doi: 10.1088/0004-6256/135/4/1598.
- DS Mathewson and JN Clarke. Supernova remnants in the large magellanic cloud. *The Astrophysical Journal*, 180:725–738, 1973.
- S Mattila et al. Vlt detection of a red supergiant progenitor of the type ii-p supernova 2008bk. *The Astrophysical Journal Letters*, 688(2):L91, 2008.

- S. Mattila et al. Core-collapse supernovae missed by optical surveys. *The Astrophysical Journal*, 756(2):111, aug 2012. doi: 10.1088/0004-637x/756/2/111. URL <https://doi.org/10.1088/0004-637x/756/2/111>.
- S. Mattila et al. Supernovae and radio transients in M82. *Monthly Notices of the Royal Astronomical Society*, 431(3):2050–2062, 03 2013. ISSN 0035-8711. doi: 10.1093/mnras/stt202. URL <https://doi.org/10.1093/mnras/stt202>.
- J. R Maund, S.J Smartt, and I. J. Danziger. The progenitor of sn 2005cs in the whirlpool galaxy. *Monthly Notices of the Royal Astronomical Society: Letters*, 364(1):L33–L37, 2005.
- J. R. Maund et al. The massive binary companion star to the progenitor of supernova 1993J,. , 427(6970):129–131, January 2004a. doi: 10.1038/nature02161.
- J. R. Maund et al. The massive binary companion star to the progenitor of supernova 1993J,. , 427(6970):129–131, January 2004b. doi: 10.1038/nature02161.
- J. R andand others Maund. Whatever happened to the progenitors of supernovae 2008cn, 2009kr and 2009md? *Monthly Notices of the Royal Astronomical Society*, 447(4):3207–3217, 2015.
- J.R. Maund and S. J. Smartt. Hubble space telescope imaging of the progenitor sites of six nearby core-collapse supernovae. *Monthly Notices of the Royal Astronomical Society*, 360(1):288–304, 2005.
- J.R Maund, E. Reilly, and S. Mattila. A late-time view of the progenitors of five type iip supernovae. *Monthly Notices of the Royal Astronomical Society*, 438(2): 938–958, 2014.
- JR Maund et al. The yellow supergiant progenitor of the type ii supernova 2011dh in m51. *The Astrophysical Journal Letters*, 739(2):L37, 2011.
- JR Maund et al. Supernova 2012ec: identification of the progenitor and early monitoring with pessto. *Monthly Notices of the Royal Astronomical Society: Letters*, 431(1):L102–L106, 2013.

- J.R. et al. Maund. The yellow supergiant progenitor of the type II supernova 2011dh in M51. *739(2):L37*, sep 2011. doi: 10.1088/2041-8205/739/2/137. URL <https://doi.org/10.1088/2041-8205/739/2/137>.
- S. Maximilian et al. Optical photometry of the type Ia supernova 1999ee and the type Ibc supernova 1999ex in IC5179. *The Astronomical Journal*, 124(4):2100–2117, oct 2002. doi: 10.1086/342544. URL <https://doi.org/10.1086/342544>.
- P. A. Mazzali, L. B. Lucy, I. J. Danziger, C. Gouiffes, E. Cappellaro, and M. Turatto. Models for the early-time spectral evolution of the 'standard' type Ia supernova 1990N. *Astronomical Journal*, 269:423–445, March 1993.
- P. A. Mazzali, K. Nomoto, K. Maeda, and J. Deng. Asphericity in Type Ic Supernovae: A link to GRBs. *Nuovo Cimento B Serie*, 121(10):1223–1228, October 2006b. doi: 10.1393/ncb/i2007-10238-5.
- P. A. Mazzali et al. The Type Ic Hypernova SN 2002ap. *Astronomical Journal*, 572(1):L61–L65, June 2002. doi: 10.1086/341504.
- P. A. Mazzali et al. The Metamorphosis of Supernova SN 2008D/XRF 080109: A Link Between Supernovae and GRBs/Hypernovae. *Science*, 321(5893):1185, August 2008. doi: 10.1126/science.1158088.
- C. McCully et al. The rapid reddening and featureless optical spectra of the optical counterpart of GW170817, AT 2017gfo, during the first four days. *The Astrophysical Journal*, 848(2):L32, oct 2017. doi: 10.3847/2041-8213/aa9111. URL <https://doi.org/10.3847/2041-8213/aa9111>.
- ros P. Mé, szá, Razzaque S., and Zhang B. GeV-TeV emission from γ , -ray bursts. *Astronomical Journal*, 48(5-6):445–451, apr 2004. doi: 10.1016/j.newar.2003.12.022.
- T. Melson et al. Neutrino-driven explosion of a 20 solar-mass star in three dimension enabled by strange-quark contribution to neutrino-neutrino scattering. *The Astrophysical Journal*, 808(2):L42, Jul 2015. ISSN 2041-8213. doi: 10.1088/2041-8205/808/2/142. URL <http://dx.doi.org/10.1088/2041-8205/808/2/142>.
- B. D. Metzger. Kilonovae. *Living Reviews in Relativity*, 23(1):1, 2019. doi: 10.1007/s41114-019-0024-0. URL <https://doi.org/10.1007/s41114-019-0024-0>.

- M Miceli, S Sciortino, E Troja, and S Orlando. Spatial distribution of x-ray emitting ejecta in tycho's snr: indication od shocked titanium. *The Astrophysical Journal*, 805(2):120, may 2015. doi: 10.1088/0004-637x/805/2/120. URL <https://doi.org/10.1088/0004-637x/805/2/120>.
- E. Michaely and H.B. Perets. Supernova and prompt gravitational-wave precursors to LIGO, gravitational-wave sources and short GRBs,. *The Astrophysical Journal*, 855(1):L12, mar 2018. doi: 10.3847/2041-8213/aaacfc. URL <https://doi.org/10.3847/2041-8213/aaacfc>.
- D. Milisavljevic and R. A. Fesen. *The Supernova – Supernova Remnant Connection*, pages 2211–2231. Springer International Publishing, Cham, 2017. ISBN 978-3-319-21846-5. doi: 10.1007/978-3-319-21846-5_97. URL https://doi.org/10.1007/978-3-319-21846-5_97.
- D. Milisavljevic et al. Metamorphosis of sn 2014c: delayed interaction between a hydrogen poor core-collapse supernova and a nearby circumstellar shell. *The Astrophysical Journal*, 815(2):120, 2015.
- R. Minkowski. Spectra of Supernovae. , 53(314):224, August 1941. doi: 10.1086/125315.
- M. Modjaz, K. Z. Stanek, P. M. Garnavich, P. Berlind, S. Blondin, W. Brown, M. Calkins, P. Challis, A. M. Diamond-Stanic, H. Hao, M. Hicken, R. P. Kirshner, and J. L. Prieto. Early-Time Photometry and Spectroscopy of the Fast Evolving SN 2006aj Associated with GRB 060218. , 645(1):L21–L24, July 2006. doi: 10.1086/505906.
- Maryam Modjaz, Claudia P. Gutierrez, and Iair Arcavi. New Regimes in the Observation of Core-Collapse Supernovae. *Nature Astron.*, 3(8):717–724, 2019. doi: 10.1038/s41550-019-0856-2.
- T. J. Moriya, M. V. Pruzhinskaya, M. Ergon, and S. I. Blinnikov. On the nature of rapidly fading Type II supernovae,. *Monthly Notices of the Royal Astronomical Society*, 455(1):423–430, 11 2015. ISSN 0035-8711. doi: 10.1093/mnras/stv2336. URL <https://doi.org/10.1093/mnras/stv2336>.

- V. Morozova, D. Radice, A. Burrows, and D. Vartanyan. The Gravitational Wave Signal from Core-collapse Supernovae,. *The Astrophysical Journal*, 861(1):10, jun 2018. doi: 10.3847/1538-4357/aac5f1. URL <https://doi.org/10.3847/1538-4357/aac5f1>.
- V. Morozova, A. L. Piro, J. Fuller, and S. D. Van Dyk. The influence of late-stage nuclear burning on red supergiant supernova light curves. *The Astrophysical Journal*, 891(2):L32, mar 2020. doi: 10.3847/2041-8213/ab77c8. URL <https://doi.org/10.3847/2041-8213/ab77c8>.
- J. W. Murphy, C. D. Ott, and A. Burrows. A model for gravitational wave emission from neutrino-driven core-collapse supernovae,. *The Astrophysical Journal*, 707(2):1173–1190, dec 2009. doi: 10.1088/0004-637x/707/2/1173. URL <https://doi.org/10.1088/0004-637x/707/2/1173>.
- A. Muzzin et al. The evolution of dusty star formation and stellar mass assembly in clusters: Results from the irac 3.6, 4.5, 5.8, and 8.0 μm cluster luminosity functions. *The Astrophysical Journal*, 686(2):966, 2008.
- A. Muzzin et al. A Public K_s -selected Catalog in the COSMOS/ULTRAVISTA Field: Photometry, Photometric Redshifts, and Stellar Population Parameters. , 206(1):8, May 2013. doi: 10.1088/0067-0049/206/1/8.
- Takayoshi Nakamura, Paolo A. Mazzali, Ken’ichi Nomoto, and Koichi Iwamoto. Light Curve and Spectral Models for the Hypernova SN 1998BW Associated with GRB 980425. , 550(2):991–999, April 2001. doi: 10.1086/319784.
- National Research Council. *Astronomy and Astrophysics in the New Millennium*,. The National Academies Press, Washington, DC, 2001. ISBN 978-0-309-07031-7. doi: 10.17226/9839. URL <https://www.nap.edu/catalog/9839/astronomy-and-astrophysics-in-the-new-millennium>.
- National Research Council. *Connecting Quarks with the Cosmos: Eleven Science Questions for the New Century*,. The National Academies Press, Washington, DC, 2003a. ISBN 978-0-309-07406-3. doi: 10.17226/10079. URL <https://www.nap.edu/catalog/10079/connecting-quarks-with-the-cosmos-eleven-science-questions-for-the>.

- National Research Council. *New Frontiers in the Solar System: An Integrated Exploration Strategy*,. The National Academies Press, Washington, DC, 2003b. doi: 10.17226/10432. URL <https://www.nap.edu/catalog/10432/new-frontiers-in-the-solar-system-an-integrated-exploration-strategy>.
- National Research Council. *New Worlds, New Horizons in Astronomy and Astrophysics*,. The National Academies Press, Washington, DC, 2010. ISBN 978-0-309-15799-5. doi: 10.17226/12951. URL <https://www.nap.edu/catalog/12951/new-worlds-new-horizons-in-astronomy-and-astrophysics>.
- L. Nava. High-energy emission from gamma-ray bursts,. *International Journal of Modern Physics D*, 27(13):1842003, jan 2018. doi: 10.1142/S0218271818420038.
- M. T. B. Nielsen, M. Gilfanov, Á. Bogdán, T. E. Woods, and G. Nelemans. Upper limits on the luminosity of the progenitor of Type Ia supernova SN 2014J. , 442(4):3400–3406, August 2014. doi: 10.1093/mnras/stu913.
- Jr. Oemler, A. and B. M. Tinsley. Type I supernovae come from short-lived stars. , 84:985–992, July 1979. doi: 10.1086/112502.
- C. D Ott. TOPICAL REVIEW: The gravitational-wave signature of core-collapse supernovae. *Classical and Quantum Gravity*, 26(6):063001, March 2009. doi: 10.1088/0264-9381/26/6/063001.
- A. Pastorello and M. Fraser. Supernova impostors and other gap transients. *Nature Astronomy*, 3:676–679, August 2019. doi: 10.1038/s41550-019-0809-9.
- A. Pastorello et al. Low-luminosity type ii supernovae: spectroscopic and photometric evolution. *Monthly Notices of the Royal Astronomical Society*, 347(1):74–94, 2004.
- A. Pastorello et al. Sn 2005cs in m51–i. the first month of evolution of a subluminous sn ii plateau. *Monthly Notices of the Royal Astronomical Society*, 370(4):1752–1762, 2006.
- A. Pastorello et al. The type iib sn 2008ax: spectral and light curve evolution. *Monthly Notices of the Royal Astronomical Society*, 389(2):955–966, 2008.

- A. Pastorello et al. Sn 2005cs in m51–ii. complete evolution in the optical and the near-infrared. *Monthly Notices of the Royal Astronomical Society*, 394(4):2266–2282, 2009a.
- A. Pastorello et al. Sn 1999ga: a low-luminosity linear type ii supernova? *Astronomy & Astrophysics*, 500(3):1013–1023, 2009b.
- A. Pastorello et al. Interacting Supernovae and Supernova Impostors: SN 2009ip, is this the End? , 767(1):1, April 2013. doi: 10.1088/0004-637X/767/1/1.
- A. Pastorello et al. Massive stars exploding in a He-rich circumstellar medium - IV. Transitional Type Ibn supernovae. , 449(2):1921–1940, May 2015. doi: 10.1093/mnras/stu2745.
- A. Pastorello et al. Luminous red novae: Stellar mergers or giant eruptions? , 630:A75, October 2019a. doi: 10.1051/0004-6361/201935999.
- A. Pastorello et al. Luminous red novae: Stellar mergers or giant eruptions? *Astronomy & Astrophysics*, 630:A75, 2019b.
- F. Patat et al. The type ia supernova 1994d in ngc 4526: the early phases. *Monthly Notices of the Royal Astronomical Society*, 278(1):111–124, 1996.
- F. Patat et al. The metamorphosis of sn 1998bw. *The Astrophysical Journal*, 555(2):900, 2001.
- F. Patat et al. Properties of extragalactic dust inferred from linear polarimetry of Type Ia Supernovae. , 577:A53, May 2015. doi: 10.1051/0004-6361/201424507.
- Daniel J. Patnaude and Robert A. Fesen. A Comparison of X-Ray and Optical Emission in Cassiopeia A. , 789(2):138, July 2014. doi: 10.1088/0004-637X/789/2/138.
- S.M Percival, M. Salaris, S. Cassisi, and A. Pietrinferni. A large stellar evolution database for population synthesis studies. integrated properties and spectra. *The Astrophysical Journal*, 690(1):427–439, dec 2008. doi: 10.1088/0004-637x/690/1/427. URL <https://doi.org/10.1088/0004-637x/690/1/427>.

- M. A. Pérez-Torres et al. Constraints on the Progenitor System and the Environs of SN 2014J from Deep Radio Observations. , 792(1):38, September 2014. doi: 10.1088/0004-637X/792/1/38.
- S. Perlmutter et al. Measurements of the cosmological parameters $\{upOmega$ and $\{upLambda$ from the first seven supernovae at $z \geq 0.35$. *The Astrophysical Journal*, 483(2):565–581, jul 1997. doi: 10.1086/304265. URL <https://doi.org/10.1086/304265>.
- S. Perlmutter et al. Measurements of Omega and Lambda from 42 High-Redshift Supernovae. In J. Paul, T. Montmerle, and E. Aubourg, editors, *19th Texas Symposium on Relativistic Astrophysics and Cosmology*, page 146, December 1998.
- K. Perrett et al. Evolution in the volumetric type ia supernova rate from the supernova legacy survey. *The Astronomical Journal*, 144(2):59, 2012.
- P. Podsiadlowski, P. C. Joss, and J. J. L. Hsu. Presupernova Evolution in Massive Interacting Binaries,. , 391:246, May 1992a. doi: 10.1086/171341.
- Ph. Podsiadlowski, P. C. Joss, and J. J. L. Hsu. Presupernova Evolution in Massive Interacting Binaries,. , 391:246, May 1992b. doi: 10.1086/171341.
- M. Pozzo et al. On the source of the late-time infrared luminosity of sn 1998s and other type ii supernovae. *Monthly Notices of the Royal Astronomical Society*, 352(2):457–477, 2004.
- Yu. P. Pskovskii. Mean Integral Absolute Magnitudes of Galaxies of Different Subtypes in Our Neighborhood of the Metagalaxy and in the Virgo Cluster. , 5:387, December 1961.
- Yu. P. Pskovskii. The Type and Absolute-Magnitude Distributions of Galaxies Containing Supernovae. , 44:1139, January 1967.
- M. L. Pumo and L. Zampieri. Evolution of the main observables in core-collapse supernova events: a radiation-hydrodynamical modelling. *Memorie della Societa Astronomica Italiana Supplementi*, 19:201, January 2012.

- S. P. Reynolds. Supernova remnants at high energy. *Annual Review of Astronomy and Astrophysics*, 46(1):89–126, 2008. doi: 10.1146/annurev.astro.46.060407.145237. URL <https://doi.org/10.1146/annurev.astro.46.060407.145237>.
- D. Richardson, R. L. Jenkins III, J. Wright, and L. Maddox. Absolute-magnitude distributions of supernovae. *The Astronomical Journal*, 147(5):118, 2014.
- Michael W. Richmond, Richard R. Treffers, Alexei V. Filippenko, Young Paik, Bruno Leibundgut, Eric Schulman, and Caroline V. Cox. UBVRI Photometry of SN 1993J in M81: The First 120 Days. , 107:1022, March 1994. doi: 10.1086/116915.
- M.W. Richmond et al. UBVRI Photometry of the Type IA SN 1994D in NGC 4526,. , 109:2121, May 1995. doi: 10.1086/117437.
- Wilson Ricks and Vikram V. Dwarkadas. Excavating the explosion and progenitor properties of type IIP supernovae via modeling of their optical light curves. *The Astrophysical Journal*, 880(1):59, jul 2019. doi: 10.3847/1538-4357/ab287c. URL <https://doi.org/10.3847/1538-4357/ab287c>.
- A. G. Riess et al. Observational evidence from supernovae for an accelerating universe and a cosmological constant. *The Astronomical Journal*, 116(3):1009–1038, sep 1998. doi: 10.1086/300499. URL <https://doi.org/10.1086/300499>.
- V. Riot et al. Lsst camera optics design. *Proc SPIE*, 09 2012. doi: 10.1117/12.926710.
- L.F. Roberts et al. The influence of neutrinos on r-process nucleosynthesis in the ejecta of black hole–neutron star mergers,. *Monthly Notices of the Royal Astronomical Society*, 464(4):3907–3919, 10 2016. ISSN 0035-8711. doi: 10.1093/mnras/stw2622. URL <https://doi.org/10.1093/mnras/stw2622>.
- P. Ruiz-Lapuente. Tycho brahe’s supernova: light from centuries past. *The Astrophysical Journal*, 612(1):357, 2004.
- P. Ruiz-Lapuente et al. Modeling the Iron-dominated Spectra of the Type IA Supernova SN 1991T at Premaximum,. , 387:L33, March 1992. doi: 10.1086/186299.
- S Ryder et al. Sn 1978k: an extraordinary supernova in the nearby galaxy ngc 1313. *The Astrophysical Journal*, 416:167, 1993.

- Kullback S. and Leibler R. A. On information and sufficiency. *The Annals of Mathematical Statistics*, 22(1):79–86, 1951. ISSN 00034851.
- D. K. Sahu, G. C. Anupama, S. Srividya, and S. Muneer. Photometric and spectroscopic evolution of the Type IIP supernova SN 2004et. , 372(3):1315–1324, November 2006. doi: 10.1111/j.1365-2966.2006.10937.x.
- M. Sako et al. Photometric Type Ia Supernova Candidates from the Three-year SDSS-II SN Survey Data. , 738(2):162, September 2011. doi: 10.1088/0004-637X/738/2/162.
- L. Salmon, L. Hanlon, R. M. Jeffrey, and A. Martin-Carrillo. Web application for galaxy-targeted follow-up of electromagnetic counterparts to gravitational wave sources. , 634:A32, February 2020. doi: 10.1051/0004-6361/201936573.
- E. M. Schlegel. H α Profiles of Type II Supernovae. In *Bulletin of the American Astronomical Society*, volume 22, page 1214, September 1990.
- B. P. Schmidt et al. Measuring Cosmic Deceleration and Global Curvature from Observations of Distant Supernovae. In *American Astronomical Society Meeting Abstracts*, volume 189 of *American Astronomical Society Meeting Abstracts*, page 108.05, December 1996.
- K. Scholberg. Supernova neutrino detection. *Annual Review of Nuclear and Particle Science*, 62(1):81–103, 2012. doi: 10.1146/annurev-nucl-102711-095006. URL <https://doi.org/10.1146/annurev-nucl-102711-095006>.
- D. Van Dyk Schuyler, Li Weidong, and V. Filippenko Alexei. On the progenitor of the type II,-plateau supernova 2003gd in m74. *Publications of the Astronomical Society of the Pacific*, 115(813):1289–1295, nov 2003. doi: 10.1086/378308. URL <https://doi.org/10.1086/378308>.
- M. Shibata and K. Taniguchi. Coalescence of Black Hole-Neutron Star Binaries,. *Living Reviews in Relativity*, 14(1):6, August 2011. doi: 10.12942/lrr-2011-6.
- L. P Singer et al. The first two years of electromagnetic follow-up with advanced ligo and virgo. *The Astrophysical Journal*, 795(2):105, 2014.

- M.F. Skrutskie et al. The Two Micron All Sky Survey (2MASS),. *The Astronomical Journal*, 131(2):1163–1183, feb 2006. doi: 10.1086/498708. URL <https://doi.org/10.1086/498708>.
- S. Smartt et al. Detection of a red supergiant progenitor star of a type ii-plateau supernova. *Science*, 303(5657):499–503, 2004a.
- S. J. Smartt. Progenitors of Core-Collapse Supernovae,. , 47(1):63–106, September 2009. doi: 10.1146/annurev-astro-082708-101737.
- S. J. Smartt. Observational Constraints on the Progenitors of Core-Collapse Supernovae: The Case for Missing High-Mass Stars,. , 32:e016, April 2015. doi: 10.1017/pasa.2015.17.
- S. J Smartt et al. An upper mass limit for the progenitor of the type ii-p supernova sn 1999gi. *The Astrophysical Journal Letters*, 556(1):L29, 2001.
- S. J Smartt et al. The nature of the progenitor of the type ii-p supernova 1999em. *The Astrophysical Journal*, 565(2):1089, 2002a.
- S. J. Smartt et al. PESSTO: survey description and products from the first data release by the Public ESO Spectroscopic Survey of Transient Objects,. , 579:A40, jul 2015. doi: 10.1051/0004-6361/201425237.
- SJ Smartt, JJ Eldridge, RM Crockett, and JR Maund. The death of massive stars—i. observational constraints on the progenitors of type ii-p supernovae. *Monthly Notices of the Royal Astronomical Society*, 395(3):1409–1437, 2009.
- SJ Smartt et al. On the progenitor of the type ic supernova 2002ap. *The Astrophysical Journal Letters*, 572(2):L147, 2002b.
- SJ Smartt et al. Mass limits for the progenitor star of supernova 2001du and other type ii-p supernovae. *Monthly Notices of the Royal Astronomical Society*, 343(3):735–749, 2003.
- S.J. Smartt et al. Detection of a red supergiant progenitor star of a type ii-plateau supernova. *Science (New York, N. Y.)*, 303(5657):499—503, January 2004b.

ISSN 0036-8075. doi: 10.1126/science.1092967. URL <https://doi.org/10.1126/science.1092967>.

- M. Smith et al. The sdss-ii supernova survey: parameterizing the type ia supernova rate as a function of host galaxy properties. *The Astrophysical Journal*, 755(1):61, jul 2012. doi: 10.1088/0004-637x/755/1/61. URL <https://doi.org/10.1088/0004-637x/755/1/61>.
- N. Smith. *Interacting Supernovae: Types II_n and Ib_n*, page 403. 2017. doi: 10.1007/978-3-319-21846-5_38.
- N. Smith et al. Discovery of precursor luminous blue variable outbursts in two recent optical transients: the fitfully variable missing links ugc 2773-ot and sn 2009ip. *The Astronomical Journal*, 139(4):1451, 2010.
- N. Smith et al. Episodic mass loss in binary evolution to the Wolf-Rayet phase: Keck and HST proper motions of RY Scuti’s nebula,. , 418(3):1959–1972, December 2011. doi: 10.1111/j.1365-2966.2011.19614.x.
- L. Spitzer Jr. *Physical processes in the interstellar medium*. John Wiley & Sons, 2008.
- K. Z. Stanek, D. Bersier, P. M. Garnavich, S. T. Holland, and T. Matheson. GRB030329/SN2003dh: Late Time Light Curve, Jitter Event. In *American Astronomical Society Meeting Abstracts*, volume 203 of *American Astronomical Society Meeting Abstracts*, page 132.03, December 2003.
- I. A. Steele et al. The Liverpool Telescope: performance and first results. In Jr. Oschmann, Jacobus M., editor, *Ground-based Telescopes*, volume 5489 of *Society of Photo-Optical Instrumentation Engineers (SPIE) Conference Series*, pages 679–692, October 2004. doi: 10.1117/12.551456.
- L-G. Strolger et al. The Hubble Higher z Supernova Search: Supernovae to $z \sim 1.6$ and Constraints on Type Ia Progenitor Models. , 613(1):200–223, September 2004. doi: 10.1086/422901.

- M. Sullivan et al. Rates and Properties of Type Ia Supernovae as a Function of Mass and Star Formation in Their Host Galaxies. , 648(2):868–883, September 2006. doi: 10.1086/506137.
- Patrick J. Sutton. A Rule of Thumb for the Detectability of Gravitational-Wave Bursts. *arXiv e-prints*, art. arXiv:1304.0210, March 2013.
- F. Taddia et al. Carnegie Supernova Project: Observations of Type II_n supernovae. , 555:A10, July 2013. doi: 10.1051/0004-6361/201321180.
- K Takáts et al. Sn 2009ib: a type ii-p supernova with an unusually long plateau. *Monthly Notices of the Royal Astronomical Society*, 450(3):3137–3154, 2015.
- O. Takeshi et al. Implications for galaxy evolution from cosmic evolution of the supernova rate density. , 60:169, April 2008. doi: 10.1093/pasj/60.2.169.
- G. A. Tammann. *Remarks on Outlying Supernovae and the Structure of Their Parent Galaxies*, volume 45, page 215. 1974. doi: 10.1007/978-94-010-2166-1_25.
- L Tartaglia et al. The progenitor and early evolution of the type iib sn 2016gkg. *The Astrophysical Journal Letters*, 836(1):L12, 2017.
- S. Taubenberger. *The Extremes of Thermonuclear Supernovae*, page 317. 2017. doi: 10.1007/978-3-319-21846-5_37.
- S. Taubenberger et al. SN 2004aw: confirming diversity of Type Ic supernovae,. , 371(3):1459–1477, September 2006. doi: 10.1111/j.1365-2966.2006.10776.x.
- S. et al Taubenberger. The He-rich stripped-envelope core-collapse supernova 2008ax,. , 413(3):2140–2156, May 2011. doi: 10.1111/j.1365-2966.2011.18287.x.
- S. Tawny and M.K. Ness. The age distribution of stars in the milky way bulge. *The Astrophysical Journal*, 900(1):4, aug 2020. doi: 10.3847/1538-4357/ab9ff6. URL <https://doi.org/10.3847/1538-4357/ab9ff6>.
- The LIGO Scientific Collaboration, the Virgo Collaboration, R. Abbott, T. D. Abbott, et al. GW190412: Observation of a Binary-Black-Hole Coalescence with Asymmetric Masses. *arXiv e-prints*, art. arXiv:2004.08342, April 2020.

- C C Thöne et al. Sn 2015bh: Ngc 2770’s 4th supernova or a luminous blue variable on its way to a wolf-rayet star? *Astronomy & Astrophysics*, 599:A129, 2017.
- L. Tomasella et al. Comparison of progenitor mass estimates for the type iip sn 2012a. *Monthly Notices of the Royal Astronomical Society*, 434(2):1636–1657, 2013.
- J. L. Tonry et al. ATLAS: A High-cadence All-sky Survey System. , 130(988):064505, June 2018. doi: 10.1088/1538-3873/aabadf.
- E. Troja et al. Swift/bat detection of hard x-rays from tycho’s supernova remnant: evidence fro titanium-44. *The Astrophysical Journal*, 797(1):L6, nov 2014. doi: 10.1088/2041-8205/797/1/16. URL <https://doi.org/10.1088/2041-8205/797/1/16>.
- M. Turatto. *Classification of Supernovae.*, volume 598, pages 21–36. 2003. doi: 10.1007/3-540-45863-8_3.
- M. Turatto et al. The properties of the peculiar type ia supernova 1991bg—i. analysis and discussion of two years of observations. *Monthly Notices of the Royal Astronomical Society*, 283(1):1–17, 1996.
- M. et al Turatto. The properties of supernova 1997cy associated with grb 970514. *The Astrophysical Journal Letters*, 534(1):L57, 2000.
- V. P. Utrobin. An optimal hydrodynamic model for the normal type IIP supernova 1999em. , 461(1):233–251, January 2007. doi: 10.1051/0004-6361:20066078.
- V. P. Utrobin and N. N. Chugai. High mass of the type IIP supernova 2004et inferred from hydrodynamic modeling. , 506(2):829–834, November 2009. doi: 10.1051/0004-6361/200912273.
- V. P. Utrobin and N. N. Chugai. Parameters of type IIP SN 2012A and clumpiness effects. , 575:A100, March 2015. doi: 10.1051/0004-6361/201424822.
- M. Vaccari et al. The VOICE Survey : VST Optical Imaging of the CDFS and ES1 Fields. In *The 4th Annual Conference on High Energy Astrophysics in Southern Africa (HEASA 2016)*, page 26, January 2016.

- S. Valenti et al. The broad-lined Type Ic supernova 2003jd*. *Monthly Notices of the Royal Astronomical Society*, 383(4):1485–1500, 12 2007. ISSN 0035-8711. doi: 10.1111/j.1365-2966.2007.12647.x. URL <https://doi.org/10.1111/j.1365-2966.2007.12647.x>.
- S. Valenti et al. The Carbon-rich Type Ic SN 2007gr: The Photospheric Phase, , 673 (2):L155, February 2008. doi: 10.1086/527672.
- S. at al. Valenti. Sn 2009jf: a slow-evolving stripped-envelope core-collapse supernova. *Monthly Notices of the Royal Astronomical Society*, 416(4):3138–3159, 2011.
- S. van den Bergh and R. D. McClure. Supernova rates and galaxy inclinations. *The Astrophysical Journal*, 359:277–279, 1990.
- S. Van den Bergh, R. D. McClure, and R. Evans. The supernova rate in shapley-ames galaxies. *The Astrophysical Journal*, 323:44–53, 1987.
- Sidney van den Bergh. Supernova Rates, Galaxy Emission, and Hubble Type. , 101: 845, March 1991. doi: 10.1086/115729.
- S. Van Dyk et al. The progenitor of supernova 2011dh/ptf11eon in messier 51. *The Astrophysical Journal Letters*, 741(2):L28, 2011a.
- S. Van Dyk et al. The red supergiant progenitor of supernova 2012aw (ptf12bvh) in messier 95. *The Astrophysical Journal*, 756(2):131, 2012.
- S. Van Dyk et al. The type iib supernova 2013df and its cool supergiant progenitor. *The Astronomical Journal*, 147(2):37, 2014.
- S. D Van Dyk. The direct identification of core-collapse supernova progenitors. *Philosophical Transactions of the Royal Society A: Mathematical, Physical and Engineering Sciences*, 375(2105):20160277, 2017.
- S. D. Van Dyk, W. Li, and A. V. Filippenko. On the progenitor of supernova 2001du in ngc 1365. *Publications of the Astronomical Society of the Pacific*, 115(806):448, 2003a.
- S. D Van Dyk et al. Sn 1997bs in m66: another extragalactic η carinae analog? *Publications of the Astronomical Society of the Pacific*, 112(778):1532, 2000.

- S. D Van Dyk et al. Supernova 2008bk and its red supergiant progenitor. *The Astronomical Journal*, 143(1):19, 2011b.
- S.D Van Dyk, W. Li, and A. V Filippenko. A search for core-collapse supernova progenitors in hubble space telescope images. *Publications of the Astronomical Society of the Pacific*, 115(803):1, 2002.
- S.D Van Dyk, W. Li, and A.V. Filippenko. On the progenitor of the type ii-plateau supernova 2003gd in m74. *Publications of the Astronomical Society of the Pacific*, 115(813):1289, 2003b.
- A. J. Van Marle, S. P. Owocki, and N. J. Shaviv. Continuum-driven winds from super-*eddington* stars: A tale of two limits. In Brian W. O’Shea and Alexander Heger, editors, *First Stars III*, volume 990 of *American Institute of Physics Conference Series*, pages 250–253, March 2008. doi: 10.1063/1.2905555.
- M. H. P. M. van Putten et al. Prospects for multi-messenger extended emission from core-collapse supernovae in the Local Universe. *European Physical Journal Plus*, 134(10):537, October 2019. doi: 10.1140/epjp/i2019-12932-3.
- J. Veitch et al. Parameter estimation for compact binaries with ground-based gravitational-wave observations using the LALInference software library, . , 91(4): 042003, February 2015. doi: 10.1103/PhysRevD.91.042003.
- T. Virginia. The distance to the crab nebula and NP 0532. *Publications of the Astronomical Society of the Pacific*, 85:579, oct 1973. doi: 10.1086/129507. URL <https://doi.org/10.1086/129507>.
- Zhao W. and Santos L. Model-independent measurement of the absolute magnitude of type ia supernovae with gravitational-wave sources. *Journal of Cosmology and Astroparticle Physics*, 2019(11):009–009, nov 2019. doi: 10.1088/1475-7516/2019/11/009. URL <https://doi.org/10.1088/1475-7516/2019/11/009>.
- X. Wang et al. The progenitor of SN 2004dj in a star cluster. *The Astrophysical Journal*, 626(2):L89–L92, jun 2005. doi: 10.1086/431903. URL <https://doi.org/10.1086/431903>.

- D. C. Warren and J. M. Blondin. Three-dimensional numerical investigations of the morphology of type Ia SNe. *Monthly Notices of the Royal Astronomical Society*, 429(4):3099–3113, 2013.
- J. C. Wheeler. Introduction of supernovae., In J. C. Wheeler, T. Piran, and S. Weinberg, editors, *Supernovae, Jerusalem Winter School for Theoretical Physics*, pages 1–93, January 1990.
- J. C. Wheeler and R. P. Harkness. Type I supernovae. *Reports on Progress in Physics*, 53(12):1467–1557, December 1990. doi: 10.1088/0034-4885/53/12/001.
- J. C. Wheeler and R. Levreault. The peculiar type I supernova in NGC 991. , 294: L17–L20, July 1985. doi: 10.1086/184500.
- J. C. Wheeler, R. P. Harkness, A. Clocchiatti, S. Benetti, M. S. Brotherton, D. L. Depoy, and J. Elias. SN 1994I in M51 and the nature of type IBC supernovae. , 436:L135–L138, December 1994. doi: 10.1086/187651.
- G. L. White and D. F. Malin. Possible binary star progenitor for SN 1987a. *Nature*, 327 (6117):36–38, 1987.
- S. M. Wilkins, C. C. Lovell, and E. R. Stanway. Recalibrating the cosmic star formation history. , 490(4):5359–5365, December 2019. doi: 10.1093/mnras/stz2894.
- R. J. Williams et al. The evolving relation between size, mass, surface density and star formation in 10^4 galaxies since $z = 2$. *The Astrophysical Journal*, 713(2):738–750, mar 2010. doi: 10.1088/0004-637x/713/2/738. URL <https://doi.org/10.1088/0004-637x/713/2/738>.
- L. Woltjer. Supernova remnants. *Annual Review of Astronomy and Astrophysics*, 10 (1):129–158, 1972. doi: 10.1146/annurev.aa.10.090172.001021. URL <https://doi.org/10.1146/annurev.aa.10.090172.001021>.
- S. E. Woosley and J. S. Bloom. The Supernova Gamma-Ray Burst Connection. , 44 (1):507–556, September 2006. doi: 10.1146/annurev.astro.43.072103.150558.

- S. E. Woosley and T. A. Weaver. The Evolution and Explosion of Massive Stars. II. Explosive Hydrodynamics and Nucleosynthesis, , 101:181, nov 1995. doi: 10.1086/192237.
- S. E. Woosley, P. A. Pinto, P. G. Martin, and T. A. Weaver. Supernova 1987A in the Large Magellanic Cloud: The Explosion of a approximately 20 M_{sun} , Star Which Has Experienced Mass Loss?, , 318:664, July 1987. doi: 10.1086/165402.
- L. Xiao and J. J. Eldridge. Core-collapse supernova rate synthesis within 11 mpc. *Monthly Notices of the Royal Astronomical Society*, 452(3):2597–2605, 07 2015. ISSN 0035-8711. doi: 10.1093/mnras/stv1425. URL <https://doi.org/10.1093/mnras/stv1425>.
- L. Xiao, W. Reich, E. Fürst, and J. L. Han. Radio properties of the low surface brightness SNR G65.2+5.7. , 503(3):827–836, September 2009. doi: 10.1051/0004-6361/200911706.
- L. Zampieri. Exploring the Physics of Type II Supernovae,. In Tiziana di Salvo, Gian Luca Israel, Luciano Piersant, Luciano Burderi, Giorgio Matt, Amedeo Tornambe, and Maria Teresa Menna, editors, *The Multicolored Landscape of Compact Objects and Their Explosive Origins*, volume 924 of *American Institute of Physics Conference Series*, pages 358–365, August 2007. doi: 10.1063/1.2774881.
- W. Zheng et al. Estimating the First-light Time of the Type Ia Supernova 2014J in M82. , 783(1):L24, March 2014. doi: 10.1088/2041-8205/783/1/L24.
- Z. Zou, X. Zhou, and Y.-F. Huang. The gravitational wave emission of double white dwarf coalescences. *Research in Astronomy and Astrophysics*, 20(9):137, September 2020. doi: 10.1088/1674-4527/20/9/137.
- F. Zwicky. On the frequency of supernovae. ii. *The Astrophysical Journal*, 96:28, July 1942. doi: 10.1086/144430.
- F Zwicky. Ngc 1058 and its supernova 1961. *The Astrophysical Journal*, 139:514, 1964.
- F. Zwicky. Basic results of the international search for supernovae. *Annales d’Astrophysique*, 27:300, 1970. doi: 1964AnAp...27..300Z.